THE ROLE OF HYALURONAN-RICH ECM IN THE REGULATION OF GUT AND VASCULAR MORPHOGENESIS

A Dissertation

Presented to the Faculty of the Graduate School

of Cornell University

In Partial Fulfillment of the Requirements for the Degree of

Doctor of Philosophy

by

Aravind Sivakumar

August 2017

THE ROLE OF HYALURONAN-RICH ECM IN THE REGULATION OF GUT AND VASCULAR MORPHOGENESIS

Aravind Sivakumar, Ph.D.

Cornell University 2017

During embryonic development, organ morphogenesis is driven by coordination and alignment of local cellular behaviors with the three body axes: dorsal-ventral (DV), anterior-posterior (AP) and left-right (LR) axes. This involves translation and amplification of molecular chirality defined by genetically encoded spatial cues into asymmetric cell behavior that is critical for defining the organ's form and function.

The gastrointestinal tract, displaying profound LR asymmetries, presents itself as a powerful model to study the asymmetric mechanisms involved in the establishment of its stereotypical looping topology and patterning of its vasculature. Asymmetric looping morphogenesis of the gut initiates with a critical leftward tilt directed by the evolutionarily conserved LR pathway. Failure to do so leads to gut malrotation and the catastrophic midgut volvulus, highlighting an urgent need to define the molecular basis of this process. Previous research in mice and birds has shown that the leftward tilt of the gut is established by cellular and extracellular asymmetries across the LR axis of the dorsal mesentery (DM), which suspends the gut tube. The left DM condenses while the right expands causing the DM to tilt the gut tube leftward, and this critical bias determines gut chirality. Concomitantly, vasculogenesis of the gut proceeds within the left DM but is excluded on the right, suggesting that the cellular processes within the DM are also employed to pattern abdominal blood vessels. While the left DM has been

shown to be under the control of the left-determining transcription factor Pitx2, the mechanisms that regulate the expansion and vascular exclusion specific to the right DM have remained unknown.

Surprisingly, my research demonstrates that the expansion of the right DM *precedes all other cell asymmetries* that collectively deform this structure, suggesting that the key initiator of asymmetric gut tilting derives from the right side. Hyaluronan (HA), a unique and highly conserved glycosaminoglycan, predominates in the extracellular matrix (ECM) of the right DM. Targeted degradation of HA in the right DM ablates expansion, gut tilting and results in aberrant retention of vasculature in the right DM. This unexpected finding demonstrates that HA is a critical regulator of the ECM expansion and vascular exclusion necessary for asymmetric gut looping and vascular morphogenesis. Investigating into how HA enacts its functions, I show that the tumor necrosis factor alpha-inducible protein 6 (Tsg6/Tnfaip6), an enzyme that covalently modifies HA *to form a stable heavy chain (HC) HA complex*, is restricted to the right DM. Knockdown of Tsg6 on the right prevents ECM expansion, gut tilting, and disrupts the normal process of vascular exclusion, leading to aberrant gut vascular patterning. Furthermore, misexpression of Tsg6 in the left DM prevents the formation of abdominal blood vessels demonstrating that Tsg6 is both necessary and sufficient to inhibit gut vascular development. The ability of Tsg6 to mediate ECM expansion and vascular exclusion is dependent on its enzymatic ability to covalent modify HA. Further analysis of Tsg6 knockout mice revealed randomized gut looping chirality and gut malrotations in Tsg6 mutant embryos that predispose them volvulus.

Collectively, my study identifies a new pathway during LR organogenesis initiated by HA-rich ECM on the right side of the embryo and presents a novel mouse model to understand the origin of gut malrotations and vascular anomalies.

BIOGRAPHICAL SKETCH

Aravind Sivakumar was born on 24th May 1988 in Pondicherry, one of the Union territories of India and a beautiful city with a rich historic past and a very diverse culture due to the colonial influences of the Dutch, Portuguese, British and French. It is also considered as the land of many saints & sadhus.

He had his primary education at The Sacred Heart Convent School which is a century old institution in the district of Villupuram, Tamil Nadu. He pursued his secondary education at DAV Public School and Junior college at Padma Seshadri Bala Bhavan in the district of Chennai, Tamilnadu. Growing up in a traditional Indian family, Aravind's parents enrolled him in Violin classes to learn Carnatic Music at the age of five which continued till his junior college. Apart from his educational excellence, he actively participated in several inter-school dramas and music competitions and won rolling cups and individual medals.

In 2005, he got admission in Birla Institute of Technology, Goa (BITS-Goa) for pursuing his undergraduate studies after clearing the premier BITSAT entrance exam in the first year of its introduction. He chose the five-year dual degree program in BE (hons) Mechanical engineering and MSc (hons) Biological Sciences after being inspired to study artificial organ engineering by his cousins. At BITS-Goa, his curiosity in biology was crystallized into a strong passion for doing research in Biological Sciences due to the excellent mentorship that he received from Dr. Utpal Roy, Dr. SK Ray, Dr. Meenal Kowshik and particularly from Dr Kuttalaprakash Chudalayandi who was most instrumental in igniting the relentless curiosity and inspiring him to consider research as a fulfilling career. In his final year (2009), via the Practice School program, he did his

MSc thesis at the National Centre for Biological Sciences (TIFR), Bangalore under the mentorship of Dr. Shiva Shankar where he got introduced to the field of Mechanobiology.

After completing his undergraduate studies, he worked briefly as a research assistant at the Stem Cell Research lab, Vision research foundation, Sankara Nethralaya, Chennai (2010-2011) under the guidance of Dr. S. Krishnakumar, MD. Finding research as an exciting career option, he decided to do PhD in Biological Sciences. He applied and got admission to pursue his PhD studies at Cornell University in 2011. At Cornell he joined Dr. Natasza Kurpios's lab due to his inherent fascination with embryos as the ultimate feat of nature's engineering. It is his personal opinion that it was here where he learnt the true meaning and satisfaction of hard work. It was also here, where Aravind met his wife Dr. Aparna Mahadevan, his partner in life, science and music. Under the immense guidance of Dr. Kurpios, his confidence in his innate ability to do science has increased several fold and he is currently excited to give his best to have a career in academia as he strides towards the future.

DEDICATION

I dedicate this thesis:

To my deeply spiritual parents, who have given me physical ability to observe, the mental capacity to imagine and the spiritual capacity to wonder, who have nurtured me to where I am today, seeing me through every season, every joy and pain I have been through, who have been the most supportive in every of my decisions, who have showered me with so much of unrequited love, care and affection, who have always kept the faith in me, and always prayed for the best for me;

To my sister who did not live to see me do this, but whose presence I have always felt in my life;

To my parents-in-law, for their understanding, patience, inspiration and faith that have bestowed in me, and for their unwavering support and prayers;

To my dear loving wife, my symbiotic soulmate, my strongest pillar of support, my inspiration, life partner who celebrates my joys as hers, who has put up with my flaws and whose limitless patience has comforted me at times of desolation and frustration, who has given me the inner strength to endure challenges and convert them into conquests, who shares the same inner desire to evolve into the highest possibility of being a human, while being by my side at all times, ensuring my sanity and making this a joyous memorable experience;

To the embryo, whose accuracy and precision humbles the engineer in me, whose elegance and grace makes me realize my insignificance and my worries even more insignificant, whose existence is so much beyond my understanding that it is frustrating and maddening, and yet addictive and hypnotizing to try and comprehend its secrets.

ACKNOWLEDGEMENTS

First and foremost, I would like to express my deepest gratitude to my advisor Dr. Natasza Kurpios, whom I regard as an ideal guru. The word guru in Sanskrit refers to a person who creates, sustains knowledge and destroys weeds of ignorance. From Day 1, her exceptional guidance and straight forward style of mentorship has been key in enabling me to refine my passion for asking questions, for giving me the mental strength to challenge what I perceived as my limitations, for being extremely accessible and open to my ideas and for the numerous occasions in which she has provided the intellectual and the personal counselling that have been key in contributing to my success and shaping my personality.

I would like to sincerely thank my committee members Dr. Kelly Liu for her exceptional kindness, thoughtfulness, and intellectual discussions and support during the committee meetings, and Dr. Jonathan Butcher, for inspiring out of the box thinking by challenging me with thought provoking questions, and ideas. I am also extremely thankful to Drs. Drew Noden, Vince Hascall, Rusty Lansford and the late Dr. Mark Lauer for their invaluable intellectual and technical contributions that were critical to the development of my project.

I would also like to take this opportunity to thank the Kurpios lab family for their endless help, support that have contributed to my growth in the lab, starting with David Gludish whose timely advice and profound insights immensely inspired me when I first joined the lab. Special thanks to Dr. Ian Welsh (Vanilla Ice Sensei), who as the first graduate student, set the standard for intellectual rigor and taught me how to look at the embryo, in addition to teaching a bit of yoga, martial arts while simultaneously sharing useful insights about the scientific world. I am extremely thankful to Dr. Aparna Mahadevan (Choconut) (my lab mate who became my wife) for giving me

countless hours of much needed intellectual, mental, technical and emotional support and for having the godly hand that can surgically insert a burger in the embryo if needed without killing it. Special thanks to Frances Chen, my fellow member of the Kurpios right lab for the many enjoyable and fascinating scientific and philosophical discussions about life, universe and everything. Many thanks and good karma wishes to Shing Hu, the new Lab Ninja for her humor, for sharing the same passion for food and for putting up with my cultural and historic ramblings. Special thanks to Brittany Laslow, for handling my mutant mice with a lot of care and affection. I would also like to specially thank all undergrads, rotation students and technicians whom I have trained and worked with - Siddhesh Ramesh, Ricky Narvaez, Athina Angel, Melissa Werner, Samah Hoque, Prerana Bhattacharya, Mike Thomson, Joel Brown, Jeff Jorgensen, Asmita Bhattacharya, Adam O' Neal for their phenomenal technical assistance and for helping me to drive my project at a faster pace that would not have been possible otherwise without them.

I would also like to thank Dr. Rebecca Williams, Carol Bayles and Johannah de la Cruz for training me in confocal, multiphoton and light sheet microscopy. Special thanks to Debra Crane, Cindy Grey, Robin Beebe, Vicki Shaff, Ginger Tomassini, Greg Mitchell for providing the administrative and peripheral support for navigating grad school.

Last but not the least, my salutation of gratitude to the mice, chickens, quails, universe, cosmos and the blessings of Lord Ganesha and Shirdi Sainath that enabled me to reach this milestone.

TABLE OF CONTENTS

CHAPTER 1: INTRODUCTION

1.1 Organ morphogenesis – an interplay between shape, form, and function

Morphogenesis is a dynamic process that is elegantly choreographed to sculpt the embryo as it transitions from a formless single cell into a multicellular organism with an exquisitely defined form and structure. The initial phase of embryonic development involves rapid proliferation to give rise to a population of cells while maintaining the spherical symmetry of the single cell state. To transform this spherical ball of cells into a functional organism requires the timely break of symmetries based on genetically encoded spatial cues defined by heterogeneous molecular distributions that define the coordinate axes (anterior-posterior, AP; dorsal-ventral, DV; and left-right, LR) of the embryo (Nelson CM, 2012). These global spatial cues are then differentially interpreted across fields of cells resulting in the specification of unique cellular identities which determine the cell fates (Weischaus E, 2016). Accompanying the specification of cell fates are complex changes in gene expression and epigenetic states that ultimately modify the physical properties and behavior of cells to generate the stereotypical morphological patterns (Cheedipudi S, 2014). A principal challenge in studying organ morphogenesis is how global patterning signals and individual cellular responses are coordinated for tissue growth and remodeling.

At the level of a single cell, morphogenesis is choreographed by integration of global signaling cues with cell intrinsic transcriptional networks. This regulates cell–cell adhesion, cell-matrix adhesion, cytoskeletal remodeling and actomyosin-based contractility in order to modulate the cortical tension within cells that defines the cell's shape and how the cell packaged within the tissue. The resulting changes range from large-scale changes, such as cell elongation, to local modulations in cell shape, such as the formation of specialized cell protrusions (Lecuit T, 2007). Within cell populations, the global signaling networks are integrated with cues in the microenvironment which regulates cellular behaviors such as oriented cell division, cell migration,

cellular rearrangements and programmed cell death (Bischoff M, 2009). *This concept forms the premise for Chapter 3 of this thesis* (Invited review for the Journal of Cell Biology). At the level of tissues, interactions between different cell populations lead to the formation and remodeling of tissue-specific connective matrices. The matrices reciprocally modulate the cellular behaviors and integrate the forces generated at the cellular level to give rise to global alterations in tissue morphology such as bending of epithelial sheets, tissue rotations, tissue narrowing and extension due to cell intercalation (Bonnans C, 2014). These processes are coordinated with the establishment of organ-specific vascular and neuronal networks to ultimately give rise to functional organs.

1.2 Overview of asymmetric left-right (LR) morphogenesis

While the precise mechanisms involved in the specification of coordinate axes during organ morphogenesis have been challenging to study in vertebrate systems, it is known that the AP and DV axes are defined before or during fertilization (Cowan CR, 2004; Goldstein B, 1996; St Johnston D, 1992). Following the definition of the AP and DV axes, vertebrates subsequently specify their left- right (LR) axes (Levin M, 2005). On the exterior, the body plan of vertebrates appears bilaterally symmetric. Yet, internally, the vertebrate body plan exhibits striking and conserved asymmetries in the position or shape of the viscera (Neville C, 1976). Failure to follow the conserved asymmetries results in an important class of birth defects such as heterotaxia (where the individual organ systems are mispositioned randomly on the left or the right sides), dextrocardia (reversal of the positioning and morphology of the heart), isomerisms (mirroring of the LR axis resulting in the loss of unpaired organs) and situs inversus total (a complete reversal of the left and right sides) (Casey B., 2000) (Figure 1.1).

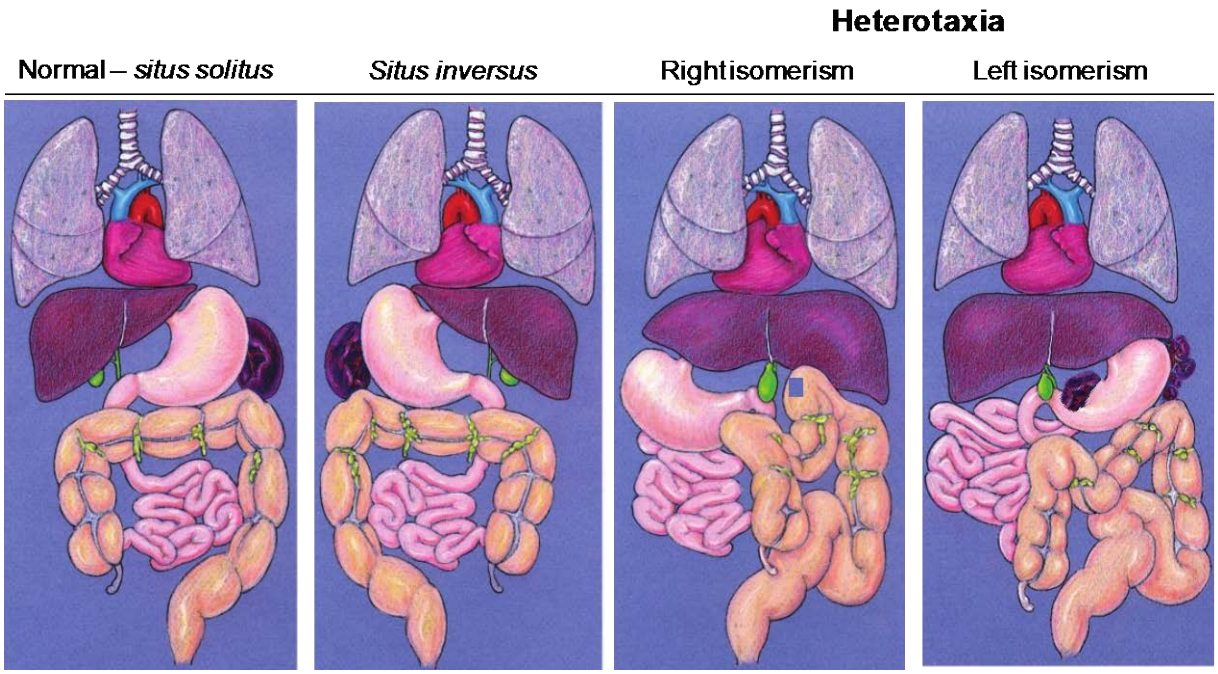

Figure 1.1: Classification of *situs solitus* and *situs* anomalies. (Top panel – left to right) Under normal situs (*situs solitus*), organs are positioned in their respective locations. *Situs inversus* is a condition where all the organs have a reversed orientation. Right isomerism and left isomerism fall under the group of conditions known as heterotaxia. In cases for right isomerism (double-right), there is absence of the spleen (asplenia) and in cases of left isomerism (double left) there is bilateral presence of the spleen (polysplenia). The abdominal organs in both cases have ambiguous positions and intestinal malrotation is frequently observed. (Figure adapted from Fulcher AS and Turner MA, 2002)

Importantly the LR asymmetries extend beyond the basic body plan and contribute to structure, circuitry and function of organs. Well-studied examples include the heart, brain, gut and abdominal vasculature (Davis NM, 2008; Guglielmotti V, 2006; Kurpios NA, 2008; Mahadevan A, 2014; Roussigne M, 2012; Savin T, 2011; Welsh IC, 2013). Additionally, LR biases have also been observed in cancers (mammary, ovarian, lung and testicular) (Wilting J, 2011), disease conditions (infection of the kidney and eyes) (Schreuder MF, 2011; Vaibhav P. Pai, 2012) and birth defects (cleft palate, unilateral polydactyly) (Paulozzi LJ, 1999; Schnall BS, 1974). Thus, the

study of the generation of asymmetry holds fundamental importance for both developmental biology and biomedical applications.

The traditional model for the establishment of LR asymmetries during development is a linear model where the first phase involves the breaking of the bilateral symmetry relative to the AP and DV axes using biophysical mechanisms (Levin M, 2007; Wang G, 2013). One physical candidate for providing the chirality is the directional fluid flow triggered by motile cilia in the node of early neurulating embryos (Basu B, 2008). The resulting directional fluid flow is thought to contribute to the asymmetric accumulation of morphogens to the left side of the midline resulting in induction of differential expression of genes on the left and right sides of the midline in the second phase (Tanaka Y, 2005). In the third phase, the differential expression of genes triggers differential cell behavior downstream of the gene expression pathways to drive asymmetric positioning and shape of organs. While mouse models provide strong evidence for the ciliary flow mechanism as the physical regulator of LR asymmetry (Basu B, 2008; McGrath J, 2003; Tabin CJ, 2003), this does not explain the establishment of LR asymmetries in other vertebrates and animals with non-motile cilia or lacking ciliated structures (snails, sea urchins, C. Elegans, Drosophila, chick and pig) (Adams DS, 2006; Gros J, 2009; Männer J, 2001; Okumura T, 2008). Furthermore, while the model of ciliary flow as the initiator of asymmetry presumes the existence of bilateral symmetries before the initiation of ciliary rotation, asymmetric distributions of small signaling molecules have been shown to exist prior to cilial formation (Albrieux M, 2000; Bunney TD, 2003; Roberts RM, 2011). Thus, the search for the origin of asymmetry extends far upstream of neurulation. In addition to the cilial model, other competing models have been proposed that attribute the initiation of LR asymmetries to intracellular chiralities observed within the blastula such as asymmetric placement of K+ and ATPase ion pumps, anti-clockwise rotation

of the centrioles, the chiralities of the cytoskeleton and asymmetric chromatid segregation (Danilchik MV, 2011; Levin M, 2007; Qiu D, 2005; Sauer S, 2012) (Figure 1.2A). While considerable evidence supports these models, it is not clear how these sub-cellular asymmetries are prioritized and amplified to give rise to LR asymmetries. Furthermore, none of the proposed models have been able to explain the full range of experimental results suggesting that multiple mechanisms could contribute to the physical initiation of asymmetry (Vandenberg LN, 2009).

Downstream of physical chiralities, physiological mechanisms and gene regulatory networks function to amplify the subcellular chiralities into asymmetric cell behavior. These gene regulatory networks consist of sequentially interacting left and right sided genes (Figure 1.2B). The asymmetric gene expression initiates with Sonic hedgehog (Shh), a signaling molecule initially expressed within the ectoderm of the node, which becomes restricted to the left side of the node due to the presence of Activin receptor IIA (cAct-RIIA), a known repressor of Shh on the right side (Levin M, 1998; Streit, 1994). Thus, the inhibition of Shh on the right side gives rise to the left side-restricted gene expression during early development. The expression of Shh subsequently induces the expression of Nodal in the adjacent ectodermal cells of the node. Nodal, being a member of the TGF-β superfamily and an extracellular morphogen that can induce its own expression, is rapidly induced in the left lateral plate mesoderm (LPM) and serves as the master regulator that is necessary and sufficient for establishing the left sided identity (Levin M, 1997). At the same time, the notochord drives the expression of Lefty1, an antagonizer of Nodal in the embryonic midline to restrict Nodal to the left side (Bisgrove BW, 1999).

A

	Chromatid segregation	Ion flux	Ciliary flow
Origin of asymmetry	Epigenetic mark Centriole, mitotic apparatus	Entry of sperm sets DV axis Centriole, chiral cytoskeleton	Cilia Centriole at base of cilia
Mechanism	Epigenetic mark on a left-right specifying GeneX causes differential imprinting and asymmetrically activates Nodal cascade	Chiral cytoskeleton, asymmetrically distributes ion transporters, and allows positively charged molecules which repress Nodal to accumulate on the right side.	Biased cilia-driven fluid flow causes morphogens and Ca ions, which induce Nodal expression to be accumulated on the left side
Induction of gene expression	Epigenetic mark GeneX GeneX Nodal	Nodal Nodal Nodal Nodal	Ca Ca Nodal

B

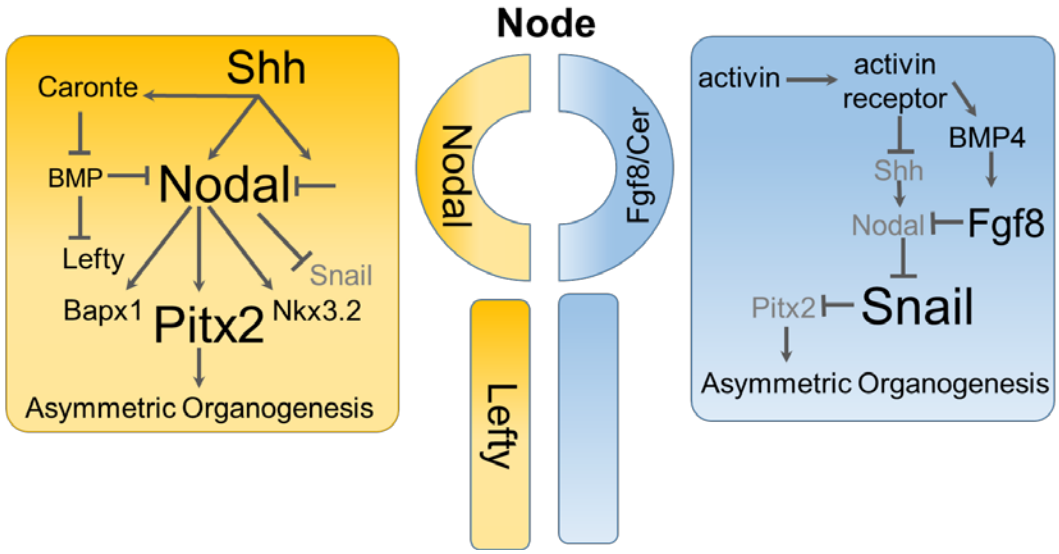

Figure 1.2: A) Competing models for the initiation of chirality: chromatid segregation, ion flux and ciliary flow model all of them serve to establish asymmetric expression of Nodal in LPM **B)** The early gene regulatory networks of the left and the right side. While left has specific regulators to drive asymmetric morphogenesis, the right sided genes mainly function to repress the left sided genes. (Adapted from (McDowell G, 2016 #46;Levin M, 2005 #2)

Perturbation and misexpression studies have revealed that while the expression of Nodal in the left LPM is transient, timed expression of nodal during early development is sufficient to activate a dense cascade of left sided genes (Levin M, 2005). The most distal member of this network is the homeobox transcription factor Pitx2, which serves as the memory of Nodal and is expressed strictly in the left LPM. However, unlike the other LR genes, asymmetric expression of *Pitx2* is maintained in the visceral organs that later become lateralized (Raya A, 2006). Also, Pitx2 is the most downstream effector that directly regulates organ-specific left-sided cellular behaviors to direct asymmetric organ morphogenesis (Piedra ME, 1998). This left-sided activation of Nodal, Pitx2, and the corresponding inhibitor Lefty is one of the most conserved and canonical pathways in vertebrates and mammals for specification of the left side identity. Intriguingly, while much is known about the genes that regulate cellular behavior on the left side, the right side remains unexplored with little known about the downstream genes involved in the regulation of the right-sided cellular behavior.

Recent studies investigating proteins with roles in the establishment of early embryonic symmetry have revealed surprising anomalies to the Nodal-Lefty-Pitx2 pathway (McDowell G, 2016). While misexpression of intercellular myosin motor proteins in the blastula results in incorrect expression of Nodal on the right side, the number of embryos with reversed organs is drastically reduced compared to embryos with incorrect Nodal expression (McDowell GS, 2016). Thus, the misexpression of Nodal despite its established role as a “master regulator” of the left side identity, does not lead to a reversal of organs in all the cases. Hence the pathway from Nodal to organ situs is not as linear as had been assumed (McDowell G, 2016). These observations also suggest the presence of other Nodal-Pitx2 independent mechanisms that reinforce and reinstate the proper asymmetric positioning of organs.

1.3 LR asymmetric morphogenesis of the intestine

The human intestine is of remarkable length, approximately a 30 feet long. Yet, it is very efficiently packaged within the limited space of the body cavity. This is accomplished by timely introduction of loops during gut development. Although, the intestine may appear as a random bundle of loops, the topology of looping is evolutionarily conserved across organisms of the same species. Failure to follow this stereotypical pattern of looping leads to intestinal malrotation anomalies which are fairly frequent in humans, occurring in 1 in 500 live births (Torres AM, 1993). Different classifications of intestinal malrotations have been described in the literature. These have been categorized into: 1) True malrotation with a narrow mesenteric stalk; 2) Nonrotation with a broad mesentery; 3) Atypical malrotation defined as malpositioning of the duodenum and the cecum with respect to one another (Graziano K, 2015). Those individuals with true malrotation are at greatest risk where the contorted twisting of different segments of the gut tube around each other leads to a life-threatening condition known as midgut volvulus characterized by gastrointestinal (GI) occlusion and strangulation of the associated mesenteric vasculature (Filston HC, 1981; Torres AM, 1993) (Figure 1.3). Furthermore, malrotation of the intestines has been reported to occur frequently in association with other malformations (or syndromes) such as gut atresias, short bowel syndrome, biliary/liver/pancreatic malformations, heart defects, and recurrent respiratory symptoms including asthma and aspirations, which often tend to overshadow malrotations during diagnosis in terms of severity and significance (Langer JC, 2017). This observed association of intestinal malrotations with GI and cardiovascular deformities suggest that the regulatory mechanisms of gut looping morphogenesis are common to and may affect the functional morphogenesis of other organs. Furthermore, congenital malrotations are currently

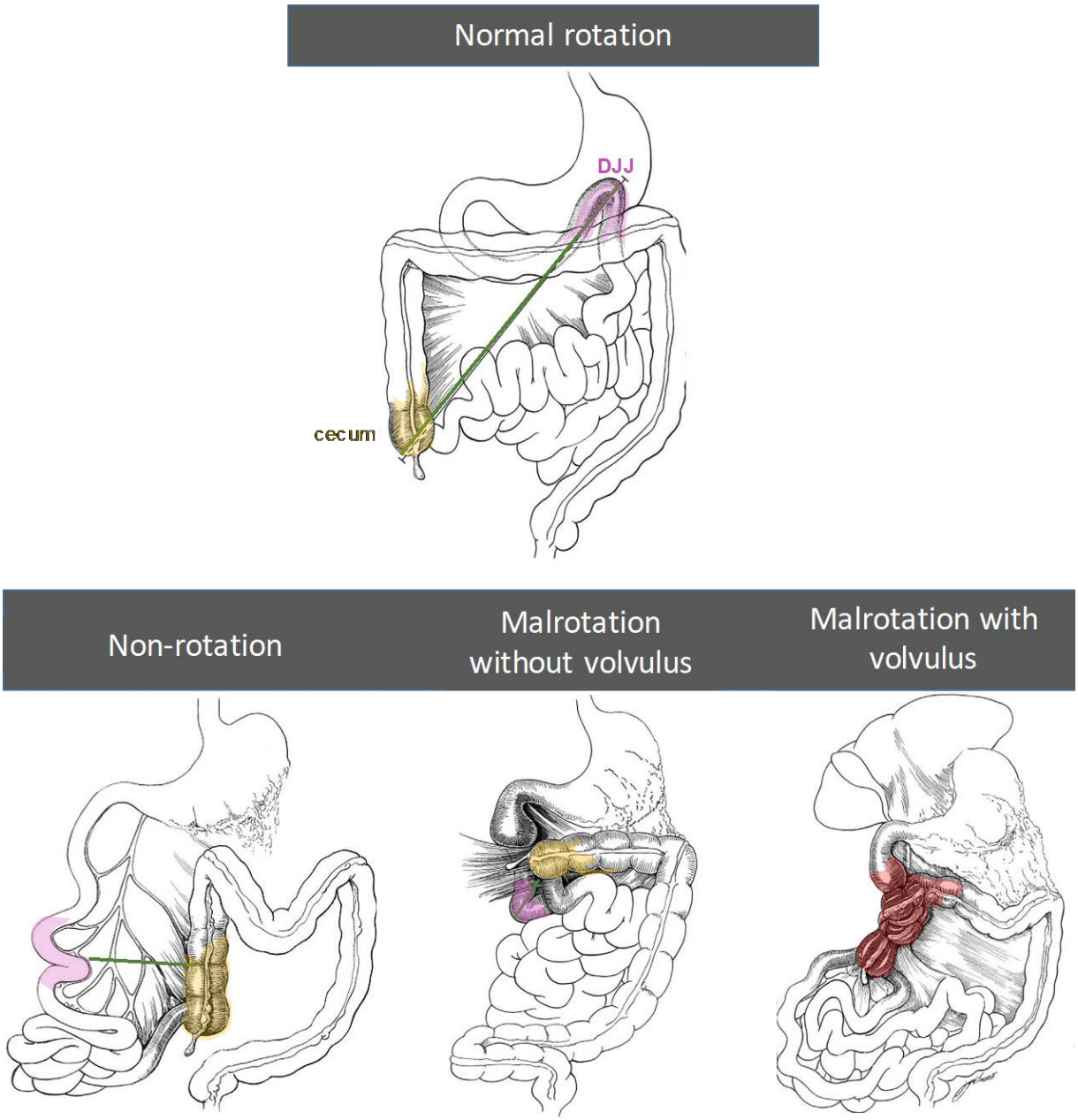

Figure 1.3: Spectrum of intestinal malrotation anomalies. Top panel shows normal rotation where cecum and the duodeno-jejunal junction (DJJ) are fixed with respect to one another. In non-rotation (Category 2), neither point is fixed. During malrotation without volvulus (Category 3), the cecum is fixed in a wrong position. The final one indicates malrotation with volvulus where the intestine wraps around the Superior Mesenteric Artery and Superior Mesenteric Vein (Category 1). The green lines represent the positioning of cecum with respect to DJJ- an important factor in identifying intestinal malrotation. Figure modified from (Langer JC, 2017)

regarded to be relatively asymptomatic due to lack of proper diagnostic tools and methods and may be missed leading to catastrophic volvulus, or delayed diagnosis because it becomes too late to operate due to the extent of necrosis. Hence it is critical to understand the regulatory mechanisms that drive the proper looping morphogenesis of the gut tube.

Amongst the different organ systems, the GI tract is arguably the first organ to initiate a break in symmetry during development to undergo stereotypical looping morphogenesis (Boorman CJ, 2002). Furthermore, the intestine, to the first approximation, remains as a relatively simple cylindrical tube as it elongates and loops. Thus, the intestine simplifies the challenge in studying LR asymmetric organ morphogenesis by reducing the problem to the question of how the asymmetric mechanisms provide directionality for the looping of this structure (Davis NM, 2008). The development of the vertebrate GI tract initiates when the endodermal layer of the tri-laminar embryo, folds to form a midline tube along the AP axis of the embryo (Burn SF, 2009). This results in the endoderm recruiting the lateral limbs of the splanchnic mesoderm to form the outer layer of the primitive gut tube. The dorsal part of the splanchnic mesoderm called the "*dorsal mesentery*" remains distinct from the gut tube and serves to separate and suspend the gut tube from the body wall (Davis NM, 2008). As the primitive gut tube develops, it is progressively patterned along the AP axis and is specified into foregut, midgut, and hindgut based on its vascular supply (Aaron MZ, 2009). Following the specification of the regions, the primitive gut tube undergoes differential elongation along the AP axis. The midgut, which gives rise to the intestine, elongates disproportionately compared to the other regions of the primitive gut and undergoes physiological herniation, extending out of the body cavity (Soffers JHM, 2015). Simultaneously, the symmetry of the midgut is broken along the LR axis by the initiation of a characteristic "*leftward tilt*" that causes the elongating gut tube to undergo a critical counterclockwise rotation which sets the stage

Figure 1.4: A) Asymmetric gut morphogenesis is initiated with a leftward tilt of the gut tube that results in a counterclockwise rotation critical for subsequent conserved looping morphogenesis. This tilt is initiated by an asymmetric shape change of the dorsal mesentery DM shown in orange that suspends the gut tube from the dorsal body wall. **B)** asymmetric changes in the cellular organization across the LR axis underlies the shape change of the dorsal mesentery. Prior to initiation tilt, the left and right sides of DM are symmetric with dense mesenchyme sandwiched by an epithelial bilayer. The left and right sides have vascular cords running through at symmetric DM. At the onset of the counterclockwise rotation, the left side condenses and the right side expands leading to the deformation of the mesentery and providing a physical force to tilt the gut tube leftward. Simultaneously, the right side becomes excluded of vasculature and has an anti angiogenic microenvironment.

A

Gut tube symmetry is first broken by the conserved counterclockwise rotation

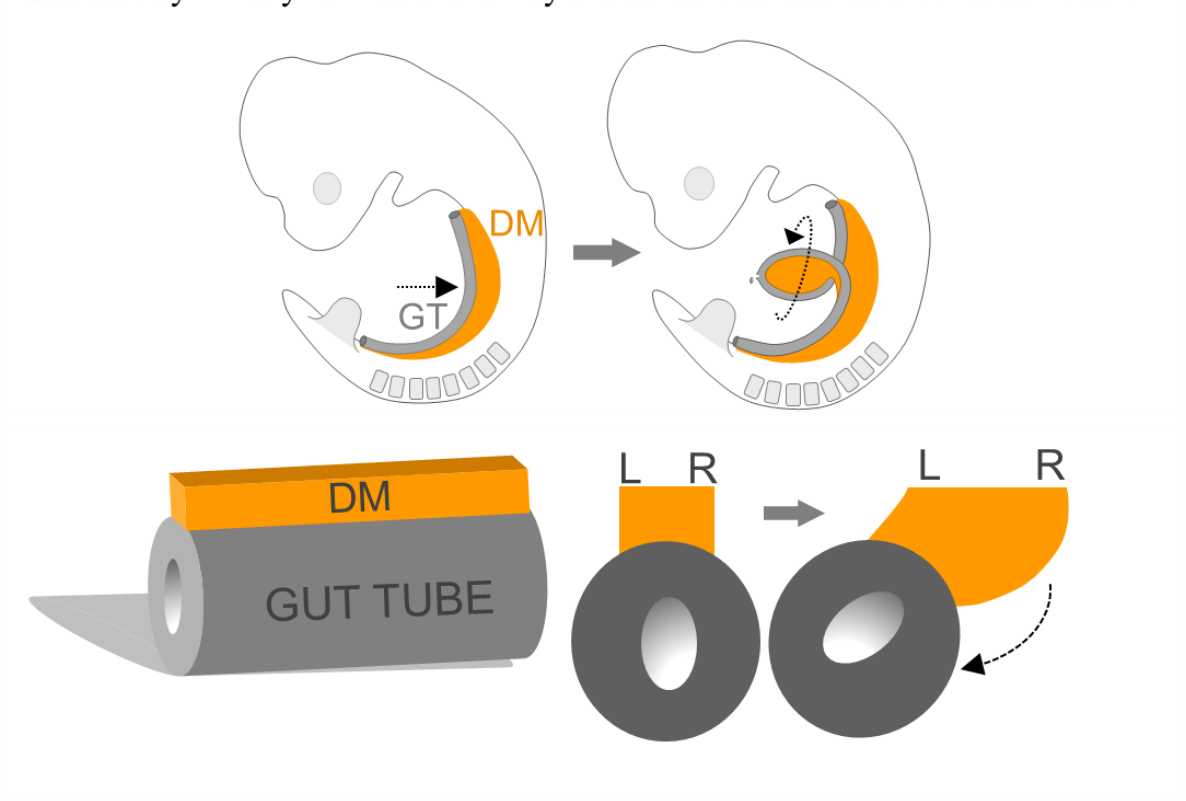

B

Dynamic cellular asymmetries in the DM is critical for gut rotation and gut vasculature

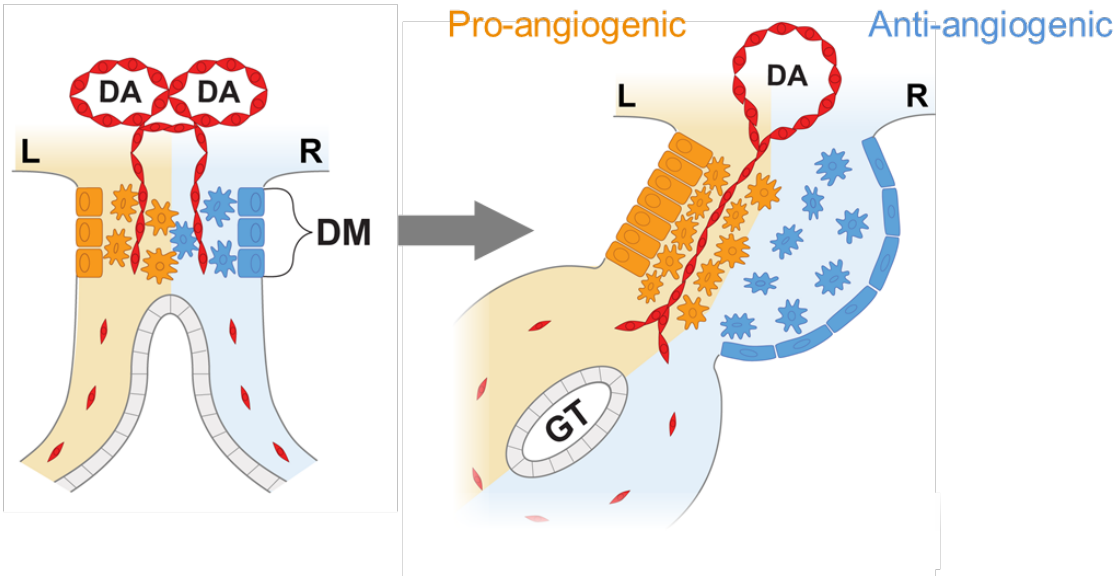

for subsequent looping morphogenesis (Davis NM, 2008). Surprisingly, this leftward tilt is mediated by a reorganization of the cellular architecture of the DM across the LR axis while the gut tube maintains its cylindrical symmetry (Kurpios NA, 2008).

Prior to the initiation of the leftward tilt, the DM is a *symmetric structure* comprising of dense mesenchyme sandwiched by an epithelial bilayer. However, during the initiation of the tilt, the left mesenchymal cells of the DM become densely packed resulting in the condensation of the left mesenchymal compartment while the right mesenchymal cells become sparsely distributed with a dramatic increase in cell-free spaces resulting in the expansion of the right mesenchymal compartment. These changes are accompanied by the cuboidal to columnar transformation of the left epithelia while the right epithelia transitions from cuboidal to squamous morphology (Davis NM, 2008; Kurpios NA, 2008; Welsh IC, 2013). As a consequence of these cellular asymmetries, the dorsal mesentery deforms to tilt the gut tube leftward and initiate the counterclockwise midgut rotation.

Recent work by our lab has shown that, in addition to directing the gut rotation, the DM also initiates the formation of gut-specific arteries commensurate with the onset of gut rotation. Intriguingly, whereas the left DM is pro- angiogenic in nature and serves as the origin of gut arteries, the right DM becomes devoid of all vasculature and remains anti-angiogenic (Mahadevan A, 2014). Thus, the DM displays both cellular and vascular asymmetries that serve to initiate gut rotation and the formation of intestinal vasculature (Figure 1.4).

Previous studies in birds and mice have established that the left specific transcription factor Pitx2 is expressed in the left DM and is sufficient and necessary for the induction of the left specific cellular and vascular behaviors in the DM (Davis NM, 2008; Kurpios NA, 2008; Savin T, 2011; Welsh IC, 2013). Pitx2-null mice failed to initiate the leftward tilt, exhibit randomized

chirality of gut rotation, and display loss of gut vasculature (Mahadevan A, 2014; Welsh IC, 2013). To understand the downstream targets of Pitx2 in the left DM, we previously performed transcriptional profiling of the different cellular compartments of the chicken DM using laser capture microdissection (Welsh IC, 2015). This elucidated the Pitx2-mediated mechanisms that regulate the mesenchymal condensation and the pro-angiogenic microenvironment specific to the left side of the DM. Particularly, Pitx2 was discovered to potentiate the non-canonical Wnt-dependent activation of a formin called Daam2, which stabilized cadherin-based junctions in the left DM leading to tighter packing and condensation of the left mesenchymal compartment (Welsh IC, 2013). To maintain arteriogenesis in the left DM, Pitx2 regulates the expression of the Cxcl12 ligand and its G-protein-coupled-receptor Cxcr4 which establishes the morphogenic gradient needed for vascular remodeling in the left DM (Mahadevan A, 2014). While these studies highlight the role of Pitx2 in mediating the left side-specific cellular behavior in the DM, the mechanisms that regulate the right side have remained unknown. *This question sets the premise for Chapter 2 of this thesis where I show that the asymmetric accumulation of Hyaluronan (HA) – a non-sulfated glycosaminoglycan in the extracellular matrix (ECM) of right DM mediates its mesenchymal expansion and avascularity. Importantly, I show that the transformations specific to the right side precede changes taking place on the left and thus provide the first symmetry-breaking mechanism required to initiate gut rotation.* Furthermore, targeted degradation of HA ablates expansion, gut tilting and results in aberrant gut arterial development (Manuscript in preparation).

1.4 Extracellular matrix (ECM) as a critical regulator of organogenesis

The ECM is a three-dimensional connective matrix that is ubiquitously present in tissues and is a prerequisite for multicellular life processes. In addition to providing a physical scaffold for

organizing the cellular architecture of tissues, it functions to create chemically distinct microenvironments within tissues by governing the heterogeneous distribution of biochemical signals (i.e. growth factors, chemokines, and cytokines) to regulate and coordinate diverse cellular behaviors within the tissue (Heisenberg CP, 2013; Mouw JK, 2014). The cells reciprocally play a critical role in dynamic remodeling and reorganization of the ECM by targeted degradation and reassembly of its components thereby giving rise to unique tissue-specific composition and organization of the ECM (Hynes RO, 2009; Kim HY, 2012). This dynamic reciprocal communication between cells and the ECM plays a fundamental role during organogenesis.

Despite the tissue-specific differences, ECM can be broadly categorized into two main classes: interstitial connective matrices- and basement membrane (Bonnans C, 2014). The interstitial connective matrices provide the underlying support and tensile strength to the tissue and are mainly composed of water, polysaccharides and structural scaffolding proteins such as collagen I and fibronectins (Mouw JK, 2014). Often, the interstitial connective matrices are embedded with narrow zones of biochemically and biomechanically distinct pericellular matrices that surround the cells of a particular cell type within the tissue to elicit localized, cell-type specific responses to external stimuli (Mecham RP, 2001). In contrast, the basement membrane is a specialized compact form of ECM that separates epithelia from the surrounding stroma and interacts with cell-surface receptors to transduce extracellular signals that regulate adhesion, migration, proliferation, apoptosis and differentiation of the epithelia (Lu P, 2012). Despite the organization differences, the two classes of matrices are often continuous and well integrated within the tissues enabling the tissues to respond optimally to physiological challenges and maintain homeostasis.

The functional importance of the ECM in organogenesis is highlighted by the loss of function studies where genetic deletion of specific ECM components result in a wide range of tissue defects that ultimately contribute to embryonic lethality (Bonnans C, 2014; Mouw JK, 2014). Given the distinct structure and function of organs, it is not surprising to note that the ECM assembly, modification, and degradation are unique and organ specific (Faulk DM, 2014). This specificity allows the ECM to play distinct permissive and instructive roles in different organs to regulate cellular and vascular behaviors needed for proper development and functioning of the organ.

Recent chemical characterization and analysis of the human and mouse genomes have revealed a core set of 300 odd protein complexes and polysaccharides that constitute the ECM, and this set of molecules are commonly referred to as the matrisome (Hynes RO, 2012). While the largest set of macromolecules in the matrisome are structural and adhesive fibrous proteins such as collagens (Blum RS, 2011), fibronectin and laminin (Schwarzbauer JE, 2011), the second largest category of macromolecules are glycosaminoglycans (GAGs) which predominantly contribute to the non-Newtonian viscous component of ECM that forms a gel-like lattice in the interstitial spaces of the tissues (Gandhi NS, 2008). In addition to functions such as lubrication, this gel also acts as a reservoir of biochemical signals and enables selective and rapid diffusion of small signaling molecules to facilitate rapid cell-cell communication (Kirkpatrick CA, 2004). In the following sections, we take a closer look at the structural and functional aspects of GAGs.

1.5 Glycosaminoglycans (GAGs) – Not Just Goo!

The GAGs are polymeric sugar chains of linear repeating disaccharide units, with each unit composed of a hexosamine and a hexose or a hexuronic acid. The macromolecules that form up this group are Hyaluronan (HA), dermatan sulfate, keratan sulfate, chondroitin, chondroitin sulfate, heparin, and heparan sulfate. Except for HA, the other GAGs exist in the form of proteoglycans, a class of carbohydrates that are covalently linked to protein cores. In general, the proteoglycans can have one or more GAGs covalently attached to it (Esko JD, 2009; Gandhi NS, 2008; Raman R, 2005).

Historically, the first isolation of sulfated GAGs was carried out in the late 1800's, while HA was first isolated in 1930 (Esko JD, 2009). By 1960's, advances in characterization of the chemical structure of GAGs provided insights into their *in vivo* chemical states. With the exception of HA, the other classes of GAG chains underwent further modifications such as sulfation and epimerization and displayed varying stoichiometry of substitutions with other GAGs when covalently linked to their protein cores (Habuchi H, 2004; Yanagishita M, 1993). Thus, while the chemical structure of HA was reproducible across species, the proteoglycans exhibited differences in the number and length of GAG chains, and the arrangement of sulfated residues along the chains (Hascall V, 2009). By 1970's analytical methods for purification of GAGs from tissues such as cartilages were developed that yielded information regarding the *in vivo* non-covalent interactions between proteoglycans, HA and link proteins. During this period, it was also realized that proteoglycans and GAGs were present on the cell surface, inside the cell, and in the ECM of all animal tissues leading to further investigation and appreciation of the manifold roles of the GAGs in regulating a variety of cellular behavior (Figure 1.5).

Figure 1.5: Schematic representation of the family of GAGs comprising a diverse set of molecules. Amongst ECM GAGs, the largest member is Hyaluronan (HA,shown in blue) in the extracellular space. The other ECM proteoglycans such as aggrecan and versican bind to HA via the link domains (purple hexagons) and form a gel-like lattice in the interstitial space. In addition to the HA binding GAGs, the ECM GAGs also encompass smaller secreted proteoglycans such as perlecan, biglycan and decorin. The cell surface GAGs include membrane-traversing GAGs such as syndecan and GAGs that are bound to outer plasma membranes such as glypicans.

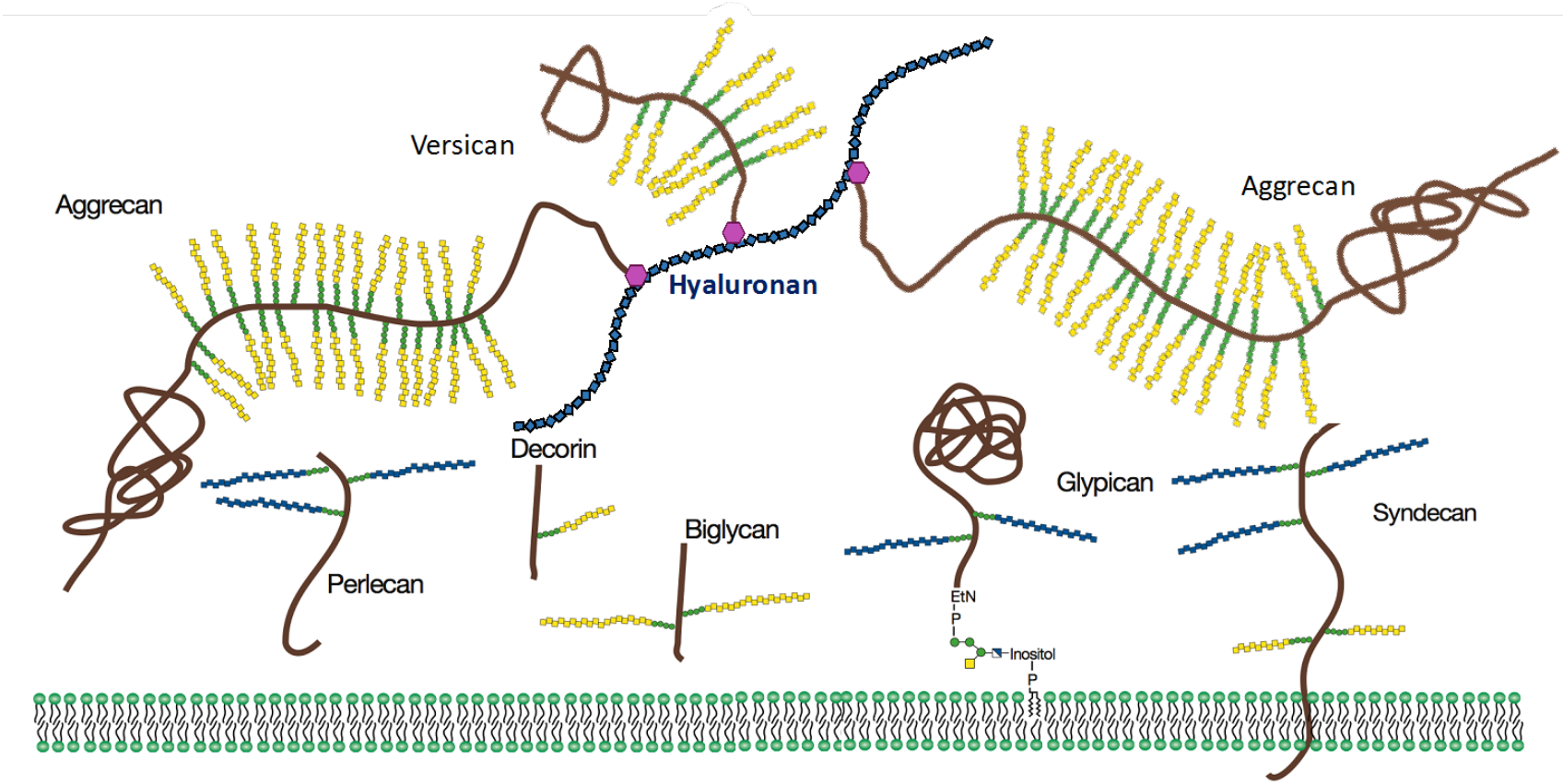
Versican
Aggrecan
Hyaluronan
Aggrecan
Decorin
Glypican
Syndecan
Biglycan
Perlecan
EtN
P
P
Inositol
P

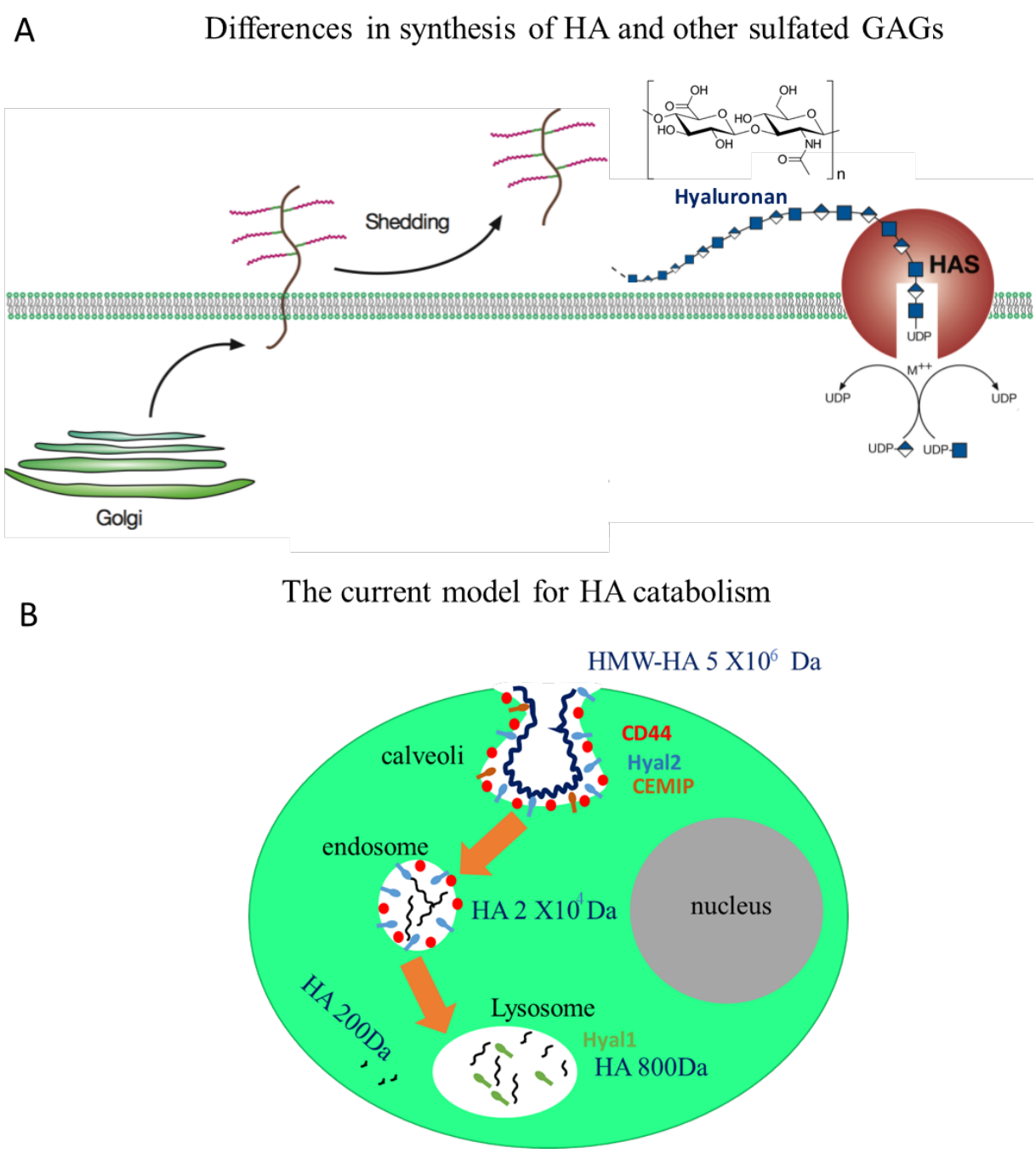

Figure 1.6: A) Differences in synthesis of sulfated GAGs attached to a proteoglycan and the non-sulfated GAG HA. While the sulfated GAGs are synthesized in the golgi, attached to the protein core and secreted to the plasma membrane, the non-sulfated HA is synthesized by Has enzymes in plasma membrane which directly utilize the cytoplasmic sugar pools to synthesize HA. Hence HA has a higher rate and degree of polymerization **B)** Current model for HA catabolism: the HMW HA is tethered to the cell surface by the HA receptor, CD44 (red dots), which creates caveolin coated pits that maintain an acidic environment and activates HA degrading enzyme hyaluronidase 2 (Hyal2, blue oval-sticks) and CEMIP (brown oval-sticks). Hyal2 then cleaves the HA polymer to 20kDA fragments which are internalized through the endosomes and ultimately transported to the lysosomes where Hyal1 degrades the 20kDa fragments to small tetrasaccharides which are further cleaved into mono and disaccharides by lysosomal exoglucosidases. (modified from (Csoka AB, 2001 #91;Hascall V, 2009 #76))

The GAGs in the ECM can be classified based on the type of ECM they are associated with. For example, the interstitial GAGs represent a diverse class of molecules, differing in size and composition. They can contain high molecular weight HA (HMW-HA), chondroitin sulfate, and dermatan sulfate which have the ability to bind water to form gel-like hydrated matrices that regulate tissue volume and macro-mechanical properties of tissues. In cartilages, the interstitial aggregates of proteoglycans and HA provide a stable matrix capable of absorbing high compressive forces by water desorption and resorption. The interstitial GAGs can also comprise of the small leucine-rich family of proteoglycans, which stabilize and organize collagen fibers as observed in tendons and cornea (Esko JD, 2009).

Proteoglycans comprising of GAGs containing low molecular weight HA (LMW-HA), heparan sulfate, and chondroitin sulfate are present in the basement membrane and play a significant role in its organization and are key for modulating the permeability properties of specialized basement membranes (Iozzo RV, 2005). Both the interstitial GAGs and the GAGs in the basement membrane can bind to biochemical signals (cytokines, chemokines, growth factors, and morphogens), protect them against proteolysis and facilitate the formation of gradients essential for cellular functions (Lindhardt RJ, 2004).

The cellular and intracellular GAGs are membrane bound and are present in a variety of vesicles from secretory to endocytic intercellular vesicles. The membrane GAGs have been shown to interact with integrins and other cell adhesion receptors to regulate cell attachment, cell-cell interactions, and cell motility (Kim SH, 2011). They have also been shown to act as co-receptors for various growth factor receptors and function as endocytic receptors for clearance of bound ligands (Christianson HC, 2014). GAGs are also found in secretory vesicles and have a role in packaging granular contents, maintaining matrix proteases in an active state, and regulating

various biological activities after secretion, such as coagulation, host defense, and wound repair (Kolset SO, 2008).

The following section describes how the structural and chemical attributes of the unique non-sulfated GAG, HA, contributes to its highly diverse and critical biological functions, particularly in the context of development.

1.6 Hyaluronan (HA) - the sweet, giant non-sulfated GAG molecule

1.6.1 Structure of Hyaluronan

Hyaluronan is a non-sulfated GAG and the largest polysaccharide found in ECM of vertebrates. It exists as a linear unbranched polymer and consists of repeating disaccharide units that are composed of N-acetylglucosamine (GlcNAc) and glucuronic acid (GlcA) linked by alternating β-(1,4) and β-(1,3) glycosidic bonds (Figure 1.6). In aqueous environments, HA exists in the polyanionic form due to the carboxyl groups of the glucuronic acid residues, and at the macroscopic level, it has a large hydrodynamic volume (Hascall V, 2009). The anionic nature of hyaluronan together with stereochemical restrictions around the glycosidic bonds results in HA behaving as stiffened random coils at the macroscopic level (Cowman MK, 2005). HA lacks a protein core, and its chemical structure and properties are highly reproducible across species. Numerous hyaluronan-binding proteins (commonly referred to as hyaladherins) and several enzymes responsible for its synthesis and degradation are present in the vertebrate genome and enable HA to play essential roles in development, tissue organization, cell proliferation and signal transduction pathways across the plasma membrane (Day AJ, 2002).

1.6.2 Hyaluronan synthesis

The synthesis of HA is catalyzed by enzymes called Hyaluronan synthases (also known as Has enzymes) that are localized to the inner plasma membrane. The Has enzymes possess the catalytic activities needed to synthesize HA by sequestering the N-acetylglucosamine and glucuronic acid units from the corresponding nucleotide sugars in the cytoplasm and to extrude the growing polymer into the extracellular environment (Itano N, 2002). While the sulfated GAGs are assembled on the non-reducing end of the core proteins of proteoglycans as they transit through the Golgi, HA synthesis normally occurs at the inner surface of the plasma membrane and new units are added at the reducing end (Vigetti D, 2014; Weigel, 2015). Furthermore, since HA is directly extruded into the extracellular space, HA has a high degree of polymerization in the range of 10^4 disaccharides (Figure 1.6A).

In the mammalian genome, there are three Has enzymes. These enzymes differ in their enzymatic properties, and the differences are thought to underlie physiologically distinct functions. Has3 is intrinsically more catalytically active followed by Has2 and Has1. In vitro experiments suggest that the product size generated by each Has are significantly different with Has1 and Has2 producing high molecular weight chains of 2×10^6 Da while Has3 produces shorter chains of 2×10^5 Da (Itano N, 1999). The catalytic activity of Has enzymes can be regulated at the transcriptional and the post-translational level (Tammi RH, 2011). At the transcriptional level, *Has2* is the most widely expressed form of Has during embryonic development, and its expression is critical for tissue expansion, cell motility, and growth. Has3 is expressed late in embryonic development and in many adult tissues and is significantly upregulated during inflammatory conditions (Vigetti D, 2014). While the knockouts of Has1 and Has3 survive, loss of Has2 results in early embryonic lethality highlighting the importance of HA synthesis by Has2 during

embryonic development (Camenisch TD, 2000). At the post-translational level, the activity of the Has enzymes can be regulated by phosphorylation, O-GlcNAcylation, or ubiquitination. In addition, the concentration of the UDP- GlcNAc, and UDP- GlucA in the cytoplasmic pools is also a major determinant of Has activity (Tammi RH, 2011). How these mechanisms are integrated and coordinated in a tissue-specific manner to achieve localized accumulation of HA during organogenesis is currently unknown and warrants further investigation.

1.6.3 Catabolism of HA

There is rapid turnover of HA levels in vertebrate tissues. Hence tight regulation of HA catabolism is crucial for modulating steady state levels of HA that is important for normal homeostasis, embryonic development, wound healing, regeneration, and repair (Csoka AB, 2001; Frost GI, 1996). Hyaluronidase (Hyal) enzymes are a class of enzymes (endo-β-N-acetyl-hexosaminidases) which degrade HA by employing non-processive substrate hydrolysis involving the cleavage of the β1,4 glycosidic bond between the disaccharides generating mostly tetrasaccharides (Gushulak L, 2012). In the human genome, homology-based sequence analysis has identified six genes coding for hyaluronidase-like sequences. They include human Hyal1, Hyal2, Hyal3, Hyal4, and PH-20/Spam1, as well as a pseudogene Phyal1 (Csoka AB, 2001). Of these, Hyal1 and Hyal2 are the somatically active HA-degrading enzymes (Frost GI, 1997) while PH-20 or SPAM1 (SPerm Adhesion Molecule 1), is a sperm-specific Hyal that is necessary for allowing the sperm to penetrate through the cumulus mass to the ovum. Hyal3 although widely expressed in tissues does not appear to have Hyal activity while the Hyal4 gene, encodes for a chondroitinase (Hemming R, 2008).

A characteristic feature of the vertebrate Hyal enzymes is their ability to produce a wide range of HA oligomers with size-specific biological activities (Stern R, 2006). For example, the

HMW-HA is anti-angiogenic and immunosuppressive (Deed R, 1997; Slevin M, 2007). In vitro studies show that Hyal-1 degrades the HMW-HA into small oligomers, primarily to tetrasaccharides which are anti-apoptotic and inducers of heat shock proteins (Triggs-Raine B, 1999). Hyal2, on the other hand degrades HMW-HA to an approximately 20 kDa product (~50 disaccharide units) (Lepperdinger G, 1998) which have been shown to be pro-angiogenic and pro-inflammatory (Deed R, 1997). A popular model of HA degradation in the HA field suggests that HMW-HA is first tethered to cell surfaces by the HA receptor CD44, concentrated in caveolin-rich lipid rafts. It is then cleaved by Hyal2 into intermediate-size fragments in acidic microenvironments created by the Na+-H+ exchanger. The generated intermediate-size fragments participate in signaling processes and are finally broken down to oligosaccharides within cells by Hyal1 present in the lysosomes in coordination with lysosomal β-glucuronidase and β-N-acetyl-glucurosaminidase (Erickson M, 2012) (Figure 1.6B). However, this model fails to explain the mechanism by which HA is degraded in tissues and cell culture systems that do not express the Hyal family of genes (Csóka AB, 1999) suggesting that new HA-degradation pathways independent of the Hyal1, Hyal2, and CD44 system may exist.

Recent studies have shown that apart from the Hyal family of hyaluronidases, the hyaldherin CEMIP, also known as KIAA1199, possess HA binding and degrading activities (Hiroyuki Yoshida, 2013). Originally discovered as a gene related to deafness but with unknown function, CEMIP has a principle role in binding and depolymerization of HA (Hiroyuki Yoshida, 2013). In addition to the enzymatic processes that cleave HA, HA can be degraded by oxidation reactions, particularly, by reactive oxygen species (ROS) and free radicals. Originally discovered for its ability to degrade HA in the synovial fluid (Stern R, 2007), ROS has been shown to induce HA fragmentation directly and indirectly through a p38 MAPK-dependent signaling pathway in

normal human bronchial epithelial cells (Casalino-Matsuda SM, 2009). However, Further studies to elucidate the kinetics of the HA degradation by KIAA1199 and ROS are needed to understand the mechanisms cells employ *in vivo* to catabolize HA.

1.6.4 Role of HA in development

HA has multiple roles in early development, tissue organization, and cell migration and HA localization in the embryo correlates with tissue expansion, motility, and vascular remodeling (Hascall V, 2009). Over the years, perturbation studies have revealed essential roles that HA play during the development of several organ systems. Particularly, the discovery of embryonic lethal phenotype in Has2-null mice at the time of heart formation (Camenisch TD, 2000) provided a genetic window for manipulating and understanding the significance of HA-rich matrices in developing embryos by selective perturbation of Has2.

A pioneering example of the requirement for HA-rich matrices in tissue expansion during early development is the process of cumulus cell-oocyte expansion in the mammalian pre-ovulatory follicle critical for fertility (Salustri A, 1992). Prior to hormonal stimulation, the mammalian oocyte, arrested at the prophase of the first meiotic division, is surrounded by about 1000 cumulus cells that are densely packed. In response to the circulatory gonadotrophin surge, the cumulus cells upregulate Has2 and a link module family hyaladherin encoded by tumor necrosis factor-stimulated gene 6 (Tsg6) (Fülöp C, 2003; Salustri A, 1992). Simultaneously, the follicle becomes permeable to serum, introducing inter-α-trypsin inhibitor (IαI), composed of the protease inhibitor bikunin and two heavy chains that are covalently bound to the chondrioitin sulfate chain. In a complex process, Tsg6 catalyzes the transfer of heavy chains from chondroitin sulfate onto the newly synthesized HA, stabilizing the HA-rich matrices and causing rapid expansion of the cumulus cell-oocyte complex (Mukhopadhyay D, 2004). This HA-mediated

expansion is critical for the transport of the oocytes into the follicle and for sperm binding during fertilization (Fülöp C, 2003; Mukhopadhyay D, 2004; Salustri A, 1992). The cumulus cell-oocyte complexes fail to expand in Tsg6-deficient female mice because of the inability of the cumulus cells to assemble their HA-rich ECM. As a consequence, Tsg6-/- female mice are sterile (Mukhopadhyay D, 2004).

The essential role of HA in synchronized cell motility during early development is well illustrated by studies that have investigated cell movements that accompany gastrulation (Fenderson BA, 1993). Knockout of Has2 using antisense morpholinos in zebrafish embryos resulted in the failure of the ventrolateral cells to develop lamellipodia and migrate dorsally resulting in the blockage of dorsal convergence during gastrulation (Fenderson BA, 1993). Ectopic expression of Has2 in axial cells led to the formation of supernumerary lamellipodia and blockage of axis extension. Importantly, epistasis analysis showed that HA, rather than acting as an essential structural component, functions as an autocrine signal to stimulate activation of Rac1, a small GTPase known to regulate cytoskeletal remodeling to trigger cell motility (Bakkers J, 2004). A similar role for HA in mediating synchronized cell migration in organ development has been studied in cases of myocardial involution during the formation of the heart tube (Smith KA, 2008) and in the migration of neural crest cells during craniofacial morphogenesis (Casini P, 2012). The most impressive role of HA in cell motility essential for organ development has been demonstrated during the formation of cardiac cushions. Studies by Roger Markwald's group as early as 1970s showed that that endothelial cells outlining the cardiac cushions migrated into an HA-rich ECM in the cardiac jelly during development implicating HA in this process (Markwald RR, 1978). Indeed, this was proven when the embryonic knockout of Has2 displayed a complete loss of

cardiac jelly and cardiac cushions in addition to the defective vasculature and other heart abnormalities (Camenisch TD, 2000).

Some of the earliest investigations of the role of HA in vascular remodeling and in organizing ECM were carried out in the developing limb (Feinberg RN, 1983; Li Y, 2007). Particularly, HA was discovered to be a major component of the ECM of the apical ectodermal ridge and the distal subapical mesenchymal cells associated with it. In contrast, the ECM of the proximal central core of the limb bud was devoid of HA during the condensation of the cartilage elements (Kosher RA, 1981). Overexpression of Has2 in the chick limb bud resulted in the formation of shortened and severely malformed limbs that lacked one or more skeletal elements while the ectopic introduction of HA-soaked beads in the proximal central core resulted in inhibition of the pre-cartilage condensation needed for cartilage differentiation and the creation of ectopic avascular zones (Feinberg RN, 1983; Li Y, 2007). Similarly, conditional inactivation of Has2 in the distal limb bud mesoderm also resulted in the shortening of the skeletal elements of Has2 deficient limbs suggesting that the distal localization of HA is essential for normal growth of all limb skeletal elements (Matsumoto K, 2009). The distal localization of Has2 was regulated at the transcriptional level by the transcription factor Gli3 downstream of Shh signaling (Liu J, 2013). Furthermore, the condition knockout of Has2 in limbs resulted in mislocalized distributions of chondroitin sulfate proteoglycans, aggrecan and the link protein (Matsumoto K, 2009). Taken together these investigations show that HA regulates various aspects of limb morphogenesis.

HA is also essential for Xenopus tadpole tail regeneration (Contreras EG, 2009), zebrafish tail fin regeneration (Ouyang X, 2017), and in the formation of perineuronal nets around neurons in the cerebral cortex (Carulli D, 2006). These HA-mediated repair mechanisms are areas of active

investigations. Collectively, these studies clearly establish the importance of HA-rich matrices in embryonic development.

1.6.5 Pathobiology of HA matrices

The increased accumulation of HA in the ECM is one of the hallmarks for pathologies related to inflammation such as rheumatoid arthritis, respiratory diseases like asthma, chronic obstructive pulmonary disease, inflammatory liver and bowel diseases, in diabetic nephropathies and transplant rejections (Petrey AC, 2014). In normal tissues, HA mainly exists in the form of HMW-HA and suppresses inflammation by decreasing the levels of cytokines such as TNF-alpha and interleukins through activation of NF-κB and promoting the suppressive effects of regulatory T-cells in a TLR4-dependent manner (Nakamura K, 2004). However, in cases of inflammation and tissue injury, HA is significantly more poly-dispersed and contains fragments of varying length and overlapping functions (Petrey AC, 2014). Particularly, there is a considerable enrichment of the smaller fragments of HA which triggers pro-inflammatory effects by stimulating transcription of inflammation-related genes including TNF-α, IL-12, IL-1β, and matrix metalloproteinases by signaling through TLR4 and TLR2 as well as CD44 (Do Y, 2004; Taylor KR, 2007; Termeer C, 2002). Furthermore, the inflammatory conditions trigger a reorganization of HA matrices, where the HA polymers of variable sizes are organized into cable-like structures that are decorated with HA-binding proteins like heavy chains of IαI, Tsg6 and versican (de la Motte CA, 2003). These cables act as a biological sink for binding monocytes and platelets, and these interactions likely modulate the pro-inflammatory stimuli (Lauer ME, 2009). While these studies clearly highlight the importance of HA-mediated signaling during inflammation, more investigations would enable us to understand the interactions between HA, HA-binding proteins, and HA receptors during inflammation.

In addition to regulating inflammatory stimuli, HA is a critical regulator of angiogenesis, which facilitates chronic inflammation. HMW-HA is anti-angiogenic and suppresses endothelial cell proliferation and vessel formation, while fragmented HA is a pro-angiogenic stimulator (Deed R, 1997). The endothelial cell interactions with HA matrices are mediated by a variety of HA-binding proteins and HA interacting proteoglycans which regulate angiogenic responses to different degrees (Savani RC, 2001). This generation of a pro-tumorigenic inflammatory environment and the ability to modulate angiogenesis has also resulted in HA being investigated from the context of tumorigenesis, wound healing, regeneration, and repair (Hascall V, 2009). Several investigations have demonstrated that HA regulates tumor cell migration and invasion *in vitro* and tumor growth and progression *in vivo* particularly in the context of breast and ovarian cancers (Ween MP, 2011; Yahya RS, 2014). Interestingly, extreme HMW-HA has also been credited to provide a mechanism responsible for the naked mole rat's cancer resistance (Tian X, 2013).

1.7 Regulators of HA function

The preceding sections have outlined the diverse biological roles of HA which include functioning as a regulator of tissue homeostasis during normal conditions; as an organizer of ECM to facilitate localized tissue volume changes, cell migration and vascular remodeling during embryonic development (Hascall V, 2009); as an activator and regulator of immune cells during inflammation and related pathologies (Petrey AC, 2014); and as a critical regulator of cancer, wound healing, regeneration, and repair (Ween MP, 2011; Yahya RS, 2014). Also, HA often demonstrates opposing functions in the above-mentioned contexts. This diversity in function appears to be a consequence of the distribution of interactors of HA in a given microenvironment, the size of HA

molecules and cell-specific factors (such as the type of receptor being expressed) in a given tissue (Cyphert JM, 2015). The following sections explore hyaladherins which define the composition and organization of HA-rich matrices and the signaling pathways that HA can participate in a given tissue microenvironment.

1.7.1 Introduction to hyaladherins- structure, classification

The interaction of HA with various hyaladherins (HA-binding proteins) is thought to stabilize different structural conformations of the HA polymer and at the same time, leads to the formation of multi-molecular complexes with distinct structural arrangements (or architectures) that underlie their different functions (Day AJ, 2002). Most hyaladherins interact with HA via HA-binding domains (HABD), composed of structural motifs called link modules (Figure 1.7A). The link module is of ~100 amino acids in length and is composed of two α-helices and two triple-stranded antiparallel β sheets. The binding of the link module to HA has been attributed to the hydrogen bonds and the aromatic stacking interactions between HA and the aromatic amino acids of the link module, and the stacking and ionic interactions between the carboxylic acid groups of the glucuronic acid residues of HA and the positively charged amino acid residues of the link module (Higman VA, 2014). The HABD of different hyaladherins differs in the number of link modules and in the N and C-terminal extensions of the link modules and can be classified into type A, type B, and type C. Type A HABD consists of a single link module domain and can be found in hyaladherin Tsg6 (Kohda D, 1996). Type B HABDs extend the β-sheet structure and forms an extra lobe that is in intimate contact with the link module. The hyaladherins CD44 and Lyve1 possess the type B HABD (Teriete P., 2004). Type C HABD contains contiguous pairs of link modules and is found in the lectican superfamily (aggrecan, brevican, neurocan, and versican) and link proteins (HAPLN1–4) (Seyfried NT, 2005) (Figure 1.7B).

Figure 1.7: A) Domain structures of the different Hyaladherins in the vertebrate genome. All of them contain the link module which is essential for binding to HA. B) Classification of hyaladherins depending on the structure and the number of link modules.

A Differences in the domain structure of hyaladherins

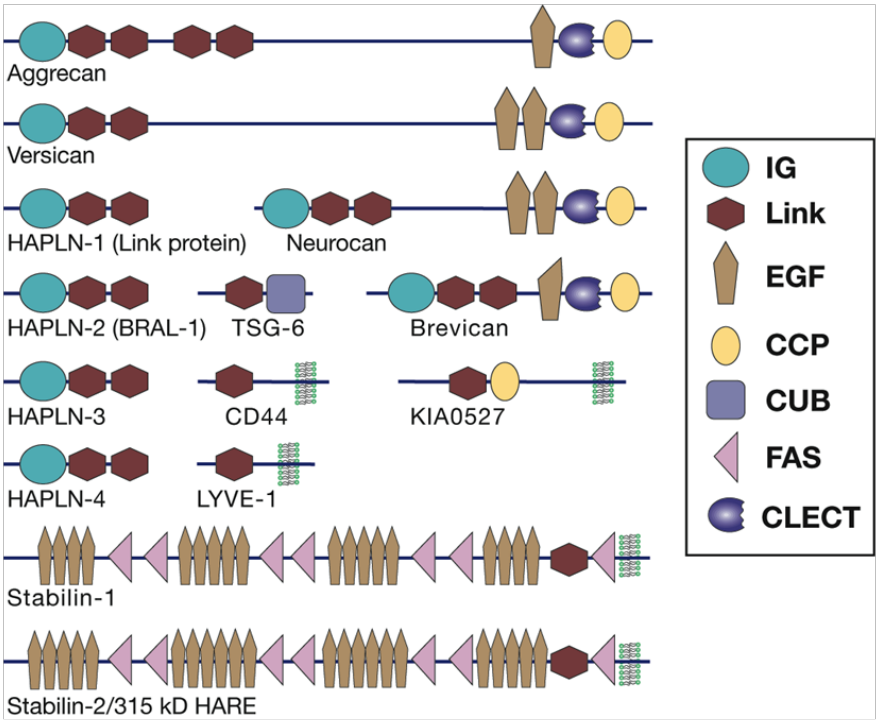

B Classification of the HA binding domains in hyaladherins

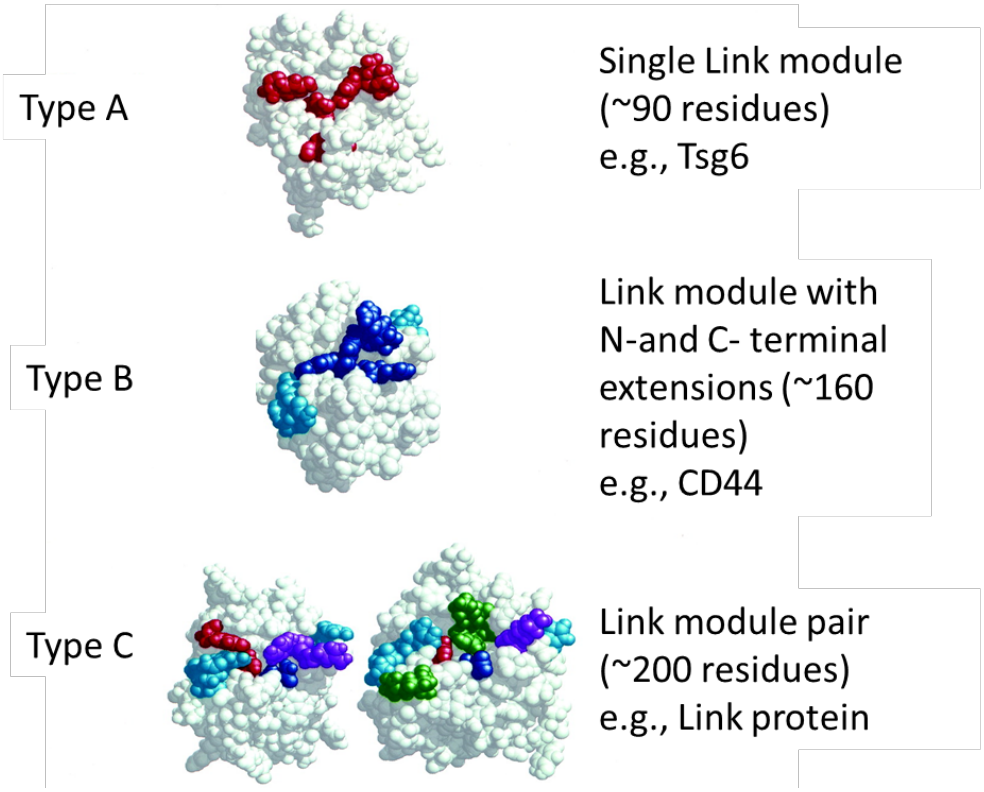

In addition to the link module containing hyaladherins, recent studies have revealed hyaladherins that can bind HA without the link module such as RHAMM, CD38, plasma Hyaluronan Binding Protein, P-32, IHABP4, IMP-50, and SPACRCAN (Day AJ, 2002). While the domains that participate in HA binding have been identified in these molecules, the exact HA binding sites are unknown and needs to be established.

1.7.2 Tsg6, a unique member of the hyaladherin family: structural and biochemical properties

The hyaladherin Tsg6 is a 35-kDa secreted enzyme that is usually expressed in response to pro-inflammatory stimuli at sites undergoing ECM remodeling. Originally discovered from a cDNA library derived from TNF-treated human fibroblasts, both the gene sequence of Tsg6 and its encoded protein demonstrate a high degree of sequence conservation (Milner CM, 2003). The domain structure of Tsg6 comprises of the link and CUB modules that are flanked by N- and C-terminal sequences respectively (Day AJ, 2002). The link domain enables Tsg6 to bind ligands such as HA, chondroitin 4-sulfate, and heparin. While there is considerable overlap between the binding sites for HA and chondroitin 4-sulfate, the binding sites for heparin are distinct (Parkar AA, 1997). The binding of Tsg6 to HA can directly crosslink HA chains via the formation of HA induced Tsg6 oligomers (Baranova NS, 2011). This crosslinking of HA could serve to remodel ECM. Similarly, Tsg6 binding to HA has also been shown to enhance and induce the interaction of HA and CD44 on lymphocyte cell lines possibly by the promotion of CD44 clustering or by switching CD44 into a high-affinity conformation (Lesley J, 2004). The binding of Tsg6 has also been found to be chondroprotective in murine models of inflammatory arthritis where its serum concentration correlated with the severity of the disease (Bárdos T, 2001).

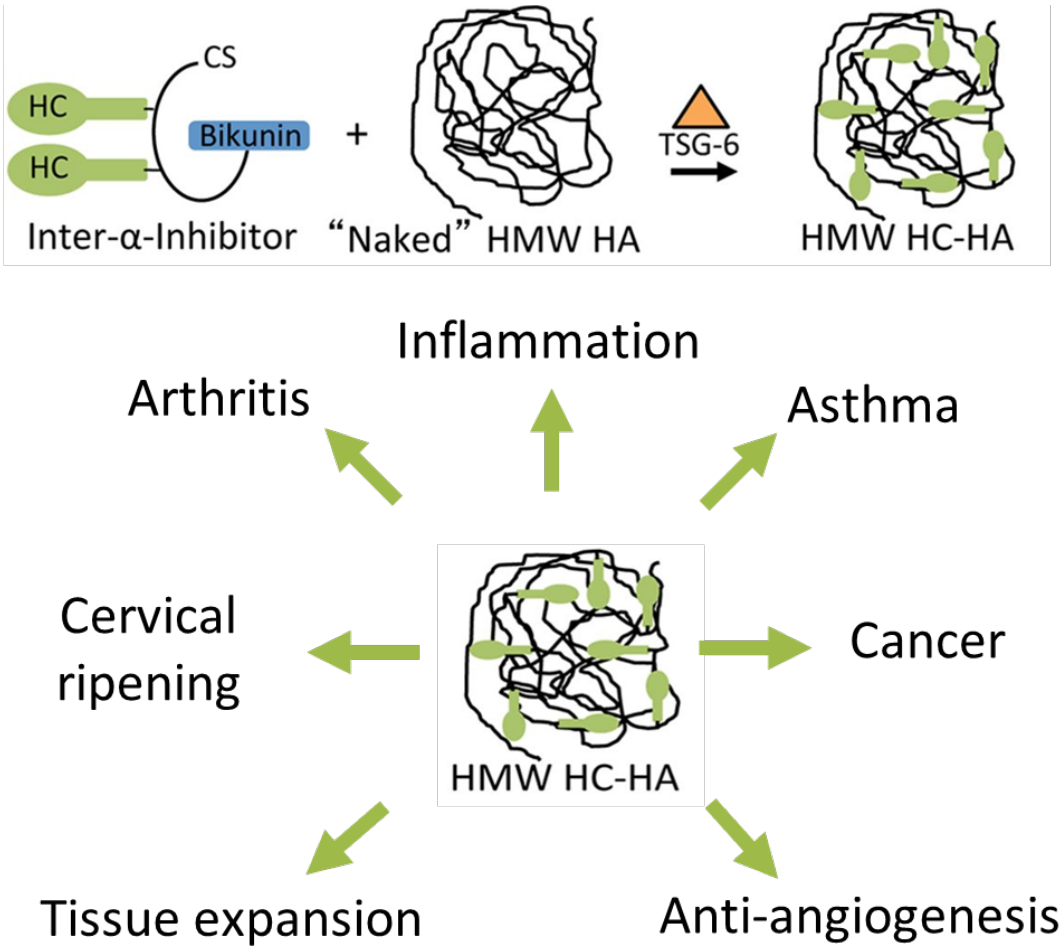

Figure 1.8: Tsg6 is the only hyaladherins that can also function as an enzyme to covalently modify HA. This covalent modification occurs in the presence of Inter-α- inhibitor (IαI) complex which consists of the protease bikunin and heavy chain (HC) peptides. Tsg6 catalyzes the covalent transfer of HC from IαI on to HA. This modified form of HA, known as HC- HA has numerous physiological and pathological roles. Of relevance are its ability to modulate tissue volume changes and increase anti-angiogenic potential of HA. Figure adapted from (Lauer ME, 2013)

In addition to its inflammation associated functions, it is well established that Tsg6 is essential for female fertility in mice, for the assembly of an HA-rich ECM in the cumulus cells surrounding the oocyte prior to ovulation (Fülöp C, 2003). Upon hormonal stimulation, this HA-rich matrix undergoes a striking, nearly 20-fold, expansion. Interestingly, Tsg6 binding to HA is not sufficient to trigger this expansion. Instead, a covalent complex formed by HMW-HA and the heavy chain (HC) from the serum proteoglycan inter-α-inhibitor (IαI) is required. Formation of this HC-HA complex is mediated by Tsg6, which catalyzes the transfer of HC from IαI to HA (Mukhopadhyay D, 2004). This modification results in the formation of a stable gel-like HA-rich matrix, which subsequently maintains the integrity of the cumulus cell-oocyte complex critical for female fertility (Salustri A, 1992).

The mechanism of the Tsg6-mediated HC transfer to HA has been shown to involve the formation of covalent HC·Tsg6 complexes as intermediates (Figure 1.8). These HC·Tsg6 complexes are linked through ester bonds between Ser-28 of Tsg6 and the C-terminal aspartates of the HCs (Sanggaard KW, 2008). This transesterification reaction is preceded by the formation of non-covalent complexes between Tsg6 and IαI that inhibit the HA-binding activity of Tsg6 and promote Tsg6 catalytic function. The calcium chelating site in the CUB domain of Tsg6 has been shown to mediate this non-covalent interaction by correctly orienting the Tsg6 molecule relative to IαI to facilitate the transfer of HC to Ser-28 of Tsg6 (Briggs DC, 2015). The HCs are then transferred from Tsg6 onto HA presumably when the HC·Tsg6 complex and HA interact, for which the mechanisms are not yet fully understood. It is worthy of mention that HC-HA complexes are also formed in contexts other than ovulation. Recently, studies have detected HC-HA complexes to be present in the chick amniotic membrane and to have anti-angiogenic functions (Shay E, 2011). This suggests that the formation of the HC-HA complex is an ancient process in

vertebrates predating cumulus expansion in mammals and can have diverse functions depending on the exact composition (e.g. number and type of HCs, the size of HA, etc.) and the identity of other associated structural/signaling molecules.

In Chapter 2, investigating into how HA enacts its function, I show that the expression of Tsg6 is right sided in the DM and that it plays critical roles in regulating the HA-mediated expansion and avascularity in the DM important for asymmetric gut morphogenesis. Together, my work described in detail in Chapter 2 identifies a novel pathway during gut development where asymmetric enrichment of HA in right DM results in tissue expansion and vascular exclusion in the right DM that is critical for the conserved counterclockwise rotation of the gut and development of the gut arterial blood supply.

1.8 References

Aaron MZ, J.M. (2009). Vertebrate Endoderm Development and Organ Formation. Annu Rev Cell Dev Biol *25*, 221-251.

Adams DS, R.K., Fukumoto T, Yuan S, Albertson RC, Yelick P, Kuo L, McSweeney M, Levin M. (2006). Early, H+-V-ATPase-dependent proton flux is necessary for consistent left-right patterning of non-mammalian vertebrates. Development *133*, 1657-1671.

Albrieux M, V.M. (2000). Bilateral asymmetry of the inositol trisphosphate-mediated calcium signaling in two-cell ascidian embryos. Biol Cell *92*, 277-284.

Bakkers J, K.C., Pothof J, Quaedvlieg NE, Spaink HP, Hammerschmidt M. (2004). Has2 is required upstream of Rac1 to govern dorsal migration of lateral cells during zebrafish gastrulation. Development *131*, 525-537.

Baranova NS, N.E., Haller FM, Briggs DC, Svedhem S, Day AJ, Richter RP. (2011). The inflammation-associated protein TSG-6 cross-links hyaluronan via hyaluronan-induced TSG-6 oligomers. J Biol Chem *286*, 25675-25686.

Bárdos T, K.R., Mikecz K, Glant TT. (2001). Anti-inflammatory and chondroprotective effect of TSG-6 (tumor necrosis factor-alpha-stimulated gene-6) in murine models of experimental arthritis. Am J Pathol *159*, 1711-1721.

Basu B, B.M. (2008). Cilia multifunctional organelles at the center of vertebrate left-right asymmetry. Curr Top Dev Biol *85*, 151-174.

Bischoff M, C.Z. (2009). Cell rearrangements, cell divisions and cell death in a migrating epithelial sheet in the abdomen of Drosophila. Development *136*, 2403-2411.

Bisgrove BW, E.J., Yost HJ. (1999). Regulation of midline development by antagonism of lefty and nodal signaling. Development *126*, 3253-3262.

Blum RS (2011). The collagen family. Cold Spring Harb Perspect Biol *13*, a004978.

Bonnans C, C.J., Werb Z. (2014). Remodelling the extracellular matrix in development and disease. Nat Rev Mol Cell Biol *15*, 786-801.

Boorman CJ, S.S. (2002). The evolution of left-right asymmetry in chordates. Bioessays *24*, 1004-1011.

Briggs DC, B.H., Ali T, Rugg MS, Waltho JP, Ievoli E, Jowitt TA, Enghild JJ, Richter RP, Salustri A, Milner CM, Day AJ. (2015). Metal Ion-dependent Heavy Chain Transfer Activity of TSG-6 Mediates Assembly of the Cumulus-Oocyte Matrix. J Biol Chem *290*, 28708-28723.

Bunney TD, D.B.A., Levin M. (2003). Fusicoccin signaling reveals 14-3-3 protein function as a novel step in left-right patterning during amphibian embryogenesis. Development *130*, 4847-4858.

Burn SF, H.R. (2009). Left-right asymmetry in gut development: what happens next? Bioessays *31*, 1026-1037.

Camenisch TD, S.A., Brehm-Gibson T, Biesterfeldt J, Augustine ML, Calabro A Jr, Kubalak S, Klewer SE, McDonald JA. (2000). Disruption of hyaluronan synthase-2 abrogates normal cardiac morphogenesis and hyaluronan-mediated transformation of epithelium to mesenchyme. J Clin Invest *106*, 349-360.

Carulli D, R.K., Brown DJ, Bonnert TP, Pollack SJ, Oliver K, Strata P, Fawcett JW. (2006). Composition of perineuronal nets in the adult rat cerebellum and the cellular origin of their components. J Comp Neurol *494*, 559-577.

Casalino-Matsuda SM, M.M., Day AJ, Forteza RM. (2009). Hyaluronan fragments/CD44 mediate oxidative stress-induced MUC5B up-regulation in airway epithelium. Am J Respir Cell Mol Biol *40*, 277-285.

Casey B., H.B. (2000). Left-right axis malformations in man and mouse. Curr Opin GenetDev *10*, 257-261.

Casini P, N.I., Ori M. (2012). Hyaluronan is required for cranial neural crest cells migration and craniofacial development. Dev Dyn *241*, 294-302.

Cheedipudi S, G.O., and Dobreva G, (2014). Epigenetic inheritance of cell fates during embryonic development. Front Genet *5*.

Christianson HC, B.M. (2014). Heparan sulfate proteoglycan as a cell-surface endocytosis receptor. Matrix Biol *35*, 51-55.

Contreras EG, G.M., Sánchez N, Carrasco H, Larraín J (2009). Early requirement of Hyaluronan for tail regeneration in Xenopus tadpoles. Development *136*, 2987-2996.

Cowan CR, H.A. (2004). Asymmetric cell division in C. elegans: cortical polarity and spindle positioning Annu Rev Cell Dev Biol *20*, 427-453.

Cowman MK, S.C., Kudasheva D, Li M, Dyal A, Kanai S, Balazs EA. (2005). Extended, relaxed, and condensed conformations of hyaluronan observed by atomic force microscopy. Biophys J *88*, 590-602.

Csoka AB, F.G., Stern R. (2001). The six hyaluronidase-like genes in the human and mouse genomes. Matrix Biol *20*, 499-508.

Csóka AB, S.S., Stern R (1999). Expression analysis of six paralogous human hyaluronidase genes clustered on chromosomes 3p21 and 7q31. Genomics *60*, 356-361.

Cyphert JM, T.C., Garantziotis S. (2015). Size Matters: Molecular Weight Specificity of Hyaluronan Effects in Cell Biology. int J Cell Biol *2015*.

Danilchik MV, B.E., Riegert K. (2011). Intrinsic chiral properties of the Xenopus egg cortex: an early indicator of left–right asymmetry. Development *133*, 4517-4526.

Davis NM, K.N., Sun X, Gros J, Martin JF, Tabin CJ. (2008). The chirality of gut rotation derives from left-right asymmetric changes in the architecture of the dorsal mesentery. Dev Cell *15*, 134-145.

Day AJ, P.G. (2002). Hyaluronan-binding proteins: tying up the giant. J Biol Chem *277*, 4585-4588.

de la Motte CA, H.V., Drazba J, Bandyopadhyay SK, Strong SA. (2003). Mononuclear leukocytes bind to specific hyaluronan structures on colon mucosal smooth muscle cells treated with polyinosinic acid:polycytidylic acid: inter-alpha-trypsin inhibitor is crucial to structure and function. Am J Pathol *163*, 121-133.

Deed R, R.P., Kumar P, Norton JD, Smith J, Freemont AJ, Kumar S. (1997). Early-response gene signalling is induced by angiogenic oligosaccharides of hyaluronan in endothelial cells. Inhibition by non-angiogenic, high-molecular-weight hyaluronan. Int J Cancer *71*, 251-256.

Do Y, N.P., Nagarkatti M. (2004). Role of CD44 and hyaluronic acid (HA) in activation of alloreactive and antigen-specific T cells by bone marrow-derived dendritic cells. J Immunother *27*, 1-12.

Erickson M, S.R. (2012). Chain gangs: new aspects of hyaluronan metabolism. Biochem Res int *2012*, 893-947.

Esko JD, K.K., Lindahl U (2009). Proteoglycans and Sulfated Glycosaminoglycans (Cold Spring Harbor (NY: Cold Spring Harbor Laboratory Press).

Faulk DM, J.S., Zhang L, Badylak SF. (2014). Role of the extracellular matrix in whole organ engineering. J cell Physiol *229*, 984-989.

Feinberg RN, B.D. (1983). Hyaluronate in vasculogenesis. Science *220*, 1177-1179.

Fenderson BA, S.I., Aruffo A. (1993). Localization of hyaluronan in mouse embryos during implantation, gastrulation and organogenesis. Differentiation *54*, 85-98.

Filston HC, K.D. (1981). Malrotation - the ubiquitous anomaly. J Pediatr Surg *16*, 614-620.

Frost GI, C.A., Wong T, Stern R. (1997). Purification, cloning, and expression of human plasma hyaluronidase. Biochem Biophys Res Commun *236*, 10-15.

Frost GI, C.T., Stern R (1996). The hyaluronidases: a chemical, biological and clinical overview. Trends Glycosci Glycotech *8*, 419-434.

Fülöp C, S.S., Mukhopadhyay D, Bárdos T, Kamath RV, Rugg MS, Day AJ, Salustri A, Hascall VC, Glant TT, Mikecz K. (2003). Impaired cumulus mucification and female sterility in tumor necrosis factor-induced protein-6 deficient mice. Development *130*, 2253-2261.

Gandhi NS, M.R. (2008). The structure of glycosaminoglycans and their interactions with proteins. Chem Biol Drug Des *72*, 455-482.

Goldstein B, H.S. (1996). Specification of the anteroposterior axis in Caenorhabditis elegans. Development *122*, 1467-1474.

Graziano K, I.S., Dasgupta R, Lopez ME, Austin M, Chen LE, Goldin A, Downard CD, Renaud E, Abdullah F (2015). Asymptomatic malrotation: Diagnosis and surgical management: An American Pediatric Surgical Association outcomes and evidence based practice committee systematic review. J Pediatr Surg *50*, 1783-1790.

Gros J, F.K., Viebahn C,Blum m,Tabin CJ. (2009). Cell movements at Hensen's node establish Left/Right asymmetric gene expression in the chick. Science *324*, 941-944.

Guglielmotti V, C.L. (2006). The interplay between the pineal complex and the habenular nuclei in lower vertebrates in the context of the evolution of cerebral asymmetry. Brain Res Bull *69*, 475-488.

Gushulak L, H.R., Martin D, Seyrantepe V, Pshezhetsky A, Triggs-Raine B. (2012). Hyaluronidase 1 and β-hexosaminidase have redundant functions in hyaluronan and chondroitin sulfate degradation. J Biol Chem *287*, 16689-16697.

Habuchi H, H.O., Kimata K. (2004). Sulfation pattern in glycosaminoglycan: does it have a code? Glycoconj *21*, 47-52.

Hascall V, E.J. (2009). Hyaluronan. In Essentials of Glycobiology, C.R. Varki A, Esko JD, et al.,, ed. (Cold Spring Harbor (NY): Cold Spring Harbor Laboratory Press).

Heisenberg CP, B.Y. (2013). Forces in tissue morphogenesis and patterning. Cell *153*, 948-962.

Hemming R, M.D., Slominski E, Nagy JI, Halayko AJ, Pind S, Triggs-Raine B. (2008). Mouse Hyal3 encodes a 45- to 56-kDa glycoprotein whose overexpression increases hyaluronidase 1 activity in cultured cells. Glycobiology *18*, 280-289.

Higman VA, B.D., Mahoney DJ, Blundell CD, Sattelle BM, Dyer DP, Green DE, DeAngelis PL, Almond A, Milner CM, Day AJ. (2014). A refined model for the TSG-6 link module in complex with hyaluronan: use of defined oligosaccharides to probe structure and function. J Biol Chem *289*, 5619-5634.

Hiroyuki Yoshida, A.N., Ayumi Kusaka-Kikushima Megumi Tobiishi, Keigo Kawabata, Tetsuya Sayo, Shingo Sakai, Yoshinori Sugiyama, Hiroyuki Enomoto, Yasunori Okada, and Shintaro Inouea (2013). KIAA1199, a deafness gene of unknown function, is a new hyaluronan binding protein involved in hyaluronan depolymerization. Prot Natl Acad Sci USA *110*, 5612-5617.

Hynes RO (2009). The extracellular matrix: not just pretty fibrils. Science *326*, 1216-1219.

Hynes RO, N.A. (2012). Overview of the matrisome--an inventory of extracellular matrix constituents and functions. Cold Spring Harb Perspect Biol *4*, a004903.

Iozzo RV (2005). Basement membrane proteoglycans: from cellar to ceiling. Nat Rev Mol Cell Biol *6*, 646-656.

Itano N, K.K. (2002). Mammalian hyaluronan synthases. IUBMB life *54*, 195-199.

Itano N, S.T., Yoshida M, Lenas P, Yamada Y, Imagawa M, Shinomura T, Hamaguchi M, Yoshida Y, Ohnuki Y, Miyauchi S, Spicer AP, McDonald JA, Kimata K. (1999). Three isoforms of mammalian hyaluronan synthases have distinct enzymatic properties. J Biol Chem *274*, 25085-25092.

Kim HY, N.C. (2012). Extracellular matrix and cytoskeletal dynamics during branching morphogenesis. Organogenesis *8*, 56-64.

Kim SH, T.J., Guimond S. (2011). Extracellular matrix and cell signalling: the dynamic cooperation of integrin, proteoglycan and growth factor receptor. J Endocrinol *209*, 139-151.

Kirkpatrick CA, D.B., Rawson JM, Selleck SB. (2004). Spatial regulation of Wingless morphogen distribution and signaling by Dally-like protein. Dev Cell *7*, 513-523.

Kohda D, M.C., Parkar AA, Hatanaka H, Inagaki FM, Campbell ID, Day AJ (1996). Solution structure of the link module: a hyaluronan-binding domain involved in extracellular matrix stability and cell migration. Cell *86*, 767-775.

Kolset SO, T.H. (2008). Serglycin--structure and biology. Cell Mol Life Sci *65*, 1073-1085.

Kosher RA, S.M., Walker KH. (1981). A gradation of hyaluronate accumulation along the proximodistal axis of the embryonic chick limb bud. J Embryol Exp Morphol *63*, 85-98.

Kurpios NA, I.M., Davis NM, Lui W, Katz T, Martin JF, Izpisúa Belmonte JC, Tabin CJ. (2008). The direction of gut looping is established by changes in the extracellular matrix and in cell:cell adhesion. Prot Natl Acad Sci USA *105*, 8499-8506.

Langer JC (2017). Intestinal rotation abnormalities and midgut volvulus. Surgical clinics of North America *97*, 147-159.

Lauer ME, F.C., Mukhopadhyay D, Comhair S, Erzurum SC, Hascall VC. (2009). Airway smooth muscle cells synthesize hyaluronan cable structures independent of inter-alpha-inhibitor heavy chain attachment. J Biol Chem *284*, 5313-5323.

Lecuit T, L.P. (2007). Cell surface mechanics and the control of cell shape, tissue patterns and morphogenesis. Nat Rev Mol Cell Biol *8*, 633-644.

Lepperdinger G, S.B., Kreil G. (1998). HYAL2, a human gene expressed in many cells, encodes a lysosomal hyaluronidase with a novel type of specificity. J Biol Chem *273*, 22466-22470.

Lesley J, G.I., Mahoney DJ, Cordell MR, Rugg MS, Hyman R, Day AJ, Mikecz K. (2004). TSG-6 modulates the interaction between hyaluronan and cell surface CD44. J Biol Chem *279*, 25745-25754.

Levin M (1998). The roles of activin and follistatin signaling in chick gastrulation. Int J Dev Biol *42*, 553-559.

Levin M (2005). Left-right asymmetry in embryonic development: a comprehensive review. Mech Dev *122*, 3-25.

Levin M, P.A. (2007). Left-right patterning from the inside out: widespread evidence for intracellular control. Bioessays *29*, 271-287.

Levin M, P.S., Roberts DJ, Cooke J, Kuehn MR, Tabin CJ. (1997). Left/right patterning signals and the independent regulation of different aspects of situs in the chick embryo. Dev Biol *189*, 57-67.

Li Y, T.B., Dealy CN, and Kosher RA (2007). Hyaluronan in Limb Morphogenesis. Dev Biol *305*, 411-420.

Lindhardt RJ, T.T. (2004). Role of Glycosaminoglycans in Cellular Communication. Accounts of Chemical research *37*, 431-438.

Liu J, L.Q., Kuehn MR,Litingtung Y, Vokes SA, Chiang C. (2013). Sonic hedgehog signaling directly targets Hyaluronic Acid Synthase 2, an essential regulator of phalangeal joint patterning. Dev Biol *375*.

Lu P, W.V., Werb Z. (2012). The extracellular matrix: a dynamic niche in cancer progression. J Cell Biol *196*, 395-406.

Mahadevan A, W.I., Sivakumar A, Gludish DW, Shilvock AR, Noden DM, Huss D, Lansford R, Kurpios NA. (2014). The left-right Pitx2 pathway drives organ-specific arterial and lymphatic development in the intestine. Dev Cell *31*, 690-706.

Männer J (2001). Does an equivalent of the "ventral node" exist in chick embryos? A scanning electron microscopic study. Anat Embryol *203*, 481-490.

Markwald RR, F.T., Bank H, Bernanke DH (1978). Structural analyses on the matrical organization of glycosaminoglycans in developing endocardial cushions. Dev Biol *62*, 292-316.

Matsumoto K, L.Y., Jakuba C, Sugiyama Y,Sayo T, Okuno M, Dealy CN, Toole BP, Takeda J,Yamaguchi Y,Kosher RA, (2009). Conditional inactivation of Has2 reveals a crucial role for hyaluronan in skeletal growth, patterning, chondrocyte maturation and joint formation in the developing limb. Development *136*, 2825-2835.

McDowell G, R.S., Levin M. (2016). From cytoskeletal dynamics to organ asymmetry: a nonlinear, regulative pathway underlies left-right patterning. Philos Trans R Soc Lond B Biol Sci *371*.

McDowell GS, L.J., Paré JF, Cammarata G, Lowery LA, Levin M. (2016). Conserved roles for cytoskeletal components in determining laterality. Integr Biol (Camb) *8*, 267-286.

McGrath J, S.S., Makova S, Tian X, Brueckner M (2003). Two populations of node monocilia initiate left-right asymmetry in the mouse. Cell *114*, 61-73.

Mecham RP (2001). Overview of extracellular matrix. Curr Protoc Cell Biol *10*.

Milner CM, D.A. (2003). TSG-6: a multifunctional protein associated with inflammation. J Cell Sci *116*, 1863-1873.

Mouw JK, O.G., Weaver VM. (2014). Extracellular matrix assembly: a multiscale deconstruction. Nat Rev Mol Cell Biol *15*, 771-785.

Mukhopadhyay D, A.A., Rugg MS, Day AJ, Fülöp C. (2004). Specificity of the tumor necrosis factor-induced protein 6-mediated heavy chain transfer from inter-alpha-trypsin inhibitor to hyaluronan: implications for the assembly of the cumulus extracellular matrix. J Biol Chem *279*, 11119-11128.

Nakamura K, Y.S., Yoneda M, Okamoto S, Tamaki Y, Ito T, Okada M, Aso K, Makino I. (2004). High, but not low, molecular weight hyaluronan prevents T-cell-mediated liver injury by reducing proinflammatory cytokines in mice. J Gastroenterol *39*, 346-354.

Nelson CM (2012). Symmetry breaking during morphogenesis in the embryo and in engineered tissues. AiChE *58*, 3608-3613.

Neville C (1976). Animal asymmetry (London UK: Illustrated).

Okumura T, U.H., Kuroda J, Gittenberger E, Asami T, Matsuno K. (2008). The development and evolution of left-right asymmetry in invertebrates: lessons from Drosophila and snails. Dev Dyn *237*, 3497-3515.

Ouyang X, P.N., Talbott MD, Payumo AY, Halluin C, Longaker MT, Chen JK (2017). Hyaluronic acid synthesis is required for zebrafish tail fin regeneration. PloS One *12*, e0171898.

Parkar AA, D.A. (1997). Overlapping sites on the Link module of human TSG-6 mediate binding to hyaluronan and chondroitin-4-sulphate. FEBS Letters *410*, 413-417.

Paulozzi LJ, L.J. (1999). Laterality patterns in infants with external birth defects. Teratology *60*, 265-271.

Petrey AC, d.l.M.C. (2014). Hyaluronan, a crucial regulator of inflammation. Front Immunol *5*.

Piedra ME, I.J., Albajar M, Rodriguez-Rey JC, Ros MA. (1998). Pitx2 participates in the late phase of the pathway controlling left-right asymmetry. Cell *94*, 319-324.

Qiu D, C.S., Wozniak L, McSweeney M, Perrone E, Levin M. (2005). Localization and loss-of-function implicates ciliary proteins in early, cytoplasmic roles in left-right asymmetry. Dev Dyn *234*, 176-189.

Raman R, S.V., Sasisekharan R. (2005). Structural insights into biological roles of protein-glycosaminoglycan interactions. Chem Biol *12*, 267-277.

Raya A, I.B.J. (2006). Left-right asymmetry in the vertebrate embryo: from early information to higher-level integration. Nat Rev Genet *7*, 283-293.

Roberts RM, K.M., Magnuson SR, Falduto MT, Torres KE. (2011). Transcript profiling of individual twin blastomeres derived by splitting two-cell stage murine embryos. Biol Reprod *84*, 487-494.

Roussigne M, B.P., Wilson SW (2012). Breaking symmetry: the zebrafish as a model for understanding left– right asymmetry in the developing brain. Dev Neurobiol *72*, 269-281.

Salustri A, Y.M., Underhill CB, Laurent TC, Hascall VC. (1992). Localization and synthesis of hyaluronic acid in the cumulus cells and mural granulosa cells of the preovulatory follicle. Dev Biol *151*, 541-551.

Sanggaard KW, S.C., Krogager TP, Kristensen T, Wisniewski HG, Thøgersen IB, Enghild JJ. (2008). TSG-6 Transfers Proteins between Glycosaminoglycans via a Ser28-mediated Covalent Catalytic Mechanism. J Biol Chem *283*, 33919-33926.

Sauer S, K.A. (2012). Left-right symmetry breaking in mice by left-right dynein may occur via a biased chromatid segregation mechanism, without directly involving the Nodal gene. Front Oncol *2012,* 166.

Savani RC, C.G., Pooler PM, Zaman A, Zhou Z, DeLisser HM. (2001). Differential involvement of the hyaluronan (HA) receptors CD44 and receptor for HA-mediated motility in endothelial cell function and angiogenesis. J Biol Chem *276*, 36770-36778.

Savin T, K.N., Shyer AE, Florescu P, Liang H, Mahadevan L, Tabin CJ. (2011). On the growth and form of the gut. Nature *476*, 57-62.

Schnall BS, S.D. (1974). Nonrandom laterality of malformations in paired structures. J Pediatr *85*, 509-511.

Schreuder MF (2011). Unilateral anomalies of kidney development: why is left not right? Kidney Int *80*, 740-745.

Schwarzbauer JE, D.D. (2011). Fibronectins, their fibrillogenesis, and in vivo functions. Cold Spring Harb Perspect Biol *3*, a005041.

Seyfried NT, M.G., Almond A, Mahoney DJ, Dudhia J, Day AJ. (2005). Expression and purification of functionally active hyaluronan-binding domains from human cartilage link protein, aggrecan, and versican. Formation of ternary complexes with defined hyaluronan oligosaccharides. J Biol Chem *280*.

Shay E, H.H., Sakurai S, Tseng SC. (2011). Inhibition of angiogenesis by HC·HA, a complex of hyaluronan and the heavy chain of inter-α-inhibitor, purified from human amniotic membrane. Invest Opthalmol Vis Sci *52*, 2669-2678.

Slevin M, K.J., Gaffney J, Matou S, West D, Delisser H, Savani RC, Kumar S. (2007). Hyaluronan-mediated angiogenesis in vascular disease: uncovering RHAMM and CD44 receptor signaling pathways. Matrix Biol *26*, 58-68.

Smith KA, C.S., von der Hardt S, de Pater E, Soufan A, Bussmann J, Schulte-Merker S, Hammerschmidt M, Bakkers J. (2008). Rotation and asymmetric development of the zebrafish heart requires directed migration of cardiac progenitor cells. Dev Cell *14*, 287-297.

Soffers JHM, H.J., Mekonen HK, Koehler SE, and . Lamers WH (2015). The growth pattern of the human intestine and its mesentery. BMC Dev Biol *15*.

St Johnston D, N.-V.C. (1992). The origin of pattern and polarity in the Drosophila embryo. Cell *68*, 201-219.

Stern R, a.J.M. (2006). Hyaluronidases: their genomics, structures, and mechanisms of action. Chem Rev *106*, 818-839.

Stern R, K.G., Jedrzejas MJ, Soltes L. (2007). The many ways to cleave hyaluronan. Biotechnol Adv *25*, 537-557.

Streit, A.e.a. (1994). Of mice and frogs. Trends in Genetics *10*, 181-183.

Tabin CJ, V.K. (2003). A two-cilia model for vertebrate left-right axis specification. Genes Dev *17*, 1-6.

Tammi RH, P.A., Rilla K, Karousou E, Vigetti D, Makkonen K, Tammi MI. (2011). Transcriptional and post-translational regulation of hyaluronan synthesis. FEBS J *278*, 1419-1428.

Tanaka Y, O.Y., Hirokawa N. (2005). FGF-induced vesicular release of Sonic hedgehog and retinoic acid in leftward nodal flow is critical for left-right determination. nature *435*, 172-177.

Taylor KR, Y.K., Radek KA, Di Nardo A, Goodarzi H, Golenbock D, Beutler B, Gallo RL (2007). Recognition of hyaluronan released in sterile injury involves a unique receptor complex dependent on Toll-like receptor 4, CD44, and MD-2. J Biol Chem *282*, 18265-18275.

Teriete P., B.S., Noble M., Blundell C. D., Wright A. J., Pickford A. R., Lowe E., Mahoney D. J., Tammi M. I., Kahmann J. D., Campbell I. D., Day A. J., Jackson D. G. (2004). Structure of the regulatory hyaluronan binding domain in the inflammatory leukocyte homing receptor CD44. Mol Cell *13*, 483-496.

Termeer C, B.F., Sleeman J, Fieber C, Voith U, Ahrens T, Miyake K, Freudenberg M, Galanos C, Simon JC. (2002). Oligosaccharides of Hyaluronan activate dendritic cells via toll-like receptor 4. J Exp Med *195*, 99-111.

Tian X, A.J., Hine C, Vaidya A, Myakishev-Rempel M, Ablaeva J, Mao Z, Nevo E, Gorbunova V, Seluanov A. (2013). High-molecular-mass hyaluronan mediates the cancer resistance of the naked mole rat. Nature *499*, 346-349.

Torres AM, Z.M. (1993). Malrotation of the intestine. World J Surg *17*, 326-331.

Triggs-Raine B, S.T., Zhang H, Wicklow BA, Natowicz MR. (1999). Mutations in HYAL1, a member of a tandemly distributed multigene family encoding disparate hyaluronidase activities, cause a newly described lysosomal disorder, mucopolysaccharidosis IX. Prot Natl Acad Sci USA *96*, 6296-6300.

Vaibhav P. Pai, L.N.V., Douglas Blackiston, and Michael Levin (2012). Neurally Derived Tissues in Xenopus laevis Embryos Exhibit a Consistent Bioelectrical Left-Right Asymmetry. Stem Cells Int *2012*.

Vandenberg LN, L.M. (2009). Perspectives and open problems in the early phases of left-right patterning. Semin Cell Dev Biol *20*, 456-463.

Vigetti D, K.E., Viola M, Deleonibus S, De Luca G, Passi A. (2014). Hyaluronan: biosynthesis and signaling. Biochim Biophys Acta *1840*, 2452-2459.

Wang G, Y.H., Amack JD. (2013). Analysis of gene function and visualization of cilia-generated fluid flow in Kupffer's vesicle. J vis Exp *31*.

Ween MP, O.M., and Ricciardelli C (2011). Role of Versican, Hyaluronan and CD44 in Ovarian Cancer Metastasis. Int J Mol Sci *12*, 1009-1029.

Weigel, P.H. (2015). Hyaluronan Synthase: The Mechanism of Initiation at the Reducing End and a Pendulum Model for Polysaccharide Translocation to the Cell Exterior. Int J Cell Biol *2015*, 15 pages

Weischaus E (2016). Positional Information and Cell Fate Determination in the Early Drosophila Embryo. Curr Top Dev Biol *117*, 567-579.

Welsh IC, K.H., Chen FL, Werner M, Shopland LS, Danko CG, Lis JT, Zhang M, Martin JF, Kurpios NA (2015). Chromatin Architecture of the Pitx2 Locus Requires CTCF- and Pitx2-Dependent Asymmetry that Mirrors Embryonic Gut Laterality. Cell Rep *13*, 337-349.

Welsh IC, T.M., Gludish DW, Alfonso-Parra C, Bai Y, Martin JF, Kurpios NA. (2013). Integration of left-right Pitx2 transcription and Wnt signaling drives asymmetric gut morphogenesis via Daam2. Dev Cell *26*, 629-644.

Wilting J, H.M. (2011). Left-right asymmetry in embryonic development and breast cancer: common molecular determinants? Curr Med Chem *18*, 5519-5527.

Yahya RS, E.-B.A., El-Mezayen HA, Abdelmasseh HM, Eissa MA (2014). Biochemical evaluation of hyaluronic acid in breast cancer. Clin lab *60*, 1115-1121.

Yanagishita M (1993). Function of proteoglycans in the extracellular matrix. Acta pathol Jpn *43*, 283-293.

CHAPTER 2: RIGHT-SIDED HYALURONAN BREAKS LEFT-RIGHT SYMMETRY DURING GUT ROTATION AND PATTERNS THE GUT VASCULATURE

Aravind Sivakumar[1], Aparna Mahadevan[1], Mark E. Lauer[**], Siddesh Ramesh[1], Ricky J. Narvaez[1], Vincent C. Hascall[2], and Natasza A. Kurpios[1,*]

[1]Department of Molecular Medicine, College of Veterinary Medicine, Cornell University, Ithaca, NY 14853, USA

[2]Department of Biomedical Engineering, Cleveland Clinic Lerner Research Institute, Cleveland, Ohio 44195, USA

The work described in this chapter has been submitted to the journal, Cell and is under review as of July 30, 2017 . N.A.K. and A.S. designed the research with additional contributions from A.M, M.E.L and V.C.H. A.S. performed all the experiments. A.M. contributed data in Figures 7E (middle panel), S1B, S3C, S6B and technical expertise to experimental design for Figures 8A, 8B, 8C. S.R. contributed data in Figures 1C, 1E, 7A. R.J.N. contributed data in Figure 1C, 1E, S1B. M.E.L. and V.C.H contributed technical expertise and tools

2.1 Abstract

Counterclockwise intestinal rotation prevents midgut volvulus, a catastrophic strangulation of abdominal vasculature. We previously showed that cellular asymmetries within the midgut dorsal mesentery (DM) initiate this rotation and pattern the gut vasculature. Whereas the left-right *Pitx2* orchestrates all organ laterality, its expression in the left DM long precedes any morphological asymmetries, indicating that rotation does not initiate by *Pitx2* alone. Here we show that the extracellular matrix (ECM) component hyaluronan (HA) breaks lateral symmetry within the DM and initiates gut rotation. Unexpectedly, HA is produced on the right side and induces robust ECM expansion as the first evidence of DM morphological asymmetry. This is dependent on modification of HA by the asymmetrically expressed enzyme Tsg6, forming stable matrices to mechanically expand the right mesenchyme. Tsg6-null mice are predisposed to both malrotation and volvulus. Our studies reveal novel ECM-driven laterality signals, and may illuminate the origins of gut and vascular anomalies.

2.2 Introduction

An essential aspect of organ morphogenesis is the timely introduction of molecular asymmetries to spatially pattern the developing organ's form and its vascular supply. Mechanistic studies of these events are challenging because they are often confounded by tissue multi-dimensionality and by the dynamic remodeling of structures to achieve the complex final form. The embryonic midgut (intestine) serves as a powerful model to simplify and study organ asymmetry in vivo. In contrast to the heart or stomach, which, in addition to looping, exhibit complex patterns of ballooning, differentiation, and asymmetric growth, the midgut remains as a simple cylindrical tube throughout its morphogenesis. This simplicity is evident when the gut is viewed in cross-section (Figure 2.1A), where asymmetries in cell architecture and extracellular matrix (ECM) composition that drive midgut looping can be studied in a single visual plane. Thus, using the midgut, the problem of LR organ asymmetry can be distilled to the initial events that establish directional gut looping. This is a critical paradigm because while vertebrates exhibit a high degree of bilateral symmetry, the initially symmetrical gut tube later loops and rotates in a highly conserved, asymmetrically looped pattern (Savin et al., 2011). This complex process correctly packs the gut tube into the limiting space of the body cavity subject to strict topological and evolutionary constraints, and is also intimately linked to gut absorptive function. Even simple errors in the events that loop the gut lead to catastrophic birth defects, such as intestinal malrotation and midgut volvulus (Applegate, 2009; Savin et al., 2011).

Formation of intestinal loops is the result of homogeneous and isotropic forces that arise from the differential growth of the gut tube and its tissue anchor, the dorsal mesentery (DM) (Savin et al., 2011). However, the chirality of gut looping is initiated by a directional bias during the first gut tilting event, driven by left-right (LR) asymmetric changes in the cellular and

extracellular architecture of the DM (Davis et al., 2008; Kurpios et al., 2008). The embryonic chicken DM arises on day 2.5 (Hamburger-Hamilton [HH] stage 17, akin to mouse embryonic [E] day 10) (Hamburger and H.L., 1992) from the fusion of the left and right splanchnic mesoderm. While morphologically symmetrical in cross-section, the early DM consists of molecularly distinct left and right cellular compartments (Figure 2.1A). Shortly thereafter (HH20, E10.5 in mice), initial DM symmetry is broken during a dramatic reorganization where the left mesenchyme condenses and the right side expands, causing a trapezoidal deformation of the DM that swings the gut tube leftward (Figure 2.1A). This critical leftward tilt provides a directional bias for the conserved counterclockwise gut rotation, disruption of which randomizes gut looping chirality (Davis et al., 2008; Kurpios et al., 2008; Savin et al., 2011; Welsh et al., 2013).

In addition to directing gut rotation, the DM is the conduit for the extensive network of blood and lymphatic vessels that nourish and drain the intestine and provide the necessary channels for transport of dietary lipids. We recently showed that vascular development of DM arteries is highly stereotypical, commensurate with the onset of gut rotation, and proceeds strictly on the DM left side (Mahadevan et al., 2014). Interestingly, whereas arterial endothelial progenitors are initially present on both sides of the DM, they become progressively excluded on the right side. Thus, intestinal blood vessel development is restricted to the left side (Mahadevan et al., 2014), intimately linked to the pathways driving morphologic asymmetry of the parent organ itself. How and why this vascular asymmetry is established remains unknown.

Initial LR symmetry-breaking decisions are made early at the node and lead to left-sided secretion of the highly conserved ligand Nodal throughout the left splanchnic mesoderm (Levin et al., 1995). While Nodal expression is transient, Nodal induces the homeobox transcription factor Pitx2 at E7.5 (HH7-8) (Piedra et al., 1998), which persists to maintain the left side identity of all

Figure 2.1: Expansion of the right side of the DM initiates LR asymmetric gut rotation. A The symmetrical primitive gut tube (GT, grey), in the chicken at HH17 (mouse E9.5) suspended by the DM (blue-right; orange-left) undergoes a critical counterclockwise rotation to drive gut looping. Leftward tilt of the GT (HH21, mouse E10.5) mediated by changes in cell architecture across the LR axis of the initially symmetric DM (HH17), initiates this counterclockwise rotation. **B** *Pitx2* expression in the left DM appears prior to the initiation of the leftward tilt (*Pitx2* RNA ISH). **C** H&E staining of Z3 midgut sections from HH17-21 shows that right-sided expansion breaks the symmetry of the DM at HH18, prior to left-sided condensation at HH20. **D** Quantification of intercellular (cell-free) spaces from C; right expansion: $p = 0.0001$, left condensation: $p = 0.0044$ (unpaired two-tailed Student's t-test). Error bars represent mean ± SEM for 10 chicken embryos per developmental stage. **E** Angle of midgut tilting from HH17-21, measured as displacement of GT from the midline (notochord) reveals significant increase in tilting angle at HH18 coincident with expansion. Gut tilting on expansion $p = 0.0012$ (unpaired two-tailed T-test with Holm-Sidak correction for multiple comparisons). Error bars represent mean ± SEM for 10 chicken embryos per developmental stage for HH17, 18 and 19, and 7 embryos per developmental stage for HH20 and HH21. See also Figure S1. **Scale bars: B** (100 μm); **C** (50 μm).

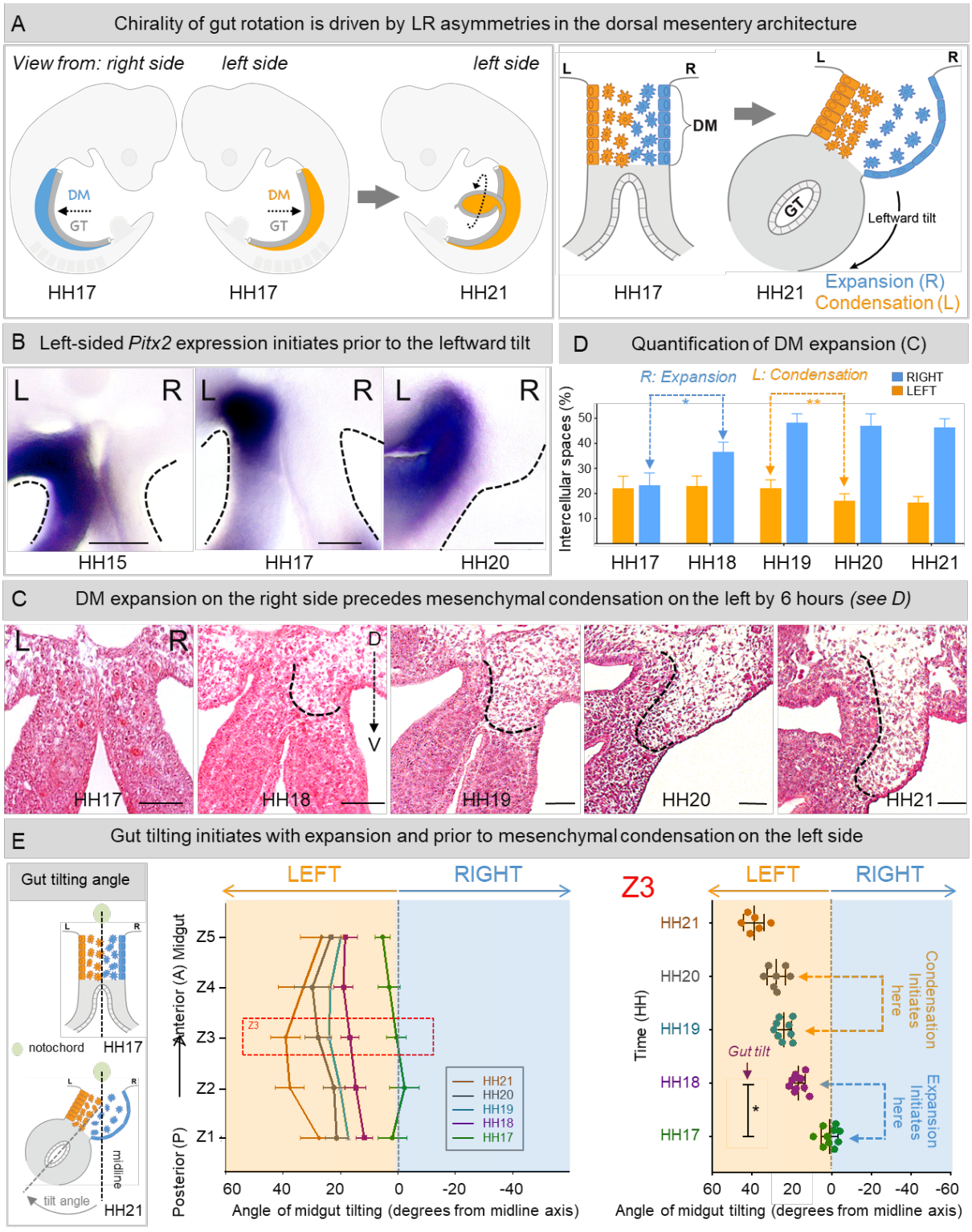
A
Chirality of gut rotation is driven by LR asymmetries in the dorsal mesentery architecture
View from: right side
left side
left side
DM
GT
HH17
HH17
HH21
L
R
DM
GT
Leftward tilt
HH17
HH21
Expansion (R)
Condensation (L)
B
Left-sided Pitx2 expression initiates prior to the leftward tilt
L
R
HH15
HH17
HH20
D
Quantification of DM expansion (C)
R: Expansion
L: Condensation
RIGHT
LEFT
Intercellular spaces (%)
HH17
HH18
HH19
HH20
HH21
C
DM expansion on the right side precedes mesenchymal condensation on the left by 6 hours (see D)
D
V
HH17
HH18
HH19
HH20
HH21
E
Gut tilting initiates with expansion and prior to mesenchymal condensation on the left side
Gut tilting angle
notochord
midline
tilt angle
HH17
HH21
LEFT
RIGHT
Anterior (A) Midgut
Posterior (P)
Z5
Z4
Z3
Z2
Z1
HH21
HH20
HH19
HH18
HH17
Angle of midgut tilting (degrees from midline axis)
Z3
Time (HH)
Gut tilt
Condensation Initiates here
Expansion Initiates here
Angle of midgut tilting (degrees from midline axis)

organ primordia to which the splanchnic mesoderm contributes. This Pitx2-driven asymmetry is evolutionarily conserved, and altered Pitx2 activity disrupts visceral laterality, including chiral and positional randomization of multiple organs and vessels (Shiratori et al., 2006). In the chicken and mouse DM, Pitx2 induces a left-specific gene signature that drives cell behavior only on the left side and Pitx2-null mice are unable to generate the leftward tilt (Davis et al., 2008; Kurpios et al., 2008; Mahadevan et al., 2014; Welsh et al., 2013). However, despite the importance of Pitx2 during gut rotation, Pitx2 expression in chickens and mice initiates in the splanchnic mesoderm long prior to any morphological asymmetries within the DM, and even in locations of the intestine that do not loop. Thus, Pitx2 expression alone is insufficient to break LR symmetry within the DM that is required to initiate the leftward tilt; other factors expressed in the region of the looping midgut must intersect with Pitx2 target genes to drive intestinal rotation.

Unexpectedly, here we show that the mesenchymal expansion specifically on the right side of the DM precedes all other DM cellular asymmetries taking place on the left, suggesting that events on the right side break initial DM symmetry. Moreover, the timing of expansion coincides spatiotemporally with the progressive loss of vascular progenitor cells observed on the right, suggesting a shared mechanism driving right mesenchymal expansion and left sided formation of gut vasculature. Hyaluronan (HA), a non-sulfated glycosaminoglycan, is the predominant ECM component on the right side of the DM (Kurpios et al., 2008). We now show that HA drives right-sided symmetry breaking events by a mechanism that is dependent on its covalent modification by the enzyme tumor necrosis factor alpha-inducible protein 6 (Tnfaip6, also known as Tsg6). Moreover, the loss of modified HA in Tsg6-null mice caused randomized gut looping and vascular patterning defects. Interestingly, we have found that intact HA matrices on the right side are required to exclude gut vasculature by repressing right-sided *Cxcl12* expression, highlighting the

tightly interwoven nature of the pathways driving gut looping morphogenesis. Taken together, our studies identify a novel ECM-derived pathway driving LR organogenesis initiated on the right side of the embryo, and may shed light on the origin of gut and vascular anomalies.

2.3 Results

2.3.1 Expansion of the right side of the DM initiates LR asymmetric gut rotation

The cellular asymmetries observed in the left and right DM are transient and serve to initiate gut rotation by deforming the DM and tilting the gut tube leftward (Figure 2.1A) (Davis et al., 2008; Kurpios et al., 2008). We previously demonstrated that these asymmetries include condensation of the left mesenchymal compartment and expansion restricted to the right side (Figure 2.1A). While Pitx2 is necessary for the molecular and cellular properties within the left DM, *Pitx2* expression in the left lateral plate mesoderm initiates at E7.5 in mice and HH7-8 in chickens (Piedra et al., 1998), several days prior to the leftward tilt (HH20) (Figure 2.1B). This provides evidence that *Pitx2* expression alone does not break the cellular symmetry within the DM to initiate the tilt (Davis et al., 2008). To identify the symmetry-breaking mechanism, we performed careful histological analysis of the LR DM mesenchymal architecture prior to the formation of the leftward tilt (HH17-HH21, Figures 2.1C and 2.1D).

The DM of the embryonic midgut is formed via the fusion of the left and right splanchnic mesoderm at HH17 (28-32 somites) (Hamburger and H.L., 1992). To quantify the LR differences in the mesenchymal architecture of the midgut DM, tissue sections from caudal (posterior, P) to rostral (anterior, A) midgut were stained with Hemotoxylin and Eosin (H&E) and the intercellular (cell-free) spaces in the left and right DM were quantified (Figures 2.1C, S1A, and S1B). To understand how these changes subsequently affect the tilting of the midgut, the angle of the tilt

was quantified as a tilt of the midgut with respect to the embryonic midline (Figure 2.1E). At HH17, the cellular architecture of the entire AP length of the midgut was symmetric with both the left and right mesenchymal compartments densely packed (Figures 2.1C, 2.1D and S1B) (Davis et al., 2008). Correspondingly, the axis of the midgut was closely aligned with the embryonic midline demonstrating that gut tilting had not yet initiated (Figure 2.1E).

Within 4 hours, by HH18 (34-36 somites), the fusion of the splanchnic mesoderm progressed further resulting in the ventral extension of DM (Figure 2.1C). Strikingly, within these 4 hours, while the cellular architecture of the left mesenchyme remained unchanged, the acellular mesenchymal compartment on the right became significantly expanded (Figures 2.1C and 2.1D, dotted line, percentage of intercellular spaces in HH18 right side DM is ~37% (36.57 ± 1.248) vs. HH17 right side DM, ~23% (23.27 ± 1.557), n = 10, p = 0.0007). Thus, the early symmetry of the DM is first broken by changes taking place on the right. Coincidentally, the axis of the midgut tilted significantly to the left of the midline (Figure 2.1E). Thus, the tilting of the midgut appears to be linked with the changes taking place on the right.

We also observed a rostral to caudal variation in the expansion of the right DM with the rostral end of the midgut showing significantly more expansion compared to the caudal expansion (Figure S1; n = 10: caudal vs. midcaudal: p = 0.0219, caudal vs. central: p = 0.0185). Concomitantly, the tilting angle of the rostral midgut was more significant in comparison to the caudal midgut (Figure S1, n = 10, p = 0.007). Hence, the tilt of the midgut is spatially coordinated with the rostral-caudal variation in the expansion of the right DM.

Surprisingly, it was not until HH20 (6 hours after expansion) that we observed mesenchymal condensation on the left (Figures 2.1C and 2.1D, percentage of intercellular spaces HH20 left side DM is ~37% (37.09 ± 0.9789), n = 8 vs. HH17 left side DM, ~23% (22.11 ± 1.112), n = 9,

p = 0.0041). A significant increase in the tilting angle of the midgut was again observed (Figure 2.1E, HH21 (38.99 ± 2.123) degrees, n = 6 vs. HH19 (23.95 ± 1.26) degrees, n = 9, p = 0.001), which can be attributed to the changes in the left DM. This observation is consistent with our previous work showing that changes in both the left and right DM compartments contribute equally to the tilting of the gut tube (Kurpios et al., 2008). Thus, leftward gut tilting is initiated by DM expansion on the right side, independent of mesenchymal condensation within the left DM.

2.3.2 HA accumulation within the right DM coincides with DM expansion

We previously uncovered dramatic LR asymmetries in the ECM composition of the DM that accompany changes in mesenchyme architecture (Kurpios, 2008). Specifically, on the right, we identified hyaluronan (HA) as the prominent ECM component. HA is an extremely long glycosaminoglycan (GAG) polymer (Hascall and Esko, 2009), in which the disaccharide unit of glucuronic acid and N-acetyl-glucosamine can be repeated several thousand times (Fülöp et al., 1997). HA is the simplest of all the GAGs, and unlike the other GAGs, is not sulfated (Hascall and Esko, 2009). HA is required for cardiovascular development, and HA synthase (Has)-2 knockout mice die mid gestation at E9.5 (Camenisch et al., 2000). HA functions both as a structural component of tissues and as a signaling molecule that can influence many aspects of cell behavior. In general, our knowledge of the developmental and mechanistic roles of HA remain incomplete.

To test whether HA enrichment in the right DM coincides with the observed expansion in the DM, we performed HA immunohistochemistry (de la Motte and Drazba, 2011) between HH17-21 (Figures 2.2A, 2.2B and S2). To quantify the LR differences in HA distribution, we obtained

Figure 2.2: Hyaluronan (HA) drives the right-sided mesenchymal expansion of the DM. A. Immunohistochemistry for HA using biotinylated HABP shows that asymmetric enrichment of HA is first observed in the dorsal right DM at HH18, at the onset of mesenchymal expansion, and proceeds to extend ventrally to cover the entire right DM. **B.** Quantification of HA accumulation reveals significant enrichment of HA in the right DM at HH18, $p = 0.0007$. Average intensity profile of HA distribution across the LR axis of 7 embryos at HH19, confirms extensive HA accumulation in the right DM (blue) compared to the left DM (orange). Fold enrichment calculated by measurement of area under intensity profile graph generated for each embryo. **C.** Targeting of the right chicken DM with MU-Xyl. MU-Xyl soaked beads are surgically inserted into the right coelomic cavity (HH14) prior to DM formation to target splanchnic mesoderm (DM precursor). Beads remain intact at HH21 when embryos are analyzed. **D**. MU-Xyl treated DM shows significant reduction in HA accumulation when compared to vehicle (DMSO) treated controls (quantified in right panel, $p = 0.0031$). **E**. Depletion of HA in MU-Xyl treated embryos results in the loss of right-sided DM expansion (quantified by measurements of intercellular spaces in the right panel: MU-Xyl vs. DMSO, $p = 0.0012$; WT vs. Hyal2, $p = 0.0053$). Unpaired two-tailed Student's t-test has been used to compare fold-enrichment values and measurements of intercellular spaces and obtain statistical significance. Error bars represent mean ± SEM. See also Figure S2. **Scale bars: A** (50 µm); **D** (30 µm); **E** (50 µm).

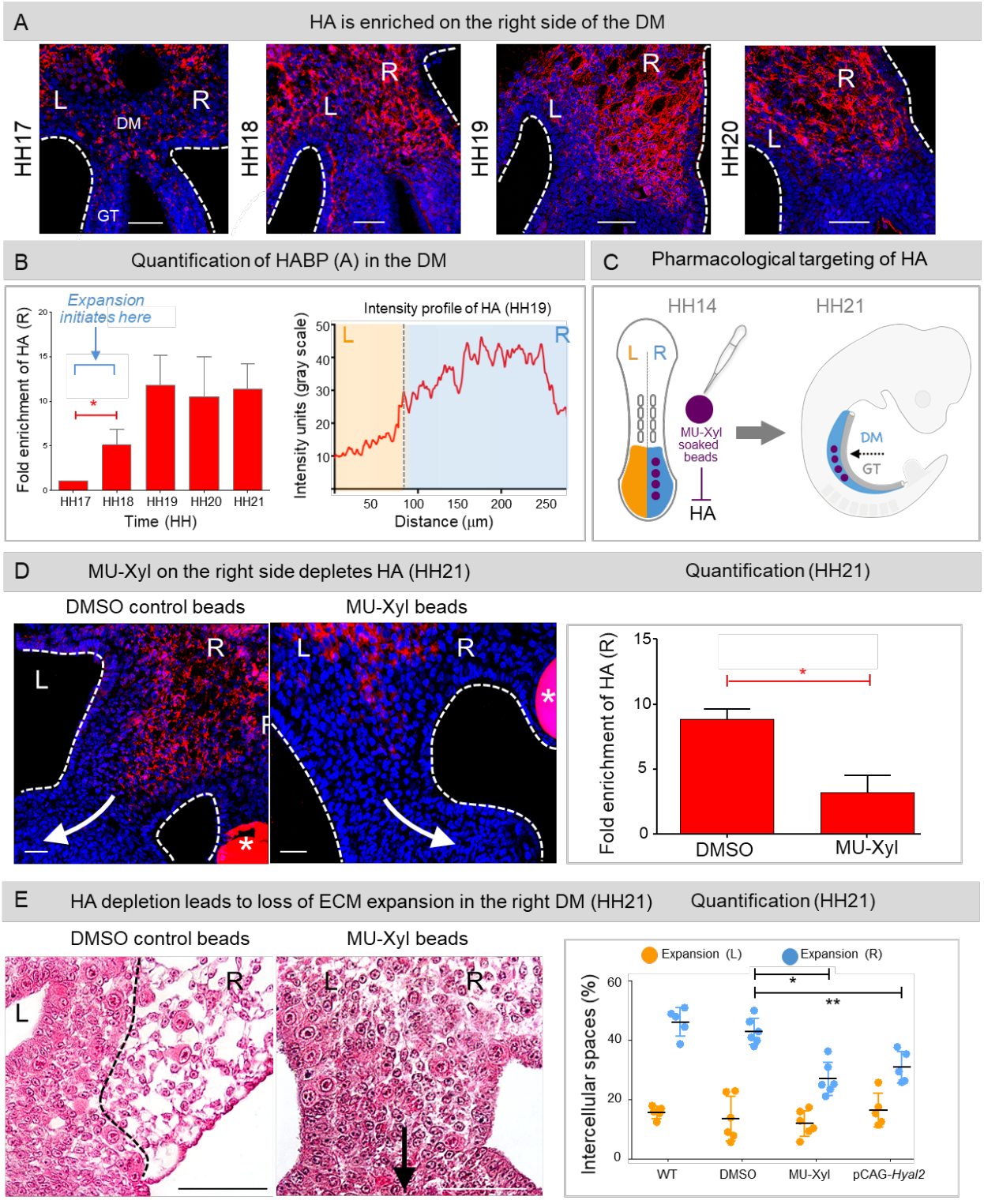
A
HA is enriched on the right side of the DM
HH17
HH18
HH19
HH20
L
R
DM
GT
B
Quantification of HABP (A) in the DM
Expansion initiates here
Fold enrichment of HA (R)
Time (HH)
Intensity profile of HA (HH19)
Intensity units (gray scale)
Distance (μm)
C
Pharmacological targeting of HA
HH14
HH21
MU-Xyl soaked beads
HA
D
MU-Xyl on the right side depletes HA (HH21)
Quantification (HH21)
DMSO control beads
MU-Xyl beads
DMSO
MU-Xyl
E
HA depletion leads to loss of ECM expansion in the right DM (HH21)
Quantification (HH21)
DMSO control beads
MU-Xyl beads
Expansion (L)
Expansion (R)
Intercellular spaces (%)
WT
DMSO
MU-Xyl
pCAG-Hyal2

the intensity profiles of the HA signal in the left and right DM using ImageJ and calculated the area under the curve to estimate the amount of HA present (Figures 2.2A and 2.2B).

At HH17, the DM had a basal level of HA accumulation with no detectable enrichment of HA in the left or right DM consistent with no observable DM expansion at this developmental stage (Figures 2.2A and 2.2B). HA accumulation was seen in the region surrounding the notochord as previously reported (Solursh and Morriss, 1977) and served as a positive control for HA staining (Figure S2). Strikingly at HH18, we observed HA-rich ECM in the dorsal right DM (Figure 2.2A) that spatially overlapped with the domain of initiation of DM expansion (Figures 2.1C and 2.1D). The ECM of the left DM had lower levels of HA that was uniformly distributed throughout the mesenchyme (Figures 2.2A and 2.2B). A comparison of the intensity profiles across the LR axis revealed that the right DM overall had more HA accumulation than the left side (Figure 2.2B). Remarkably, by HH19, the HA-rich ECM extended ventrally towards the gut tube to cover the entire right side of the DM, resulting in ~12-fold (11.76 ± 3.43) enrichment of HA levels in the right DM as compared to the left (Figures 2.2A and 2.2B). Thus, HA accumulation within the right DM spatiotemporally correlates with its expansion.

2.3.3 Hyaluronan is required for ECM expansion and the leftward gut tilting

To test the role of HA in the chicken DM, we surgically inserted resin beads soaked in 4-Methylumbelliferone-β-D-Xyloside (MU-Xyl), an inhibitor of endogenous HA synthesis (Hamati et al., 1989; Kakizaki et al., 2004), in the right coelomic cavity of the splanchnic mesoderm (DM precursor) prior to DM formation (HH15) (Figure 2.2C) (Mahadevan et al., 2014). Compared to vehicle (DMSO) controls, the MU-Xyl-treated embryos had significantly reduced levels of HA in the right DM (Figure 2.2D; DMSO beaded: ~9-fold enrichment (8.83 ± 0.78) vs. MU beaded: ~3-

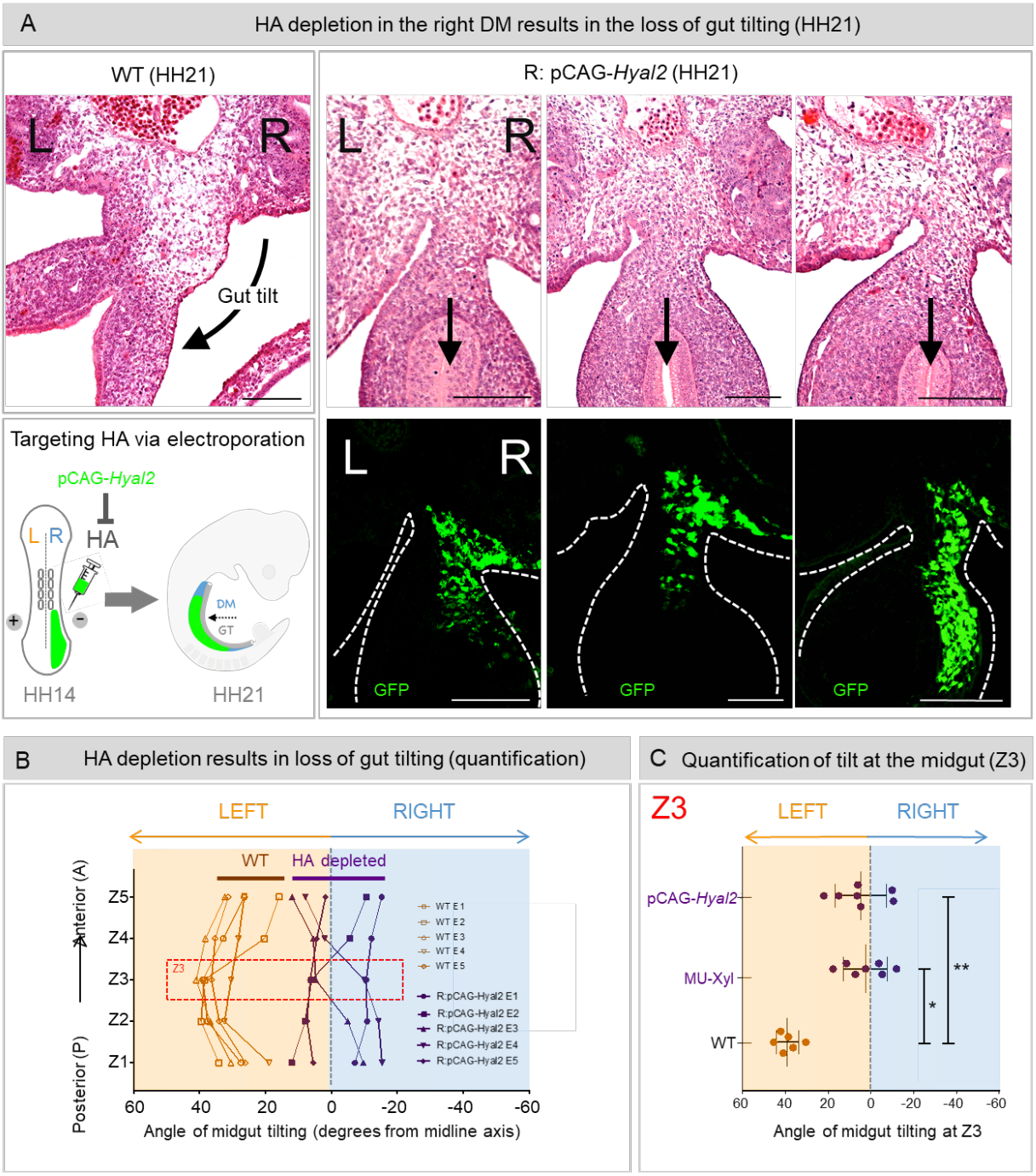

Figure 2.3: Genetic depletion of right-sided HA causes loss of gut tilting.
A Targeted degradation of HA in the right DM via electroporation of pCAG-*Hyal2* shows loss of expansion (top panel, H&E, R: pCAG-Hyal2) and gut tilting (quantified in **B** across the AP axis of the midgut). Bottom panel of **A** shows region of pCAG-*Hyal2* electroporation indicated by co-electroporation of GFP. **C** Depleting HA in the right DM via Hyal2 degradation or MU-Xyl inhibition of HA synthesis ablates gut tilting in the Z3 region of the midgut. MU-Xyl vs. WT, p = 0.00016; pCAG-Hyal2 vs. WT, p = 0.0025 (unpaired two-tailed T-test with Holm-Sidak correction for multiple comparisons). Error bars represent mean ± SEM for 7 chicken embryos per experimental condition. See also **Figure S4A**. **Scale bar: A** (100 µm).

fold enrichment (3.18 ± 1.36), n = 7, p = 0.0031), with a corresponding significant reduction of ECM expansion (Figure 2.2E; R: MU-Xyl vs. R: DMSO: n = 7 for each, p = 0.0053).

While MU-Xyl inhibits HA synthesis, it may also affect synthesis of other GAGs such as chondroitin sulfate, albeit to a much lesser extent (Hamati et al., 1989). To selectively deplete HA, we electroporated the right splanchnic mesoderm at HH14 with Hyaluronidase 2 (*Hyal2)*, encoding a highly specific enzyme that degrades extracellular HA (Albeiroti et al., 2015; Harada and Takahashi, 2007) (Figure 2.3A), marking targeted cells with co-electroporated GFP (Figure 2.3A, green). GFP-positive cells were found only on the electroporated right side at HH21, and electroporations with GFP alone had no effect on DM expansion (Figures 2.2E and 2.3A). However, similar to the MU-Xyl beading experiments, DM expansion was significantly reduced in *Hyal2* electroporated embryos (Figures 2.2E and 2.3A, n = 7, p = 0.0025). Thus, HA is required for ECM expansion of the right DM.

To determine the impact of HA on gut tilting, we quantified the tilting angles in the MU-Xyl-beaded and *Hyal2* electroporated embryos at HH21, as described above. Compared to control embryos, the leftward tilt of the midgut was lost in both the MU-Xyl-beaded and *Hyal2* electroporated embryos (Figures 2.3A-C, n = 7, MU-Xyl vs. WT: p = 0.00016, Hyal2 vs. WT: p = 0.0025). Moreover, the slight tilting that we observed in manipulated embryos was oriented randomly (L vs. R, Figure 2.3B). Collectively, these results establish that HA mediates ECM expansion of the right DM and plays a pivotal role in the initiation of gut tilting.

2.3.4 Loss of HA disrupts the normal process of vascular exclusion in the right DM

The gut vascular system derives from incompletely identified progenitors (Pardanaud et al., 1989) that form a bilaterally symmetric endothelial plexus residing in the left and right splanchnic mesoderm (Mahadevan et al., 2014; Thomason et al., 2012). We previously showed that at the onset of gut tilting, vascular endothelial cells within the right mesenchyme become progressively excluded, and at HH21, only the left-sided vascular endothelial cords remain (Figure 2.4A) (Mahadevan et al., 2014). We named these dorso-ventral (DV) cords, because they course dorsoventrally between the dorsal aorta and the gut vascular plexus (Figure 2.4A1, red arrow) (Mahadevan et al., 2014). Thus, blood vascular development within the DM is restricted to the left side via loss of vasculature on the right.

We also demonstrated that during subsequent gut development (beyond HH21), the left-sided DV cords remodel to form the highly stereotypical gut arterial branches within the left DM (Figure 2.4A2, red arrowhead) (Mahadevan et al., 2014). The first arterial branch to form, the primary longitudinal artery (1°LA, HH23, red arrowhead), becomes the ileocolic artery in the adult supplying the cecum, ileum, and appendix (human) (Mahadevan et al., 2014). Shortly after, a secondary longitudinal artery (2°LA, HH25) forms that extends cranially and is positioned halfway between the dorsal aorta and the gut tube (Figure 2.4D, green arrowhead). The 2°LA becomes the middle colic artery in the adult (Mahadevan et al., 2014).

Because the timing of HA accumulation and ECM expansion coincides spatiotemporally with the progressive vascular exclusion observed on the right, we hypothesized that HA-mediated mechanisms are responsible for the generation of avascular DM (Feinberg and Beebe, 1983). To test the relationship between HA and DM vasculature, we initially performed time series experiments to learn when vascular exclusion is first initiated. We used RNA in situ hybridization

Figure 2.4: Loss of HA from the right DM perturbs gut arterial vasculature.
A Model of gut arteriogenesis in WT embryos where endothelial cells of the right-sided DV cords at HH17 emigrate to establish the avascular right side. At HH21, only the left-sided arterial DV cords remain. Subsequent remodeling of left-sided cords form the 1°longitudinal artery (1°LA, red arrowhead) by HH23. 2°LA (green arrowhead) forms by HH26 as shown in **D**. **B** *VE-cadherin* RNA ISH shows ectopic maintenance of DV cords at HH21 due to loss of HA. **C** This aberrant maintenance of DV cords in the right DM disrupts remodeling of the DV cords to form the 1°LA. Instead, an abnormally large arterial vessel forms (green arrows) seen in the transverse vibratome section of the midgut (*Cx40* RNA ISH). **E** This ectopic mutant vessel (green arrows) forms in the anatomical position of the 2°LA at HH24, before the initiation of the WT 2°LA at HH25 in **F**. The 1°LA, in HA-depleted embryos (**E**, **F**, red arrow) is significantly shorter than in WT embryos, or is missing (RNA ISH for *Cx40*). **G** Quantification of the length and thickness of 1°LA and thickness of 2°LA in WT and HA-depleted embryos. Length of 1°LA is significantly shorter in HA-depleted embryos, $p = 0.0019$; 2°LA is thicker in HA-depleted embryos, $p = 0.0088$ (unpaired two-tailed Student's t-test). Error bars represent mean ± SEM for 7 chicken embryos per experimental condition. **H** Model summarizes defects in gut arteriogenesis due to loss of the right sided HA. CMV, cranial mesenteric artery; DA, dorsal aorta; DV cords, dorso-ventral cords. See also **Figures S3 and S4A**. **Scale bars: B, C** (100 μm); **E, F** (200 μm).

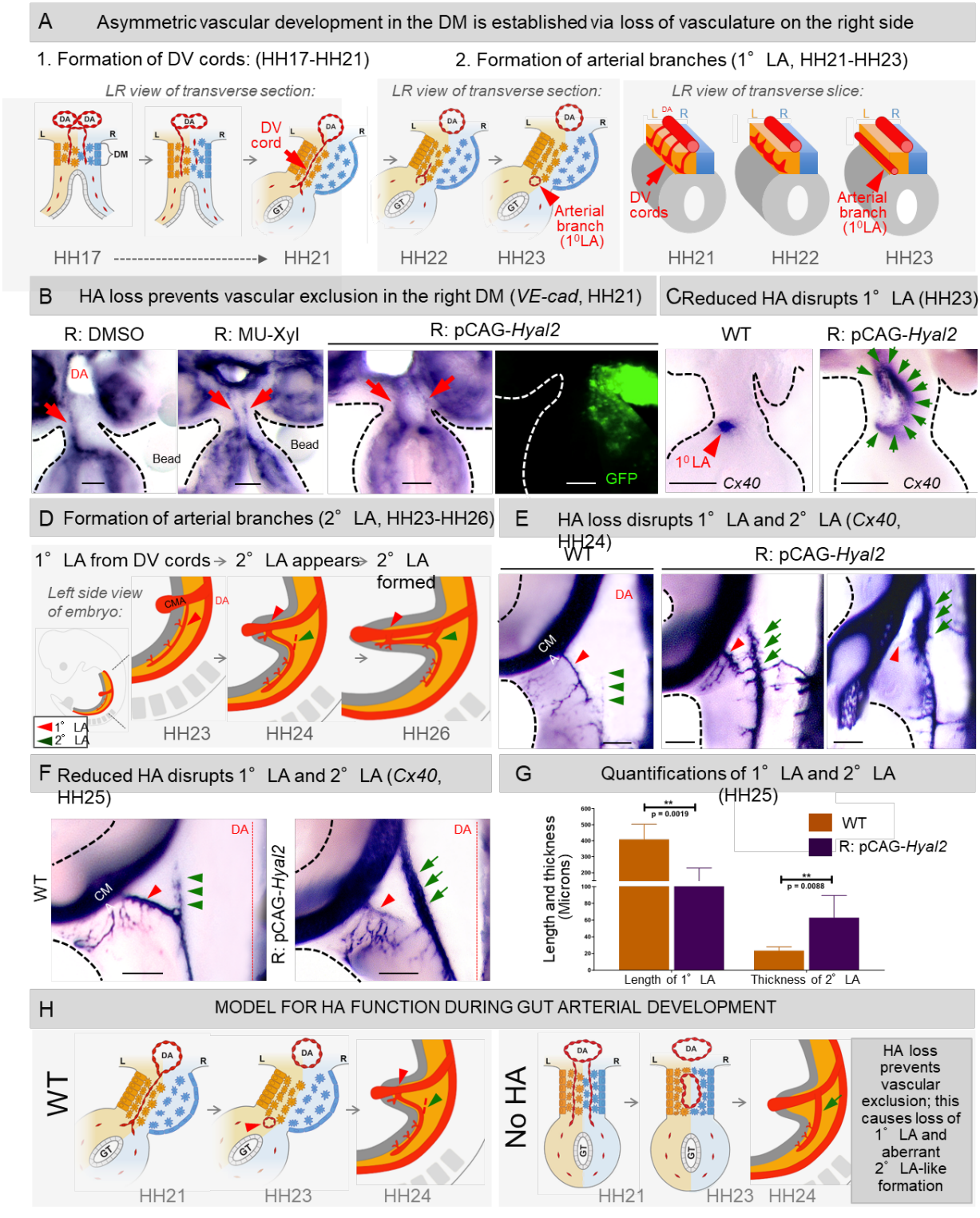
A Asymmetric vascular development in the DM is established via loss of vasculature on the right side
1. Formation of DV cords: (HH17-HH21)
2. Formation of arterial branches (1° LA, HH21-HH23)
LR view of transverse section:
LR view of transverse section:
LR view of transverse slice:
DA
DM
DV cord
GT
Arterial branch (1°LA)
DV cords
HH17
HH21
HH22
HH23
B HA loss prevents vascular exclusion in the right DM (VE-cad, HH21)
C Reduced HA disrupts 1° LA (HH23)
R: DMSO
R: MU-Xyl
R: pCAG-Hyal2
WT
Bead
GFP
1° LA
Cx40
D Formation of arterial branches (2° LA, HH23-HH26)
E HA loss disrupts 1° LA and 2° LA (Cx40, HH24)
1° LA from DV cords → 2° LA appears → 2° LA formed
Left side view of embryo:
CMA
CM
1° LA
2° LA
HH23
HH24
HH26
F Reduced HA disrupts 1° LA and 2° LA (Cx40, HH25)
G Quantifications of 1° LA and 2° LA (HH25)
R: pCAG-Hyal2
Length and thickness (Microns)
p = 0.0019
p = 0.0088
Length of 1° LA
Thickness of 2° LA
H MODEL FOR HA FUNCTION DURING GUT ARTERIAL DEVELOPMENT
WT
No HA
HH21
HH23
HH24
HA loss prevents vascular exclusion; this causes loss of 1° LA and aberrant 2° LA-like formation

(ISH) to *VE-cadherin*, a pan-vascular endothelial marker, on tissue sections isolated from WT chicken embryos between HH17-21 (Figure S3A). In addition, we performed immunohistochemistry on tissue sections isolated from transgenic Tie1:H2B-eYFP quail embryos (HH17-21) (Figure S3B).

At HH17, when the DM had a basal level of HA accumulation on both sides, we noted bilateral vascular plexuses traversing both the left and right sides of the DM and connecting with the dorsal aortae. Thus, at HH17, the DM exhibits both cellular and vascular symmetry (Figure S3). Remarkably, at HH18, while the vascular endothelial cords of the left DM remained continuous and fused with the dorsal aorta, we noted disrupted continuity of cords in the dorsal right region with loss of the endothelial cells (Figures S3A and S3B). This region aligns with the domain of initial ECM expansion and HA accumulation in the right DM (Figures 2.1C, 2.1D, 2.2A and 2.2B). By HH19-20, at peak expansion and HA accumulation (Figures 2.1C, 2.1D, 2.2A and 2.2B), we observed complete loss of vasculature from the right side (Figure S3). Thus, vascular exclusion within the right DM spatiotemporally correlates with DM expansion and HA accumulation.

To determine whether HA is required for vascular exclusion, we used *VE-cadherin* ISH in MU-Xyl-beaded or *Hyal2*-electroporated chicken embryos. In HH21 control embryos, DV cords were only present in the left, but not the right DM (Figure 2.4B, red arrow). However, DV cords were observed on both sides of the DM in HA-depleted embryos (HH21, a “double-left” phenotype, n = 10/15). While the “double-left” phenotype was previously observed only when Pitx2 was misexpressed in the right DM (Mahadevan et al., 2014; Welsh et al., 2013), the expression of *Pitx2* and a downstream target, Gpc3 remained restricted to the left DM in HA depleted embryos (Figure S4A). Thus, loss of HA on the right disrupts the normal process of

vascular exclusion without the loss of "*Pitx2*-negative" right side identity. Collectively, HA-rich ECM on the right side is anti-angiogenic and likely restricts vessel development to the left side. Furthermore, depletion of this HA-rich matrix causes loss of right-sided avascularity and aberrant maintenance of DV cords.

2.3.5 Reduced HA synthesis perturbs the formation of gut arterial branches

In wild type embryos, once formed at HH21, DV cords remodel ventrally to form the highly stereotypical 1°LA and 2°LA (Figure 2.4D, red and green arrowheads, respectively) (Mahadevan et al., 2014). We hypothesized that vascular exclusion on the DM right side must be necessary to allow for such stereotypical formation of gut arteries. To address this, we perturbed HA synthesis in the right DM as described above and asked whether the aberrant maintenance of DV cords on the right interferes with the subsequent formation of 1° and 2°LAs. We used RNA in situ hybridization (ISH) to *Connexin 40 (Cx40),* an arterial-specific vascular endothelial marker, on vibrotome-generated tissue slices of the DM and gut tube. At HH23, all WT embryos formed proper 1°LA located at the junction of the left DM and the gut tube (Figure 2.4C, red arrowhead). In contrast, we observed a single, abnormally large *Cx40*-positive arterial vessel positioned along the DM midline in embryos electroporated with *Hyal2* on the right (Figure 2.4C, green arrows, n = 5/10). We concluded that the loss of HA-driven avascularity on the DM right side interferes with proper patterning of the 1°LA.

To further characterize how the 1°LA is affected upon HA loss (*Hyal2* overexpression), we performed ISH to *Cx40* on whole embryos, and extended these analyses to two additional time points (HH24, 25) to learn whether 2°LA formation is also affected by *Hyal2*. First, in 3 of 8 embryos electroporated with *Hyal2* the 1°LA was absent, and was reduced in length in the remaining five embryos (Figures 2.4E and 2.4F, red arrowhead). Again, we observed an

abnormally large *Cx40*-positive arterial vessel positioned halfway between the dorsal aorta and the gut tube, anatomically resembling the 2°LA (Figures 2.4E-2.4G, green arrows, thickness of 1°LA WT embryos = 23.4 ± 4.54 μm, thickness of abnormal vessel resembling 2°LA R: pCAG-*Hyal2* embryos = 62.5 ± 26.58 μm, p = 0.0088). It is important to note that in WT embryos, 2°LA formation does not initiate until HH24-25 and is complete by HH26 (Mahadevan et al., 2014). In contrast, in embryos electroporated with *Hyal2*, the anomalous vessel resembling 2°LA was fully developed at HH23-24 (Figures 2.4C and 2.4E), a difference of ~12 hours. This indicates that HA-driven vascular exclusion may also control the precise timing of blood vessel development, and underscores the complexity of coordinating development of an asymmetric organ with that of its nascent vasculature (Figure 2.4H).

2.3.6 Tsg6 regulates HA-mediated expansion and vascular exclusion in the right DM

In wild type embryos, once formed at HH21, DV cords remodel ventrally to form the highly stereotypical 1°LA and 2°LA (Figure 2.4D, red and green arrowheads, respectively) (Mahadevan et al., 2014). We hypothesized that vascular exclusion on the DM right side must be necessary to allow for such stereotypical formation of gut arteries. To address this, we perturbed HA synthesis in the right DM as described above and asked whether the aberrant maintenance of DV cords on the right interferes with the subsequent formation of 1° and 2°LAs. We used RNA in situ hybridization (ISH) to *Connexin 40 (Cx40),* an arterial-specific vascular endothelial marker, on vibrotome-generated tissue slices of the DM and gut tube. At HH23, all WT embryos formed proper 1°LA located at the junction of the left DM and the gut tube (Figure 2.4C, red arrowhead). In contrast, we observed a single, abnormally large *Cx40*-positive arterial vessel positioned along the DM midline in embryos electroporated with *Hyal2* on the right (Figure 2.4C, green arrows, n

Figure 2.5: Tsg6 expression in the DM is right-sided and necessary for DM expansion and gut tilting.

A Cartoon shows Tsg6 modification of HA via transfer of heavy chain complexes from the inter-α-inhibitor. A catalytically inactive form of Tsg6 (S28A) fails to covalently modify HA. **B** Laser capture microarray data and RNA ISH for *Tsg6* in the chicken DM reveal right-sided expression at HH21. **C** Onset of *Tsg6* expression in the right DM at HH19 (bottom panel) coincides with vascular exclusion (top panel left: Tie1-H2B-YFP quail embryos; right: RNA ISH for *VE-cadherin*). **D** Knockdown of Tsg6 via electroporation of translation blocking morpholinos causes reduced right-sided DM expansion and subsequent loss of gut tilting. **E** Quantification of intercellular spaces in Tsg6-MO-knockdown embryos confirms reduced right DM expansion compared to scrambled MO control (left panel, $p = 0.0001$). Loss of gut tilting is also quantified in the graph on the right, $p = 0.0036$ (unpaired two-tailed Student's t-test). Error bars represent mean ± SEM for 5 chicken embryos per experimental condition. See also **Figures S3, S4B, S5 and S6B**. Scale bars: **B, C** (100 μm); **D** (50 μm). .

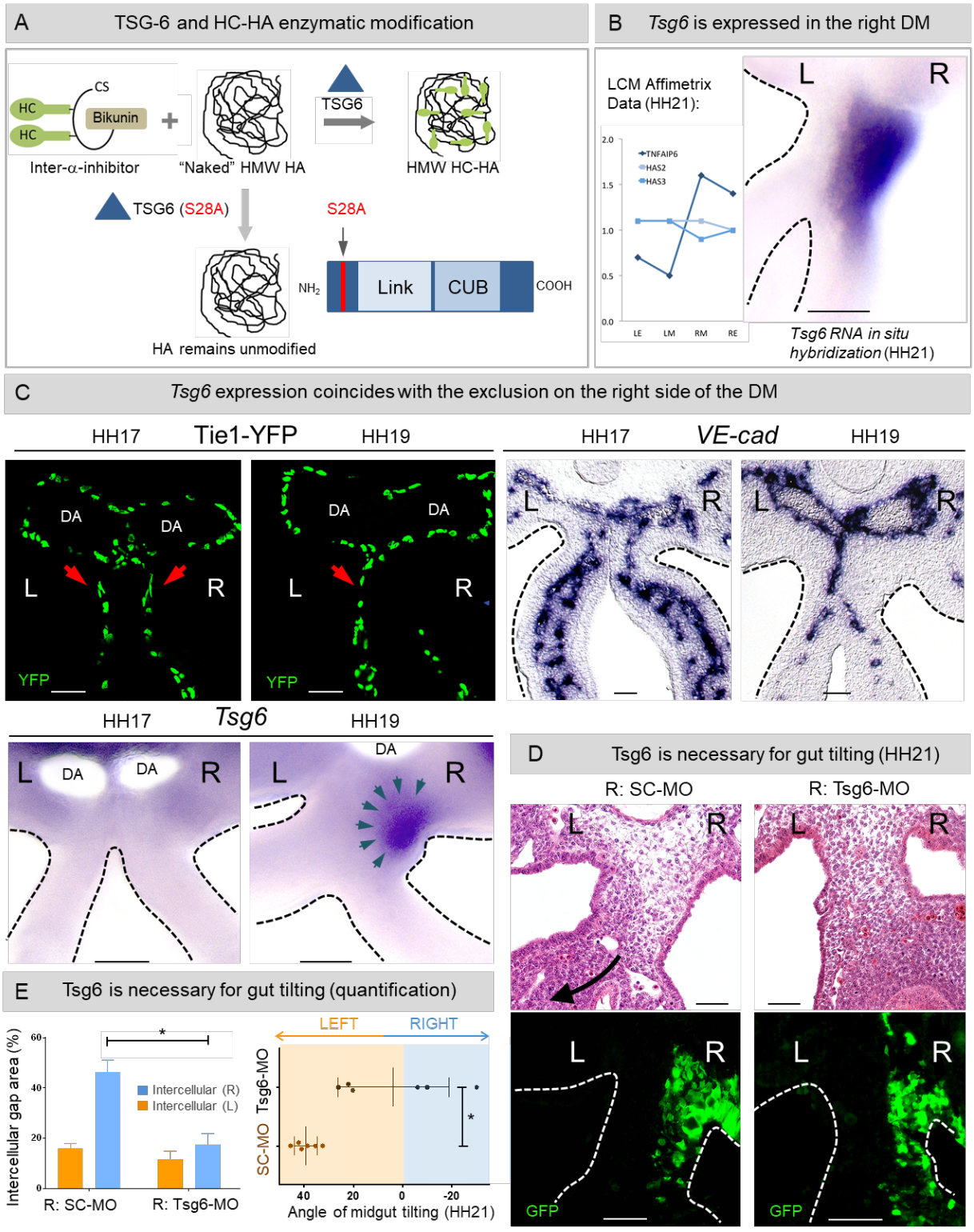
A
TSG-6 and HC-HA enzymatic modification
CS
HC
HC
Bikunin
Inter-α-inhibitor
"Naked" HMW HA
TSG6
HMW HC-HA
TSG6 (S28A)
S28A
NH2
Link
CUB
COOH
HA remains unmodified
B
Tsg6 is expressed in the right DM
LCM Affimetrix Data (HH21):
TNFAIP6
HAS2
HAS3
LE
LM
RM
RE
L
R
Tsg6 RNA in situ hybridization (HH21)
C
Tsg6 expression coincides with the exclusion on the right side of the DM
HH17
Tie1-YFP
HH19
DA
YFP
HH17
VE-cad
HH19
HH17
Tsg6
HH19
D
Tsg6 is necessary for gut tilting (HH21)
R: SC-MO
R: Tsg6-MO
GFP
E
Tsg6 is necessary for gut tilting (quantification)
Intercellular gap area (%)
Intercellular (R)
Intercellular (L)
R: SC-MO
R: Tsg6-MO
LEFT
RIGHT
SC-MO
Tsg6-MO
Angle of midgut tilting (HH21)

= 5/10). We concluded that the loss of HA-driven avascularity on the DM right side interferes with proper patterning of the 1°LA.

To further characterize how the 1°LA is affected upon HA loss (*Hyal2* overexpression), we performed ISH to *Cx40* on whole embryos, and extended these analyses to two additional time points (HH24, 25) to learn whether 2°LA formation is also affected by *Hyal2*. First, in 3 of 8 embryos electroporated with *Hyal2* the 1°LA was absent, and was reduced in length in the remaining five embryos (Figures 2.4E and 2.4F, red arrowhead). Again, we observed an abnormally large *Cx40*-positive arterial vessel positioned halfway between the dorsal aorta and the gut tube, anatomically resembling the 2°LA (Figures 2.4E-2.4G, green arrows, thickness of 1°LA WT embryos = 23.4 ± 4.54 μm, thickness of abnormal vessel resembling 2°LA R: pCAG-*Hyal2* embryos = 62.5 ± 26.58 μm, $p = 0.0088$). It is important to note that in WT embryos, 2°LA formation does not initiate until HH24-25 and is complete by HH26 (Mahadevan et al., 2014). In contrast, in embryos electroporated with *Hyal2*, the anomalous vessel resembling 2°LA was fully developed at HH23-24 (Figures 2.4C and 2.4E), a difference of ~12 hours. This indicates that HA-driven vascular exclusion may also control the precise timing of blood vessel development, and underscores the complexity of coordinating development of an asymmetric organ with that of its nascent vasculature (Figure 2.4H).

2.3.7 Tsg6 catalysis on HA is pivotal to ECM expansion and vascular exclusion

Tsg6 catalyzes the transfer of HC proteins from the inter-α-trypsin inhibitor (IαI) to HA to form the highly stable HC-HA matrices (Figure 2.5A) (Lauer et al., 2013b). To understand whether the anti-vascular effects of Tsg6 on the right side depend on its covalent modification of HA, we obtained catalytically inactive human Tsg6 (Tsg6-S28A, gift from J. Enghild), mutated at a residue

Figure 2.6: Covalent modification of HA by Tsg6 is necessary and sufficient for gut vascular development.

A Knockdown of *Tsg6* via electroporation of morpholinos, but not scrambled control morpholinos, prevents vascular exclusion in the right DM at HH21 (red arrow, right DM), leading to the formation of the thicker ectopic 2°LA-like vessel at HH25 (**B**, red arrow, right panel). RNA ISH for *Cx40*; GFP marks electroporated cells. **C** Ectopic left *Tsg6* expression is sufficient to inhibit vascular development in the DM (RNA ISH for *Cx40* and *VE-cadherin*). **D** Catalytically dead Tsg6 mutant (S28A) fails to inhibit arteriogenesis (red arrow) when introduced into the left DM (RNA ISH for *Cx40*). **E** Exogenous right-sided expression of catalytically dead Tsg6 mutant (S28A) serves as a dominant-negative Tsg6 and competes with endogenous WT Tsg6, preventing right-sided vascular exclusion (red arrow) at HH21 (RNA ISH for *Cx40*). See also **Figure S6A**. **Scale bars: A, C, D, E** (100 μm); **B** (200 μm).

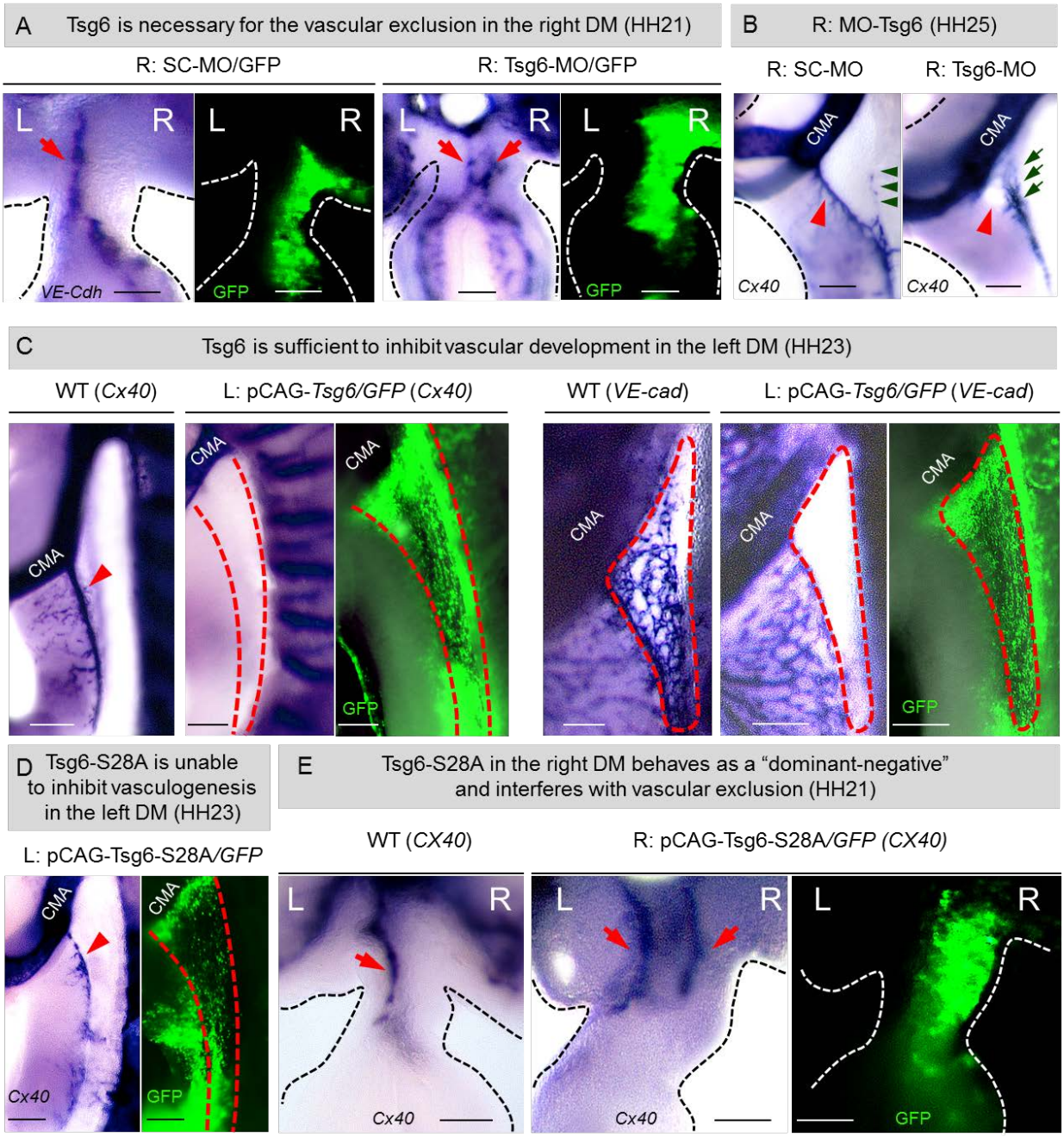
A Tsg6 is necessary for the vascular exclusion in the right DM (HH21)
R: SC-MO/GFP
R: Tsg6-MO/GFP
L
R
VE-Cdh
GFP
B R: MO-Tsg6 (HH25)
R: SC-MO
R: Tsg6-MO
CMA
Cx40
C Tsg6 is sufficient to inhibit vascular development in the left DM (HH23)
WT (Cx40)
L: pCAG-Tsg6/GFP (Cx40)
WT (VE-cad)
L: pCAG-Tsg6/GFP (VE-cad)
CMA
GFP
D Tsg6-S28A is unable to inhibit vasculogenesis in the left DM (HH23)
L: pCAG-Tsg6-S28A/GFP
E Tsg6-S28A in the right DM behaves as a "dominant-negative" and interferes with vascular exclusion (HH21)
WT (CX40)
R: pCAG-Tsg6-S28A/GFP (CX40)

required for transfer of HC from IαI to HA (Figure 2.5A) (Sanggaard et al., 2008). *In vitro*, this one residue change ablates HC transfer activity without affecting HA binding capacity (Sanggaard et al., 2008). First, we electroporated a full-length *Tsg6* WT construct (pCAG-Tsg6) on the left side of the (vascularized) DM to learn whether Tsg6 is sufficient to cause avascularity. We found that *Tsg6* on the left resulted in the loss of DV cords at HH21 (not shown) and loss of the 1°LA at HH23 (ISH to *Cx40*, Figure 2.6C, n = 11/19 embryos showing complete loss of 1°LA, 8/19 with partial loss of 1°LA). Tsg6-mediated loss of vasculature depended on the dosage of electroporated Tsg6 in the DM. For example, at low Tsg6 doses in the left DM, vascular development was only partially inhibited (Figure S6A). We confirmed this anti-angiogenic effect of Tsg6 on the left with ISH to *VE-cadherin* (Figure 2.6C).

To understand whether Tsg6 ablation of vessels on the left depends on its enzymatic activity, we repeated this experiment with the pCAG-Tsg6-S28A mutant. Strikingly, this had no effect on DM vasculature suggesting that the covalent modification of HA by Tsg6 is responsible for its anti-angiogenic function in the chicken DM (ISH to *Cx40*, Figure 2.6D). This result also argues that endogenous HA in the left DM, however weak in HA staining, may have a role, consistent with bilateral *Has2* expression in the DM (Figure 2.5B, graph). Interestingly, electroporating either the WT or mutant Tsg6 on the left was insufficient to overcome the left-sided condensation downstream of Pitx2 (Figure S6B), highlighting the optimal environment in the right DM for HA-mediated expansion that is suppressed on the left side by Pitx2. Thus, whereas Tsg6 is sufficient to cause vascular exclusion, it is not sufficient to induce ECM expansion on the left. These data also imply that the process of vascular exclusion driven by the HA/Tsg6 pathway may occur independent of ECM expansion.

Next, to prevent the formation of HC-HA on the right side of the DM, we electroporated the right side with the inactive pCAG-Tsg6-S28A construct to compete with the WT Tsg6 protein for HA binding (to act as a dominant-negative) (Sanggaard et al., 2008). H&E sections revealed a significant reduction of expansion in the right DM in embryos electroporated with pCAG-Tsg6-S28A (Figure S6C, n = 5, p = 0.0015). Moreover, ISH staining for *VE-cadherin* revealed double-left cords in pCAG-Tsg6-S28A embryos and normal left-sided DV cords in WT controls (Figure 2.6E, red arrows). Collectively, these experiments suggest that Tsg6 catalysis on HA is pivotal to ECM expansion and vascular exclusion.

2.3.8 HA negatively regulates Cxcl12 expression at the level of transcription

Our previous live imaging of *Tie1*:H2B-eYFP quail embryos revealed that vascular exclusion in the right DM is dependent on endothelial cell migration (Mahadevan et al., 2014). Of specific interest to this process is the chemokine Cxcl12, a ligand for the G protein-coupled receptor Cxcr4 (Mahadevan et al., 2014). We previously identified *Cxcl12* as a direct target gene of Pitx2 and showed that mesenchymal expression of *Cxcl12* is restricted to the left where it governs neighboring *Cxcr4*-positive arterial endothelial cell migration (Mahadevan et al., 2014). Mice lacking the Cxcr4/Cxcl12 axis display defective DM arteriogenesis and fail to form arterial DV cords (Mahadevan et al., 2014; Tachibana et al., 1998).

We previously showed that prior to the rise of DM asymmetries, when the intervening vascular endothelial plexus is initially bilateral (HH17), *Cxcl12* mRNA expression in the DM is also bilateral (Figure 2.7A, HH17) but becomes lost on the right side commensurate with HA accumulation and vascular exclusion of DV cords (Figure 2.7A, HH19) (Mahadevan et al., 2014). This observation led us to hypothesize that loss of *Cxcl12* expression on the right is driven by HA production. To test this, we investigated *Cxcl12* expression in HA-depleted chicken embryos (via

Figure 2.7: HA negatively regulates *Cxcl12* mRNA expression.
A Bilateral *Cxcl12* expression at HH17 in WT embryos becomes restricted to the left side concurrent with expansion and vascular exclusion at HH19. **B** Depletion of HA from the right via pCAG-*Hyal2* electroporation causes abnormal maintenance of *Cxcl12* mRNA in the right DM at HH19. **C** Model showing dynamics of *Cxcl12* expression in WT embryos where the left-restricted *Cxcl12* progressively acquires a dorso-ventral (DV) gradient at HH23 and becomes concentrated in the ventral DM, adjacent to the gut tube. Loss of HA aberrantly maintains *Cxcl12* in the right DM and perturbs the DV gradient of *Cxcl12* in the left DM. **D** Perturbing the DV gradient of *Cxcl12* by overexpressing pCAG-*Cxcl12* in the left DM leads to loss of positional information for 1°LA, which fails to traverse along the gut tube-DM border and instead forms along the anatomical position of the 2°LA (red arrowhead: WT, green arrows: L-pCAG-*Cxcl12*). RNA ISH for *Cx40*; GFP marks electroporated cells. Scale bars: **A, B** (100 μm); **D** (50 μm).

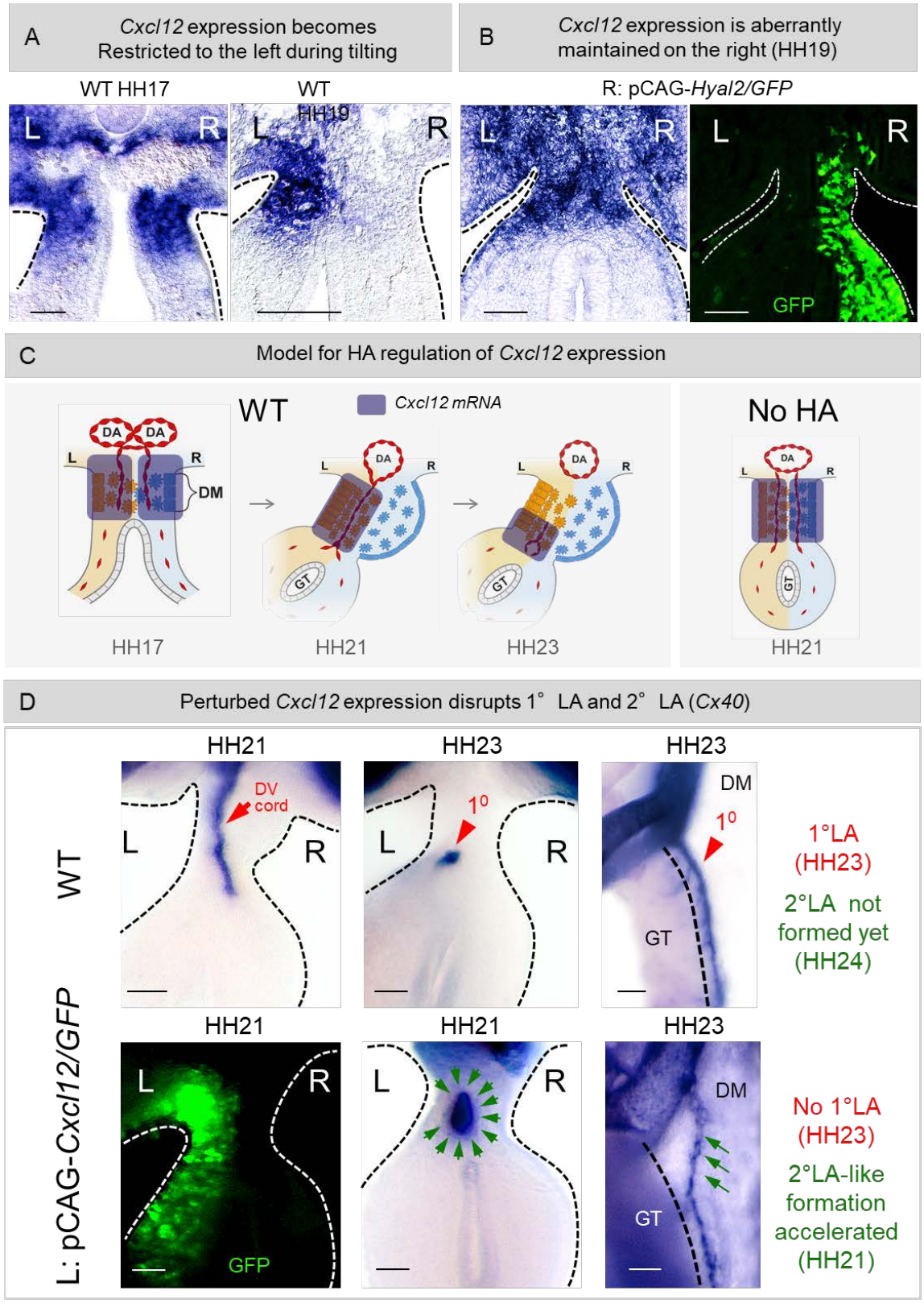
A
Cxcl12 expression becomes Restricted to the left during tilting
B
Cxcl12 expression is aberrantly maintained on the right (HH19)
WT HH17
WT HH19
R: pCAG-Hyal2/GFP
L
R
GFP
C
Model for HA regulation of Cxcl12 expression
WT
Cxcl12 mRNA
No HA
DA
DM
GT
HH17
HH21
HH23
HH21
D
Perturbed Cxcl12 expression disrupts 1° LA and 2° LA (Cx40)
HH21
HH23
HH23
WT
L: pCAG-Cxcl12/GFP
DV cord
1°
DM
GT
1°LA (HH23)
2°LA not formed yet (HH24)
HH21
HH21
HH23
No 1°LA (HH23)
2°LA-like formation accelerated (HH21)

pCAG-*Hyal2* electroporation). Strikingly, *Cxcl12* expression on the right was abnormally maintained suggesting that HA negatively regulates *Cxcl12* at the transcriptional level (Figure 2.7B). In WT embryos, accompanying the formation of the 1°LA from DV cords on the left, *Cxcl12* expression subsequently develops DV gradient asymmetry in the left DM, with its highest concentration ventrally where the 1°LA forms (Figure 2.7C, HH23) (Mahadevan et al., 2014). Thus, to understand whether perturbed gradient of *Cxcl2* expression could be the cause of the aberrant formation of the 2°LA and loss of the 1°LA that we observed in HA-depleted embryos, in a separate experiment, we overexpressed Cxcl12 in the left DM. Intriguingly, this resulted in the loss of the 1°LA and accelerated formation of the 2°LA-like vessel (Figure 2.7D, green arrows, n = 3/5), phenotypes similar to those obtained when HA or Tsg6 was depleted (Figures 2.4E, 2.4F and 2.6B). Thus, loss of the Cxcl12/Cxcr4 angiogenic signal may be one mechanism by which HA accumulation in the right DM mediates vascular exclusion and hence restricts vascular development to the left DM.

2.3.9 Tsg6-null mice display defects in gut looping chirality

Beyond fertility, the developmental role of Tsg6 is not known. To explore the role of Tsg6 in the mouse intestine, we characterized *Tsg6* +/+, Tsg6 +/- and Tsg6 -/- mouse embryos (Fülöp et al., 2003) at E18.5, when the final topology of the digestive tract is achieved (Kurpios et al., 2008; Savin et al., 2011). Unexpectedly, our preliminary genetic characterization of Tsg6-null mice suggested a significant departure from the expected Mendelian inheritance ratios, pointing to potentially lethal or sub-lethal phenotypes associated with loss of Tsg6 (not shown). As expected, in *Tsg6* +/+ and *Tsg6* +/- mouse embryos at E18.5, we observed stereotypical looping topology with jejunal and ileal loops tightly packed without entanglement (Figure 2.8A). Strikingly, in Tsg6 -/- embryos, a spectrum of perturbations to the gut looping topology was observed

Figure 2.8: *Tsg6*-/- mice display altered gut looping morphogenesis.
A Analysis of gut looping in E18.5 mouse embryos. In Tsg6 +/- and Tsg6 +/+ embryos, the distal jejunal loop is reproducibly aligned perpendicular to the ileal loop (red), located adjacent to the proximal jejunum. In Tsg6 -/- embryos, proximal distension of the jejuno-ileal loops is observed and the distal jejunal loop crosses over the ileum, indicating gut malrotation. **B** Analysis of gut looping in E13.5 mouse embryos shows defects in orientation of the jejunal and ileal loops in Tsg6 -/- embryos compared to Tsg6 +/- embryos. In Tsg6 +/- embryos, the jejunal loops exist in different planes compared to the ileal loop while in the mutants, the jejunal and ileal loops traverse in parallel. **C** In Tsg6 +/+ embryos, the apex of the midgut consisting of distal ileum and jejunum undergoes characteristic tilting pointing towards the cranial axis. This tilt is lost in Tsg6 -/- embryos. **D** Model for HA function in the gut: HA production and stabilization of HA matrix via Tsg6 expressed on the right side initiates counterclockwise gut rotation. The HA matrix negatively regulates *Cxcl12* in the right DM leading to vascular exclusion and left-side restricted arterial patterning. See also **Figure S7**. Scale bars: **A** (1000 μm); **B** (500 μm); **C** (200 μm).

A *Tsg6 -/-* mice display altered gut looping chirality (E18.5)

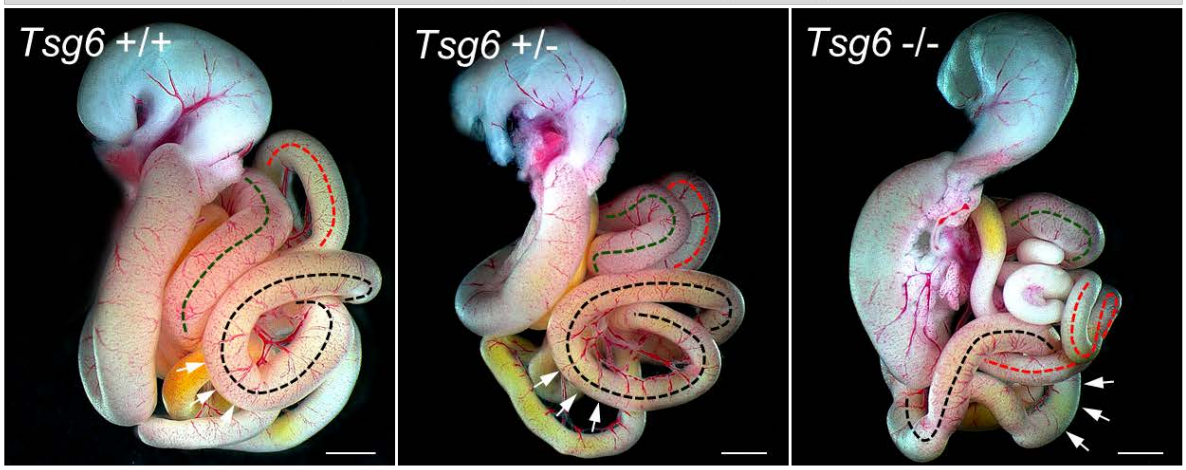

Green: proximal jejunum Black: distal jejunum Red: ileum

In *Tsg6 -/-* embryos the distal jejunal loop is crossing over the ileum

B *Tsg6 -/-* mice display altered gut looping chirality (E13.5)

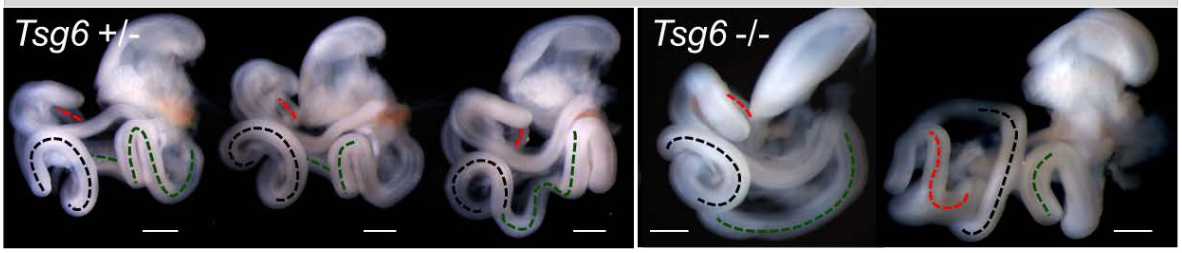

C *Tsg6 -/-* mice display altered gut looping chirality (E12.5)

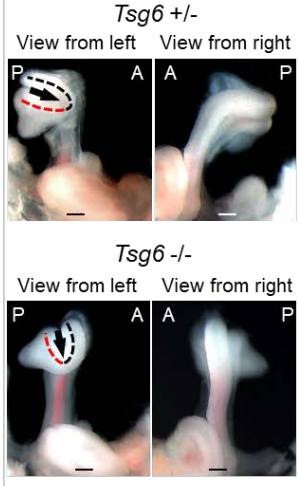

D Model for HA matrix function during LR gut and vascular development

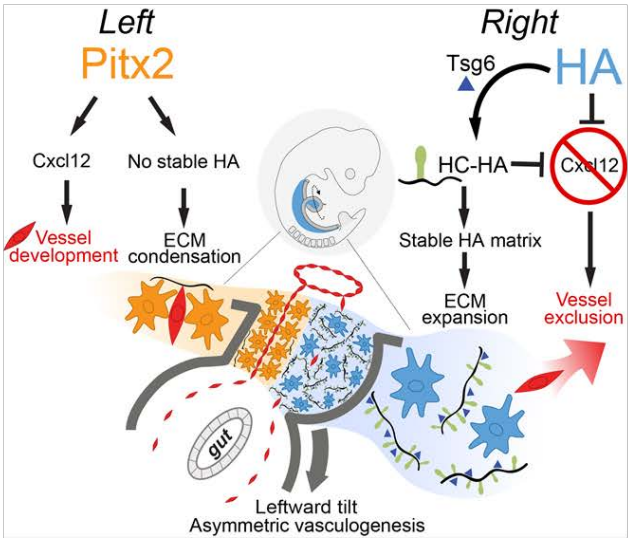

(Figure 2.8A, n = 4/5) with the ileum traversing a loop of distal jejunum, causing entanglement of the loops (Figure 2.8A, n = 2/4).

Whereas most intestinal malrotations do not lead to volvulus, some possess characteristics that strongly predispose to this deadly strangulation (Langer, 2017) (Pelayo and Lo, 2016). These include mispositioning of the duodenojejunal junction (DJJ) and the cecum, resulting in the distance between the DJJ and the ileocecal junction (ICJ) being less than half the width of the abdomen, leading to a narrow mesenteric stalk (Langer, 2017). Out of five Tsg6 -/- embryos obtained from multiple litters, four of the mutant embryos displayed mispositioning of the cecum, where the distance between the DJJ and the ICJ was less than half of the abdominal width, strongly indicating the occurrence of malrotation due to a narrow mesenteric stalk (Figure S7).

To understand the origins of the looping defect observed in the Tsg6 -/- embryos, we analyzed gut looping at two earlier time points, E12.5 and E13.5, during formation of the primary and secondary loops, respectively. At the onset of gut looping, the cranial tilt of the apex of the midgut loop was lost in Tsg6 -/- mutant embryos, suggestive of defective primary looping morphogenesis (Figure 2.8C, n = 4/4 mutants). At E13.5, three of five Tsg6 -/- embryos showed large deviations from the otherwise highly reproducible looping geometry commonly observed in age-matched Tsg6 +/- embryos (Figure 2.8B). This included altered positioning and orientation of the distal jejunal and ileal loops and mispositioning of the cecum, an important characteristic of intestinal malrotation (Langer, 2017; Pelayo and Lo, 2016).

2.4 Discussion

In the present study, we have shown that the leftward tilt of the vertebrate midgut results from the break in the midline symmetry initiated by the rapid expansion of the mesenchymal compartment

within the right side of the DM. Concomitantly, vascular development of the DM becomes restricted to the left side via exclusion of endothelial DV cords from the right. Our results reveal that the timely asymmetric accumulation of HA-rich matrix in the right DM and its covalent modification by Tsg6 orchestrates the mesenchymal expansion and vascular exclusion unique to the DM right side. Thus, initiation of the leftward tilt of the midgut and asymmetric assembly of gut arteries are driven by signals derived from the right, not left, DM (Figure 2.8D).

Following the right-sided initiation of cellular and vascular asymmetries, the downstream targets of Pitx2 mediate the condensation of the left mesenchymal compartment as the gut tube tilts further to the left. Simultaneously, the left-sided DV cords remodel to form the permanent gut arteries. Thus, while the right side-restricted cellular and vascular transformations of the DM serve to initiate asymmetric morphogenesis of the midgut, subsequent transformations on the left side likely serve to further the tilt and initiate subsequent remodeling of the vasculature to give rise to the stereotypical gut looping and vascular topology. Our studies uncover the first LR symmetry-breaking event regulated by the ECM that triggers evolutionarily conserved gut rotation and vasculogenesis.

2.4.1 ***HA-dependent mechanisms in vivo***

The association of increased HA accumulation in the ECM with tissue volume changes during embryonic development has been known for decades (Toole, 2001). Knockout of the embryonically active Has2 results in early embryonic lethality at E9.5 and is accompanied by a severe reduction of cell-free matrix defined spaces such as cardiac jelly, resulting in loss of cardiac cushions (Camenisch et al., 2000). Similarly, the role of HA in vessel development and disease has been long appreciated, but the mechanisms are challenging to study in vivo and are mostly unknown (Wang et al., 2011; Wang et al., 2015). This is primarily attributed to the structural variability of

HA that enables it to participate in a complex spectrum of interactions (Cowman and Matsuoka, 2005), existence of multiple HA receptors that bind to HA with different affinities within the same microenvironment (Jaime et al., 2015) and the heterogeneous distribution of HA polymers of different sizes in vivo, which regulates distinct signaling pathways that can sometimes result in opposing biological responses (Jaime et al., 2015; Pardue et al., 2008).

Currently, our understanding of how HA facilitates tissue expansion and vascular exclusion is aided by the use of ex vivo model systems such as the cumulus cell-oocyte complex and *in vitro* cell culture-based assays (Fülöp et al., 2003; Shay et al., 2011). The cumulus cell-oocyte complex is formed by the maturing oocyte surrounded by ~1500 cumulus cells. Upon hormonal stimulation, the complex undergoes a rapid, striking, nearly 20-fold HA-mediated expansion, that ejects the oocyte into the oviduct for subsequent fertilization (Salustri et al., 1989). HA or Tsg6 alone are insufficient in this process; formation of the HC-HA complex by Tsg6 initiates the expansion and maintains the integrity of the cumulus cell-oocyte complex (Fülöp et al., 2003; Mukhopadhyay et al., 2004).

Tsg6-modified HC-HA has further been shown to inhibit angiogenesis in culture (Deed et al., 1997) and in amniotic membrane (Tseng, 2016) and is 100-fold more potent than HA alone in suppressing endothelial cell proliferation in HUVEC cell culture (Shay et al., 2011).

While the use of these ex vivo and in vitro models have enabled us to gain very valuable insights into HA biology, the molecular and cellular mechanisms by which HA mediates biological and pathophysiological responses in vivo are complex, context-dependent and mostly unexplored due to the lack of a robust system to study HA in living animals. Most in vivo studies are often compromised by the three-dimensionality and inaccessibility of tissues and organs, or suffer complications of isolating specific regions from global and often lethal effects of transgenic

studies. For example, loss of *Has2* results in early (E9.5) embryonic lethality, making it challenging to study the role of HA in embryogenesis (Camenisch et al., 2000). In contrast, the chicken DM is a binary planar structure that has left (HA-negative) and right (HA-positive) sides that are juxtaposed yet distinct, with strict boundaries for transcription factors and cellular effectors that are highly conserved and readily amenable for separate molecular and functional in vivo analyses.

2.4.2 Significance of vascular asymmetry within the DM

In addition to the essential role of gaseous exchange, the intestinal vasculature has critical functional roles in absorption and transport of dietary nutrients. The DM serves as the major conduit for the blood vessels that supply the gut. We previously showed that DM vasculogenesis proceeds strictly on the left side because endothelial cells are progressively excluded from the right, coincident with gut rotation (Mahadevan et al., 2014). This temporally regulated LR vascular asymmetry is a key feature employed by the DM to pattern abdominal vasculature, and is driven by active migration of endothelial cells from the right DM (Mahadevan et al., 2014). Why the embryonic DM excludes angiogenesis on the right side has remained an open question. In the present study, we address the significance of vascular exclusion using several methods to compromise HA production and *Tsg6* expression in the chicken and mouse DM. Both HA depletion and loss of Tsg6 function caused vasculature on the right side to be aberrantly maintained at the time of the leftward tilt resulting in disrupted patterning of gut vasculature during subsequent gut looping morphogenesis. While this phenotype mirrors the “double-left” vascular lesion obtained when *Pitx2* is misexpressed on the right (Mahadevan et al., 2014), the loss of avascularity in *Pitx2*-misexpressed embryos is due to the loss of right side identity (double-left isomerism), whereas the aberrant maintenance of DV cords on the right in HA or Tsg6-depleted embryos

results from the change in the local microenvironment while retaining the Pitx2-negative identity of the right side. Indeed, none of the chemical perturbations disrupted the normal left-sided expression of *Pitx2* (Figure S4). Thus, our studies highlight the importance of the local ECM during organ-specific vascular patterning.

The appropriate patterning of vessels during development is achieved primarily via endothelial cell migration (Bentley and Chakravartula, 2017). Whereas this process involves spatial distribution of specific molecular cues (chemoattractant/repellant cues) within the local tissue microenvironment, time-dependent regulation of these cues is essential for establishing the architecture of the organ-specific vascular pattern (Bentley and Chakravartula, 2017; Kim et al., 2011; Potente et al., 2011; Zambrano et al., 2016). In the DM, the emigration of the vascular endothelial cells from the right side and the subsequent remodeling of the left-sided DV cords to pattern the DM arterial vasculature proceeds in a highly spatiotemporally regulated manner dependent on *Cxcl12* expression (Mahadevan et al., 2014). Our current study shows that depletion of HA alters *Cxcl12* expression resulting in abnormal retention of the right-sided DV cords and subsequent defects in arterial patterning. Importantly, these defects resemble vascular lesions obtained upon *Cxcl12* misexpression known to aberrantly accelerate DM arteriogenesis and perturb arterial patterning (Mahadevan et al., 2014) (Figure 2.7D). This suggests that the HA-rich ECM is a critical spatiotemporal modulator of arterial patterning within the gut DM. Indeed, depletion of HA or reduced expression of Tsg6 results in the loss of 1°LA and accelerated formation of the 2°LA-like vessel, highlighting how vascular process within the DM must carefully unfold over time and at the right place to generate pattern formation.

A similar role for *Cxcl12* has been described in other development systems. For example, in the mouse embryonic heart, perturbation to *Cxcl12* expression results in the absence or abnormal

positioning of coronary arterial stems (Ivins et al., 2015). In the zebrafish hindbrain, knockdown of Cxcl12 results in the formation of misdirected abnormal connections (Fujita et al., 2011). Similarly, inhibition of Cxcl12 in ex vivo retinal explants results in altered branching morphogenesis of the retinal vasculature (Unoki et al., 2010). Collectively, these data suggest that the regulation and timing of *Cxcl12* expression may be a global mechanism required for proper establishment of organ-specific vascular patterning.

2.4.3 Mechanisms downstream of HA

We previously identified *Cxcl12* as a direct target of Pitx2 and showed that mesenchymal expression of *Cxcl12* governs neighboring *Cxcr4*-positive arterial endothelial cell migration (Mahadevan et al., 2014). We now show that HA negatively regulates *Cxcl12* expression at the transcriptional level suggesting that loss of the Cxcl12/Cxcr4 angiogenic signal may be one mechanism by which HA mediates vascular exclusion.

How does HA regulate *Cxcl12* expression on the right side? There have been several factors reported to regulate *Cxcl12* expression including both canonical (Tamura et al., 2011) and noncanonical Wnt signaling (Tamura et al., 2011; Witze et al., 2008), hypoxia-inducible factor-1 and -2 (Ceradini et al., 2004; Martin et al., 2010), and VegfA (Hong et al., 2006). We previously showed that the tyrosine kinase receptors for VegfA, *VegfR1* (*Flk1/KDR*) and *Vegfr2*, are expressed on the arterial endothelium of DV cords in the left DM (HH21) (Mahadevan et al., 2014), whereas *VegfA* is expressed in the left DM mesenchyme where it mimics *Cxcl12* expression (unpublished). Moreover, studies involving the hindbrain and retinal vasculature have shown that *VegfA* expression exists in a positive feedback loop with expression of *Cxcl12* (Hong et al., 2006; Ping et al., 2011; van Weel et al., 2007; Zagzag et al., 2006) and targeted ectopic expression of *Cxcl12* in the right DM induces *VegfA* expression (unpublished data). Thus, HA on the right may

inhibit VEGF signaling either transcriptionally, or act as an extracellular sink to sequester VEGF away from its tyrosine kinase receptor.

In the heart, degradation of HMW HA into small HA oligosaccharides induces *VEGF* mRNA and protein expression in primary mouse endocardial cushions whereas HMW HA inhibits these activities (Rodgers et al., 2006). In zebrafish vasculature, small HA fragments are thought to induce VEGF signaling by liberating Vegf molecules from the ECM, with no effect on transcription (De Angelis et al., 2017). Given the critical role for VEGF in the formation of blood vessels (Ferrara, 2009) the relationship between HA, *Cxcl12* expression, and the VEGF pathway in the chicken and mouse DM warrants future investigation. Moreover, we have previously shown that patterning of DM arteries is critical for subsequent initiation of gut lymphatic development (Mahadevan et al., 2014). Thus, the HA mediated mechanisms that regulate the arterial patterning may also play a role in the proper establishment of the gut lymphatic network.

Of note, our studies suggest that HA is likely to employ distinct downstream signaling mechanisms to drive ECM expansion and vascular exclusion during gut looping because whereas *Tsg6* misexpression on the left was sufficient to inhibit vasculature, it failed to induce expansion on the left (Figure S6B). This may highlight that additional factors at play that are differentially expressed across the LR axis, including Pitx2 or other hyaladherins, may affect the biological function of HA, or that distinct properties of the HA molecule itself are produced on the right versus the left side of the DM.

2.4.4 Mechanisms upstream of HA

While the current study provides insights into how HA functions in the DM to generate cellular and vascular asymmetries, the mechanisms that result in the asymmetric accumulation of HA in the right DM remain unclear. Whereas the expression of *Has2* is the first determinant of active HA

synthesis, our results show that this enzyme is not differentially expressed in the DM, yet only the right side expands whereas the left side condenses. Consistent with bilateral *Has2* expression in the DM, some HA production can be seen on the left side of the DM. These observations suggest that *Has2* may not be responsible for the enriched levels of HA on the right and that HA synthesis alone may not account for the right-sided ECM expansion. Indeed, *Has2* expression may be the same bilaterally, but to achieve right-sided expansion subsequent synthesis of HA can be asymmetrically modulated by many additional factors, including Tsg6 mediation of Has2 activity (Lauer et al., 2013a) and HC-HA stabilization of matrix (Fülöp et al., 2003; Mukhopadhyay et al., 2004).

What regulates the LR asymmetric right-sided *Tsg6* expression in the DM? Leveraging data from our published laser capture microdissection of the left versus right halves of the DM (Welsh et al., 2015), we have identified *Atf3*, the anti-inflammatory cyclic AMP-dependent transcription factor 3, to be differentially expressed on the right side of the DM commensurate with *Tsg6* expression (unpublished). Similar to *Tsg6*, previous studies have implicated the function of *Atf3* in the ovarian cumulus HC-HA matrix (Inan et al., 2006). Importantly, we found a highly evolutionarily conserved region immediately upstream of *Tsg6* that is enriched for the binding sequence of *Atf3*, suggesting direct regulation (unpublished). Moreover, Pitx2 directly binds the promoter region of *Atf3* in mouse neonatal hearts where it suppresses *Atf3* transcription (Wang et al., 2014) and forced *Pitx2* expression in the right chicken DM inhibits *Atf3*, *Tsg6* and HA production (unpublished).

The T-box transcription factor *Tbx18* is one of the most highly differentially expressed genes on the right side of the chicken DM tilt (Davis et al., 2008). *Tbx18* expression pattern is specific to the midgut region and coincides spatiotemporally with the initiation of the leftward gut tilt (Davis et al.,

2008). In chickens and mice, *Tbx18* expression is negatively regulated by Pitx2 (Davis et al., 2008; Kurpios et al., 2008). These observations suggest that the cellular transformations unique to the DM right side may be downstream of *Tbx18*. Whether *Tbx18* or *Atf3* are responsible for the right-sided HA production and *Tsg6* expression stands unexplored and warrants further investigation. One possibility by which these transcription factors could contribute to the asymmetric production of HA on the right is via regulating signaling pathways that serve to differentially modulate Has2 function via distinct posttranslational modifications (Tammi et al., 2011). However, mechanisms independent of Has2 function in the DM are equally possible where Tsg6 in the DM may regulate HA stability by preventing HA catabolism (Lauer et al., 2013a). Future investigations are needed to elucidate these important mechanisms.

2.4.5 Role of Tsg6 during intestinal malrotation and volvulus

Gut malrotation is a complex congenital disorder of abnormal gut rotation that arises from failure to follow the stereotypical pattern of gut looping. Intestinal malrotation anomalies are relatively frequent in humans, occurring once in 500 live births (Torres and Ziegler, 1993). Serious consequences are observed when contorted twisting of the different segments of the gut tube around each other lead to a life-threatening lesion known as midgut volvulus characterized by gastrointestinal occlusion and strangulation of the associated mesenteric vasculature (Filston and Kirks, 1981; Torres and Ziegler, 1993). During embryonic development, the herniating midgut can be anatomically segmented into the cranial and caudal limbs by the cranial (superior) mesenteric artery (CMA) (Mahadevan et al., 2014; Noden and DeLahunta, 1985). The cranial limb of the midgut refers to the region of the midgut between the hepatic vein and the CMA while the caudal limb of the midgut extends from the apex of the midgut to the cecum (Soffers et al., 2015). The primary counterclockwise rotation (90 degrees), which begins at E10.75 in mouse embryos, serves

to bring the cranial and the caudal limbs of the midgut to the same plane (Onouchi et al., 2013; Ueda et al., 2016). During subsequent gut development, the formation of the four secondary loops initiates. The first secondary loop, also known as the duodenal flexure, extends rightward and caudally, and eventually extends leftward to establish the duodenal rotation (Onouchi et al., 2013; Soffers et al., 2015). The other secondary loops form in the regions of the midgut that give rise to the proximal and distal jejunum and the ileum (Soffers et al., 2015).

Mouse mutants which have defects in the formation of these secondary loops exhibit a disorganized looping topology, suggestive of malrotation which is characterized by severe perturbations to the relative positioning of the duodeno-jejunal junction and the cecum (Langer, 2017; Pelayo and Lo, 2016). The current mouse models that exhibit defects in gut looping chirality include *Pitx2*^{HD} (Lu et al., 1999), *Pitx2*$^{\Delta ASE/\Delta ASE}$ (Shiratori et al., 2006) and *Nodal*$^{neo/neo}$ (Saijoh et al., 2003). The Pitx2^{HD} mice (Pitx2-null) display loss of the duodenal rotation but die due to heart failure during early embryonic development prior to the formation of the tertiary loops (Lu et al., 1999; Soffers et al., 2015). The *Pitx2*$^{\Delta ASE/\Delta ASE}$ mutant embryos (lack the asymmetric *Pitx2*c isoform expression) and *Nodal*$^{neo/neo}$ (hypomorphic for *Nodal*) display aberrant duodenal rotation and an overall disorganized looping topology. However, a fraction of these embryos suffer from early embryonic lethality while others die immediately after birth (Saijoh et al., 2003; Shiratori et al., 2006). Hence, whether these malrotations predispose to volvulus during later development cannot be studied. In contrast, Tsg6 -/- mice are reported to survive to adulthood, albeit at non-Mendelian inheritance ratios (unpublished observation). Of note, our preliminary genetic characterization of the Tsg6-null mice confirms a significant departure from the expected Mendelian ratios, pointing to potentially lethal or sub-lethal phenotypes associated with loss of Tsg6. Whether this is a consequence of HA-dependent or -independent Tsg6 function is not known, but it is fascinating to

speculate that gut and/or vascular anomalies are the underlying cause of these phenotypes. Collectively, Tsg6 -/- mice may provide an important genetic model where the clinical consequences of early gut malrotation and volvulus can be followed throughout adult life.

Taken together, our studies unravel the first LR symmetry-breaking event in chickens and mice that triggers evolutionarily conserved gut rotation and vasculogenesis. We identify a novel ECM-derived pathway during LR organogenesis initiated by the HA matrix and its enzymatic modification dependent on Tsg6. Vasculogenesis - induction of new vessels and destruction of existing ones - is among the most important processes in human biology and vascular anomalies are the leading cause of gestational failure, but by their nature are very difficult to study. Similarly, the role of HA in vessel development and disease has been long appreciated, but the mechanisms are complex and mainly unexplored. Our work offers new insights into the mechanisms regulating HA function and addresses a critical area of vascular developmental biology and medicine, with potential relevance for developmental defects and inflammatory diseases.

2.5 Materials and Methods

2.5.1 Animals

Fertile chicken eggs (White Leghorn) or transgenic Tie1-H2b-YFP quail eggs (Ozark) were obtained from the Sunrise Farms and Cornell University Poultry Research Farm, incubated at 38^0C, and staged accordingly (Hamburger Hamilton 1951). Mouse embryos were obtained from Tsg6 mutant colony (Fülöp C, 2003) that were kindly provided by Dr. Hascall (BALB/cJ inbred background). WT BALB/cJ mice were purchased from Jackson Labs (Stock number 000651).

2.5.2 In ovo electroporation

Candidate genes were delivered to the developing DM using *in ovo* DNA electroporation as previously described (Welsh IC, 2013). Briefly, full-length genes or mutant constructs were delivered using the pCAG vector system (Matsuda T, 2004). A solution of plasmid DNA (encoding *Hyal2, Tsg6, S28ATsg6, Cxcl12*) was microinjected into the left or right coelomic cavity of HH14 chicken embryos (prior to the formation of the DM) and 3 pulses of 50V, 10mA were applied using a BTX electroporator. Eggs were then sealed and incubated until the desired stage. The pCAG vector was co-electroporated with pCAG-GFP for identification of target cells.

2.5.3 Morpholino design and electroporation

Tsg6 knockdown experiments were carried out by electroporation of targeted morpholinos (Gene Tools) targeting the right side of the DM. To target Tsg6, the following 5' UTR targeting FITC-labeled translation-blocking morpholino was designed: AGGGCAATCATCTCTTCCGAACTGT-3′. As an experimental control, FITC-conjugated standard scrambled RNA MO (Sc-MO) (Gene Tools) was used. The morpholinos were injected into the right coelomic cavity at HH14 and were electroporated at a concentration of 1.0 mM along with carrier DNA (pSlax) at a concentration of 1 μg/μl and 10 mM Tris (pH 8). The pulsing conditions were three 10 ms pulses 50 V spaced out by a 100 ms time interval.

2.5.4 In ovo bead implantation:

For inhibition of HA synthesis, vehicle (DMSO) or 40mM solution of 4 Methyl umbelliferone-B-D-Xyloside (Sigma, #M7008) was adsorbed onto AG resin beads (Bio-Rad, #143-1255) overnight (ON) at 4°C, washed and inserted into the coelom with fine forceps (Dumont 55).

2.5.5 Histology and Quantifications

WT embryos were dissected in cold 1X PBS and fixed ON using Bouin's fixative. The embryos were washed in 70% ethanol and embedded in paraffin. 6 μm tissue sections were collected on Superfrost Plus slides and were stained with H&E. Color development was moderated by controlling the exposure in 1% HCl /70% EtOH and ammonium hydroxide solution. Images of the sections taken using a 40X plan/achromat objective and the Zeiss Observer Z1 microscope. To quantify cell-free spaces within the DM (acellular compartment) sections were processed using ImageJ program for calculating the fraction of acellular compartment. To do this, random regions within the left and the right DM were selected and duplicated for processing (Figure S1A). The cell-free spaces were identified by negative thresholding using ImageJ Thresholding Tool with the dark background option, segmented into smaller parts using ImageJ Watershed Algorithm and the sum total of their areas were estimated using Image J Particle Analyzer (Figure S1A). The percent ratio of the cell-free area to the total area was identified as the parameter that quantifies extent of DM expansion in the left and right DM. Student t-test was used to test the significance of the differences. The ImageJ analysis was verified by counting nuclei of left and right DM in sections stained with DAPI (ImageJ Cell Counter Plugin).

2.5.6 HA staining and Immunohistochemistry

The distribution of HA was determined by incubating frozen or paraffin sections with biotinylated HA-binding protein (bHABP; 5μg/ ml; EMD Millipore, Cat No. 385911) in 3% Heat Inactivated Goat Serum in 1X PBS at 4°C O/N, followed by washing and incubation with AlexaFluor 568 conjugated streptavidin (Life Technologies #S11226) for 1 hour at room temperature (RT).

For GFP immunohistochemistry, embryos were dissected in cold 1X PBS, fixed ON in 4% PFA/PBS and were washed through a graded series of 30% sucrose/PBS solutions prior to freezing in a 1:1 mixture of 30% sucrose/OCT. Sections of 8-30 μm were collected, dried ON, and stored

at -80^{0}C. Rehydrated cryosections of DM were then subjected to blocking with 3% Heat Inactivated Goat Serum for 1 hour at RT. Sections were then incubated with rabbit polyclonal anti-GFP antibodies (Abcam, AB290, 1:1000) and with Alexa Fluor 488 (Life Technologies, #A11070) for 1 hour at RT. Sections were imaged using Zeiss Observer Z1 with Apotome and/or Leica SP5 confocal microscope.

Immunohistochemistry of E18.5 mouse mesenteric and gut vasculature was performed using whole mount tissue fixed in 4% PFA ON. The samples were subsequently given 3X PBS washes followed by incubation with blocking solution (1% BSA and 0.3% PBST) ON at 4^{0}C to prevent nonspecific antibody binding. Primary antibody to rat PECAM1 (CD31) (BD Biosciences, Cat No. 553370, 1:100) was diluted in blocking solution and incubated ON at 4^{0}C. Six washes with 0.3% PBST were performed prior to, and following an incubation with secondary antibodies (and then incubated with corresponding Alexa flour conjugated secondary antibodies (goat anti rabbit Alexa Fluor 488 #A11070 and donkey anti rat 594 #A21209, Life Technologies, 1:500) diluted in blocking solution ON at 4^{0}C. To image, the intestines attached to the mesentery were carefully cut into smaller pieces, and mounted on slides within a 0.5mm spacer (Invitrogen, S24735) and imaged using Zeiss 710 confocal microscopy.

2.5.7 RNA in situ hybridization, Cloning, Plasmids, and Oligonucleotides

For RNA in situ hybridization (ISH), 400 μm embryo slices were collected with a McIlwain tissue chopper (Campden Instruments), fixed in 4% PFA/PBS ON, dehydrated, and stored in 100% methanol prior to processing. ISH on embryo slices, whole embryos or frozen cryosections was performed by following standard protocols as previously described (Welsh IC, 2013). Probes for RNA ISH were cloned using TA cloning kit (Qiagen, #231124) or oligo-dT primed cDNA reverse transcription (Superscript III, Life Technologies, #4368814) using RNA pooled from HH19 and

21 whole chicken embryos. The following ESTs or cDNA clones were used to generate antisense riboprobes: chicken Tsg6 (NM_001037837.2 Fw: 5’ to 3’ GACTATGGGGATTCGCCTCA Rv: 5’ to 3’ CGTATGTCCCTGCCTGATCT); chicken Cx40 (NM_205504.1, Fw: 5’ to 3’ TGTCGGTGTGATCTGTCTCC Rv: 5’ to 3’ CGTCTGGGAGGTTACAGTGG); chicken VE-Cdh (NM_204227.1 Fw: 5’ to 3’ CAGATAGGTATCAAGAGCCTGCC Rv: 5’ to 3’ CTCCTGCCACGAAAGTACTGTG). Human *HYAL2* cDNA was amplified from pCMV6-*HYAL2* (sc117754 OriGene) using the following primers: Fw: 5’ to 3’ AAAACTCGAGATGCGGGCAGGCCCA and Rv: 5’ to 3’ AAAAGCGGCCGCCTACAAGGTCCAGGTAAAGGCCAG (restriction enzyme sites are underlined). It was then subcloned into pCAGEN plasmid (Matsuda T, 2004) using XhoI and NotI sites. Chicken *Tsg6* cDNA was synthesized and cloned into pCAGEN using the following primers: Fw: 5’ to 3’ AAAAGAATTCGGGAGTATTTACAGCCTAAC and Rv: 5’ to 3’ TTTTGCGGCCGCTATTCTGCTCACATAAT and cloned using EcoRI and NotI sites. The catalytically inactive Tsg6-S28A mutant construct (pcDNA5/FRT S28A mutant Tsg6) was a gift from Jan J Enghild lab (Department of Molecular Biology and Genetics, Aarhus University, Aarhus, Denmark). The insert was a full length human Tsg6 whose serine 28 was mutated to an alanine. The original construct was cloned between KpnI (5'-end) and Xho1 (3'-end) in the pCDNA5/FRT vector system and was subsequently subcloned into pCAGEN system via EcoRI digest followed by sticky end ligation. All DNA clones were verified by sequencing (Cornell University Life Sciences Core Laboratories Center).

2.6 Author Contributions

N.A.K. and A.S. designed the research with additional contributions from V.C.H., M.E.L, and A.M. A.S. performed all the experiments. A.M. contributed data in Figures 7D and S1B. S.R. contributed data in Figures 1C, 1E, 7A. R.J.N. contributed data in Figure 1C, 1E, S1B. N.A.K. and A.S. wrote the paper.

2.7 Acknowledgements

We thank Dr. Aaron Petrey, Dr. Drew Noden, and David Gludish for reading the manuscript and helpful suggestions. We thank Drs. Marcos Simoes-Costa for expertise and training with in ovo morpholinos, Jan J. Enghild for providing the S28A construct, and A. Bandyopadhyay for plasmids. We are grateful to Adam O'Neal, Melissa Werner, Athina Angel, Brittany Laslow, and Cindy Westmiller for technical assistance. This work was supported by March of Dimes 1-FY11-520 (N.A.K.) and NIH R01 DK092776 (N.A.K.).

2.8 References

Albeiroti S, A.K., Hill DR, Shen B, de la Motte CA. (2015). Platelet hyaluronidase-2: an enzyme that translocates to the surface upon activation to function in extracellular matrix degradation. Blood *125(9)*, 1460-1469.

Amack JD, W.X., Yost HJ. (2007). Two T-box genes play independent and cooperative roles to regulate morphogenesis of ciliated Kupffer's vesicle in zebrafish. Dev Biol *10*, 196-210.

Applegate KE (2009). Evidence-based diagnosis of malrotation and volvulus. Pediatric Radiology *39*, S161-163.

Camenisch TD, S.A., Brehm-Gibson T, Biesterfeldt J, Augustine ML, Calabro A, Kubalak S, Klewer SE, McDonald JA. (2000). Disruption of hyaluronan synthase-2 abrogates normal cardiac morphogenesis and hyaluronan-mediated transformation of epithelium to mesenchyme. Journal of Clinical Investigation *106*, 349-360.

Campione M, S.H., Schweickert A, Deissler K, van Bebber F, Lowe LA, Nowotschin S, Viebahn C, Haffter P, Kuehn MR, Blum M. (1999). The homeobox gene Pitx2: mediator of asymmetric left-right signaling in vertebrate heart and gut looping. Development *126*, 1225-1234.

Ceradini DJ, K.A., Callaghan MJ, Tepper OM, Bastidas N, Kleinman ME, Capla JM, Galiano RD, Levine JP, Gurtner GC. (2004). Progenitor cell trafficking is regulated by hypoxic gradients through HIF-1 induction of SDF-1. Nat Med *10*, 858-864.

Chapin HC, C.M. (2010). The cell biology of polycystic kidney disease. J Cell Biol *191*, 701-710.

Cowman MK, M.S. (2005). Experimental approaches to hyaluronan structure. Carbohydrate Research *340*, 791-809.

Davis NM, K.N., Sun X,Gros J, Martin JF,Tabin CJ (2008). The Chirality of Gut Rotation Derives from Left-Right Asymmetric Changes in the Architecture of the Dorsal Mesentery. Developmental Cell *15*, 134-145.

De Angelis, J.E., Lagendijk, A.K., Chen, H., Tromp, A., Bower, N.I., Tunny, K.A., Brooks, A.J., Bakkers, J., Francois, M., Yap, A.S., *et al.* (2017). Tmem2 Regulates Embryonic Vegf Signaling by Controlling Hyaluronic Acid Turnover. Developmental cell *40*, 123-136.

de la Motte CA, D.J. (2011). Viewing Hyaluronan: Imaging Contributes to Imagining New Roles for This Amazing Matrix Polymer. Journal of Histochemistry and Cytochemistry *59*, 252-257.

Ferrara, N. (2009). VEGF-A: a critical regulator of blood vessel growth. Eur Cytokine Netw *20*, 158-163.

Fuchs, K., Hippe, A., Schmaus, A., Homey, B., Sleeman, J.P., and Orian-Rousseau, V. (2013). Opposing effects of high- and low-molecular weight hyaluronan on CXCL12-induced CXCR4 signaling depend on CD44. Cell Death Dis *4*, e819.

Fülöp C, S.A., Hascall VC (1997). Coding sequence of a hyaluronan synthase homologue expressed during expansion of the mouse cumulus-oocyte complex. Archives of Biochemistry and Biophysics *337*, 261-266.

Fülöp C, S.S., Mukhopadhyay D, Bárdos T, Kamath RV, Rugg MS, Day AJ, Salustri A, Hascall VC, Glant TT, Mikecz K (2003). Impaired cumulus mucification and female sterility in tumor necrosis factor-induced protein-6 deficient mice. Development *130*, 2253-2261.

Gage PJ, S.H., Camper SA. (1999). Dosage requirement of Pitx2 for development of multiple organs. Development *126*, 4643-4651.

Hamati HF, B.E., Carey DJ (1989). Inhibition of proteoglycan synthesis alters extracellular matrix deposition,proliferation, and cytoskeletal organization of rat aortic smooth muscle cells in culture. J Cell Biol *108(6)*, 2495-2505.

Hamburger V, H.H. (1992). A series of normal stages in the development of the chick embryo. 1951. Developmental Dynamics *195*, 231-272.

Harada H, T.M. (2007). CD44-dependent Intracellular and Extracellular Catabolism of Hyaluronic Acid by Hyaluronidase-1 and -2. Journal of Biological Chemistry *282*, 5597-5607.

Hascall V, E.J. (2009). Hyaluronan. . In In Essentials of Glycobiology, C.R.D. Varki A., Esko J.D., Freeze H.H., Stanley P., Bertozzi C.R., Hart G.W., Etzler M.E, ed. (Cold Spring Harbor, NY: Cold Spring Harbor Laboratory Press), pp. 219-228.

Hong X, J.F., Kalkanis SN, Zhang ZG, Zhang XP, DeCarvalho AC, Katakowski M, Bobbitt K, Mikkelsen T, Chopp M. (2006). SDF-1 and CXCR4 are up-regulated by VEGF and contribute to glioma cell invasion. Cancer Letters *236*, 39-45.

Ikuko Kakizaki, K.K., Keiichi Takagaki, Masahiko Endo, Reiji Kannagi, Masaki Ito, Yoshihiro Maruo, Hiroshi Sato, Tadashi Yasuda, Satoka Mita, Koji Kimata and Naoki Itano (2004). A Novel Mechanism for the Inhibition of Hyaluronan Biosynthesis by 4-Methylumbelliferone. The Journal of Biological Chemistry *279*, 33281-33289.

Inan, M.S., Al-Hassan, S., Ozand, P., and Coskun, S. (2006). Transcriptional profiling of granulosa cells from a patient with recurrent empty follicle syndrome. Reproductive biomedicine online *13*, 481-491.

Jaime MC, C.S., and Stavros Garantziotis (2015). Size Matters: Molecular Weight Specificity of Hyaluronan Effects in Cell Biology. Int J Cell Biol *563818*.

Kothapalli, D., Zhao, L., Hawthorne, E.A., Cheng, Y., Lee, E., Pure, E., and Assoian, R.K. (2007). Hyaluronan and CD44 antagonize mitogen-dependent cyclin D1 expression in mesenchymal cells. The Journal of cell biology *176*, 535-544.

Kurpios NA, I.M., Davis NM, Lui W, Katz T, Martin JF, Izpisúa Belmonte JC, Tabin CJ. (2008). The direction of gut looping is established by changes in the extracellular matrix and in cell:cell adhesion. PNAS *105*, 8499-8506.

Langer JC (2017). intestinal Rotation Abnormalities and Midgut Volvulus. Surgical clinics of North America *97*, 147-159.

Lauer ME, G.T., Mikecz K, DeAngelis PL, Haller FM, Husni ME, Hascall VC, Calabro A (2013). Irreversible Heavy Chain Transfer to Hyaluronan Oligosaccharides by Tumor Necrosis Factor-stimulated Gene-6. J Biol Chem *288*, 205-214.

Levin M, J.R., Stern CD, Kuehn M, Tabin C. (1995). A molecular pathway determining left-right asymmetry in chick embryogenesis. Cell *82*, 803-814.

Liu C, L.W., Lu MF, Brown NA, Martin JF. (2001). Regulation of left-right asymmetry by thresholds of Pitx2c activity. Development *128*, 2039-2048.

Lu MF, P.C., Dyer R, Johnson RL, Martin JF. (1999). Function of Rieger syndrome gene in left-right asymmetry and craniofacial development. Nature *401*, 276-278.

Mahadevan A, Welsh IC, Sivakumar A, Gludish DW, Shilvock AR, Noden DM, Huss D, Lansford R, Kurpios NA. (2014). The left-right Pitx2 pathway drives organ-specific arterial and lymphatic development in the intestine. Developmental Cell *31*, 690-706.

Martin SK, D.P., Williams SA, To LB, Peet DJ, Fujii N, Gronthos S, Harris AL, Zannettino AC. (2010). Hypoxia-inducible factor-2 is a novel regulator of aberrant CXCL12 expression in multiple myeloma plasma cells. Haematologica *95*, 776-784.

Matsuda T, C.C. (2004). Electroporation and RNA interference in the rodent retina in vivo and in vitro. Prot Natl Acad Sci U S A *101*, 16-22.

McDowell G, R.S., Levin M (2016). From cytoskeletal dynamics to organ asymmetry: a nonlinear, regulative pathway underlies left-right patterning. Philos Trans R Soc Londo B Bio Sci *371*.

Milner CM, D.A. (2003). TSG-6: a multifunctional protein associated with inflammation. J Cell Sci *116*, 1863-1873.

Pardanaud L, Y.F., Dieterlen-Lievre F (1989). Relationship between vasculogenesis, angiogenesis and haemopoiesis during avian ontogeny. Development *105*, 473-485.

Pardue EL, I.S., Ramamurthi A (2008). Role of hyaluronan in angiogenesis and its utility to angiogenic tissue engineering. Organogenesis *4*, 203-214.

Pelayo JC, L.A. (2016). Intestinal Rotation Anomalies. Pediatr Ann *45*, e247-250.

Piedra ME, I.J., Albajar M, Rodriguez-Rey CJ, Ros MA. (1998). Pitx2 Participates in the Late Phase of the Pathway Controlling Left-Right Asymmetry. Cell *94*, 319-324.

Rodgers, L.S., Lalani, S., Hardy, K.M., Xiang, X., Broka, D., Antin, P.B., and Camenisch, T.D. (2006). Depolymerized hyaluronan induces vascular endothelial growth factor, a negative regulator of developmental epithelial-to-mesenchymal transformation. Circ Res *99*, 583-589.

Saijoh Y, O.S., Ohishi S, Hamada H. (2003). Left-right patterning of the mouse lateral plate requires nodal produced in the node. Dev Biol *256*, 160-172.

Sanggaard KW, S.-S.C., Krogager TP, Kristensen T, Wisniewski HG, Thøgersen IB, Enghild JJ (2008). TSG-6 Transfers Proteins between Glycosaminoglycans via a Ser28-mediated Covalent Catalytic Mechanism. Journal of Biological Chemistry *283*, 33919-33926.

Savin T, K.N., Shyer AE, Florescu P, Liang H, Mahadevan L, Tabin CJ. (2011). On growth and form of the gut. Nature *476*, 57-62.

Schumann, M., Gunzel, D., Buergel, N., Richter, J.F., Troeger, H., May, C., Fromm, A., Sorgenfrei, D., Daum, S., Bojarski, C., *et al.* (2012). Cell polarity-determining proteins Par-3 and PP-1 are involved in epithelial tight junction defects in coeliac disease. Gut *61*, 220-228.

Shay E, H.H., Sakurai S, Tseng SC (2011). Inhibition of angiogenesis by HCÃ‚Â·HA, a complex of hyaluronan and the heavy chain of inter alpha inhibitor, purified from human amniotic membrane. IOVS *52*, 2669-2678.

Shen L, Z.L., Okumura A, Ishikawa T, Miyachi M, Owa Y, Ishizawa T, Sugiura N, Nagata Y, Nonami T, Kakumu S, Kimata K (2006). The SHAP-hyaluronan complex in serum from patients with chronic liver diseases caused by hepatitis virus infection. Hepatol Res *34*, 178-186.

Shiratori H, Y.K., Shen MM, Hamada H. (2006). Conserved regulation and role of Pitx2 in situs-specific morphogenesis of visceral organs. Development *133*, 3015-3025.

Simoes-Costa, M., and Bronner, M.E. (2016). Reprogramming of avian neural crest axial identity and cell fate. Science *352*, 1570-1573.

Slevin, M., Krupinski, J., Gaffney, J., Matou, S., West, D., Delisser, H., Savani, R.C., and Kumar, S. (2007). Hyaluronan-mediated angiogenesis in vascular disease: uncovering RHAMM and CD44 receptor signaling pathways. Matrix Biol *26*, 58-68.

Soffers JH, H.J., Mekonen HK, Koehler SE, Lamers WH. (2015). The growth pattern of the human intestine and its mesentery. BMC Dev Biol *15*.

Solursh M, M.G. (1977). Glycosaminoglycan synthesis in rat embryos during the formation of the primary mesenchyme and neural folds. Developmental Biology *57*, 75-86.

Tachibana K, H.S., Iizasa H, Yoshida H, Kawabata K, Kataoka Y, Kitamura Y, Matsushima K, Yoshida N, Nishikawa S, Kishimoto T, Nagasawa T (1998). The chemokine receptor CXCR4 is essential for vascularization of the gastrointestinal tract. Nature *393*, 591-594.

Tamura M, S.M., Nashimoto M. (2011). Regulation of CXCL12 expression by canonical Wnt signaling in bone marrow stromal cells. Int J Biochem Cell Biol *43*, 760-767.

Thomason RT, B.D., Winters NI (2012). Comprehensive timeline of mesodermal development in the quail small intestine. Developmental Dynamics *241*, 1678-1694.

Toole BP (2001). Hyaluronan in morphogenesis. Seminars in Cell & Developmental Biology *12*, 79-87.

Wang A, d.l.M.C., Lauer M, Hascall V (2011). Hyaluronan matrices in pathobiological processes. FEBS J *278*, 1412-1418.

Wang, A., Sankaranarayanan, N.V., Yanagishita, M., Templeton, D.M., Desai, U.R., Sugahara, K., Wang, C.P., and Hascall, V.C. (2015). Heparin interaction with a receptor on hyperglycemic dividing cells prevents intracellular hyaluronan synthesis and autophagy responses in models of type 1 diabetes. Matrix Biol *48*, 36-41.

Wang, J., Bai, Y., Li, N., Ye, W., Zhang, M., Greene, S.B., Tao, Y., Chen, Y., Wehrens, X.H., and Martin, J.F. (2014). Pitx2-microRNA pathway that delimits sinoatrial node development and inhibits predisposition to atrial fibrillation. Proceedings of the National Academy of Sciences of the United States of America.

Welsh IC, T.M., Gludish DW, Alfonso-Parra C, Bai Y, Martin JF, Kurpios NA (2013). Integration of L-R Pitx2 transcription and Wnt signaling drives asymmetric gut morphogenesis via Daam2. Developmental Cell *26*, 629-644.

Witze ES, L.E., Argast GM, Moon RT, Ahn NG. (2008). Wnt5a control of cell polarity and directional movement by polarized redistribution of adhesion receptors. Science *320*, 365-369.

Zhuo, L., Kanamori, A., Kannagi, R., Itano, N., Wu, J., Hamaguchi, M., Ishiguro, N., and Kimata, K. (2006). SHAP potentiates the CD44-mediated leukocyte adhesion to the hyaluronan substratum. The Journal of biological chemistry *281*, 20303-20314.

2.8 Supplemental figures

These supplemental figures with their legends accompany Chapter 2.

Fig. S1: Schematic for quantification of intercellular (cell-free) spaces within the LR DM from HH17-21 using ImageJ (related to Fig.2 1).

A (Left panel) Cartoon model of a transverse section of HH21 midgut-DM showing condensed left (orange) and expanded right (blue) mesenchyme. (Middle panel) H&E of HH19 midgut section. Orange and blue boxes indicate regions selected for analysis of cell-free spaces. (Right panel) The selected regions were copied to a new window in ImageJ (step 1) and cell-free spaces were identified using the ImageJ Thresholding Tool with a dark background option (step 2). These were then segmented into smaller parts using the Watershed Algorithm Tool and the sum total of their areas were estimated with the Particle Analyzer Tool. **B** Cartoon of the right lateral view of an embryo with the midgut region defined. The midgut has been segregated into five zones, Z1-Z5, where Z1 has been defined as the caudal midgut, Z2-Z3 the mid-caudal midgut, and Z4-Z5 as the central midgut. Examples of H&E images of the caudal, mid-caudal, and central midgut regions are shown in the right panel. Graphs demonstrate significant variation in expansion of the right DM across the different defined midgut regions at HH18-21 where the mid-caudal and central regions show more expansion than the caudal region (orange is left DM, blue is right DM. p-values are indicated within the graphs; unpaired two-tailed Student's t-test, with Holm-Sidak correction for multiple comparisons. Error bars represent mean ± SEM for 5 chicken embryos per developmental stage). **Scale bars**: **A, B** (50 μm).

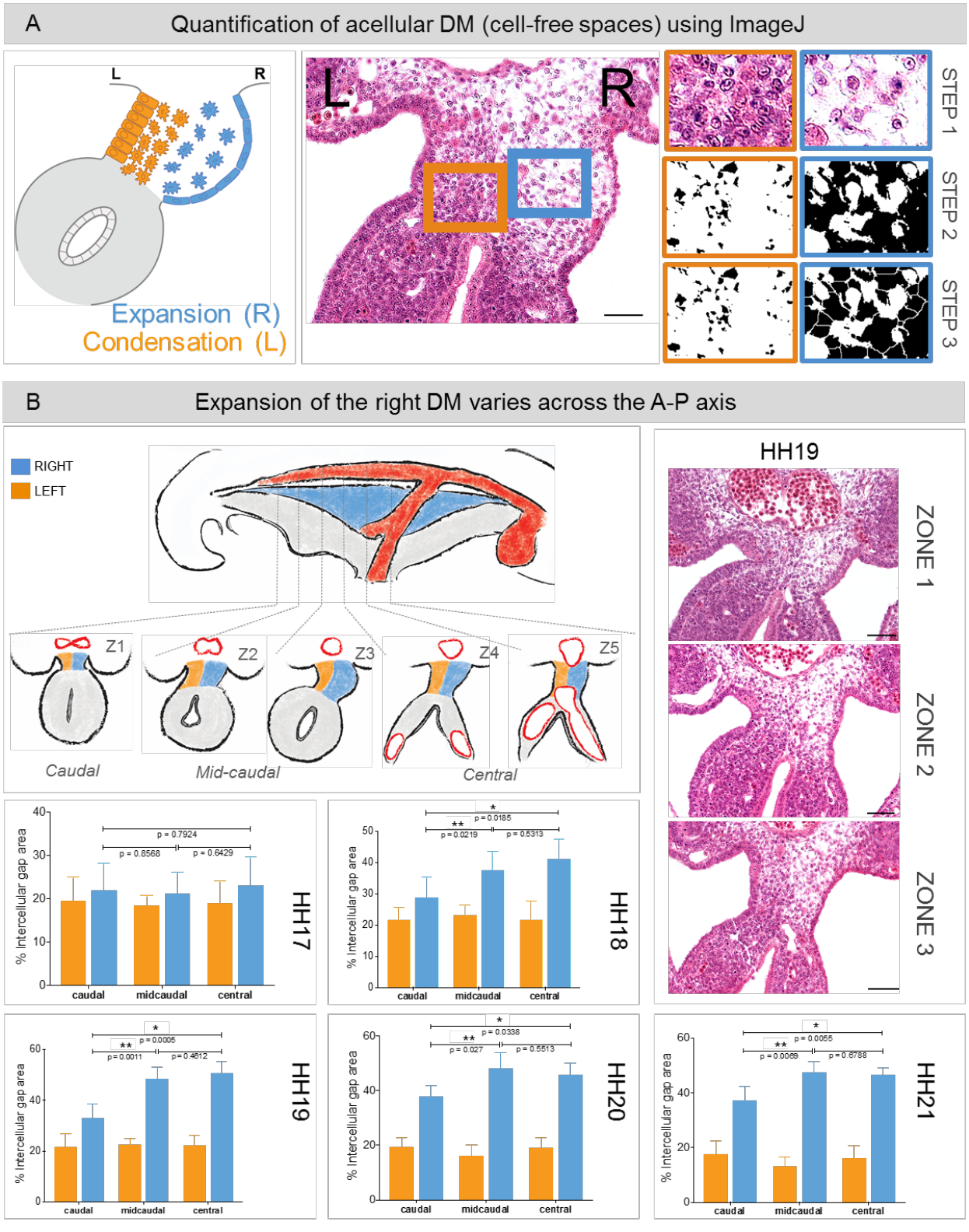
A
Quantification of acellular DM (cell-free spaces) using ImageJ
L
R
Expansion (R)
Condensation (L)
STEP 1
STEP 2
STEP 3
B
Expansion of the right DM varies across the A-P axis
RIGHT
LEFT
Z1
Z2
Z3
Z4
Z5
Caudal
Mid-caudal
Central
HH19
ZONE 1
ZONE 2
ZONE 3
HH17
HH18
HH19
HH20
HH21
% Intercellular gap area
caudal
midcaudal
central
p = 0.7924
p = 0.8568
p = 0.6429
p = 0.0185
p = 0.0219
p = 0.5313
p = 0.0005
p = 0.0011
p = 0.4612
p = 0.0338
p = 0.027
p = 0.5513
p = 0.0055
p = 0.0069
p = 0.6788

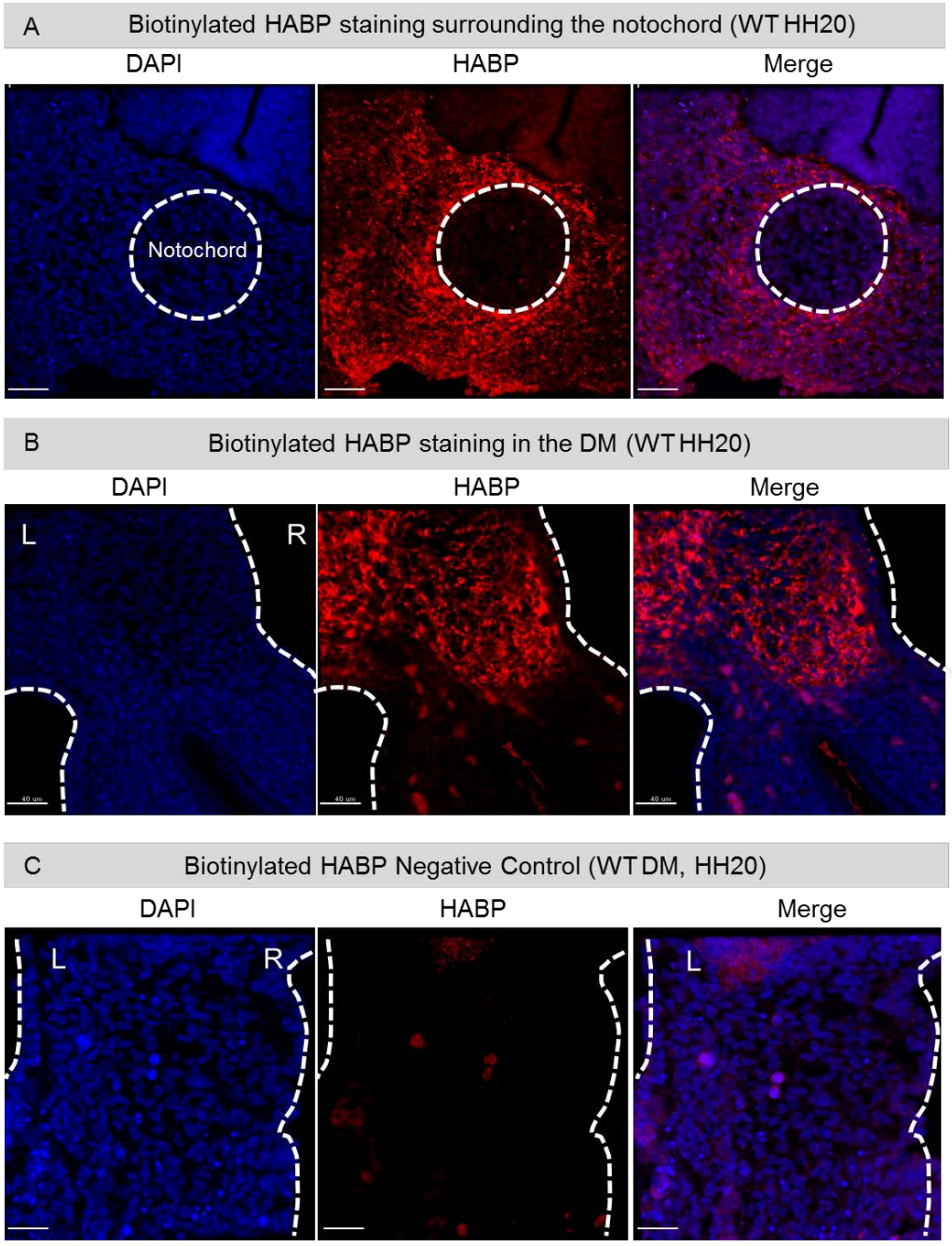

Fig. S2: Positive and negative controls for biotinylated HABP immunohistochemistry (related to Fig. 2).

A Internal positive control for biotinylated HABP immunohistochemistry showing expected HA accumulation surrounding the notochord. **B** Biotinylated HABP IHC with streptavidin conjugated Alexaflour 568 secondary antibody on HH19 WT embryos showing enriched accumulation of HA in the right DM. **C** Streptavidin conjugated Alexaflour 568 secondary antibody-only negative control showing no background signal. **Scale bars**: **A, B, C** (40 μm).

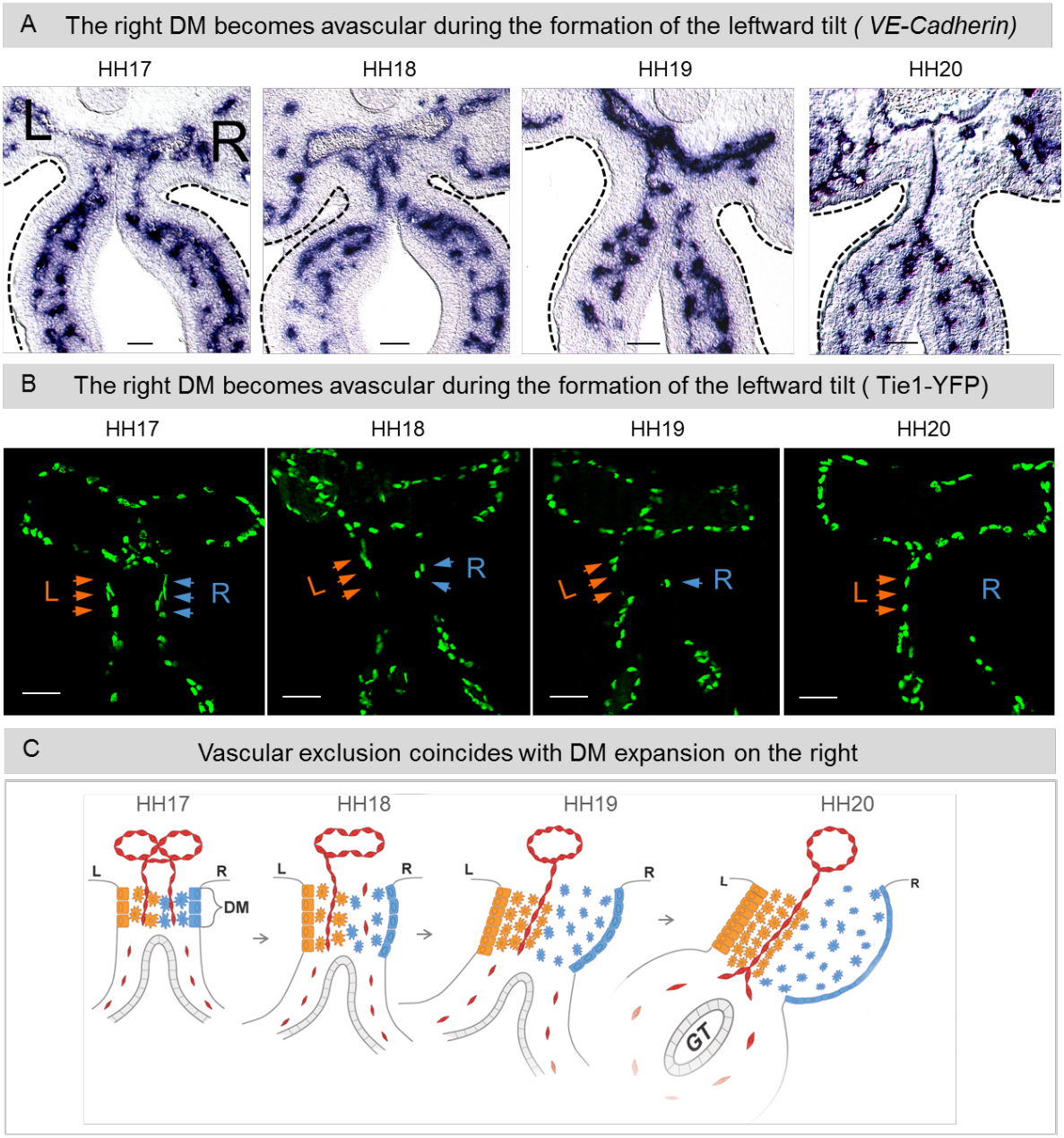

Fig. S3: Vascular exclusion on the right is coincident with initiation of the leftward gut tilt (related to Fig. 4).

Endothelial cells of the right-sided DV cords (HH17) are progressively excluded from the right as DM expansion proceeds starting at HH18, resulting in strictly left-sided DV cords at HH20. This was observed via RNA ISH for *VE-cadherin* in the chicken **A** and Tie1-H2B-YFP quail embryos **B**. **C** Model of the spatiotemporally coordinated DM expansion, formation of the leftward gut tilt, and vascular exclusion of the DV cords. Scale bars: **A, B** (100 μm).

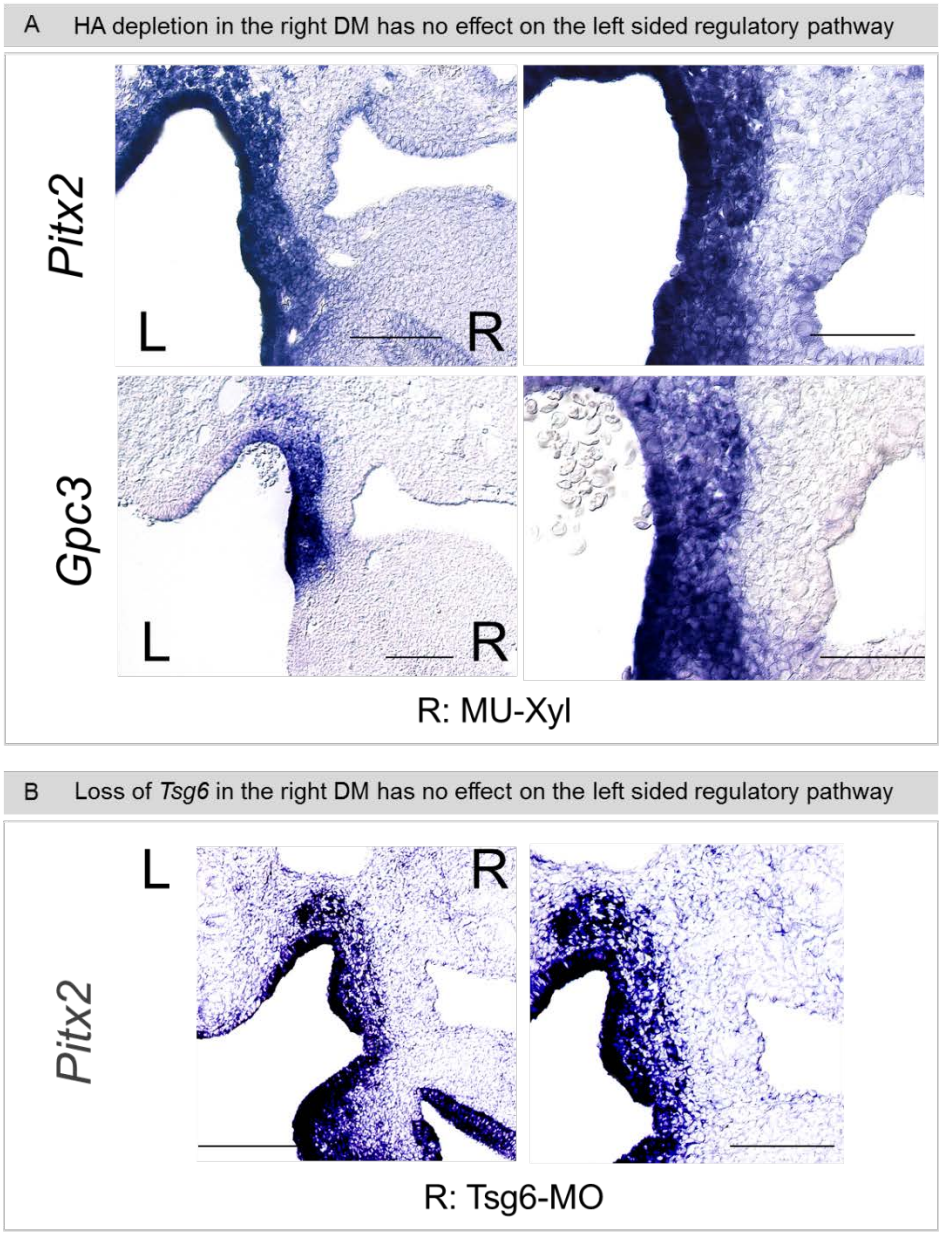

Fig. S4: Loss of HA or Tsg6 in the right DM does not alter LR asymmetric *Pitx2* expression (related to Fig. 3).

A (Top panel) *Pitx2* RNA ISH on pCAG-*Hyal2* electroporated embryos confirms left-sided Pitx2 expression in the DM. (Bottom panel) The expression of *Gpc3*, a downstream Pitx2 target and effector of the non-canonical Wnt signaling is also not altered in these embryos as demonstrated by the left-restricted DM expression of *Gpc3* (RNA ISH to *Gpc3*). **B** *Pitx2* RNA ISH on electroporated chicken embryos with Tsg6-targeting morpholinos confirms left-sided Pitx2 expression in the DM. Scale bars: **A** (left panel, 100 μm; right panel, 50 μm); **B** (left panel, 200 μm; right panel, 100 μm).

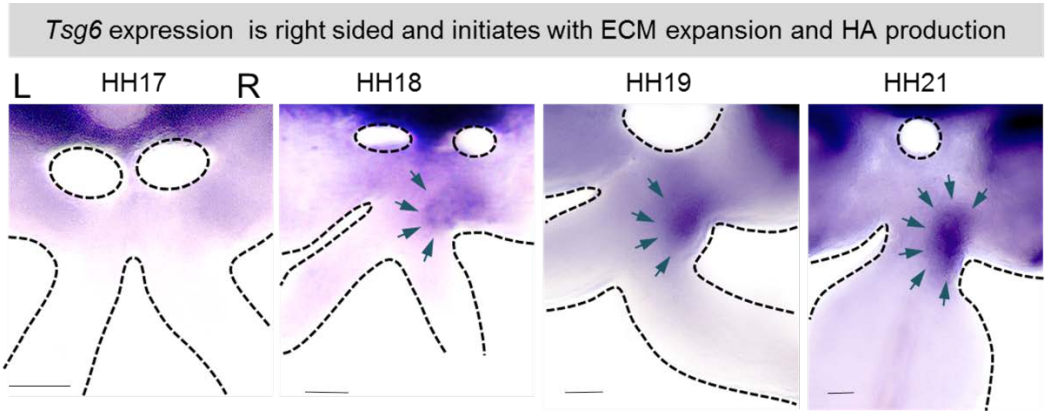

Fig. S5: Spatiotemporal expression profile of Tsg6 in the chicken DM (related to Fig. 5) RNA ISH for *Tsg6* in the chicken DM demonstrates that right-sided expression of *Tsg6* coincides with DM expansion. Scale bars: 50 μm

Fig. S6: Differential requirement for Tsg6 in the left *versus* right side of the DM (related to Fig. 6).

A (Top panel) Anti-angiogenic effect of *Tsg6* misexpression on the left is dosage dependent. Complete loss of DM vasculature is seen in embryos strongly electroporated with pCAG-*Tsg6* on the left side. (Bottom panel) Weakly electroporated embryos show only partial loss of the 1°LA. **B** (Top panel) Tsg6 is not sufficient to induce expansion of the DM mesenchyme. Condensation of the left mesenchyme is unaffected in embryos electroporated with pCAG-*Tsg6* on the left (H&E staining). (Bottom panel) DM expansion is lost in embryos electroporated with catalytically inactive Tsg6 (S28A) mutant on the right side (H&E staining). Scale bars: **A** (100 μm); **B, C** (50 μm).

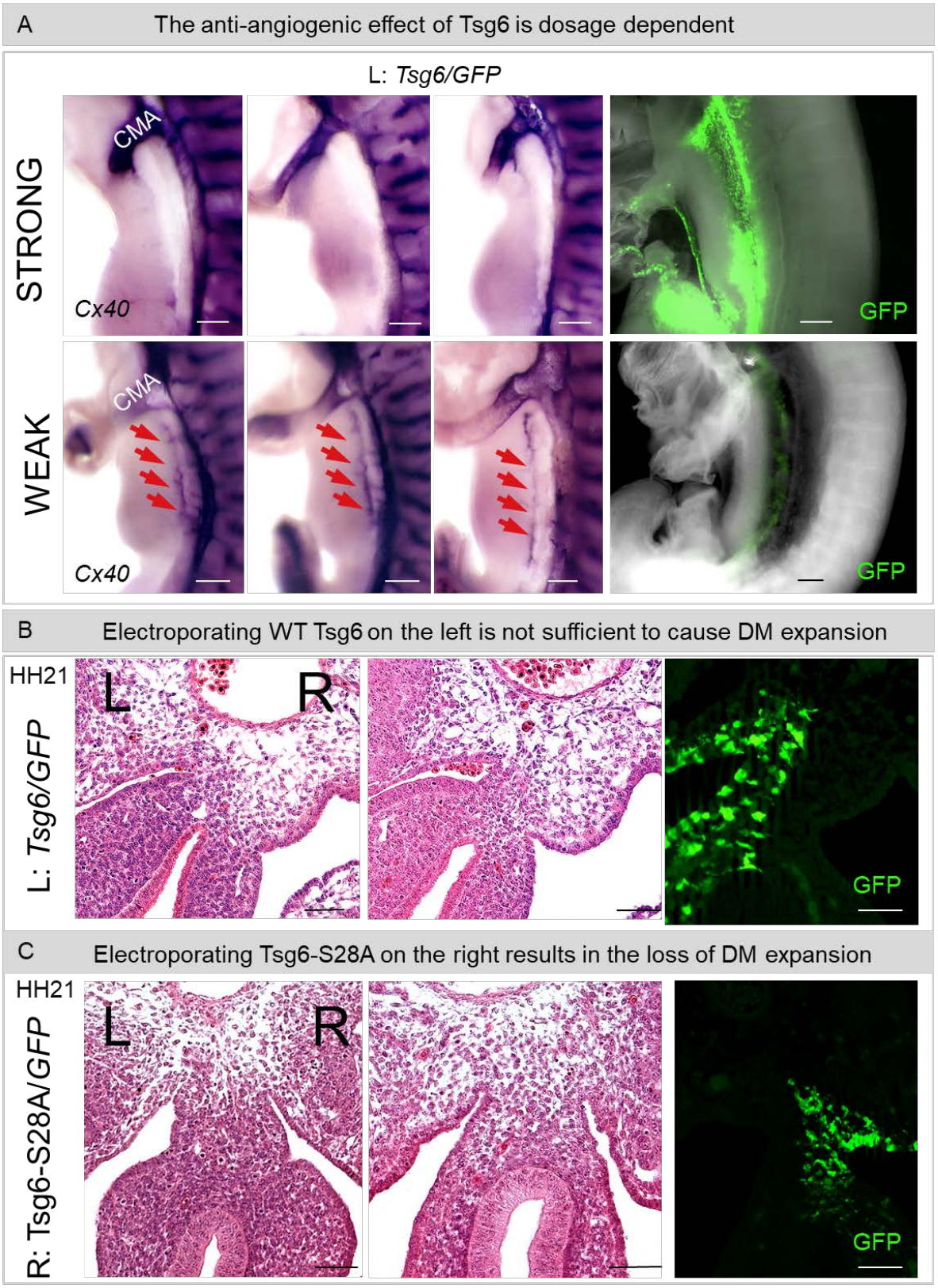
A
The anti-angiogenic effect of Tsg6 is dosage dependent
L: Tsg6/GFP
STRONG
WEAK
CMA
Cx40
GFP
B
Electroporating WT Tsg6 on the left is not sufficient to cause DM expansion
HH21
L: Tsg6/GFP
L
R
GFP
C
Electroporating Tsg6-S28A on the right results in the loss of DM expansion
HH21
R: Tsg6-S28A/GFP
L
R
GFP

Fig. S7: Tgs6-/- mice may be predisposed t midgut volvulus.
The distance (in microns) between the duodenojejunal junction (DJJ) and ileocecal junction (ICJ) (red double-headed arrow) and of the abdominal length (green double-headed arrow) was measured in Tsg6 +/+ and Tsg6 -/- E18.5 embryos (top panel). The ratio of the two values were plotted (bottom panel) and compared against the threshold value for defining a narrow mesenteric stalk (black dotted line) reflective of increased predisposition to volvulus (n = 4/5). The Tsg6 -/- mutant embryo marked with red asterisk (n = 1/5) had normal looping morphology. Scale bars: 1000 μm.

Tsg6 -/- mice may be predisposed to midgut volvulus (E18.5)

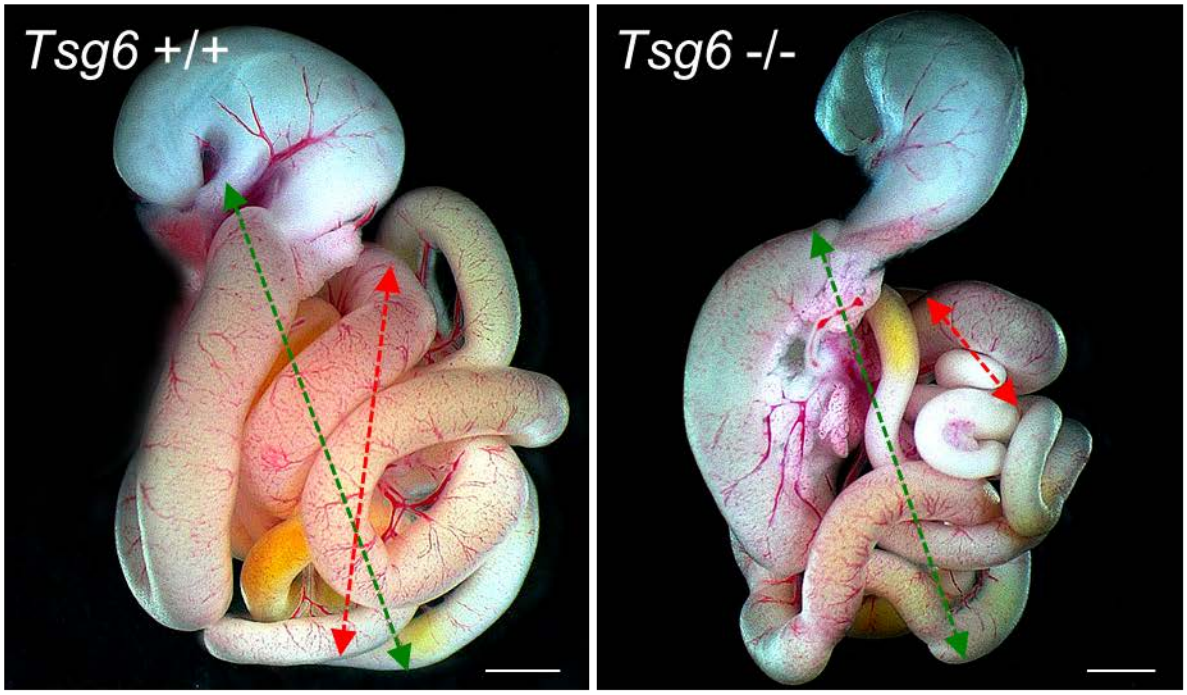

Green: abdominal length
Red: Distance between ICJ (top) and DJJ (bottom)

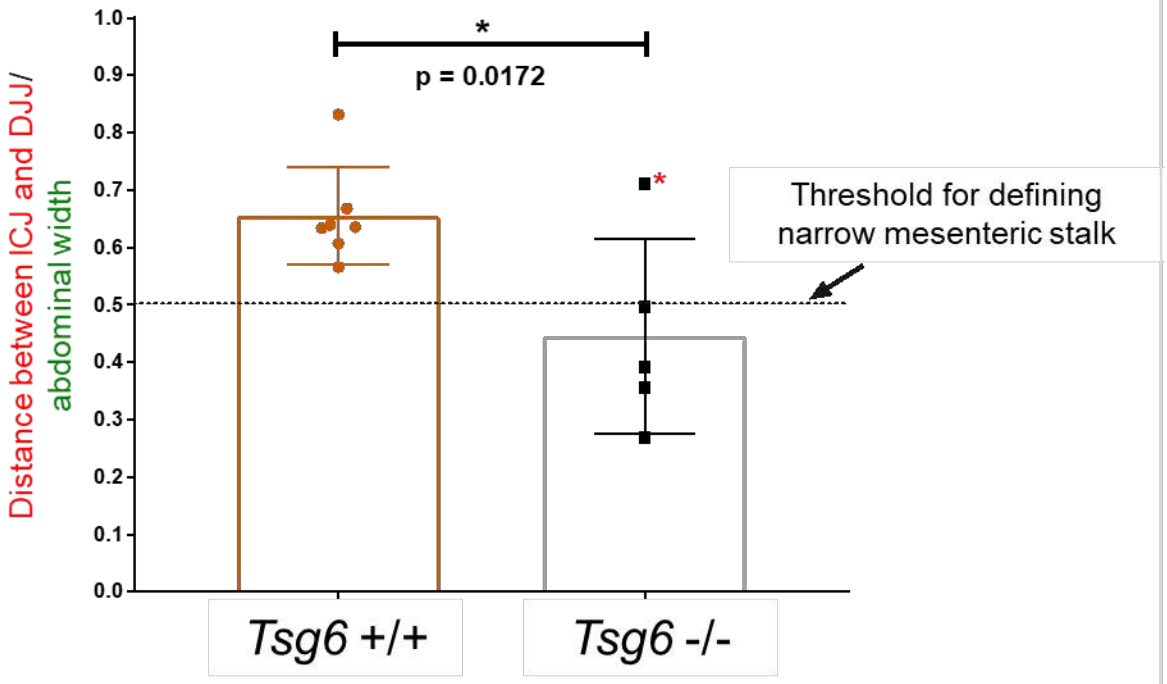

CHAPTER 3: TRANSCRIPTIONAL REGULATION OF CELL SHAPE CHANGES DURING VISCERAL ORGAN MORPHOGENESIS

This chapter is part of an invited review for the Journal of Cell Biology. It is written with Dr. Natasza A Kurpios. It has been submitted and is currently under review.

3.1 Abstract

The blossoming field of transcriptional regulation of cell shape changes during organogenesis aims to address the question of how gene regulatory networks and signaling mechanisms are integrated with cell intrinsic chromatin dynamics to produce the single most desired output- a change in cell shape. This process is fundamental to all cellular behaviors required to sculpt the organ. This review integrates concepts that have emerged from multiple studies that have contributed to the existing knowledge of transcriptional regulators, signaling pathways, and morphological processes that shape the visceral organs including heart, lungs, gastrointestinal tract and its accessory organs, and the kidneys. The review also emphasizes on the conservation of these processes across different species highlighting the best studied models in terms of cell shape changes during the different morphogenetic processes that underlie organ development. Perspectives have been provided on the questions that remain to be answered at the end of each section that may provide new research avenues and therapeutic opportunities.

3.2 Introduction

The morphogenetic processes that sculpt tissues and organs during embryogenesis univocally involve three-dimensional changes of sheets or clusters of individual cells. These complex events are regulated by precise spatial coordination of a limited repertoire of cellular behaviors such as oriented cell division, polarized growth, directional migration, differentiation, and programmed cell death – all which fundamentally involve changes in cell shape. The shape of any given cell in a cell-cluster is the result of an interplay between cell-cell, cell-matrix adhesion, and cortical tension (Lecuit T, 2007; Vogel V, 2006). While cortical tension is an isotropic regulator of cell shape, the distribution of the protein complexes involved in cell-matrix and cell-cell adhesion can be polarized and is primarily governed by two pathways: the apical-basal polarity (ABP) and the planar cell polarity (PCP) pathways which determine the cell shape perpendicular and parallel to the extracellular matrix (ECM), respectively.

The PCP pathway involves several modules of interacting proteins that function to establish specific geometric states within a cell to execute directed cellular behaviors along the sheet parallel to the matrix. The cellular behaviors include, but are not limited to, convergent extension, oriented cell division, directional migration, cellular rearrangements such as directed intercalation and polarized ciliary beating. Often, a core set of protein modules comprising of Vangl1, Vangl2, Celsr1, 2, 3, Disheveled (Dsh), Prickle, and orthologs of Fzd are generally associated with regulation of the PCP behavior. Additional regulators include an accessory module comprising the atypical cadherins, Fat and Dachous, and the Golgi resident protein Four-jointed that provide directional cues. Most often, the core and the accessory regulators also interact with tissue-specific effectors for regulating the PCP behavior. These have been thoroughly reviewed elsewhere (JB Wallingford, 2012; Karner CM, 2006; Seifert JR, 2007).

The ABP pathway involves asymmetrically localized multiprotein complexes that demarcate the boundary between the apical and basolateral membrane domains of a cell. They also serve as a barrier to intramembrane diffusion of proteins and macromolecules between the apical and basolateral membrane domains and aid in the formation of apical specializations such as brush borders. These proteins complexes include apically localized Par3-Par6 complexes, proteins that localize to apical lateral boundary such as PatJ and Stardust, and proteins that localize to the basolateral domain, Lgl2, Dlg, and Scribble. A detailed description of these can be found in the following reviews (Elsum I, 2012; Macara, 2004; Mellman I, 2008).

During embryonic development, tissue morphogenesis is driven by coordination and alignment of the local cellular behaviors with the three embryonic axes: dorsal-ventral (Bakkers J), anterior-posterior (AP) and left-right (LR) axes (Bakkers J). Since the spatiotemporal patterning in the embryo is specified by evolutionarily conserved and tissue-specific genetic and transcriptional regulatory networks, the above-mentioned polarity pathways that govern the local changes in cell shape in the embryo are ultimately regulated by these transcriptional regulatory networks. Importantly, while the morphogenetic pathways involved in regulating cell shape changes are thought to be generally permissive in nature and not instructive, recent studies have revealed that cell shape changes can be programmed by changes at the genomic level in addition to changes in protein localization (Halbleib JM, 2007). However, much remains to be explored to elucidate the complex signaling cascades that link the upstream transcriptional regulators to the cytoskeletal remodelers that are central to cell shape changes during organogenesis.

In this review, we explore how the regulatory networks specific to the structural and functional development of different organs, uniquely integrate at the transcriptional level to produce the necessary changes in cell shape and cell behavior during visceral organogenesis. For

each organ, the physical processes underlying its morphogenesis have been concisely described, followed by the cell shape changes that underlie these processes. Current knowledge about the transcriptional regulation of these morphogenetic events, gained from studies performed on different model organisms, has been integrated to bridge the link between the transcriptional machinery and cell shape changes driving the formation of the organ.

3.3 Defining the visceral organs

Visceral organs refer to the internal organs located within the cavities of the torso and can be broadly categorized into the thoracic viscera which includes the heart and lungs, and the abdominal viscera that includes the gastrointestinal (GI) tract and its accessory organs such as the liver and pancreas. They primarily arise from the splanchnopleure (comprising of the splanchnic mesoderm and endoderm) and begin as simple structures comprising of epithelial tubes, lumens and cavities. These primitive structures subsequently adopt a well defined conserved morphogenetic themes such as budding, looping, branching, and tubulogenesis in unique and specific mechanisms to transform into complex three-dimensional structures that are optimally packed within the limited space of the body cavity. These morphogenetic events are accompanied by formation of localized, molecularly distinct, spatially segregated microenvironments within the developing organ that initiate distinct cell fate specification programs involving changes in cell shape and behavior to give rise to the different cell types that are optimally organized for establishing the structure and functionality of the organs.

3.4 Transcriptional regulation of cell shape during heart development

The primitive heart is the first organ to form and function during vertebrate embryogenesis and is derived from bilateral populations of cardiac precursors that are initially present in the lateral mesoderm (Stainier DY, 2001). Its development can be broadly classified into three stages: a) formation of the primitive heart tube; b) elongation and looping of the heart tube; and c) remodeling to establish the cardiac chambers valves, and aligning the great arteries with the chambers. The formation of the primitive heart tube initiates with the synchronized migration of the lateral cardiac precursor cells towards the midline where they fuse to form a primitive tubular heart tube (Glickman NS, 2002). Subsequently, cardiac progenitors from the secondary heart field (SHF) are integrated at the arterial and venous poles resulting in rapid elongation of the heart tube (Mjaatvedt CH, 2001; Waldo KL, 2001). As the tube elongates, asymmetric processes initiate to displace the heart to the left. This is coordinated with involution and looping that result in the LR asymmetries transferred into the DV asymmetries of the cardiac tube (Rohr S, 2008). Simultaneously, the formation of the cardiac chambers and its associated valves is initiated (Moorman AF, 2003). Following the formation of the cardiac chambers, the heart undergoes significant remodeling that entails separation of the outflow tract into the aorta and pulmonary trunk and the alignment of these great arteries with their respective ventricular chambers (Sinha T, 2012). This remodeling enables the heart to attain its final form and is also accompanied by terminal differentiation of the myocardium (Hirschy A, 2006) and formation of the epicardium (Hirose T, 2006).

The cell shape changes pertinent to heart development can be observed from the earliest stages to the later remodeling stages and studies in zebrafish, chick and mice have provided us

Figure 3.1: Schematic representing processes, transcriptional factors and signaling pathways that regulate cell behavior during different stages of heart development. Figures represent the embryological processes while the text in black represents the cellular behavior that requires changes in cell shape. Each transcription factor and its downstream signaling pathway and its cytoskeletal regulators are listed in same color in adjacent columns. Eg: Tbx1- regulates Wnt5a, Wnt 11r pathway which regulates Vangl2 , Dsh to cause addition of SHF progenitors at arterial and venous poles by oriented intercalation. Genes without any known upstream or downstream interactors are listed in gray.

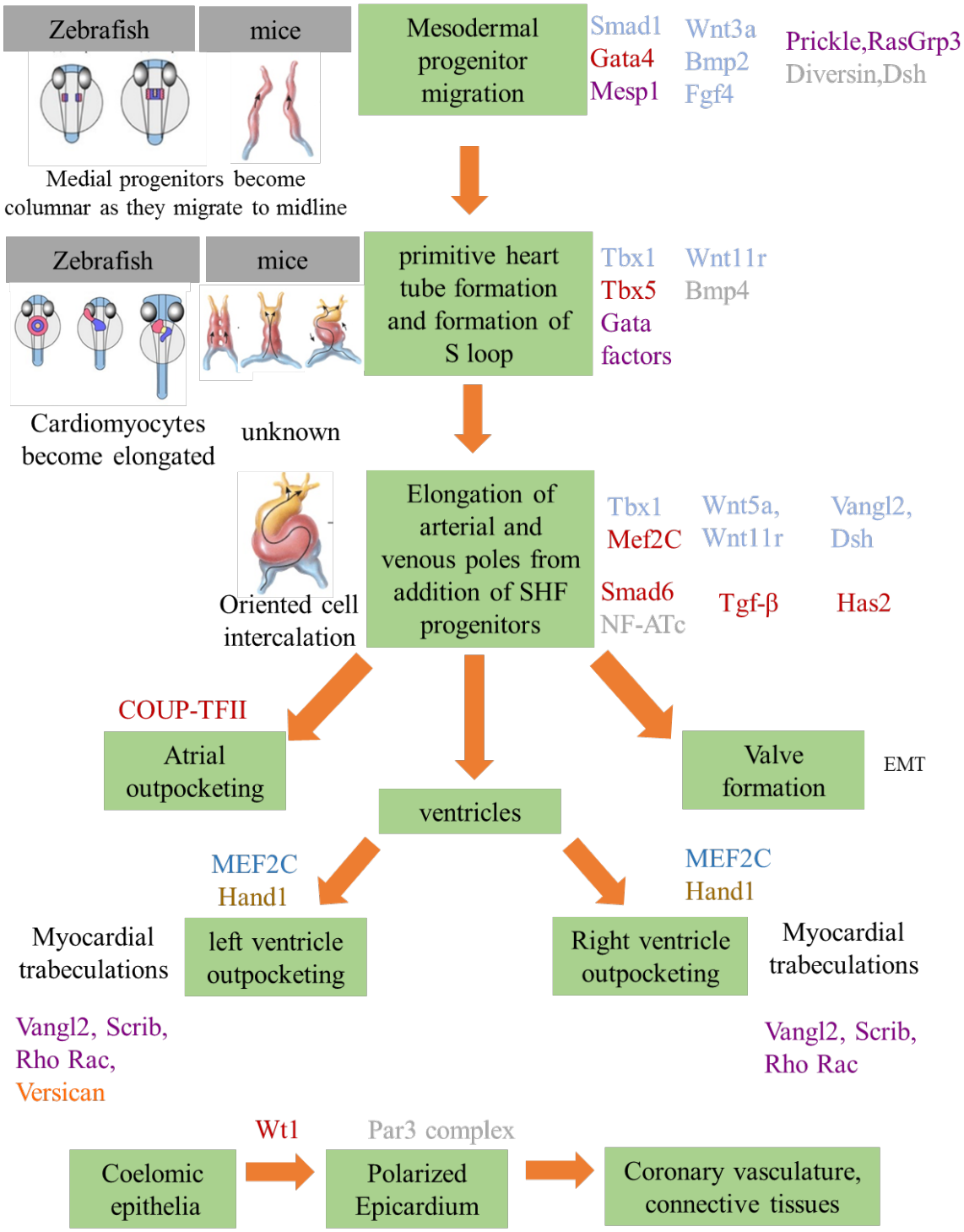
Zebrafish
mice
Mesodermal progenitor migration
Smad1
Gata4
Mesp1
Wnt3a
Bmp2
Fgf4
Prickle,RasGrp3
Diversin,Dsh
Medial progenitors become columnar as they migrate to midline
Zebrafish
mice
primitive heart tube formation and formation of S loop
Tbx1
Tbx5
Gata factors
Wnt11r
Bmp4
Cardiomyocytes become elongated
unknown
Oriented cell intercalation
Elongation of arterial and venous poles from addition of SHF progenitors
Tbx1
Mef2C
Wnt5a,
Wnt11r
Vangl2,
Dsh
Smad6
NF-ATc
Tgf-β
Has2
COUP-TFII
Atrial outpocketing
Valve formation
EMT
ventricles
MEF2C
Hand1
MEF2C
Hand1
Myocardial trabeculations
left ventricle outpocketing
Right ventricle outpocketing
Myocardial trabeculations
Vangl2, Scrib, Rho Rac, Versican
Vangl2, Scrib, Rho Rac
Wt1
Par3 complex
Coelomic epithelia
Polarized Epicardium
Coronary vasculature, connective tissues

with spatial and temporal insights into the critical molecular players and the transcriptional regulatory networks that are explored in the following sections (Figure 3.1).

3.4.1 Cell shape changes during migration of the cardiac progenitors

Towards the end of gastrulation, as the cardiac precursors migrate towards the midline, the medial myocardial progenitor cells adopt a polarized epithelial organization, becoming columnar and displaying basolateral distribution of β-catenin, apical localization of atypical protein kinase C iota (αPKCí) and junctional localization of zonula occludens (ZO-1), while the lateral myocardial progenitors remain cuboidal in shape (Rohr S, 2006). Defects in this midline migration results in cardiac bifida (formation of two hearts). Studies in zebrafish, chick and mouse embryos have shown that Wnt, Fgf, and BMP signaling pathways are major signaling pathways that regulate this migration (Yang X, 2002; Yue et al., 2008). In the chick and mouse embryos, Wnt3A and the BMP2 pathways have been shown to converge to regulate the transcription factor SMAD-1 to ensure proper migration of the cardiac progenitors (Song J, 2014). Similarly, GATA4 (Kuo CT, 1997) has also been shown to regulate the cardiac progenitor migration. However, its exact cell intrinsic roles in regulating the cell shape changes are unknown. Interestingly, Mesp1, a homeobox transcription factor, has been shown to act cell autonomously to coordinate the specification and polarity of the myocardial progenitor cells with the directional migration of the cardiac progenitors (Ref). Particularly, Mesp1 directly regulates the expression of *Prickle1*, a core component of the PCP pathway, to determine the directionality of the migrating myocardial progenitors. Additionally, Mesp1 also targets *RasGRP3*, a critical regulator of cell motility, and ERK signaling pathway, to regulate the speed of migration of these myocardial progenitors (Chiapparo G, 2016). However, how Mesp1 is integrated with the more upstream transcriptional network and signaling pathways during myocardial progenitor migration in the embryo is currently unknown. Studies in

zebrafish have shown that while the PCP components Diversin and Dsh are the major downstream regulators of cell shape changes that accompany the migration of the cardiac precursors (Moeller H, 2006), transcriptional mechanisms that directly regulate these PCP components remain to be identified.

3.4.2 Cell shape changes during initiation of heart looping and elongation

The changes in cell shape during the formation and looping of the heart tube have been more extensively studied in zebrafish embryos compared to chick and mouse embryos. In zebrafish, as the cardiac progenitors migrate to the midline, they fuse to form the cardiac cone (Figure 3.1) (Holtzman NG, 2007; Trinh LA, 2004). As the cardiac cone extends, it undergoes leftward displacement which is also called cardiac 'jogging', following which the linear heart tube gradually bends at the boundary between the ventricle and the atrium to create the S-shaped loop. While the molecular mechanisms regulating the formation of the loop are not fully understood, the changes in cell shape of the cardiomyocytes during looping is a major force driving this process (Taber, 2006). At the onset of looping, the cardiomyocytes change shape from small and rounded (isotropic) morphology of the linear heart tube to flattened and elongated in the outer curvature at the expanded chamber stage. Tbx1, a member of T-box family of transcription factors, is the cell intrinsic master regulator of the cell shape change of the cardiomyocytes during looping. In *Tbx1*$^{-/-}$ mutants, cells in the outer and inner curvatures retain the small and rounded morphology and do not elongate. Interestingly, Tbx1 directly targets Wnt11r, an ortholog of Wnt11 to regulate these cellular changes (Choudhry P, 2013). The downstream mechanisms of the Tbx1-Wnt11r signaling pathway remain to be elucidated and are an open topic for investigation. The dynamic cellular rearrangements that accompany cardiac looping are poorly understood in chick and mice and much remains to be discovered.

As the heart tube loops, it also undergoes elongation by oriented intercalation of cohesive sheets of cardiac progenitor cells derived from the secondary heart field (SHF) to its arterial and venous poles to form the right ventricle, outflow tract (OFT), and atrial myocardium tube (Figure 3.1) (Mjaatvedt CH, 2001; Waldo KL, 2001). The SHF progenitor cells originate from the dorsal wall of the coelomic cavity, and constitute an atypical polarized epithelium with monocilia on the apical side and dynamic filopodia on the basal side. In mice, Tbx1 is a critical regulator of the epithelial cell morphology of the SHF cells in addition to regulating its proliferation and differentiation. Tbx1 also regulates oriented intercalation by interacting with the BAF chromatin remodeling complex to regulate the expression of *Wnt5a*, which interacts with Wnt11, Dsh, and Vangl2 to induce cell intercalation (Chen L, 2012). In addition to the Tbx1 mediated mechanisms, the transcription factor Mef2C is known to regulate the lengthening of the OFT. However, the cellular basis of the Mef2C-mediated elongation is poorly understood (Barnes RM, 2016).

3.4.3 Cell shape changes post looping of the primary heart tube

At the time of looping, the primary heart tube within the pericardial cavity can be divided into the atrial and ventricular components along with an outflow tract. Subsequently, remodeling of these components to form the cardiac chambers is initiated (Figure 3.1). The formation of ventricles begins with the outpocketing of the inlet ventricular component to give rise to the left ventricle followed by the outpocketing of the outlet ventricular component to give rise to the right ventricle (Moorman A, 2003). The ventricular outpocketing is marked by thickening of the myocardial layer, accompanied by a change in shape of the primary spherical cardiomyocytes, where they begin to elongate, become rod shaped and polarized, with majority of cell junction proteins localized to specialized intercalated discs, joining the cells end to end to give rise to both compact and trabeculated myocardium (Passer D, 2016). While Vangl2, Scrib, and Rho kinases such as

Rac1 regulate the polarity of the myocardium, implicating a role for PCP signaling pathway in determining myocardial polarity (Phillips HM, 2008), the organization of the clustered ventricular cardiomyocytes is coordinated by Wnt11 that patterns the expression of the cell adhesion components, N-cadherin and β-catenin (Nagy I, 2010). The transcription factor Hand2, which has been implicated in the myocardial polarity in mice embryos, also drives apical-basal polarization of the myocardium in zebrafish embryos by regulating fibronectin deposition on the baso-lateral side (Trinh LA, 2005). However, signaling events downstream of Hand2 that drive this polarity have yet to be explored.

The maturing heart is enveloped by a subtype of coelomic epithelium called the epicardium that displays apical-basal polarity. A subset of cells in the epicardium undergoes epithelial to mesenchymal transition (EMT) to give rise to a group of mesenchymal cells that are known as epicardially derived cells (EPDC), which migrate into the myocardium of the ventricular wall contributing to the endothelial and smooth muscle cells and to the forming coronary vessels and connective tissue that are critical for heart development (Martinez-Estrada OM, 2010). Par3, a key apical-basal polarity component, plays a critical role in the formation of the mouse epicardium. In Par3 knockout embryos, the apical domain of proepicardial cells is disrupted, which causes the formation of epithelial cysts and prevents the formation of an intact epicardial monolayer (REF). In the absence of the resulting epicardially-derived cells, the coronary vessel network fails to form and the ventricular myocardium remains thin (Hirose T, 2006). Thus, while the transcriptional network involved in the specification of the epicardium has been discovered (Martinez-Estrada OM, 2010), the cell autonomous transcriptional regulatory mechanisms that regulate the Par3-mediated polarity in the epicardium remain unknown.

3.4.4 Perspectives on cell shape changes in heart development

Investigations in several model systems thus far have shown that the cell shape changes during cardiac progenitor cell migration towards the midline to form the heart tube are conserved. However, accompanying the general similarities are species-specific differences. In zebrafish, the cardiac progenitors migrate to form a cardiac cone, which undergoes cardiac jogging, myocardial involution, and extension to set the stage for subsequent looping morphogenesis (Holtzman NG, 2007; Trinh LA, 2004) . But, in chick and mice, the cardiac progenitors form a cardiac crescent which undergoes inversion as the cells migrate towards the midline and fuse to form the heart tube Trinh LA, 2004. While the general transcriptional mechanisms for the migration have been elucidated as described in Section 3.3.1, the exact molecular mechanisms underlying the fusion of the progenitors to form the heart tube in the vertebrate and mammalian model systems are poorly understood. Furthermore, the genomic/transcriptional regulatory programs that regulate the differences between the lateral and medial cell populations and govern the behavioral differences between the migrating cells remain unknown. Further investigations in these areas may provide mechanistic insights to improve our understanding of conditions such as cardiac bifida. Moreover, these fundamental differences in the formation of heart tube are also suggestive of different species-specific regulatory mechanisms that control the conserved cell intrinsic mechanisms to form the heart tube. For instance, while Mesp1 role as the most downstream cell autonomous transcription factor regulating speed and directionality of cardiac migration is best understood in mice, its cell-autonomous roles in zebrafish remain to be elucidated.

Compared to our current understanding of the morphogenetic mechanisms at the early stages of heart development, a lot more is unknown regarding the cellular mechanisms that contribute to morphogenesis during the later stages. This is primarily due to the challenges

involved in combining our understanding of the three-dimensionality of heart looping morphogenesis and the simultaneous occurrence of other morphogenetic processes involved in the formation and alignment of cardiac chambers. While histological and morphometric analysis provide information regarding the cell shape and organization at different stages of development, the exact role of the cell shape changes in cardiomyocytes is difficult to study as the investigations are complicated by the beating and the coordinated repetitive contractions of the cardiomyocytes. Hence investigations to further refine live-imaging techniques using transgenic models, coupled with improvements in our understanding of the basic principles of later stages of heart development, are critical to improving our ability to diagnose debilitating cardiac disorders pertaining to later stages.

3.5 Transcriptional regulation of cell shape in lung development

Lung development initiates around embryonic day (E) 9.0 in the mouse with the specification of the ventral foregut endoderm into the respiratory endoderm by the expression of the transcription factor *Nkx2.1*. Evagination and protrusion of these epithelial cells ventrally give rise to the primitive trachea and the two primary lung buds (Figure 3.2). The primitive trachea undergoes further septation to form the eosophagus and trachea, while the primary lung buds generate the left and the right lobes of the lung by undergoing a highly regulated branching morphogenesis during the pseudoglandular stage to form an arborized network of airways that increases the surface area of the lobes (Metzger RJ, 2008). This is immediately followed by the cannanicular and saccular stages, where the cells in the terminal branches undergo changes in shape, forming clusters of epithelial sacs that later develop into alveoli. Hence, concordant with the stereotypical branching morphogenesis, the epithelial progenitors undergo proximal-distal differentiation, involving

extensive interaction between the lung mesoderm and endoderm. This is required to form the conducting airways with ciliated, secretory, and basal cells in the proximal regions, and the future gas-exchange sites with saccules containing alveolar type 1 and 2 epithelial cells region at distal regions (Herriges M, 2014).

3.5.1 Cell shape changes during lung branching morphogenesis

Branching morphogenesis is critical for the formation of the structural conducting airways as well as the terminal alveolar compartments for gas exchange. Lung branching proceeds in a stereotypical manner by concurrent and repeated use of three major branching mechanisms: a) domain branching, b) planar bifurcation, and c) orthogonal bifurcation (Metzger RJ, 2008). These mechanisms are genetically hard-wired and depend upon integration of autocrine, paracrine, and juxtracrine interactions between epithelial and mesenchymal cells that influences processes such as apical–basal cell polarity, cell adhesion, and ECM remodeling. Fgf10, secreted by the mesenchyme at the distal end of the primary lung buds, regulates both initial outgrowth of the primary and secondary lung buds during the later stages of branching morphogenesis via signaling to Fgfr2 (Sekine K, 1999). The expression of *Fgf10* is regulated by the interplay of retinoic acid (RA) signaling pathway, Shh via its transcriptional activators Gli-1-3, and the BMP4/Tgf-β signaling pathways. While the following reviews (Herriges M, 2014; Warburton D, 2010) have wonderfully detailed these processes and the molecular pathways upstream of Fgf10, woefully little is known about the regulatory processes that drive cell shape changes of the airway epithelial sheet during branching morphogenesis downstream of Fgf10. Recent studies implicate changes in orientation of cell division as a mechanism of “directional-shape change” that mitigate extension of branches. This regulation of oriented cell division

Figure 3.2: Schematic of processes involved in lung morphogenesis. The main regulatory pathways underlying lung branching morphogenesis and proximal-distal differentiation have been outlined along with the processes. Transcription factors have been listed in purple, signaling molecules in brown, and cytoskeletal effectors in blue.

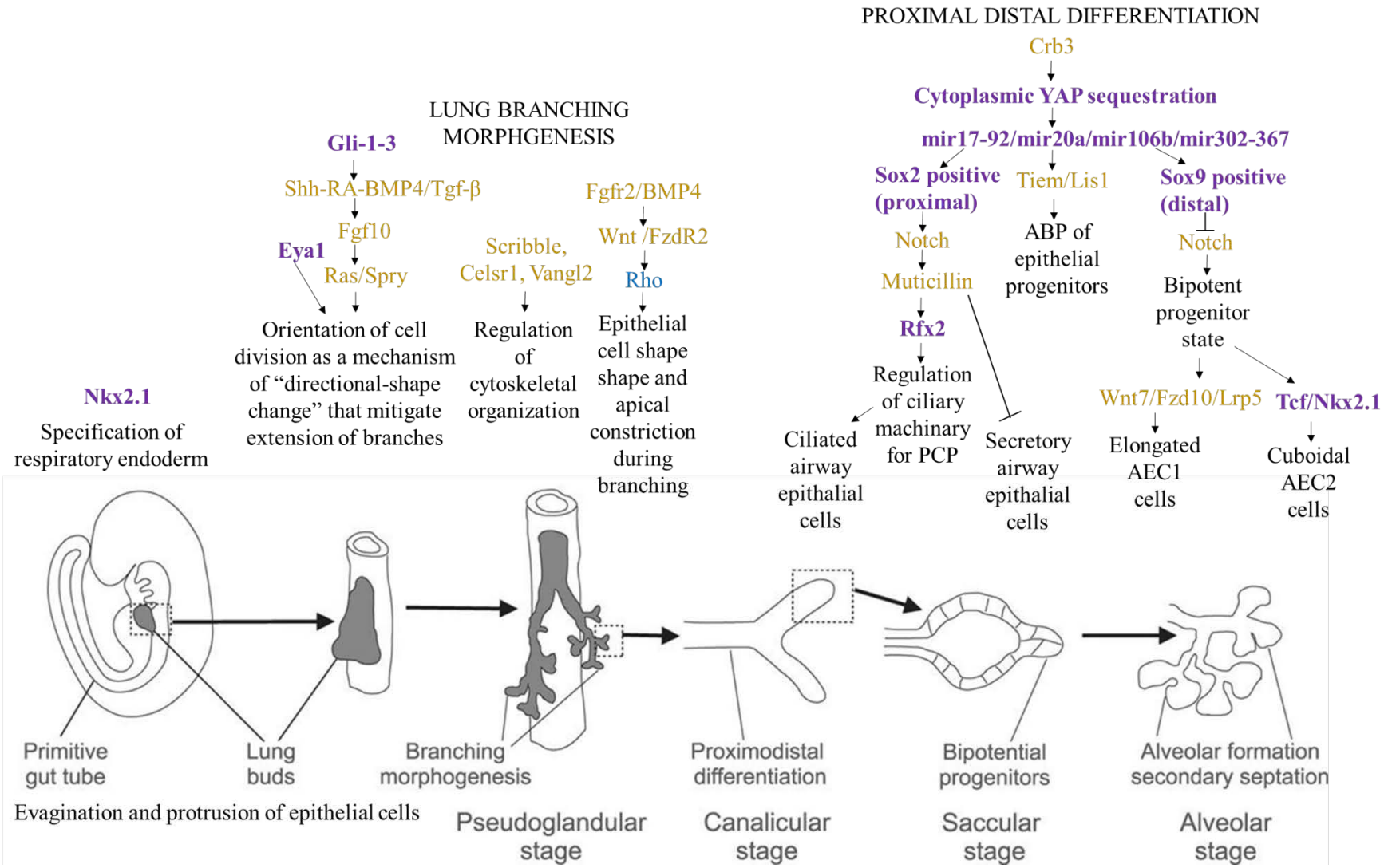
PROXIMAL DISTAL DIFFERENTIATION
Crb3
Cytoplasmic YAP sequestration
mir17-92/mir20a/mir106b/mir302-367
Sox2 positive (proximal)
Tiem/Lis1
Sox9 positive (distal)
Notch
ABP of epithelial progenitors
Notch
Muticillin
Bipotent progenitor state
Rfx2
Regulation of ciliary machinary for PCP
Wnt7/Fzd10/Lrp5
Tcf/Nkx2.1
Ciliated airway epithalial cells
Secretory airway epithalial cells
Elongated AEC1 cells
Cuboidal AEC2 cells
LUNG BRANCHING MORPHGENESIS
Gli-1-3
Shh-RA-BMP4/Tgf-β
Fgf10
Eya1
Ras/Spry
Orientation of cell division as a mechanism of "directional-shape change" that mitigate extension of branches
Scribble, Celsr1, Vangl2
Regulation of cytoskeletal organization
Fgfr2/BMP4
Wnt /FzdR2
Rho
Epithelial cell shape shape and apical constriction during branching
Nkx2.1
Specification of respiratory endoderm
Primitive gut tube
Lung buds
Branching morphogenesis
Proximodistal differentiation
Bipotential progenitors
Alveolar formation secondary septation
Evagination and protrusion of epithelial cells
Pseudoglandular stage
Canalicular stage
Saccular stage
Alveolar stage

is accomplished by the Ras/Spry activity, which occurs downstream of Fgf10 signaling and regulates spindle-pole orientation leading to a specific directionality in epithelial cell proliferation while the branches extend (Tang M, 2009). Although the direct transcriptional regulators downstream of Fgf signaling is unknown, the Notch-transcription Eya1 was found to regulate cell polarity, spindle orientation, aPKCz phosphorylation and Numb segregation in a cell autonomous manner in the distal epithelium (Ahmed HK 2011). These observations suggest potential cross-talk between the Fgf and the Notch signaling pathways. Additionally, the cell shape changes required for the epithelial sheet to bend and generate new bud tips are also regulated by the PCP components Scribble, Celsr1, and Vangl2, which regulate the cytoskeletal organization in response to Fgf signaling (Laura LY, 2013). Furthermore, Wnt/Frizzled 2 receptor signaling directly regulates Rho to control epithelial cell shape and apical constriction during branching (Kadzik RS, 2014). Disruption of canonical Wnt signaling during lung development by conditional deletion of β-catenin or overexpression of the Wnt inhibitor *Dickkopf1* severely impairs branching morphogenesis (Rajagopal J, 2008). This Wnt/Fzd-mediated signaling is regulated at least in part via Fgfr2 and BMP4 in the lung epithelium (Volckaert T, 2015). Whereas the signaling pathways that regulate the cell shape changes during branching morphogenesis have been partly identified, further studies are much needed to identify the transcriptional regulation of these signaling mechanisms.

3.5.2 Cell shape changes during differentiation along the proximal-distal axis of the lung

As the lung buds branch, proliferate, and extend distally, the lung endoderm differentiates along the proximal-distal axis of the developing airways. A nucleocytoplasmic shift in the localization of the Hippo effector, Yap, marks the boundary between the proximal airway and the distal alveolar sac lung compartments. The nuclear activity of Yap is critical for the progenitor identity

of the lung epithelia, with the removal of nuclear Yap driving airway cell differentiation (Mahoney JE, 2014). Crb3 mediated apical-basal polarity in the proximal airway epithelial cells causes Yap to bind to Lats1/2 kinases present at the apical junctions to promote cytoplasmic sequestration of Yap, and, consequently, initiates proximal airway progenitor cell differentiation (Szymaniak AD, 2015). This is accompanied by downregulation of *miR-17-92*, *miR20a*, and *miR106b* clusters (Ventura A, 2008) while the rate and extent of differentiation of the progenitors is regulated by expression of *miR302/367* cluster. This cluster coordinates the balance between proliferation and differentiation through direct regulation of Rbl2 and Cdkn1a as well as the apical-basal polarity via regulation of Tiam1 and Lis1 (Tian Y, 2011).

As the progenitors differentiate at the proximal end, they give rise to ciliated, secretory, and basal cell lineages. This is initiated by downregulating Sox9 and upregulating the transcription factor Sox2. Notch signaling also plays a key role in the differentiation of the proximal airway epithelium, including establishing and maintaining a proper balance between the ciliated and secretory cell types. The central target of Notch signaling in multiciliated cells appears to be the transcriptional cofactor Multicilin (Stubbs JL, 2012). Targets of Multicilin include several other transcription factors required for motile ciliogenesis, including multiple Rfx family members, C-Myb, and FoxJ1 (Stubbs JL, 2012). The Rfx transcription factors are broadly required for ciliogenesis in vertebrates, including in multiciliated cells. Direct targets of Rfx2 contribute to essentially all ciliary machinery including genes required for cilia assembly, cilia motility and planar polarization of directional beating (Swoboda P, 2000).

In contrast, within the distal progenitor population, Sox9 is upregulated whereas Sox2 is downregulated (Hashimoto S, 2012). These Sox9/Id2 expressing endoderm progenitors first differentiate into a bipotent progenitor state and this is accompanied by inhibition of Notch

signaling. These progenitors subsequently generate the critical alveolar epithelial lineages known as type 1 and 2 alveolar epithelial cells (AEC1 and AEC2) by promoting the program of one lineage over the other depending on cues from the microenvironment. AEC1 cells are elongated epithelial cells that form a thin barrier between the alveolar airspace and closely approximated blood-filled capillaries (Weibel ER, 2015). Activation of canonical Wnt signaling by interaction of Wnt 7 with Fzd1/10 and Lrp5, has been shown to be critical for AEC1 development (Mutze K, 2015; Wang Z, 2005). AEC2 cells, in contrast, are cuboidal cells that serve as a major manufacturing and recycling lineage of the alveoli, producing surfactant proteins for reducing surface tension. The TCF/β – catenin activity modulated by Wnt signaling as well as dosage of *Nkx2.1* expression is critical for formation of AEC2 cells (Wang Z, 2005). While the apical basal polarity is critical for AEC2 cells for apical secretion of surfactants and ions into the lumens, the cellular mechanisms needed to define the polarity at the time of AEC2 maturation and their interaction with the known signaling pathways remain to be elucidated.

3.5.3 Perspectives into regulation of cell shape changes during lung morphogenesis

The signaling pathways involved in the regulation of epithelial cell shape during early branching morphogenesis of the lung are one of the relatively well studied aspects of lung development. While the mesenchymal signaling mechanisms involved in the distal extension of lung are also well understood, the behavioral aspects such as packing of the mesenchymal compartment and polarity of mesenchymal cells in relation to the branching epithelia are less known. Epithelial cell shape changes also follow the differentiation of the epithelia along the proximal-distal axis of the branching airway to give rise to different lineages. Several studies investigating the mechanisms of the epithelial differentiation have uncovered mechanisms involving epigenetic modifications to DNA, domain-specific alterations in chromatin architecture, and microRNAs that are critical for

the differentiated state (Swarr DT, 2015). While current investigations are giving rise to an integrated picture of the transcriptional networks that regulate the epithelial differentiation, again, very little is known about how the adjacent mesenchyme is patterned, or how the transcriptional networks regulate the cell shape behavior or the crosstalk between the epithelia and the mesenchyme that contributes to overall lung branching morphogenesis. Moreover, since the mesenchyme gives rise to the vasculature, the neuronal networks, and the muscular connections critical for lung function, further studies utilizing high-throughput screening methods such as single-cell RNA-seq and single-cell proteomics could greatly enhance our understanding of the mechanisms involved in mesenchymal regulation. This could potentially uncover novel pathways and provide additional therapeutic targets for pulmonary disorders.

3.6 Transcriptional regulation of cell shape in development of the GI tract

The GI tract is derived from the primitive gut tube that arises from the endoderm and the fusion of the lateral limbs of the splanchnic mesoderm. The gut tube is divided regionally along the cranial-caudal axis into the foregut, midgut, and hindgut regions based on their vascular supply (Figure 3.3) (Roberts DJ, 1999). Following the regional specification, the primitive gut tube undergoes differential elongation along the cranial-caudal axis with the midgut elongating disproportionately compared to the other regions of the primitive gut (McGrath PS, 2015). As the gut tube elongates, asymmetries across the left-right axis initiate to establish the stomach curvature and to trigger the critical counterclockwise rotation of the midgut that sets the directionality for subsequent gut looping morphogenesis (Raya A, 2006). Concurrently, the gut endoderm undergoes radial intercalation to give rise to a single layer of polarized epithelium that undergoes cytodifferentiation to form the enterocytes and the different lineages of secretory cells (Barbara PS, 2003). In the

following sections we examine the critical molecular players and the transcriptional networks that regulate cell shape changes during gut morphogenesis across cranial-caudal, left-right, and along the radial axis.

3.6.1 Regulation of cell shape changes during cranial-caudal morphogenesis of the GI tract

Prior to gut tube elongation, the endoderm cells of the gut tube undergo a cell shape change from cuboidal to columnar morphology along the cranial-caudal axis and become radially oriented as they fuse to form the gut lumen (Chalmers AD, 2000). Subsequently, during elongation, the endodermal cells undergo oriented division and intercalate between their anterior and posterior neighbors within the gut walls to contribute to the lengthening of the endoderm (Matsumoto A, 2002). Crosstalk between the gut endoderm and its surrounding mesenchyme ultimately results in the lengthening of the gut tube (Reed RA, 2009).

In the foregut region, interaction between the forestomach gut endoderm and its surrounding mesenchyme is mediated by Shh and PCP pathways downstream of Wnt5a (Matsuyama M, 2009). While Shh secreted by the endoderm regulates surrounding mesenchyme via activation of Notch signaling, the Stbm/Vangl2 interactions with a mesenchyme-derived Wnt5a regulate the polarity needed for oriented cell division of the endodermal epithelia (Matsuyama M, 2009) (Figure 3.3). In the duodenum, elongation is accompanied by the decrease in the diameter of the epithelia and occlusion of the epithelial lumen followed by recanalization and emergence of the villi. Intriguingly, contrary to the prior notion that increased epithelial proliferation drives the occlusion phase during duodenal development, it has been suggested that convergent extension of the epithelial cells in the radial-caudal axis could be the mechanism behind

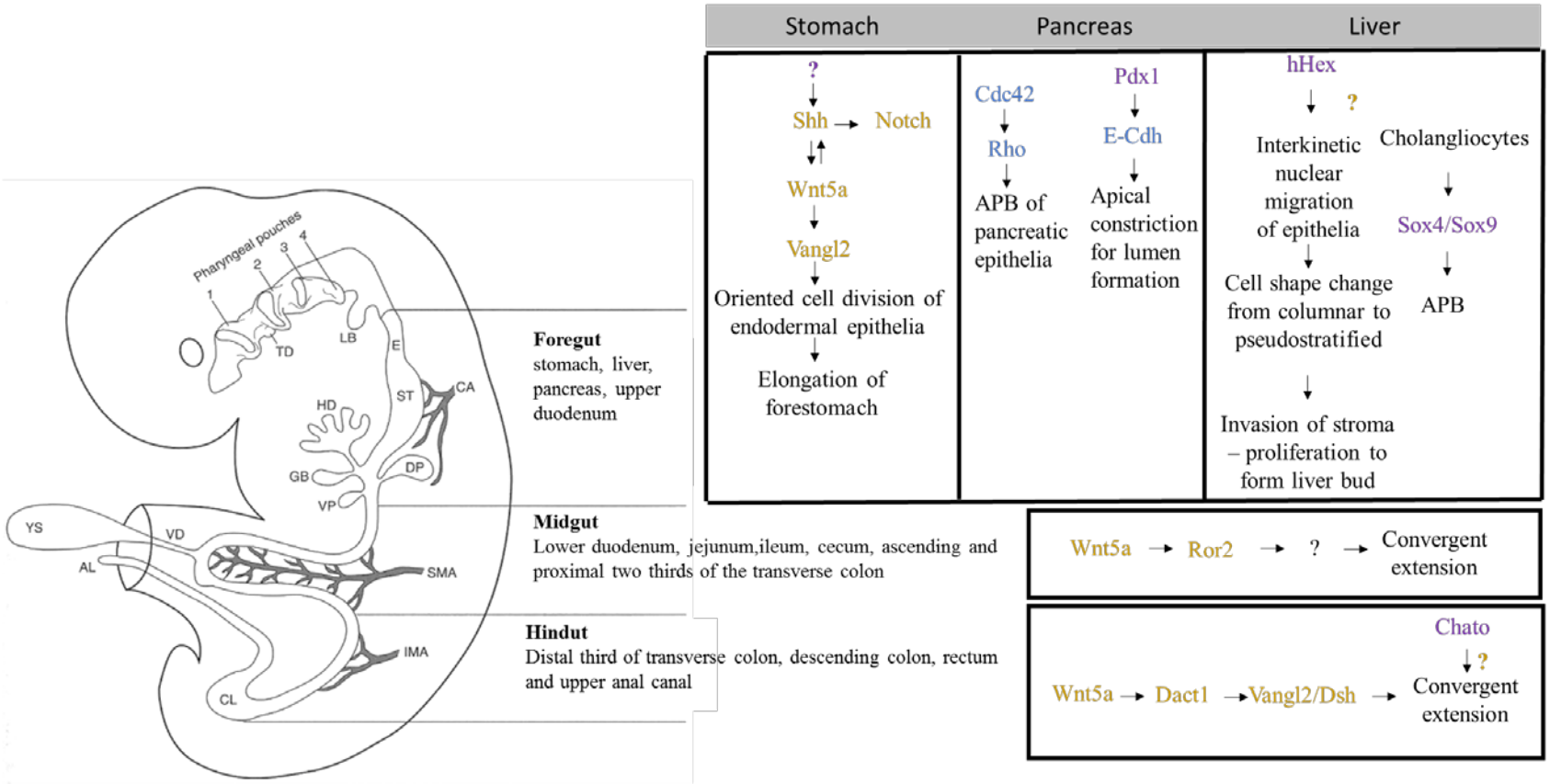

Figure 3.3: Outline of mechanisms involved in cranio-caudal morphogenesis of the GI tract and its accessory organs has been described next to the lateral view of the mammalian embryo at E11.0 (mouse) to show the relative positioning of the organs along the cranio-caudal axis. The transcription factors have been listed in purple, signaling molecules in brown and cytoskeletal effectors in blue. The expression of genes may extend before and after the specific stage shown.

duodenal elongation implicating PCP signaling as a driver of the duodenal elongation (Matsumoto A, 2002). While ECM molecules, such as fibronectin, are critical for epithelial integrity and polarity in the duodenum, the transcription factors and downstream players regulating convergent extension of the duodenum remain unknown.

At the midgut region, elongation of the gut tube results in manifold increase in the length of the gut tube within a short time compared to the crown-rump length of the embryo (Yamada M, 2010). Like the duodenum, the epithelial tube diameter of the midgut narrows as it elongates, suggesting similar mechanisms of convergent extension for elongation. In the midgut, non-canconical Wnt5a signaling is the master regulator of not only convergent extension but also polarity and proliferation of both the epithelia and mesenchyme. It also regulates re-intercalation of post-mitotic cells into the epithelium after cell division (Cervantes S, 2009). Furthermore, Ror2, a co-receptor for Wnt signaling, specifically regulates the rearrangement of the epithelia needed for the convergent extension in the midgut endoderm (Yamada M, 2010) (Figure 3.3).

The elongation of the hindgut endoderm also relies on convergent extension, where the non-canonical Wnt5a functions via Dact1 to regulate Vangl2 and Dsh for mediating convergent extension of the epithelia (Wen J, 2010). Chato, a KRAB zinc-finger protein, also controls convergent extension in the endoderm for the closure of gut tube. However, the downstream targets and the cellular mechanisms by which Chato causes this process remain to be uncovered (García-García MJ, 2008).

3.6.2 Regulation of cell shape changes during left-right morphogenesis of the GI tract

The first evidence of LR asymmetry in the gut involves a left-sided bulge and turn at the posterior end of the foregut that gives rise to the distinct, conserved shape of the stomach. Prior to the bulge, the lumen of the primitive stomach is aligned with symmetric walls with respect to the LR axis.

The initiation of stomach curvature is accompanied by an outward bend and lengthening of the left wall compared to the right wall (Davis A, 2017). Following the lengthening, a thinning of layers of the left stomach wall is observed compared to the right. This preferential bending, lengthening, and thinning of the left wall of the stomach is driven by LR asymmetric cell rearrangement (Davis A, 2017). Appearing concomitantly with these LR differences in cell rearrangement are asymmetries in apical-basal polarity of the endoderm.

Pitx2, a homeobox transcription factor and a master regulator of LR asymmetric organ morphogenesis, regulates these cell rearrangements as well as the endodermal polarities on the left wall to give rise to this curvature (Davis A, 2017) (Figure 3.4). However, the mechanisms downstream of Pitx2 remain to be elucidated.

At the midgut region, the gut tube undergoes a critical counterclockwise rotation initiated by a conserved leftward tilting of the gut tube. This leftward tilt is driven by changes across the LR axis in cell behavior and architecture of the epithelial and mesenchymal compartments of the adjoining dorsal mesentery (DM), a mesodermally-derived structure that suspends the gut tube from the body wall (Davis NM, 2008b; Hecksher-Sørensen J, 2004). Prior to the initiation of the tilt, the DM is symmetrical with a dense mesenchyme sandwiched by cuboidal epithelia. However, prior to the tilt, the left epithelial cells become columnar, the left mesenchymal cells become more compacted, the right mesenchymal cells become more sparsely distributed, and the right epithelial cells assume squamous morphology. Similar to the stomach, the left-sided expression of *Pitx2* regulates the changes in cellular behavior in both the left epithelia and mesenchyme (Kurpios NA, 2008b). In the left mesenchyme, Pitx2-specific effector Gpc3 integrates non-canonical Wnt5a signaling from the gut to activate the formin Daam2 in the left DM to stabilize cell-cell adhesion and cause compaction of the left mesenchymal compartment (Figure 3.4). Simultaneously, the

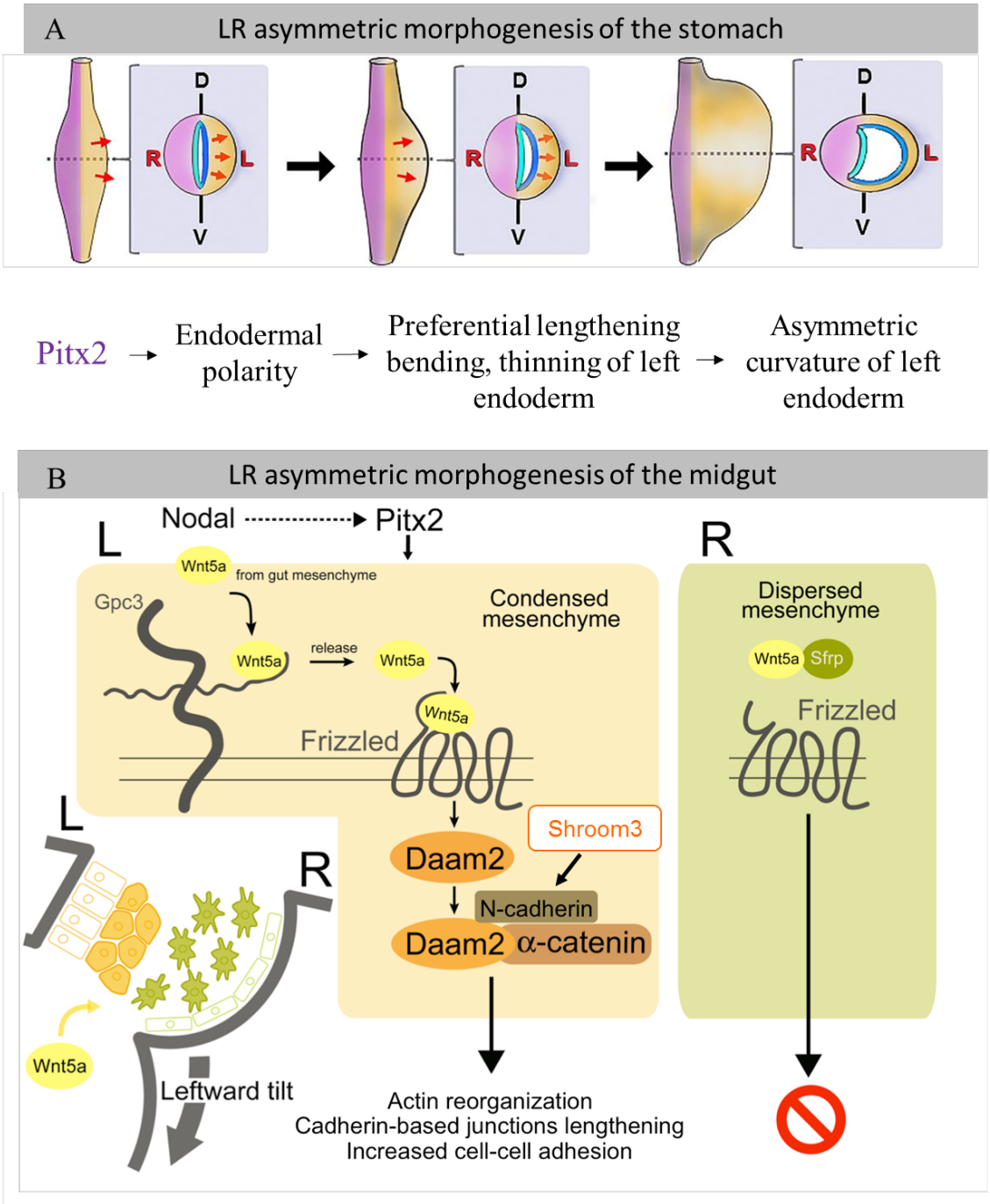

Figure 3.4: Left-right asymmetric pathways downstream of Pitx2 regulating cell shape changes during A) stomach and B) intestinal morphogenesis. Figures have been taken from (Davis A, 2017) and (Welsh IC, 2013).

cytoskeleton of the mesenchymal cells is reorganized such that they are polarized and oriented to the left across the LR axis (Welsh IC, 2013). Interestingly, this mesenchymal reorganization of the mesenchyme in the left DM is spatiotemporally linked with the maintenance and subsequent remodeling and patterning of gut specific arteries (Mahadevan A, 2014) suggesting a role for mesenchymal cell shape changes in gut arteriogenesis. In the left epithelia, loss of Pitx2 results in the formation of cuboidal instead of columnar epithelia. A similar phenotype is recaptured in embryos where Shroom3, a critical determinant of epithelial cell shape, is deleted. Interestingly, the expression of Shroom3 in the DM is not dependent on Pitx2. Rather, Shroom3 functions cooperatively with N-cadherin downstream of Pitx2 to directly regulate the epithelial cell shape changes in the left DM (Plageman TF Jr, 2011). However, the factors that regulate the shape changes and cellular organization within the right DM remain to be elucidated.

3.6.3 Cell shape changes during morphogenesis of the GI tract across the radial axis

During the process of radial patterning, the stomach endoderm invaginates into the submucosa to form deep invaginations termed crypts and glands. In contrast, the endoderm of the small intestine evaginates to form finger-like projections known as villi and crypts. Similar events take place in the colon where crypts form, but, instead of villi, a flat surface epithelium remains (Haffen K, 1987). Along the crypto-villous axis, cytodifferentiation of the gut epithelia forms the absorptive enterocytes and the secretory goblet, enteroendocrine, and Paneth cells (Barbara PS, 2003). This cytodifferentiation continues postnatal and is accompanied by shape change of the endoderm from cuboidal to pseudostratified to columnar epithelium, and is influenced by interactions with the underlying mesoderm, basement membrane proteins, and the regulators of apical-basal polarity (Sääf AM, 2007). However, the precise transcriptional regulation of this process, while widely studied in various disease conditions, remains underexplored during embryonic development.

In vitro studies using Caco-2 cells, which resemble the enterocytes lineage in morphology and function have provided a detailed genomic portrait of changes in transcript patterns during the establishment of enterocyte cell polarity. These studies have revealed that the transition from proliferating, non-polarized cells, to post-mitotic polarizing cells involves a switch in gene expression programs (Halbleib JM, 2007). While gene expression of Wnt targets is robust in mitotic non-polarized Caco-2 cells, it decreases over time as cells become post-mitotic and polarized, akin to the decreasing gradient of Wnt activity from the crypt to villi *in vivo*. After polarization, the decrease of Wnt gene expression is accompanied by an increase of β-catenin levels in the cell nucleus and is associated with TCF4 (Sääf AM, 2007). Furthermore, the transcriptional profiling has revealed a critical interplay between polarization and other signaling cascades such as the Tgfβ, Fgf, Shh, and Notch signaling pathways for which cellular details remain to be uncovered (Halbleib JM, 2007). In addition, it was also discovered that KLF4, a zinc finger transcription factor, regulates polarity-related genes, which include LKB1, EPHB2, and EPHB3 (Yu T, 2012). Thus, the Caco-2 cells serve as a useful *in vitro* model system to characterize the pathways and the regulation of cell shape changes during the differentiation of intestinal enterocytes along the radial axis.

3.6.4 Perspectives into the regulation of cell shape changes during morphogenesis of the GI tract

The events shaping gut morphogenesis are relatively understudied compared to the heart and lung, and hence comparatively less is known about the mechanisms underlying cell shape changes during early GI tract morphogenesis. Thehe current studies have made extensive use of the *in vitro* Caco-2 cell culture model system to characterize the pathways and the regulation of cell shape changes during intestinal epithelial differentiation into enterocytes along the radial axis. However,

in vivo, the endodermal epithelia differentiate not only into enterocytes but also into secretory cell types such as goblet cells, enterendocrine cells and panneth cells which have distinct cellular morphologies. Furthermore, the cytodifferentiation varies along the AP axis of the gut. Therefore, the mechanisms proposed by invitro studies fail to explain variation in the cell shapes of the other cell lineages during cytodifferentiation of the endodermal epithelia in vivo. Nevertheless, they have been useful in identifying the regulatory signaling pathways for enterocyte that the future studies can use for integrating the existing knowledge with the in vivo regulatory mechanisms.

Compared to the morphogenesis along the radial axis, the physiological relevance of the endodermal epithelial shape changes across the anterior-posterior axis are only beginning to be elucidated. Moreover, it is possible that there are significant variations in the regulation of cell shape changes across the A-P axis in different species due to differential elongation and morphogenesis of different regions of the GI tract. For instance, whereas the hindgut fermenters are known for their large colon and cecum, the ruminants and pseudo ruminants that are primarily foregut fermenters have multi-chambered stomach, known as the rumen (Cronjé P, 2000). Hence, the studies investigating regulatory mechanisms specific to cell shape changes along the AP axis should integrate analysis of multiple species to obtain a more complete understanding of the key transcriptional networks that are either common to different species or that are species-specific.

Despite the tremendous variation in intestinal looping topology observed among different animal species, within the same species the intestinal looping pattern is remarkably fixed (Davis NM, 2008a; Kurpios NA, 2008a; Savin T, 2011; Welsh IC, 2013) . Failure to follow the conserved pattern of gut looping leads to intestinal malrotation that predisposes to catastrophic midgut volvulus, where the malrotation results in contorted twisting of different segments of the gut tube resulting in strangulation of the gut tube and the accompanying blood vessels (Filston HC, 1981;

Torres AM, 1993) . Although our understanding of transcriptional regulation of the left-right asymmetric gut morphogenesis is still in its infancy, it is becoming clear that both the epithelial cell shape changes and the organization of the adjoining mesenchymal cells within the DM are essential to gut rotation. While current studies have mainly focused on understanding the mechanisms that orchestrate cell shape changes on the left side of the DM, almost nothing is known about the mechanisms that regulate the right side. Understanding the contribution from both sides of the DM is critical for developing techniques to diagnose and treat disease conditions associated with intestinal malrotations such as midgut volvulus.

3.7 Regulation of cell shape changes during development of the GI tract accessory organs

The accessory organs of the GI tract form as endodermal derivatives (diverticula) of the foregut and include the liver, the gall bladder, and the dorsal and ventral pancreas (Yin C, 2017). After hepatic specification regulated by members of the Sox family of transcription factors, the liver progenitor cells delaminate from the foregut endoderm and invade into the septum transversum mesenchyme to form the liver bud (Yin C, 2017). They subsequently differentiate into two epithelial cell types (hepatocytes and cholangiocytes), arranged into unique structures with distinct functions (Zaret KS, 2016). Further growth, morphogenesis, and differentiation during liver development are spatiotemporally regulated by numerous mechanisms (Figure 3.3).

The pancreas is a unique organ that functions as both an exocrine and an endocrine gland. It is composed of two morphologically distinct tissues. The exocrine domain contains digestive enzyme secreting cells, while the endocrine domain is arranged as Islets of Langerhans that are populated by hormone-producing cells (Fujitani Y, 2017). From specification of the pancreatic domain in the foregut endoderm to the formation of the functional exocrine and endocrine cell

types, pancreas development is a precisely orchestrated multi-stage process regulated by multiple signaling cascades (Larsen HL, 2017) (Figure 3.3).

3.7.1 Regulation of cell shape changes during liver development

The development of the liver initiates when signals from the mesothelial cells of the proepicardium and septum transversum specify the adjoining ventral domain of the anterior foregut to give rise to the hepatic diverticulum (Tremblay KD, 2005; Wilson JW, 1963). In mammals, the liver diverticulum formation involves three stages. In the first stage, elongation of the hepatic endodermal cells near sinus venosus causes the cuboidal epithelia to become columnar, resulting in the thickening of the endoderm (Bort R, 2006). The second stage involves interkinetic nuclear migration resulting in the transition of the columnar cells into a multilayer of pseudostratified cells called hepatoblasts. In the third stage, the basal laminin degrades and the hepatic endodermal cells delaminate, proliferate, and invade into the stroma forming the liver bud (Bort et al., 2006). While the cell-autonomous transcription factors that regulate the initial transition of cuboidal epithelia to columnar are unknown, hHex, a homeobox-containing transcription factor of the Antennapedia/Ftz class, is expressed in the foregut endoderm and specifically regulates the interkinetic nuclear migration to cause the cell shape transition from columnar to pseudostratified epithelium (Bort et al., 2006).

The formation of the liver bud is simultaneously accompanied by the remodeling of the adjacent endothelial cells that surround the liver diverticulum (Antoniou A, 2009). Subsequently, the hepatoblasts located further away from the portal vein differentiate into the hepatocyte lineage, the hepatoblasts located in close proximity to the portal vein differentiate into the cholangiocyte lineage (Carpentier R, 2011). While the Hippo pathway regulates the cellular architecture of

hepatocytes (Yimlamai D, 2014), the SRY-related High Mobility Group Box Transcription factors Sox 4, and Sox9 cooperatively set up the apical-basal polarity in the cholangiocyte lineages (Poncy A, 2015). However, the molecular mechanisms downstream of these transcripton factors that underlie the cell shape changes remain unknown. This information may provide novel therapeutic targets for chronic liver diseases for which the only current treatment is organ transplant.

3.7.2 Regulation of cell shape changes during pancreatic development

Pancreatic development initiates with the evagination of the dorsal gut endoderm in the posterior foregut into the surrounding condensed mesenchyme to give rise to the dorsal pancreatic bud. This is followed by evagination of the ventral endoderm in the posterior foregut caudal to the hepatic/biliary bud, resulting in the formation of the ventral pancreatic bud (Sussel, 2012). The epithelial-mesenchymal crosstalk that guides the endodermal evagination is modulated by Fgf signaling in the mesenchyme (Elghazi L, 2002).

At the onset of pancreatic bud formation, the dorsal gut endoderm is stratified and consists of an outer layer of semi-polarized cell types and an inner layer of unpolarized cells (Gittes GK, 2009). Following bud formation, the stalk elongates and initiates branching morphogenesis of the buds. This is accompanied by the transformation of the initially multilayered stratified epithelium into a single-layered polarized epithelium which invades and branches extensively into the underlying mesenchymal compartment (Fujitani Y, 2017). During this transition, small microlumens form between the epithelial cells. The rise of apical cell polarity in the epithelia results in the expansion of the microlumens to form independent luminal networks (Kesavan G, 2009). While the Cdc42-Rho signaling axis directly regulates the apical-basal polarity, the transcription factor Pdx1 drives E-cadherin to induce apical constriction necessary for lumen

formation and maintenance (Marty-Santos L, 2016). Subsequent displacement of the stomach and the duodenal looping results in the dorsal and ventral buds coming in close proximity. This is accompanied by coalescing of the dorsal and ventral luminal networks to form continuous tubular networks connect the ducts of the dorsal and ventral buds. Simultaneously, the glucagon-positive endocrine cells become converted to non-epithelial cells and lose connection with the lumen and ultimately coalesce into aggregates that represent the first islets of Langerhans, which consist of insulin-producing β-cells, glucagon-producing α-cells, somatostatin-producing δ-cells, pancreatic polypeptide-producing PP cells, and ghrelin-producing ε-cells. Moreover, the epithelial cells lining the duct undergo ductal and acinar differentiation to give rise to the fully functional pancreas. Very little is known regarding understanding of transcriptional regulation of cell shape changes that accompany the specification of the different cell lineages during pancreatic development. Such investigations may pave the way for understanding of how perturbation of these processes may lead to different forms of diabetes (Larsen HL, 2017).

3.8 Transcriptional regulation of cell shape changes during kidney development

The metanephric kidney is composed of epithelial tubules that function together with apposing endothelial capillaries and microvascular networks to purify the blood and maintain optimal blood chemistry (Carroll TJ, 2011). Development of the tubules initiate when epithelia of the mesonephric duct bud to form the ureteric bud (UB) surrounded by pre-specified intermediate mesoderm called the metanephric mesenchyme (MM) (Michos O, 2009; Saxén L, 1987). Interactions between the MM and UB induce the ureteric bud to undergo continued branching to give rise to the ureter, collecting ducts, major and minor calyces, and the renal pelvis (Figure 3.5) (Schedl A, 2007). At the same time, inductive signals produced by the ureteric bud stimulate a

subpopulation of metanephric mesenchyme to undergo mesenchymal to epithelial transition to form epithelial structures called the renal vesicles (Bertram JF, 2016) . The renal vesicles undergo a series of morphological changes transitioning through the comma and S-shaped body-structures, with distinct cellular populations giving rise to the various nephron segments (Figure 3.5). The most proximal segment is the renal corpuscle, followed by the proximal tubule, loop of Henle, distal tubule, and finally the connecting tubule that connects the distal tubule to the UB-derived collecting ducts (Dressler GR, 2006). Simultaneously, precursors of the vascular endothelial cells take their position at the tip of the renal tubules and differentiate into the cells of the definitive glomerulus. Extensive studies have characterized the regulators of cell behavior in the developing kidney (Carroll TJ, 2011; Lienkamp SS, 2012) (Michos O, 2009). An interplay between a variety of the signaling pathways regulates the cell shape changes with branching morphogenesis and tubulogenesis of the nephrons and the connecting duct. In the following sections, we explore the transcriptional regulators of these processes in the developing kidney (Figure 3.5).

3.8.1 Ureteric bud formation and early branching

Development of the metanephric kidney initiates when the UB grows out as a swelling originating in the caudal nephric duct (Michos O, 2009). This is a consequence of directed cell movements within the duct epithelium and is regulated via localized induction of *Ret* in the epithelia by GDNF, a secretory signaling molecule and *BMP4* expression in the metanephric mesenchyme (MM) (Pachnis V, 1993). Ret activates several downstream effectors pathways

Figure 3.5: Genes regulating cell shape changes during kidney morphogenesis. A growing number of transcription factors, the signaling networks and their downstream effectors have been identified in the mammalian kidney. These genes have been listed according to the processes that they are involved in. the transcription factors are in purple, signaling molecules in brown and cytoskeletal remodelers in blue. Figure modified from (Bertram JF, 2016)

Branching morphogenesis
Fzd4/8
Fgf7-10/Fgfr2
HGF/Met
Egf/Egfr2
Gdnf/Ret

Uteric bud induction and condensation
Pax2
Eya1
Six1
Hoxa11
Gata3
Hnf-β1
Ap2B
Gdnf/Ret interaction
Wnt9B
Fgf7-10/Fgfr2
Erk/MapK/Pi3K/AKT
Plcγ

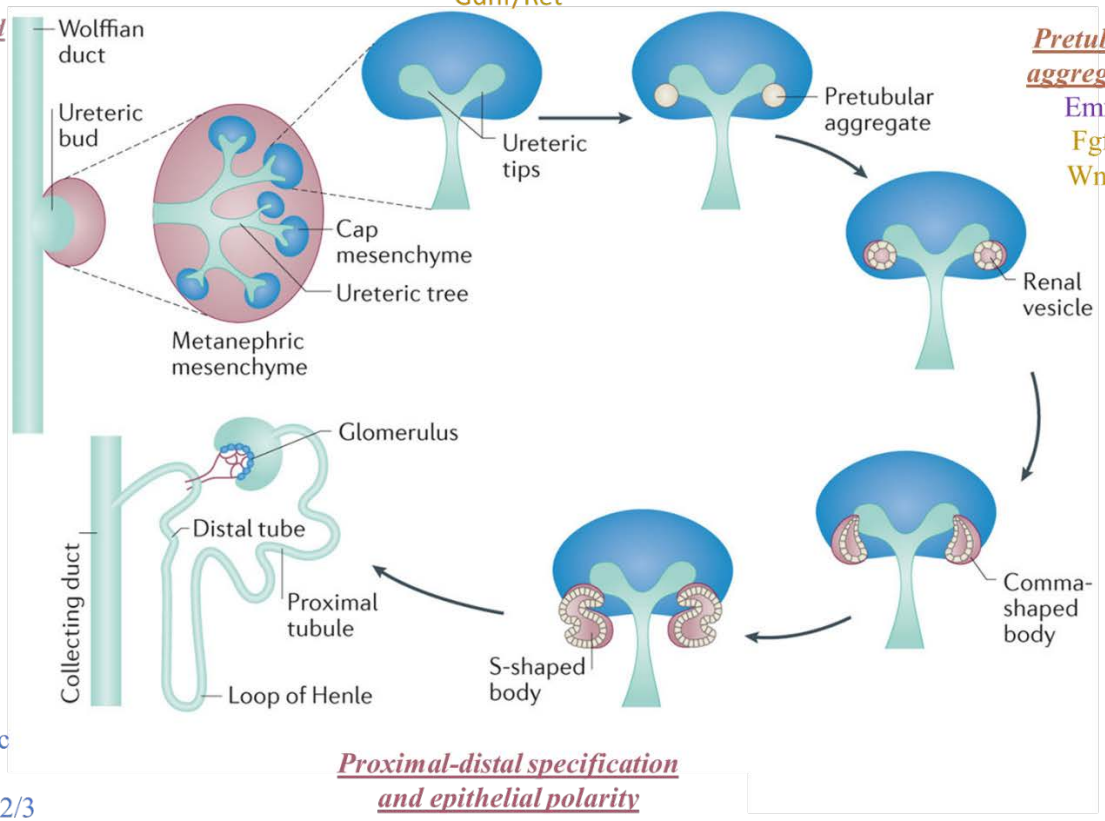

Pretubular aggregation
Emx2
Fgf8
Wnt4

Polarity of podocytes
Pax2
Wt1
Cdc42/Par3/Par6/α-Pkc
Crmbs/Pals1/Patj
Nephrin/Nck2/Wasp/Ark2/3

Proximal-distal specification and epithelial polarity
Yap
Notch/γ-secretase
Non-canonical Wnt9b
Wnt 7b, Vangl2, Fat4

including the ERK, MAPK, PI3Kinase/Akt, and PLC-γ pathways in the epithelia to regulate the directed cell movements needed for ureteric bud formation (Fisher CE, 2001; Jain S, 2006; Tang MJ, 2002). While the transcription factor Pax2 regulates the overall process of ND development and the early UB outgrowth (Brophy PD, 2001), the expression of *GDNF* in the MM is regulated by transcription factors Eya1 (Xu PX, 1999) and Hox11 and the expression of *Ret* in the epithelia is regulated by transcription factor Gata3 (Gong KQ, 2007; Grote D, 2008). The expression of *GDNF* in MM is also maintained and reinforced by expression of *Wnt11* (Majumdar A, 2003), which in turn is regulated by the canonical Wnt/β-catenin signaling pathway downstream of Wnt9b (Karner CM, 2011). The transcription factors HNFβ1 (Paces-Fessy M, 2012) and Ap-2 B (Moser M, 1997) regulate the expression of *Wnt9b* during the UB formation and outgrowth. Following the outgrowth, the UB undergoes a characteristic T-shaped branching regulated by PCP components Fzd4 and Fzd8 (Figure 3.5) (Ye X, 2011). In addition, Fgf7-10 /Fgfr2, and the synergistic interaction of the HGF/Met and Egf/Egfr pathways also play a critical role during branching morphogenesis (Sakurai H, 1997). These pathways may act in parallel or sequentially to Ret/GDNF signaling but additional studies are required to identify the relevant cellular interactions and the transcriptional mechanisms that integrate the different signaling networks to orchestrate ureteric branching morphogenesis.

3.8.2 Renal vesicle induction and morphogenesis of the segments of the nephron

As the tip cells bifurcate, *Wnt4*, *Fgf8*, and *Pax8*, expressed by the Six2+ lineage of mesenchymal cells in the MM surrounding the UB tip, initiate the formation of pre-tubular cellular aggregates that undergo mesenchymal epithelial transition (Metzger RJ) to form renal vesicles (Schmidt-Ott KM, 2008). Once the epithelial renal vesicle is formed, it further elongates and transitions into the comma and S-shaped bodies. The distal end of the S-shaped body fuses with the UB while the

remaining parts become specified to generate the proximal and distal tubules of the nephron (Schedl A, 2007). The transcriptional regulator of the Hippo pathway, Yap, regulates the distal fusion of the S-shaped body to the UB while the apical localization of Yap is regulated by Cdc42 (Reginensi A, 2013). At the proximal end, Notch/γ-secretase signaling is necessary for development of the proximal tubular and glomerular segments (Cheng HT, 2005). As the proximal-distal specification occurs, the cuboidal epithelial cells in the tubules elongate perpendicular to the proximal-distal axis of the tubule, and undergo rosette-based cell intercalation (Lienkamp SS, 2012). The non-canonical PCP pathway downstream of Wnt9b drives the myosin dependent rosette-based cell intercalation and regulates polarized cell division to cause elongation of tubules by convergent extension (Karner CM, 2009; Lienkamp SS, 2012). Concomitant with tubulogenesis, different segments of the nephron undergo a series of complex changes that are Rho-kinase activity dependent including segmentation, elongation and morphogenesis (Lindström NO, 2013).

A key feature of the proximal tubule development is the differentiation of the epithelial precursors in the proximal cleft of the S-shaped body to form podocytes, which are polarized renal glomerular cells that play a central role in regulating the formation of the glomerular ultrafiltrate. Accompanying this differentiation is a dynamic change in cell shape of the epithelia (Mundel, 2012). The specification of the podocyte precursors is thought to occur at the preceding comma body stage when the cuboidal epithelial cells acquire a columnar morphology. As the comma body evolves into the S-shaped body, the intrusion of endothelium and the formation of capillary loops due to VEGF signaling in the surrounding MM causes dramatic expansion of the apical surface of the epithelia (Schell C, 2014). This is accompanied by migration of cell-cell junctions from apical to basal aspect of the cell followed by restructuring and replacement of tight junctions with sieve-

like junctional complexes called slit diaphragms (Grahammer F, 2013). The polarity in podocyte differentiation is regulated by three main polarity complexes: the apical Crumbs complex (Crumbs, PALS1 and PATJ) identified by a genetic screen in zebrafish podocyte formation (Ebarasi L, 2009; Pieczynski J, 2011); the apical Cdc42/Par3/Par6/αPKC polarity complex as evidenced by several studies (Hartleben B, 2008; Hartleben B, 2013; Rizaldy P. Scott, 2012); and the Nephrin/Nck2/n-WASP/Ark2/3 pathway (Laura AN, 2013; Schell C, 2013). The differentiation of podocytes is regulated by the interplay between Pax2 and Wt1, which are regulators of the transcriptional network for podocyte development (Guo JK, 2002; Kobayashi N, 2004). However, the downstream factors of these genes that regulate the polarity complexes in a cell-autonomous manner remain to be elucidated.

As the proximal and distal components form, they are spatially organized in the cortico-medullary axis. While the renal corpuscles and the proximal and distal tubules are located in the cortex, the Loop of Henle and the elongated tubular network of the collecting duct system constitute the renal medulla (Little MH, 2007). In the medulla, the tubular elongation and the growth of Loop of Henle is regulated by paracrine canonical Wnt signaling via Wnt7b. In Wnt7b mutant mice , cell division planes of the collecting duct epithelium are biased along the radial axis as opposed to bias along the longitudinal axis normally observed in WT mice (Jing Yu, 2009). Interestingly, a similar loss of the medullary region has been documented in Vangl2 and Fat4 mutant mice in addition to reduced tubular formation (Yates LL, 2010), indicating that components of the core PCP network might function alongside the canonical Wnt7b signaling to drive tubulogenesis and tubular organization in the medulla.

3.8.3 Insights into regulation of cell shape changes during kidney morphogenesis

The elegant mechanisms that regulate the cell shape changes during kidney morphogenesis are better understood when compared to other organ systems of the abdominal viscera. It has been clearly established that the epithelial cell shape changes and cell polarity play a critical role throughout the development and functioning of the nephrons, from early stages of morphogenesis to the later stages of differentiation across proximal-distal axis. The perturbation of cell polarity, cell shape, and tubular dilations have been implicated in polycystic kidney disease (PKD) conditions. However, at present, it is unclear to what extent are the observed defective polarities causative or secondary consequences of the disease condition. Furthermore, the exact roles of the cytogenesis genes (implicated in PKD, kidney injury conditions in humans) in the spatiotemporal morphogenesis of the kidney remain unknown. One way of investigating would be to understand how abrogation of polarities of different cell lineages affects kidney development using conditional knockout mice. The presence of such models coupled with the transgenic reporter mice labeling specific cell types could facilitate dynamic analysis of cell shape changes during tubule formation, extension and active determination of the relationship between cell shape and kidney malformations. The interactions between the mesenchymal stroma and the epithelia is well understood during UB outgrowth. However, studies investigating the later aspects of kidney development such as formation of renal vesicle, S shaped bodies, and comma bodies have mainly focused on the epithelial cell behaviors. Hence the mechanisms that regulate the cellular behaviors and differentiation of mesenchymal cells in stroma to give rise to kidney-specific vasculature, neuronal and muscles are understudied and warrants further investigations.

3.9 Conclusion

Now is an exciting time for studying the transcriptional regulation underlying cell shape changes during organogenesis. Substantial questions and unknowns that need to be answered exists in the field and have been raised at the end of each section as perspectives. In this review, anatomic details and details pertaining to extracellular space such as cell matrix interactions have been omitted whenever possible to give emphasis to essentialities. The combination of forward and reverse genetics with a multi species approach and the advent of sensitive transcriptomic and proteomic analysis methods, including single-cell RNA-seq and tissue mass imaging spectrometry are likely to provide detailed integrated insights into molecular and cellular mechanisms during organogenesis which will hopefully result in better diagnostics and eventually new therapies to treat the wide spectrum of malformations that can result in life threatening debilitating disorders.

3.10 References

Ahmed HK , A.-A.D., Buckley S,Tokumitsu H, Bellusci S, Warburton D. (2011). Eya1 controls cell polarity, spindle orientation, cell fate and Notch signaling in distal embryonic lung epithelium. Development *138*, 1395-1407.

Antoniou A, R.P., Cordi S, Zong Y, Tronche F, Stanger BZ, Jacquemin P, Pierreux CE, Clotman F, Lemaigre FP. (2009). Intrahepatic bile ducts develop according to a new mode of tubulogenesis regulated by the transcription factor SOX9. Gastroenterology *136*, 2325-2333.

Bakkers J, K.C., Pothof J, Quaedvlieg NE, Spaink HP, Hammerschmidt M. (2004). Has2 is required upstream of Rac1 to govern dorsal migration of lateral cells during zebrafish gastrulation. Development *131*, 525-537.

Barbara PS, D.-B.G., Roberts DJ (2003). Development and differentiation of the intestinal epithelium. Cell Mol Life Sci *60*, 1322-1332.

Barnes RM, H.I., Jaehnig EJ, Sauls K, Sinha T, Rojas A, Schachterle W, McCulley DJ, Norris RA, Black BL. (2016). MEF2C regulates outflow tract alignment and transcriptional control of Tdgf1. Development *143*, 774-779.

Bertram JF, G.S., Pape L, Schaefer F, Shroff RC,Warady BA (2016). Kidney disease in children: latest advances and remaining challenges. Nature reviews nephrology *12*, 182-191.

Bort, R., Signore, M., Tremblay, K., Martinez Barbera, J.P., and Zaret, K.S. (2006). Hex homeobox gene controls the transition of the endoderm to a pseudostratified, cell emergent epithelium for liver bud development. Dev Biol *290*, 44-56.

Bort R, S.M., Tremblay K, Martinez Barbera JP, Zaret KS. (2006). Hex homeobox gene controls the transition of the endoderm to a pseudostratified, cell emergent epithelium for liver bud development. Dev Biol *290*, 44-56.

Brophy PD, O.L., Lang KM, Dressler GR. (2001). Regulation of ureteric bud outgrowth by Pax2-dependent activation of the glial derived neurotrophic factor gene. Development *128*, 4747-4756.

Carpentier R, S.R., Hul NV, Kopp JL, Beaudry JB, Cordi S, Antoniou A, Raynaud P, Lepreux S, Jacquemin P, Leclercq IA, Sander M, Lemaigre FP (2011). Embryonic Ductal Plate Cells Give Rise to Cholangiocytes, Periportal Hepatocytes and Adult Liver Progenitor Cells. Gastroenterology *141*, 1432-1438.

Carroll TJ, D.A. (2011). Planar cell polarity in kidney development and disease. Organogenesis *7*, 180-190.

Cervantes S, Y.T., Hebrok M. (2009). Wnt5a is essential for intestinal elongation in mice. Dev Biol *326*, 285-294.

Chalmers AD, S.J. (2000). The Xenopus tadpole gut: fate maps and morphogenetic movements. Development *127*, 381-392.

Chen L, F.F., Ferrentino R, Martucciello S, Illingworth EA, Baldini A. (2012). Transcriptional control in cardiac progenitors: Tbx1 interacts with the BAF chromatin remodeling complex and regulates Wnt5a. PLoS Genet *8*.

Cheng HT, K.R. (2005). The role of Notch signaling in specification of podocyte and proximal tubules within the developing mouse kidney. Kidney Int *68*, 1951-1952.

Chiapparo G, L.X., Lescroart F, Chabab S,Paulissen C,Pitisci L,Bondue A,Blanpain C. (2016). Mesp1 controls the speed, polarity, and directionality of cardiovascular progenitor migration. J Cell Biol *213*, 463-477.

Choudhry P, T.N. (2013). DiGeorge syndrome gene tbx1 functions through wnt11r to regulate heart looping and differentiation. PLoS One *8*.

Cronjé P, B.E. (2000). Ruminant Physiology: Digestion, Metabolism, Growth, and Reproduction (Wallingford, Oxfordshire, UK: CABI Pub., 2000).

Davis A, A.N., Johnson C, Bagley K, Ghashghaei HT, Nascone-Yoder N (2017). Stomach curvature is generated by left-right asymmetric gut morphogenesis. Development *144*, 1477-1483.

Davis NM, K.N., Sun X, Gros J, Martin JF, Tabin CJ. (2008a). The chirality of gut rotation derives from left-right asymmetric changes in the architecture of the dorsal mesentery. Dev Cell *15*, 134-145.

Davis NM, K.N., Sun X, Gros J, Martin JF, Tabin CJ. (2008b). The chirality of gut rotation derives from left-right asymmetric changes in the architecture of the dorsal mesentery. Dev Cell *15*, 134-145.

Dressler GR (2006). The cellular basis of kidney development. Annu Rev Cell Dev Biol *22*, 509-529.

Ebarasi L, H.L., Hultenby K, Takemoto M, Betsholtz C, Tryggvason K, Majumdar A. (2009). A reverse genetic screen in the zebrafish identifies crb2b as a regulator of the glomerular filtration barrier. Dev Biol *334*, 1-9.

Elghazi L, C.-M.C., Czernichow P, Scharfmann R (2002). Role for FGFR2IIIb-mediated signals in controlling pancreatic endocrine progenitor cell proliferation. Proc Natl Acad Sci U S A *99*, 3884-3889.

Elsum I, Y.L., Humbert PO, Richardson HE (2012). The Scribble-Dlg-Lgl polarity module in development and cancer: from flies to man. Essays Biochem *53*, 141-168.

Filston HC, K.D. (1981). Malrotation - the ubiquitous anomaly. J Pediatr Surg *16*, 614-620.

Fisher CE, M.L., Barnett MW, Davies JA. (2001). Erk MAP kinase regulates branching morphogenesis in the developing mouse kidney. Development *128*, 4329-4338.

Fujitani Y (2017). Transcriptional regulation of pancreas development and β-cell function. Endocr J.

García-García MJ, S.M., Anderson KV. (2008). Chato, a KRAB zinc-finger protein, regulates convergent extension in the mouse embryo. Development *135*, 3053-3062.

Gittes GK (2009). Developmental biology of the pancreas: a comprehensive review. Dev Biol *326*, 4-35.

Glickman NS, Y.D. (2002). Cardiac development in zebrafish: coordination of form and function. Semin Cell Dev Biol *13*, 507-513.

Gong KQ, Y.A., Sun H, Dressler GD, and Wellik DM (2007). A Hox-Eya-Pax Complex Regulates Early Kidney Developmental Gene Expression. Mol Cell Biol *27*, 761-7668.

Grahammer F, S.C., Huber TB. (2013). The podocyte slit diaphragm--from a thin grey line to a complex signalling hub. Nat Rev Nephrol *9*, 587-598.

Grote D, B.S., Souabni A, Merkel C, Chi X, Costantini F, Carroll T, Bouchard M. (2008). Gata3 acts downstream of beta-catenin signaling to prevent ectopic metanephric kidney induction. PLoS Genet *4*.

Guo JK, M.A., Gubler MC, Clarke AR, Harrison D, Hammes A, Hastie ND, Schedl A. (2002). WT1 is a key regulator of podocyte function: reduced expression levels cause crescentic glomerulonephritis and mesangial sclerosis. Hum Mol Genet *11*, 651-659.

Haffen K, K.M., Simon-Assmann P. (1987). Mesenchyme-dependent differentiation of epithelial progenitor cells in the gut. J Pediatr Gastroenterol *6*, 14-23.

Halbleib JM, S.A., Brown PO, Nelson WJ. (2007). Transcriptional modulation of genes encoding structural characteristics of differentiating enterocytes during development of a polarized epithelium in vitro. Mol Bio Cell *18*, 4261-4278.

Hartleben B, S.H., Lübben P, Bartram MP, Möller CC, Herr R, Wei C, Neumann-Haefelin E, Schermer B, Zentgraf H, Kerjaschki D, Reiser J, Walz G, Benzing T, Huber TB. (2008). Neph-Nephrin proteins bind the Par3-Par6-atypical protein kinase C (aPKC) complex to regulate podocyte cell polarity. J biol Chem *283*, 23033-23038.

Hartleben B, W.E., Suhm M, Worthmann K, Schell C, Helmstädter M, Wiech T, Walz G, Leitges M, Schiffer M, Huber TB. (2013). aPKCλ/ι and aPKCζ contribute to podocyte differentiation and glomerular maturation. J Am Soc Nephrol *24*, 253-267.

Hashimoto S, C.H., Que J, Brockway BL, Drake JA, Snyder JC, Randell SH, Stripp BR (2012). Sox2 is important for two crucial processes in lung development: Branching morphogenesis and epithelial cell differentiation. J Cell Sci *125*, 932-942.

Hecksher-Sørensen J, W.R., Lettice LA, Serup P, Eley L, De Angelis C, Ahlgren U, Hill RE. (2004). The splanchnic mesodermal plate directs spleen and pancreatic laterality, and is regulated by Bapx1/Nkx3.2. Development *131*, 4665-4675.

Herriges M, M.E. (2014). Lung development: orchestrating the generation and regeneration of a complex organ. Development *141*, 502-513.

Hirose T, K.M., Sugitani Y, Fujisawa M, Akimoto K, Ohno S, Noda T (2006). PAR3 is essential for cyst-mediated epicardial development by establishing apical cortical domains. Development *133*, 1389-1398.

Hirschy A, S.F., Ehler E, Perriard JC. (2006). Establishment of cardiac cytoarchitecture in the developing mouse heart. Dev Biol *289*, 430-441.

Holtzman NG, S.J., Tsai HJ, Yelon D. (2007). Endocardium is necessary for cardiomyocyte movement during heart tube assembly. Development *134*, 2379-2386.

Jain S, E.M., Johnson EM Jr, Milbrandt J. (2006). Critical and distinct roles for key RET tyrosine docking sites in renal development. Genes Dev *20*, 321-333.

JB Wallingford (2012). Planar cell polarity and the developmental control of cell behavior in vertebrate embryos. Annu Rev Cell Dev Biol *28*, 627-653.

Jing Yu, T.J.C., 1 Jay Rajagopal, Akio Kobayashi, Qun Ren, and Andrew P. McMahon (2009). A Wnt7b-dependent pathway regulates the orientation of epithelial cell division and establishes the cortico-medullary axis of the mammalian kidney. Development *136*, 161-171.

Kadzik RS, C.E., Morley MP, Stewart KM, Lu MM, Morrisey EE (2014). Wnt ligand/Frizzled 2 receptor signaling regulates tube shape and branch-point formation in the lung through control of epithelial cell shape. Proc Natl Acad Sci U S A *111*, 12444-12449.

Karner CM, C.R., Aoki S, Igarashi P, Wallingford JB, Carroll TJ. (2009). Wnt9b signaling regulates planar cell polarity and kidney tubule morphogenesis. Nat Genet *41*, 793-799.

Karner CM, D.A., Ma Z, Self M, Chen C, Lum L, Oliver G, Carroll TJ. (2011). Canonical Wnt9b signaling balances progenitor cell expansion and differentiation during kidney development. Development *138*, 1247-1257.

Karner CM, W.K.J., Carroll TJ. (2006). Planar cell polarity and vertebrate organogenesis. Semin Cell Dev Biol *17*, 194-203.

Kesavan G, S.F., Greiner TU, Johansson JK, Kobberup S, Wu X, Brakebusch C, Semb H. (2009). Cdc42-mediated tubulogenesis controls cell specification. Cell *139*, 791-801.

Kobayashi N, G.S., Chen J, Saito K, Miyawaki K, Li CY, Pan L, Saito S, Terashita T, Matsuda S. (2004). Process formation of the renal glomerular podocyte: is there common molecular machinery for processes of podocytes and neurons? Anat Sci Int *79*, 1-10.

Kuo CT, M.E., Anandappa R, Sigrist K, Lu MM, Parmacek MS, Soudais C, Leiden JM. (1997). GATA4 transcription factor is required for ventral morphogenesis and heart tube formation. Genes Dev *11*, 1048-1060.

Kurpios NA, I.M., Davis NM, Lui W, Katz T, Martin JF, Izpisúa Belmonte JC, Tabin CJ. (2008a). The direction of gut looping is established by changes in the extracellular matrix and in cell:cell adhesion. Prot Natl Acad Sci USA *105*, 8499-8506.

Kurpios NA, I.M., Davis NM, Lui W, Katz T, Martin JF, Izpisúa Belmonte JC, Tabin CJ. (2008b). The direction of gut looping is established by changes in the extracellular matrix and in cell:cell adhesion. Proc Natl Acad Sci U S A *105*, 8499-8506.

Larsen HL, G.-B.A. (2017). The molecular and morphogenetic basis of pancreas organogenesis. Semin Cell Dev Biol *2017*.

Laura AN, A.K.C., and Nina Jones (2013). Direct Regulation of Nephrin Tyrosine Phosphorylation by Nck Adaptor Proteins. J Biol Chem *288*, 1500-1510.

Laura LY, C.S., Lee Hazelwood, Lauren Chessum, Anju Paudyal, Helen Hilton, M. Rosario Romero, Jonathan Wilde, Debora Bogani, Jeremy Sanderson, Caroline Formstone, Jennifer N. Murdoch, Lee A. Niswander, Andy Greenfield,Charlotte H. Deana (2013). Scribble is required for normal epithelial cell–cell contacts and lumen morphogenesis in the mammalian lung. Dev Biol *373*, 267-280.

Lecuit T, L.P. (2007). Cell surface mechanics and the control of cell shape, tissue patterns and morphogenesis. Nat Rev Mol Cell Biol *8*, 633-644.

Lienkamp SS, L.K., Karner CM, Carroll TJ, Ronneberger O, Wallingford, JB, Walz G. (2012). Vertebrate kidney tubules elongate using a planar cell polarity-dependent, rosette-based mechanism of convergent extension. Nat Genet *44*, 1382-1387.

Lindström NO, H.P., Davies JA. (2013). Nephrons require Rho-kinase for proximal-distal polarity development. Sci Rep *3*, 2692.

Little MH, B.J., Georgas K, Davies JA, Davidson DR, Baldock RA, Beverdam A, Bertram JF, Capel B, Chiu HS, Clements D, Cullen-McEwen L, Fleming J, Gilbert T, Herzlinger D, Houghton D, Kaufman MH, Kleymenova E, Koopman PA, Lewis AG, McMahon AP, Mendelsohn CL, Mitchell EK, Rumballe BA, Sweeney DE, Valerius MT, Yamada G, Yang Y, Yu J. (2007). A high-resolution anatomical ontology of the developing murine genitourinary tract. Gene Expr Patterns *7*, 680-699.

Macara, I. (2004). Par proteins: partners in polarization. Curr Biol *14*, R160-162.

Mahadevan A, W.I., Sivakumar A, Gludish DW, Shilvock AR, Noden DM, Huss D, Lansford R, Kurpios NA (2014). The left-right Pitx2 pathway drives organ-specific arterial and lymphatic development in the intestine. Dev Cell *31*, 690-706.

Mahoney JE, M.M., Szymaniak AD, Varelas X, Cardoso WV. (2014). The hippo pathway effector Yap controls patterning and differentiation of airway epithelial progenitors. Dev Cell *30*, 137-150.

Majumdar A, V.S., Kispert A, McMahon J, McMahon AP. (2003). Wnt11 and Ret/Gdnf pathways cooperate in regulating ureteric branching during metanephric kidney development. Development *130*, 3175-3185.

Martinez-Estrada OM, L.L., Essafi A, Guadix JA, Slight J, Velecela V, Hall E, Reichmann J, Devenney PS, Hohenstein P, Hosen N, Hill RE, Munoz-Chapuli R, Hastie ND. (2010). Wt1 is

required for cardiovascular progenitor cell formation through transcriptional control of Snail and E-cadherin. Nat Genet *42*, 89-93.
Marty-Santos L, C.O. (2016). Pdx1 regulates pancreas tubulogenesis and E-cadherin expression. Development *143*, 101-112.
Matsumoto A, H.K., Yoshioka T, Otani H. (2002). Occlusion and subsequent re-canalization in early duodenal development of human embryos: integrated organogenesis and histogenesis through a possible epithelial-mesenchymal interaction. Anat Embryol (Berl) *205*, 53-65.
Matsuyama M, A.S., Shimono A. (2009). Sfrp controls apicobasal polarity and oriented cell division in developing gut epithelium. PLoS Genet *5*, e1000427.
McGrath PS, W.J. (2015). SnapShot: GI tract development. Cell *161*, 176-176 e171.
Mellman I, N.W. (2008). Coordinated protein sorting, targeting and distribution in polarized cells. Nat Rev Mol Cell Biol *9*, 833-845.
Metzger RJ, K.O., Martin GR, Krasnow MA. (2008). The branching programme of mouse lung development. Nature *453*, 745-750.
Michos O (2009). Kidney development: from ureteric bud formation to branching morphogenesis. Curr Opin Genet Dev *19*, 484-490.
Mjaatvedt CH, N.T., Moreno-Rodriguez R, Norris RA, Kern MJ, Eisenberg CA, Turner D, Markwald RR (2001). The outflow tract of the heart is recruited from a novel heart-forming field. Dev Biol *238*, 97-109.
Moeller H, J.A., Schaeffer HJ, Schwarz-Romond T, Mlodzik M, Hammerschmidt M, Birchmeier W. (2006). Diversin regulates heart formation and gastrulation movements in development. Proc Natl Acad Sci U S A *103*, 1590-15905.
Moorman A, W.S., Brown NA, Lamers W, and Anderson RH (2003). DEVELOPMENT OF THE HEART: (1) FORMATION OF THE CARDIAC CHAMBERS AND ARTERIAL TRUNKS. Heart *89*, 806-814.
Moorman AF, C.V. (2003). Cardiac chamber formation: development, genes, and evolution. Physiol Rev *83*, 1223-1267.
Moser M, P.A., Roth C, Becker J, Mücher G, Zerres K, Dixkens C, Weis J, Woodford LG, Buettner R, Fässler R (1997). Enhanced apoptotic cell death of renal epithelial cells in mice lacking transcription factor AP-2β. Genes Dev *11*, 1938-1948.

Mundel, A.G.a.P. (2012). Cell Biology and Pathology of Podocytes. Annu Rev Physiol *74*, 299-323.

Mutze K, V.S., Milosevic J, Eickelberg O, Königshoff M (2015). Enolase 1 (ENO1) and protein disulfide-isomerase associated 3 (PDIA3) regulate Wnt/β-catenin-driven trans-differentiation of murine alveolar epithelial cells. Dis Model Mech *8*, 877-890.

Nagy I, R.A., Rapila R, Hast T, Sormunen R, Tavi P, Räsänen J, Vainio SJ. (2010). Wnt-11 signalling controls ventricular myocardium development by patterning N-cadherin and beta-catenin expression. Cardiovasc Res *85*, 100-109.

Paces-Fessy M, F.M., Lesaulnier C, Cereghini S. (2012). Hnf1b and Pax2 cooperate to control different pathways in kidney and ureter morphogenesis. Hum Mol Genet *21*, 3143-3155.

Pachnis V, M.B., Costantini F. (1993). Expression of the c-ret proto-oncogene during mouse embryogenesis. Development *119*, 1005-1017.

Passer D, v.d.V.A., Atmanli A, Domian IJ (2016). Atypical Protein Kinase C-Dependent Polarized Cell Division Is Required for Myocardial Trabeculation. Cell Rep *14*, 1662-1672.

Phillips HM, H.V., Peat JD, Murdoch JN, Kobayashi K, Chaudhry B, Henderson DJ. (2008). Non-cell-autonomous roles for the planar cell polarity gene Vangl2 in development of the coronary circulation. Circ Res *102*, 615-623.

Pieczynski J, M.B. (2011). Protein complexes that control renal epithelial polarity. Am J Physiol Renal Physiol *300*, F589-601.

Plageman TF Jr, Z.A., Gage PJ, Lang RA. (2011). Shroom3 and a Pitx2-N-cadherin pathway function cooperatively to generate asymmetric cell shape changes during gut morphogenesis. Dev Biol *357*, 227-234.

Poncy A, A.A., Cordi S, Pierreux CE, Jacquemin P, Lemaigre FP. (2015). Transcription factors SOX4 and SOX9 cooperatively control development of bile ducts. Dev Biol *404*, 136-148.

Rajagopal J, C.T., Guseh JS, Bores SA, Blank LJ, Anderson WJ, Yu J, Zhou Q, McMahon AP, Melton DA (2008). Wnt7b stimulates embryonic lung growth by coordinately increasing the replication of epithelium and mesenchyme. Development *135*, 1625-1634.

Raya A, I.B.J. (2006). Left-right asymmetry in the vertebrate embryo: from early information to higher-level integration. Nat Rev Genet *7*, 283-293.

Reed RA, W.M., Dush MK, Tull RR, Bloom SK, Morckel AR, Devlin EW, Nascone-Yoder NM. (2009). Morphogenesis of the primitive gut tube is generated by Rho/ROCK/myosin II-mediated endoderm rearrangements. Dev Dyn *238*, 3111-3125.

Reginensi A, S.R., Gregorieff A, Bagherie-Lachidan M, Chung C,Dae-Sik L, Pawson T, Wrana J, McNeill H (2013). Yap- and Cdc42-Dependent Nephrogenesis and Morphogenesis during Mouse Kidney Development. PLoS Genet *9*.

Rizaldy P. Scott, S.P.H., Julie Ruston, Jianmei Du, Cord Brakebusch, Nina Jones, and Tony Pawson (2012). Podocyte-Specific Loss of Cdc42 Leads to Congenital Nephropathy. J Am Soc Nephrol *23*, 1149-1154.

Roberts DJ (1999). Embryology of the gastrointestinal ract (Hamilton, Ont. , London: BC Decker).

Rohr S, N.B.-A., Salim Abdelilah-Seyfried (2006). Heart and soul/PRKCi and nagie oko/Mpp5 regulate myocardial coherence and remodeling during cardiac morphogenesis. Development *133*.

Rohr S, O.C., Abdelilah-Seyfried S. (2008). Asymmetric involution of the myocardial field drives heart tube formation in zebrafish. Circ Res *102*.

Sääf AM, H.J., Chen X, Yuen ST, Leung SY, Nelson WJ, Brown PO. (2007). Parallels between global transcriptional programs of polarizing Caco-2 intestinal epithelial cells in vitro and gene expression programs in normal colon and colon cancer. Mol Biol Cell *18*, 4245-4260.

Sakurai H, T.T., Kjelsberg CA, Cantley LG, Nigam SK. (1997). EGF receptor ligands are a large fraction of in vitro branching morphogens secreted by embryonic kidney. Am J Physiol *273*, F463-472.

Savin T, K.N., Shyer AE, Florescu P, Liang H, Mahadevan L, Tabin CJ. (2011). On the growth and form of the gut. Nature *476*, 57-62.

Saxén L (1987). Organogenesis of the kidney (Cambridge: Cambridge university press).

Schedl A (2007). Renal abnormalities and their developmental origin. Nat Rev Genet *8*, 791-802.

Schell C, B.L., Salou S, Conzelmann AC, Meyer C, Helmstädter M, Wrede C, Grahammer F, Eimer S, Kerjaschki D, Walz G, Snapper S, Huber TB. (2013). N-wasp is required for stabilization of podocyte foot processes. J Am Soc Nephrol *24*, 713-721.

Schell C, W.N., Huber TB (2014). Glomerular development--shaping the multi-cellular filtration unit. Semin Cell Dev Biol *36*, 39-49.

Schmidt-Ott KM, B.J. (2008). WNT/beta-catenin signaling in nephron progenitors and their epithelial progeny. Kidney Int *74*, 1004-1008.
Seifert JR, M.M. (2007). Frizzled/PCP signalling: a conserved mechanism regulating cell polarity and directed motility. Nat Rev Genet *8*, 126.
Sekine K, O.H., Fujiwara M, Yamasaki M, Yoshizawa T, Sato T, Yagishita N, Matsui D, Koga Y, Itoh N, Kato S. (1999). Fgf10 is essential for limb and lung formation. Nat Genet *21*, 138-141.
Sinha T, W.B., Evans S,Wynshaw-Boris A, Wang J (2012). Disheveled Mediated Planar Cell Polarity Signaling is Required in the Second Heart Field Lineage for Outflow Tract Morphogenesis. Dev Biol *370*, 135-144.
Song J, M.J., Camp E,Kennerley N,Mok GF, McCormick D, Grocott T, Wheeler GN, Munsterberg AE. (2014). Smad1 transcription factor integrates BMP2 and Wnt3a signals in migrating cardiac progenitor cells. Proc Natl Acad Sci U S A *111*, 7337-7342.
Stainier DY (2001). Zebrafish genetics and vertebrate heart formatio. Nat Rev Genet *2*, 39-48.
Stubbs JL, V.E., Axelrod JD, Kintner C (2012). Multicilin promotes centriole assembly and ciliogenesis during multiciliate cell differentiation. Nat Cell Biol *14*, 140-147.
Sussel, T.L.M.a.L. (2012). The Endocrine Pancreas: insights into development, differentiation and diabetes. Wiley Interdiscip Rev Membr Transp Signal *1*, 609-628.
Swarr DT, M.E. (2015). Lung endoderm morphogenesis: gasping for form and function. Annu Rev Cell Dev Biol *31*, 553-573.
Swoboda P, A.H., Thomas JH (2000). The RFX-type transcription factor DAF-19 regulates sensory neuron cilium formation in C. elegans. Mol Cell *5*, 411-421.
Szymaniak AD, M.J., Cardoso WV, Varelas X. (2015). Crumbs3-mediated polarity directs airway epithelial cell fate through the Hippo pathway effector Yap. Dev Cell *34*, 283-296.
Taber, L. (2006). Biophysical mechanisms of cardiac looping. Int J Dev Biol *50*, 323-332.
Tang M, X.W., Wang Q, Xiao W, Xu R (2009). Potential of DNMT and its Epigenetic Regulation for Lung Cancer Therapy. Curr Genomics *10*, 336-352.
Tang MJ, C.Y., Tsai SJ, Wang YK, Dressler GR. (2002). Ureteric bud outgrowth in response to RET activation is mediated by phosphatidylinositol 3-kinase. Dev Biol *243*, 128-136.
Tian Y, Z.Y., Hurd L, Hannenhalli S, Liu F, Lu MM, and Morrisey EE (2011). Regulation of lung endoderm progenitor cell behavior by miR302/367. Development *138*, 1235-1245.

Torres AM, Z.M. (1993). Malrotation of the intestine. World J Surg *17*, 326-331.
Tremblay KD, Z.K. (2005). Distinct populations of endoderm cells converge to generate the embryonic liver bud and ventral foregut tissues. Dev Biol *280*, 87-99.
Trinh LA, S.D. (2004). Cardiac development. Methods Cell Biol *76*, 455-473.
Trinh LA, Y.D., Stainier DY. (2005). Hand2 regulates epithelial formation during myocardial diferentiation. Curr Biol *15*, 441-446.
Ventura A, Y.A., Winslow MM, Lintault L, Meissner A, Erkeland SJ, Newman J, Bronson RT, Crowley D, Stone JR, Jaenisch R, Sharp AP, Tyler Jacks (2008). Targeted deletion reveals essential and overlapping functions of the miR-17~92 family of miRNA clusters. Cell *132*, 875-886.
Vogel V, S.M. (2006). Local force and geometry sensing regulate cell functions. Nat Rev Mol Cell Biol *7*, 265-275.
Volckaert T, D.L.S. (2015). Wnt and FGF mediated epithelial mesenchymal crosstalk during lung development. Dev Dyn *244*, 342-366.
Waldo KL, K.D., Wallis KT, Stadt HA, Hutson MR, Platt DH, Kirby ML. (2001). Conotruncal myocardium arises from a secondary heart field. Development *128*, 3179-3188.
Wang Z, S.W., Lu MM, Morrisey EE (2005). Wnt7b Activates Canonical Signaling in Epithelial and Vascular Smooth Muscle Cells through Interactions with Fzd1, Fzd10, and LRP5. Mol Cell Biol *25*, 5022-5030.
Warburton D, E.-H.A., Carraro G,Tiozzo C, Sala F, Rogers O, Langhe SD, Kemp PJ, Riccardi D, Torday J, Bellusci S, Shi W, Lubkin SR,Jesudason E (2010). Lung Organogenesis. Curr Top Dev Bio *90*, 73-158.
Weibel ER (2015). On the tricks alveolar epithelial cells play to make a good lung. Am J Respir Crit Care Med *191*, 504-513.
Welsh IC, T.M., Gludish DW, Alfonso-Parra C, Bai Y, Martin JF, Kurpios NA. (2013). Integration of left-right Pitx2 transcription and Wnt signaling drives asymmetric gut morphogenesis via Daam2. Dev Cell *26*, 629-644.
Wen J, C.Y., Gao C, Xue H, Xu J, Ning Y, Hodes RJ, Gao X, Chen YG. (2010). Loss of Dact1 disrupts planar cell polarity signaling by altering dishevelled activity and leads to posterior malformation in mice. J Biol Chem *285*, 11023-11030.
Wilson JW, G.C., Leduc EH. (1963). Histogenesis of the liver. nn NY Acad Sci *111*, 8-24.

Xu PX, A.J., Peters H, Brown MC, Heaney S, Maas R. (1999). Eya1-deficient mice lack ears and kidneys and show abnormal apoptosis of organ primordia. nat genet *23*, 113-117.
Yamada M, U.J., Matsumoto A,Hashimoto R, Hatta T, Nishita M,Minami Y, Otani H. (2010). Ror2 is required for midgut elongation during mouse development. Dev Dyn *239*, 941-953.
Yang X, D.D., Münsterberg AE, Weijer CJ. (2002). Cell movement patterns during gastrulation in the chick are controlled by positive and negative chemotaxis mediated by FGF4 and FGF8. Dev Cell *3*, 425-437.
Yates LL, J.P., David A. Long, Paraskevi Goggolidou, John O. Connolly, Adrian S. Woolf, and Charlotte H. Dean (2010). The planar cell polarity gene Vangl2 is required for mammalian kidney-branching morphogenesis and glomerular maturation. Hum Mol Genet *19*, 4663-4676.
Ye X, W.Y., Rattner A, Nathans J. (2011). Genetic mosaic analysis reveals a major role for frizzled 4 and frizzled 8 in controlling ureteric growth in the developing kidney. Development *138*, 1161-1172.
Yimlamai D, C.C., Galli GG, Yanger K, Pepe-Mooney B, Gurung B, Shrestha K, Cahan P, Stanger BZ, Camargo FD. (2014). Hippo pathway activity influences liver cell fate. Cell *157*, 1324-1388.
Yin C (2017). Molecular Mechanisms of Sox transcription factors during development of liver, bile duct and pancreas. Semin Cell Dev Biol *63*, 68-78.
Yu T, C.X., Zhang W, Li J, Xu R, Wang TC, Ai W, Liu C. (2012). Krüppel-like factor 4 regulates intestinal epithelial cell morphology and polarity. PLoS One *7*.
Yue, Q., Wagstaff, L., Yang, X., Weijer, C., and Munsterberg, A. (2008). Wnt3a-mediated chemorepulsion controls movement patterns of cardiac progenitors and requires RhoA function. Development *135*, 1029-1037.
Zaret KS (2016). From Endoderm to Liver Bud: Paradigms of Cell type Specificaton and Tissue Morphogenesis. Current Topics in Developmental Biology *117*, 647-669.

CHAPTER 4: FUTURE DIRECTIONS

4.1 Summary

My work, described in Chapter 2, has demonstrated that the cellular and vascular transformations in the right DM *precede all other cell asymmetries* that collectively deform this structure, suggesting that the key initiator for leftward gut tilting derives from the right side. I have further shown that HA produced primarily on the DM right side is a key regulator of the mesenchymal expansion and vascular exclusion necessary for asymmetric gut looping and vascular morphogenesis (Figure 4.1). Investigating into how HA enacts its functions, I discovered that Tsg6, an enzyme that can covalently modify HA *to form a stable heavy chain (HC) HA complex,* is restricted to the right DM. Knockdown and misexpression studies of Tsg6 revealed that while Tsg6 is necessary for the right sided expansion and gut tilting, Tsg6 is both necessary and sufficient to inhibit vascular development on the right side. These data were further reinforced by my findings in the mouse model system where the Tsg6-null embryos demonstrated randomized gut looping chirality and gut vascular defects. Thus, these discoveries strongly support the critical role of HA-Tsg6 interaction in the initiation of mammalian gut rotation and vascular development (Figure 4.1). Furthermore, these findings pave the way for future investigations of the downstream mechanisms regulating HA in the DM, the relationship between Tsg6 and HA production, and the changes in tissue architecture that establish gut and vascular chirality. The following sections provide an outline of the possible investigations that can be carried out to understand the upstream and the downstream mechanisms of Tsg6 and HA in the DM.

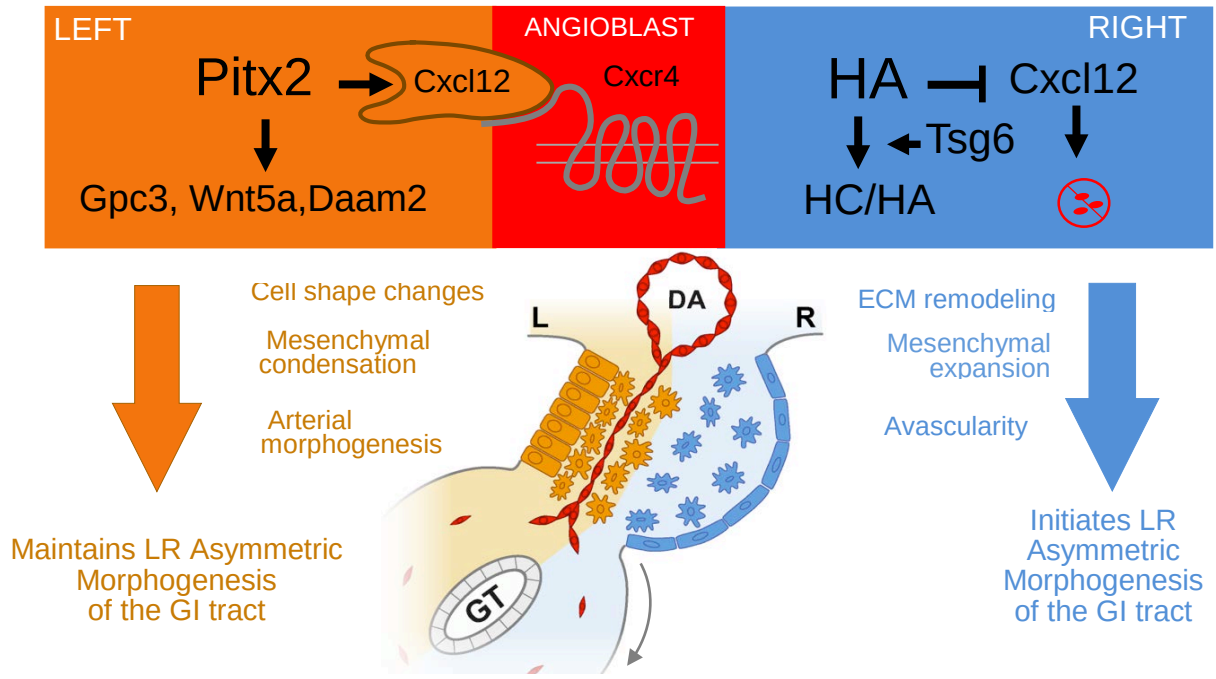

Figure 4.1: Summary of our current understanding of the cellular mechanisms that contribute to asymmetric arteriogenesis and leftward tilting of the gut.

4.2 Enzymatic evidence for HC-HA modification in the mouse DM

My results suggest but do not prove that the ability of Tsg6 to mediate avascularity in the right DM is dependent on its enzymatic ability to covalent modify HA. Hence, the first step would be to determine directly whether Tsg6 is transferring HC to HA. *In vitro* studies have shown that the covalent modification of HA occurs in the presence of ***inter-α-trypsin inhibitor*** (***IαI***), which triggers Tsg6 to function as an enzyme that mediates the covalent transfer of HC to HA forming the ***HC-HA*** complex (Briggs DC, 2015). IαI is a serum proteoglycan composed of 3 polypeptides: the trypsin inhibitor called ***bikunin*** (35 kDa) and two of the three genetically different ***heavy chains*** (HC1, HC2, and HC3), 83 kDa each (Salier et al., 1996). Tsg6 and bikunin are essential for the biosynthesis of this complex and loss of Tsg6 or bikunin in mice result in abolished

formation of HC-HA. The bikunin-null mice which lack the HC donor IαI fail to form HC-HA with nearly identical phenotypes to the Tsg6 null mice (Lauer ME, 2013; Zhuo et al., 2001). Importantly, although HC-transfer is disrupted in these mice, *Tsg6 is unaffected*. Thus, *bikunin lesion will reveal whether Tsg6 functions independently of HC transfer to HA on the right side*, affording further mechanistic insights into the role of Tsg6 in the mouse intestine. Thus comparative analysis of gut looping and vascular patterns between the bikunin nulls and Tsg6 nulls will help define whether Tsg6 functions as a HA modifying enzyme or independent of its catalytic activity. For example, if the role of Tsg6 in the gut is dependent on HA catalysis, we expect reduced HA staining, perturbed ECM expansion and altered gut looping in both Tsg6- and bikunin-null embryos because they lack the IαI substrate. If Tsg6 plays a role in the gut *independent* of HA catalysis, we expect no gut phenotypes in bikunin-null mice. Of note, beyond its role in HA catalysis, Tsg6 regulates chemokine signaling by modulating chemokine-GAG interactions (Dyer et al., 2016). Thus, the HA-independent function of Tsg6 warrants consideration.

As a corollary to addressing the central question regarding the nature of Tsg6 role in the DM, investigations to determine the DM's ability to support the enzymatic function of Tsg6 needs to be carried out. This involves characterizing the source of IαI complex in the DM. The current body of literature on IαI shows that majority of the IαI complexes in the body is synthesized by the liver hepatocytes and is secreted into the blood at high concentrations (Mizon C, 1996). Particularly the serum is enriched with the IαI complex. Furthermore, experiments *in vitro* have shown that simple mixing of serum and HA followed by incubation with Tsg6 at 37°C is sufficient to form the HC-HA complex (Yoneda M, 1990). During ovulation or inflammation, IαI has been shown to ingress into extracellular tissue spaces following increased vascular permeability, where it serves as an HC donor (Lauer ME, 2013). Therefore, the convergence of serum and HA with

Tsg6 can be an important regulator during gut rotation. Most recently, synthesis of Tsg6 and a member of the IαI family with HC3 have been noted in the mouse lung airway epithelial cells suggesting that serum is not the only source of an active IαI production (Abbadi A, 2016). Therefore, there are currently two possible sources of the IαI complex. 1) *DM cells can synthesize their own IαI substrate in the absence of serum in a manner similar to the lung epithelium; or 2) that the blood vasculature has a role in ECM expansion by supplying IαI in the DM, as shown during ovulation*. My preliminary investigations into the distribution of IαI using immunohistochemistry reveal the absence of IαI in the cells of the DM (data not shown) suggesting that the serum IαI is the likely substrate. However, further investigations need to be carried out to directly address *whether DV cords play a role in ECM expansion by supplying IαI in the DM.* The mechanistic insights obtained from the above investigations can be followed with direct validation of the HC-HA modification by extracting the HCs in the DM using Streptomyces hyaluronidase mediated digestion (*specific for HA*) and detecting the released products by mass spectrometry (Figure 4.2).

4.3 Investigating HC-HA mediated mechanisms that regulate vascular exclusion

When HA on the right DM is depleted, *Cxcl12* expression in the right is *abnormally maintained* suggesting that *HA negatively regulates Cxcl12 expression at the transcriptional level* (Figure 2.7). However, it remains to be determined whether Tsg6 is necessary to inhibit *Cxcl12* expression in right DM. Analysis of *Cxcl12* expression in Tsg6 knockdown embryos (using MO electroporations) and embryos electroporated with catalytically inactive pCAG-*Tsg6-S28A* on the right can provide potential insights into the role of Tsg6 in regulating *Cxcl12*

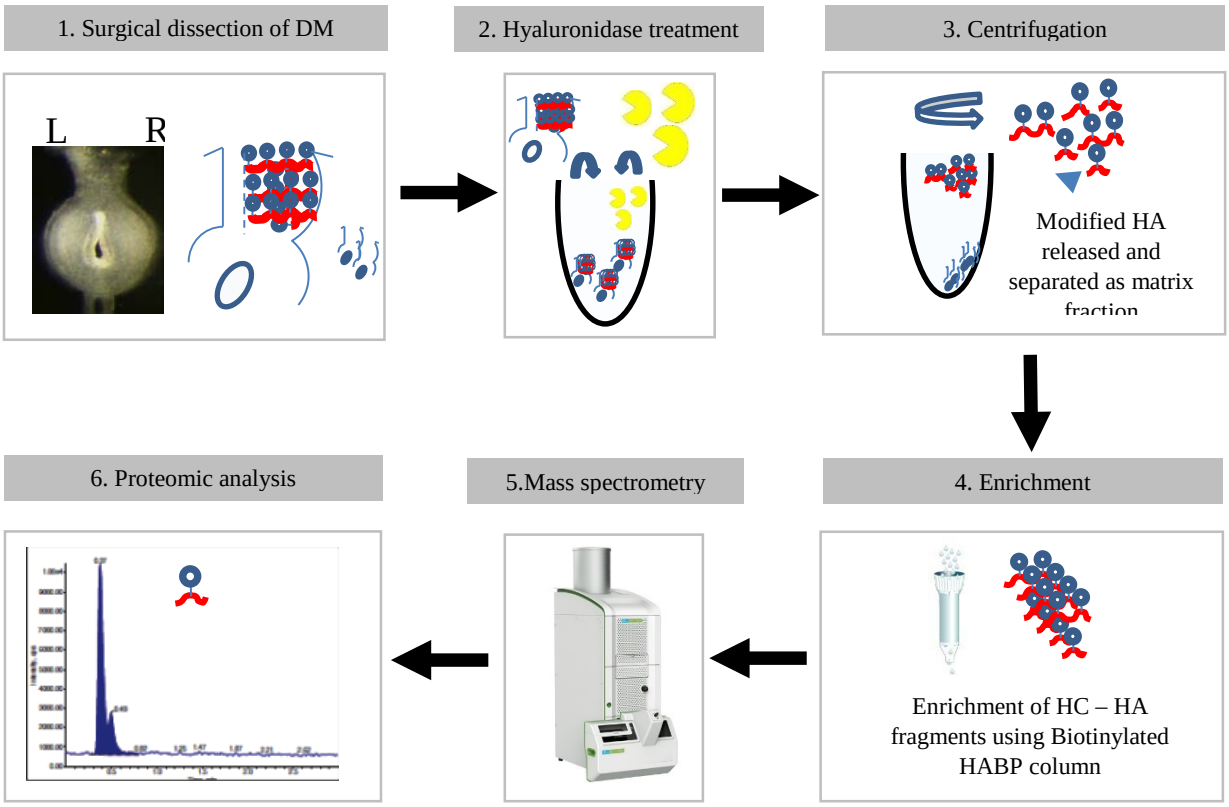

Figure 4.2: Work flow to detect HC-HA complexes in the DM using mass spectrometric approaches

expression. Another potential candidate pathway that can lie downstream of Tsg6-mediated anti-angiogenesis is the VEGF signaling pathway- a critical regulator of blood vessel formation and patterning (Ferrara N, 2009). Studies in recent times have elucidated interactions between VEGF signaling pathway and HA matrices. For example, degradation of the HMW-HA into small HA oligosaccharides induces *VEGF* mRNA and protein in primary mouse endocardial cushions in the heart whereas HMW-HA is inhibitory to these activities (Rodgers LS, 2006). Thus, the HA matrices can regulate the transcription of *VEGF*. Interestingly, studies in zebrafish support the hypothesis that the small HA fragments induce VEGF signaling by liberating VEGF molecules from the ECM, *without affecting the transcription* suggesting that HA can also act as an

extracellular sink to sequester VEGF away from its receptor (De Angelis JE, 2017). Thus, assays that perturb VEGF expression in chicken embryos where Tsg6 manipulations have been carried out can provide insights into the potential link between Tsg6 and VEGF in the DM.

4.4 Elucidating the upstream mechanisms involved in HA and Tsg6 induction in the DM

While the current study provides insights into how HA functions in the DM to generate cellular and vascular asymmetries, the mechanisms that result in asymmetric accumulation of HA in the right DM remain unclear. Since Has2 is not differentially expressed across the LR axis of the DM, it is unlikely that asymmetric regulation of its expression could be responsible for the enriched levels of HA on the right. However, since Has2 is also regulated via post-translational modifications (Tammi RH, 2011), it is possible that the differential modulation of Has2 function via distinct post-translational modifications in the left and the right DM could underlie the asymmetric accumulation of HA. Mechanisms independent of Has2 function in the DM are equally possible. One such hypothesis being asymmetric degradation of HA by HA-degrading enzymes produced either by the left mesenchymal cells or by the vascular endothelial cells present only in the left DM compartment. This would result in the asymmetric accumulation of HA in the right side. Further investigations are needed to determine the cellular expression profile of HA-degrading enzymes, such as Hyal2, in the DM.

To investigate mechanisms responsible for the timely induction of Tsg6 in the right DM, I have previously identified potential candidate transcription factors that could regulate Tsg6 expression. Using transcriptional profiling data from our previously published laser capture microdissection of the LR halves of the chicken DM, I have identified the anti-inflammatory cyclic

AMP-dependent *transcription factor Atf3* as one such gene. Previous studies have shown that both Atf3 and Tsg6 are activated downstream of TNF-α (Inoue K, 2004) and are specifically produced in ovarian cumulus cell-oocyte complex (Inan MS, 2006). They are both known to act as negative regulators of inflammation (Wisniewski HG, 1997). Furthermore, spatiotemporal analysis of *Atf3* expression revealed that *Atf3* is restricted to the right DM commensurate with the leftward tilt and with *Tsg6* expression (Figure 4.3). Importantly, I have identified a highly evolutionarily conserved region immediately upstream of *Tsg6* that is enriched for the binding sequence of Atf3, suggestive of direct regulation (Figure 4.3).

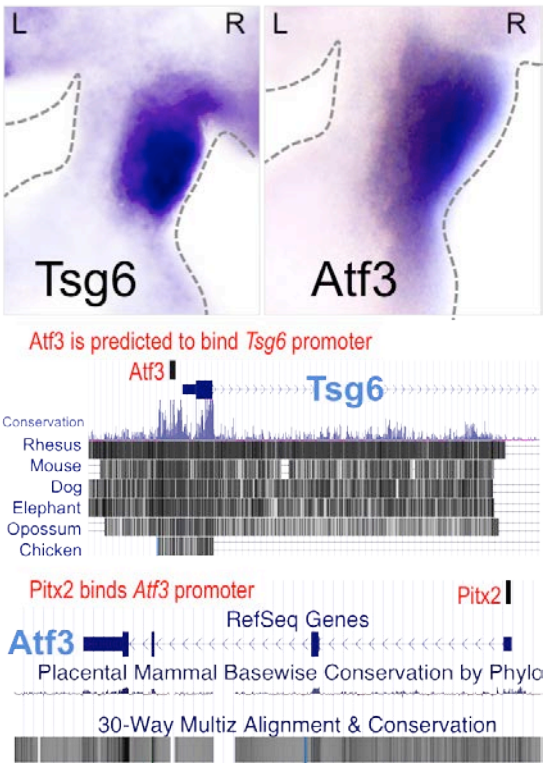

Figure 4.3: *Tsg6* and *Atf3* are both right-sided in the DM. In silico analysis of the promoter region of Tsg6 reveal a highly conserved and an enriched Atf3 binding site suggesting that Atf3 could potential regulate Tsg6 expression. ChipSeq data showing binding sites of Pitx2 upstream of Atf3 showing that Pitx2 is a possible regulator of Atf3 that serves to restrict its expression to the right DM.

Importantly, I showed previously that Pitx2 misexpression in the right chicken DM inhibits Atf3, Tsg6 and HA production (data not shown). Hence, using the chicken model system, targeted knockout of Atf3 using morpholinos or misexpression of *Atf3* on the left side can be carried out and assayed for Tsg6 expression. This can be followed up with chromatin immunoprecipitation assays to detect *in vivo* binding of Atf3 to the regulatory region of Tsg6. In addition to Atf3, I have identified other transcription factors that are right-sided in the DM (for example Tbx18, Tcf21, Smad6), which should be tested for their role in the induction of Tsg6.

4.5 The Mystery of HA in the left DM

My data argues that endogenous HA in the left DM, however weak in HA staining, may have a role, consistent with bilateral *Has2* expression in the DM. However, only the HA in the right DM is anti-angiogenic whereas the HA in the left coexists with vasculature suggesting that the HA in the right DM and left DM are functionally different. Since the function of HA in a given system is regulated by its size and its interactors (Cyphert JM, 2015), there are currently two possible hypotheses that could explain the functional differences between the left and right DM. Studies that have looked into the effect of size on the function of HA have shown that in normal tissues, native HMW-HA is anti-angiogenic whereas LMW-HA fragments stimulate angiogenesis (Deed R, 1997). Thus, *the opposing pro-angiogenic role of HA on the left could suggest the presence of LMW HA in the left compartment*. The second possibility arises from our preliminary observation that while *Tsg6* is right-sided in the DM, *another HA binding protein, versican, is expressed on the left* (Figure 4.4).

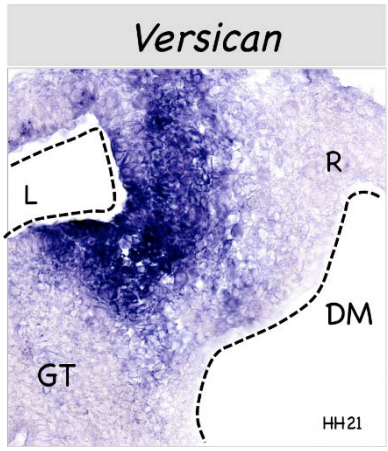

Figure 4.4: Versican is left-sided in the DM at HH21 (RNA ISH, *Vcan*).

Versican-null (*Vcan* $^{hdf/hdf}$) and mutant embryos with reduced HA binding (*Vcan* ^{delta3}) share similar cardiac phenotypes as *Has2*-null mutants, suggesting that the HA-versican interaction is crucial to cardiac development (Hatano et al., 2012; Matsumoto et al., 2003). In pathological conditions, interaction of versican and HMW-HA, but not HMW-HA alone, acts as an angiogenic modulator by promoting endothelial proliferation and migration, transmitting signals in concert with HA (Koyama et al., 2007). Thus, the second possibility that may explain the differential functions for HA in left and right DM is that HMW HA is produced on both sides of the DM but is differentially modified with Tsg6 on the right and bound by versican on the left. Further investigations involving inhibition and manipulation of versican in the chicken DM may provide us with further insights regarding the *in vivo* regulation of HA that promotes angiogenesis versus anti-angiogenesis, which have immense therapeutic applications for numerous disease conditions.

4.6 References

Abbadi A, L.M., Swaidani S, Wang A, Hascall V. (2016). Hyaluronan Rafts on Airway Epithelial Cells. J Biol Chem *291*, 1448-1455.

Briggs DC, B.H., Ali T, Rugg MS, Waltho JP, Ievoli E, Jowitt TA, Enghild JJ, Richter RP, Salustri A, Milner CM, Day AJ. (2015). Metal Ion-dependent Heavy Chain Transfer Activity of TSG-6 Mediates Assembly of the Cumulus-Oocyte Matrix. J Biol Chem *290*, 28708-28723.

Cyphert JM, T.C., Garantziotis S. (2015). Size Matters: Molecular Weight Specificity of Hyaluronan Effects in Cell Biology. Int J Cell Biol *2015*.

De Angelis JE, L.A., Chen H, Tromp A, Bower NI, Tunny KA, Brooks AJ, Bakkers J, Francois M, Yap AS, Simons C, Wicking C, Hogan BM, Smith KA. (2017). Tmem2 Regulates Embryonic Vegf Signaling by Controlling Hyaluronic Acid Turnover. Dev Cell *40*, 123-136.

Deed R, R.P., Kumar P, Norton JD, Smith J, Freemont AJ, Kumar S. (1997). Early-response gene signalling is induced by angiogenic oligosaccharides of hyaluronan in endothelial cells. Inhibition by non-angiogenic, high-molecular-weight hyaluronan. Int J Cancer *71*, 251-256.

Dyer, D.P., Salanga, C.L., Johns, S.C., Valdambrini, E., Fuster, M.M., Milner, C.M., Day, A.J., and Handel, T.M. (2016). The Anti-inflammatory Protein TSG-6 Regulates Chemokine Function by Inhibiting Chemokine/Glycosaminoglycan Interactions. The Journal of biological chemistry *291*, 12627-12640.

Ferrara N (2009). VEGF-A: a critical regulator of blood vessel growth. Eur Cytokine Netw *20*, 158-163.

Hatano, S., Kimata, K., Hiraiwa, N., Kusakabe, M., Isogai, Z., Adachi, E., Shinomura, T., and Watanabe, H. (2012). Versican/PG-M is essential for ventricular septal formation subsequent to cardiac atrioventricular cushion development. Glycobiology *22*, 1268-1277.

Inan MS, A.-H.S., Ozand P, Coskun S. (2006). Transcriptional profiling of granulosa cells from a patient with recurrent empty follicle syndrome. Reprod Biomed Online *13*, 481-491.

Inoue K, Z.T., Kamimoto T, Aoki R, Ikeda Y, Kimura H, Hagiwara M. (2004). TNFalpha-induced ATF3 expression is bidirectionally regulated by the JNK and ERK pathways in vascular endothelial cells. Genes Cells *9*, 59-70.

Koyama, H., Hibi, T., Isogai, Z., Yoneda, M., Fujimori, M., Amano, J., Kawakubo, M., Kannagi, R., Kimata, K., Taniguchi, S., *et al.* (2007). Hyperproduction of hyaluronan in neu-induced

mammary tumor accelerates angiogenesis through stromal cell recruitment: possible involvement of versican/PG-M. Am J Pathol *170*, 1086-1099.

Lauer ME, G.T., Mikecz K, DeAngelis PL, Haller FM, Husni ME, Hascall VC, Calabro A. (2013). Irreversible heavy chain transfer to hyaluronan oligosaccharides by tumor necrosis factor-stimulated gene-6. J Biol Chem *288*, 205-214.

Matsumoto, K., Shionyu, M., Go, M., Shimizu, K., Shinomura, T., Kimata, K., and Watanabe, H. (2003). Distinct interaction of versican/PG-M with hyaluronan and link protein. The Journal of biological chemistry *278*, 41205-41212.

Mizon C, B.M., Albani D, Michalski C, Burnouf T, Mizon J. (1996). Development of an enzyme-linked immunosorbent assay for human plasma inter-alpha-trypsin inhibitor (ITI) using specific antibodies against each of the H1 and H2 heavy chains. J Immunol Methods *190*, 61-70.

Rodgers LS, L.S., Hardy KM, Xiang X, Broka D, Antin PB, Camenisch TD. (2006). Depolymerized hyaluronan induces vascular endothelial growth factor, a negative regulator of developmental epithelial-to-mesenchymal transformation. Circ Res *99*, 583-589.

Salier, J.P., Rouet, P., Raguenez, G., and Daveau, M. (1996). The inter-alpha-inhibitor family: from structure to regulation. The Biochemical journal *315 (Pt 1)*, 1-9.

Tammi RH, P.A., Rilla K, Karousou E, Vigetti D, Makkonen K, Tammi MI (2011). Transcriptional and post-translational regulation of hyaluronan synthesis. FEBS J *278*, 1419-1428.

Wisniewski HG, V.J. (1997). TSG-6: an IL-1/TNF-inducible protein with anti-inflammatory activity. Cytokine Growth Factor Rev *8*, 143-156.

Yoneda M, S.S., Kimata K. (1990). Hyaluronic acid associated with the surfaces of cultured fibroblasts is linked to a serum-derived 85-kDa protein. J Biol Chem *265*, 5247-5257.

Zhuo, L., Yoneda, M., Zhao, M., Yingsung, W., Yoshida, N., Kitagawa, Y., Kawamura, K., Suzuki, T., and Kimata, K. (2001). Defect in SHAP-hyaluronan complex causes severe female infertility. A study by inactivation of the bikunin gene in mice. The Journal of biological chemistry *276*, 7693-7696.

APPENDIX: METHODS AND PROTOCOLS

A1 Introduction

Over the course of the past six years, various protocols and methods have been developed or adopted for understanding the role of right-sided mechanisms in orchestrating gut looping and vascular morphogenesis in mice and avian (chicken and quail) embryos. These include methods from accurately determining the developmental stage of the embryo based on the gut, to elucidating gene expression profiles and manipulating gene expression. A summary of the methods used for different experiments which seek to provide answers to different hypothesis have been outlined in the flowchart shown in the following page (Fig A1). These methods have been described in detail in this section with the intention of allowing any person to learn and obtain a high level of expertise in these techniques with sufficient practice, which would enable them to reproduce the results described in the earlier chapters. As shown in Fig A1, the techniques can be categorized into the following:

A. Embryology:

While there are a number of references that allow determination of the developmental stage of an embryo such as growth of forelimb, size of the allantois, pigmentation of the eyes, and somite numbers, these methods are not completely reliable in the context of gut development. Frequently, following genetic or surgical manipulation the embryo fails to develop uniformly and determination of the developmental stage with respect to how much the gut has developed becomes very difficult. To this end, I have developed methods to identify the developmental stage of the chicken and mice embryos based on the topology of the gut. These are detailed in sections AA1 and AA2.

Section AA3 describes methods of processing dissected embryos for paraffin and cryo--sectioning to generate thin sections for looking at tissue morphology or gene/protein expressions with cellular resolution.

B. Histology:

This technique is utilized extensively in biology, and especially in developmental biology to study the microscopic structure and morphology of cells and tissues under light or electron microscopes. Generally, a variety of histological stains are employed to visualize or differentially identify various cellular structures. Sections AB1, AB2 and AB3 describe in detail three different histological staining procedures for different purposes. All three staining procedures are performed on paraffin-sectioned tissue samples, described in section AA3.

C. Gene expression and manipulation:

Understanding embryonic development requires knowledge of the spatio-temporal expression of genes regulating the many different and diverse processes during development. RNA in situ hybridization allows us to look at the spatial expression of genes across different stages during embryonic development. The methods for performing RNA in situ hybridization in tissue sections of mice and chicken embryo and in whole mice and chicken embryo samples have been described in detail in the thesis of Aparna Mahadevan (Aparna Mahadevan, 2016 – Sections A1 and A2). However, recently, we have adopted another protocol for investigating gene expression profiles using commercially designed probes and reagents. This allows the week-long protocol to be shortened to just a single day, and is particularly useful for some genes which are difficult to detect using the conventional methods described by Aparna Mahadevan. This technique, termed RNAScope, from ACDBio is outlined in section AC1. It should be noted that RNAScope is almost exclusively for genes that have been proven to be extremely difficult to detect reproducibly using

the in house conventional methods, and that those methods should be tried first. Additionally, RNAScope is currently only used in tissue-sections of embryos and not whole mount samples.

After obtaining information about the spatial distribution of genes, it is important to either misexpress or knockdown the gene function to determine the functionality of the gene by addressing if it is sufficient or necessary for a particular developmental process. The chicken embryo offers itself as an excellent model to transiently misexpress/overexpress or knockdown genes in vivo, while the embryo is still developing. Following the genetic manipulation, the embryo can continue to develop and the effect of the manipulation can be observed at a later developmental stage. In the Kurpios lab, we use a method known as electroporation to specifically target the precursor cells of the dorsal mesentery. Briefly, a plasmid DNA containing the gene of interest and a ubiquitous promoter is injected into the coelomic cavity, where the precursor cells of the dorsal mesentery reside. An electric pulse is then administered to allow the cell to uptake the plasmid DNA. This technique of plasmid DNA electroporation in both chicken and quail embryos is described extensively in the thesis of Aparna Mahadevan (Aparna Mahadevan, 2016 – Section A6). However, I have developed a technique of electroporating Morpholinoes to knock down the function of genes (See Chapter 2). While the method of delivery of the Morpholino is identical to that of plasmid DNA, and will not be described here, I have outlined the procedures for designing the Morpholinoes and the how the Morpholinoes should be prepared for electroporations in section AC2.

Another method to perturb function of gene products is to utilize small molecule chemical inhibitors. These chemical inhibitors are soaked in resin beads (or other beads compatible with the inhibitor) and surgically implanted into the coelomic cavity of the developing embryo. Again, this procedure has been described in detail in the thesis of Aparna Mahadevan (Aparna Mahdevan,

2016 – Section A7). In Chapter 2 of this thesis, I have used this technique to inhibit hyaluronan synthesis by introducing the small molecule inhibitor, Mu-Xyloside. The conditions and procedures for preparing the Mu-Xyloside soaked beads along with the proper vehicle controls are described in Section AC3.

D. Immunostaining:

Immunostaining allows us to visualize the spatial distribution a protein within a tissue section of an embryo (immunohistochemistry) or within the whole embryo (wholemount immune staining). The general procedures for immunostaining in tissue sections of mice and chicken embryos and mice gut tube sections, and for whole mount immunostaining in mice and chicken embryos/intestines have been described in Aparna Mahadevan's thesis (Aparna Mahadevan, 2016 – Sections A3-5). I have developed another protocol to be used exclusively with hyaluronic acid binding protein (HABP) to determine distribution of hyaluronan in chicken embryo tissue sections (see Chapter 2 of this thesis). This protocol is described in detail in section AD1.

E. Live imaging:

Embryonic development is very dynamic with numerous processes occurring in tandem to form functional organs and organ-systems, ultimately resulting in the formation of a fully functional organism. Taking the intestines as an example, there are many cellular processes such as cell migration, cell shape changes, proliferation, cell division, differentiation, etc., which allow the simple cylindrical primitive gut tube to transform into a complex structure with complex yet reproducible looping topology and an extensive vascular network. While detailed histological or embryological characterization at different developmental stages allow us to get an overview and draw a timeline of the process, the best way to understand these cellular processes is via live imaging of the cells, which in this case are fluorescently labelled using confocal or two-

photon/multiphoton microscopy techniques. As the name implies, this technique involves tracking the different cellular processes real time, as they occur. I have developed this technique of ex vivo live imaging to track the migration of blood endothelial cells (transgenic quails), lymphatic endothelial cells (transgenic mice) and cell shape changes in the dorsal mesentery of reporter-electroporated chicken embryos. The procedures for preparing the three types of samples for live imaging has been described in detail in sections AE1. The microscope set-up varies with the microscope being used and the samples, and it is imperative that proper training on the microscope and an intuitive understanding of how the microscope functions is obtained. Due to the variability in settings in different microscopes and also taking into account the microscope softwares are updated regularly, it is almost impossible to describe them in detail and only the essential details have been provided. It is best to get properly trained with the professionals who know the microscope, when you are ready to do some live imaging with samples prepared according to the descriptions in sections AE1.

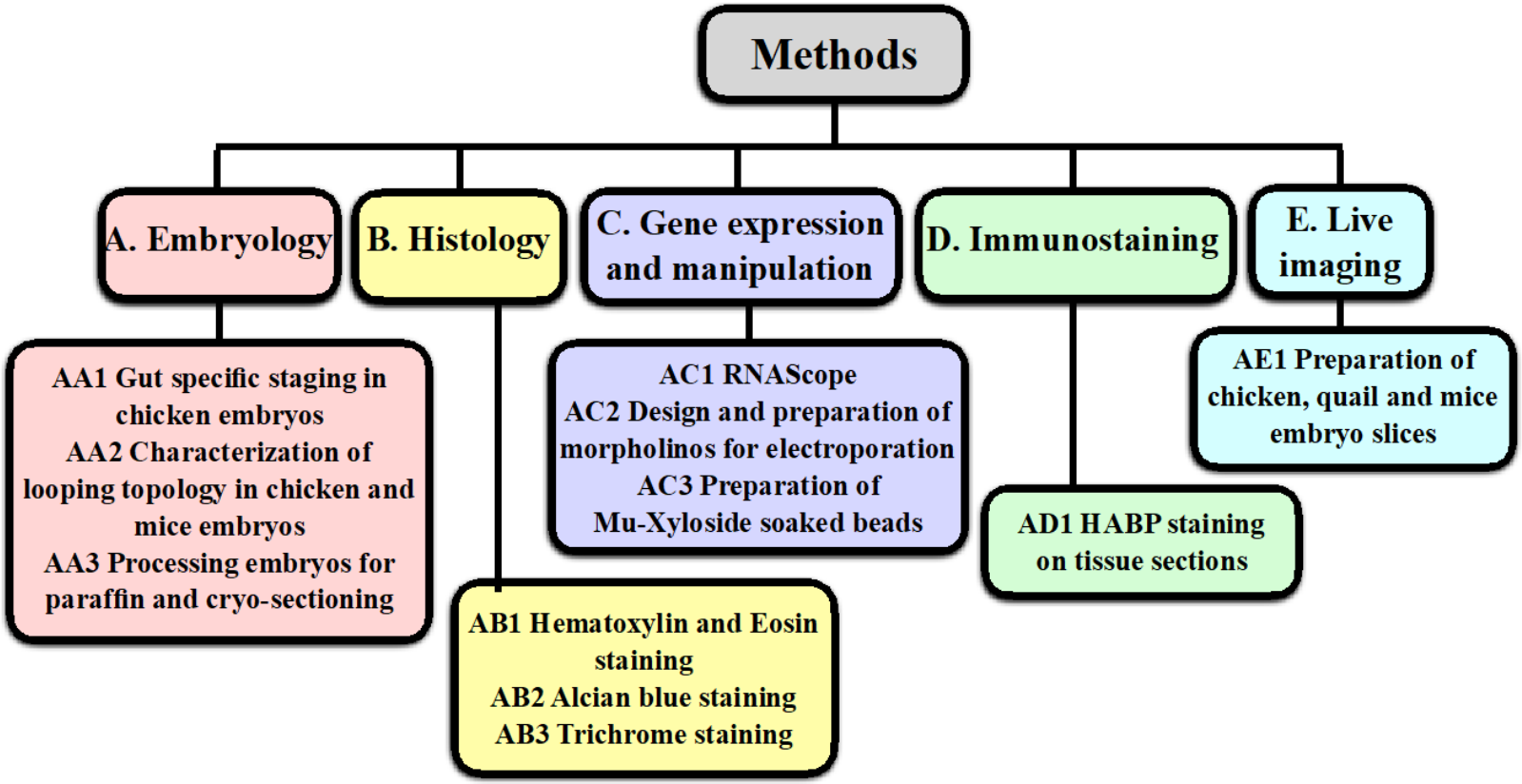

Figure A1: Methods developed to understand embryonic developmental processes. The methods have been broadly categorized into five types. The flowchart also lists the subcategories in each type.

AA1 Embryology: Gut specific staging of chicken embryos

The chick embryo has been the center piece for many embryological studies and its embryonic development have been described in a variety of ways. While its development has been described generally in terms of length of the incubation time, a wide variation in external form of the embryos could still be observed. Other specific methods of characterization based on distinguishing the embryos based on detailed morphological characteristics over the entire incubation period as worked out by Hamburger and Hamilton (1951) have greatly enabled scientists for rapid, accurate identification and synchronized staging across the world. Intriguingly, the authors of the seminal paper had acknowledged that the embryo displays independent variations of different characteristics during its development. They had indeed noted that "for instance, the progress of differentiation in the visceral arches may lag behind that in limb buds, when compared with an average sequence".

From empirical observations of others and myself in the Kurpios lab, we find that the variations in development of the different features is more extensive during the early embryonic development. These variations could arise from the fact that early embryonic development is modular and there is lesser synchronization during the early embryonic development. As development proceeds, we find that the variations become significantly lesser showing that there is greater synchronization at the later stages.

As a result of these variations, there is a strong need to develop organ specific staging methods for accurate identification of the dynamics of gut development. In my work, I have characterized the developing chick gut tube from stages HH17 - HH25 with great amount of help from Ian Welsh and Aparna Mahadevan- two senior graduate students in the lab who have guided me. I describe specific distinguishing features that will enable one to tell between the stages and

to anatomically identify the different zones of the developing gut tube. This has been based on several embryos that I had examined over the course of my PhD, illustrated in Figures A2-A7. All the illustrations and descriptions are based on material fixed in Bouin's fixative or formalin.

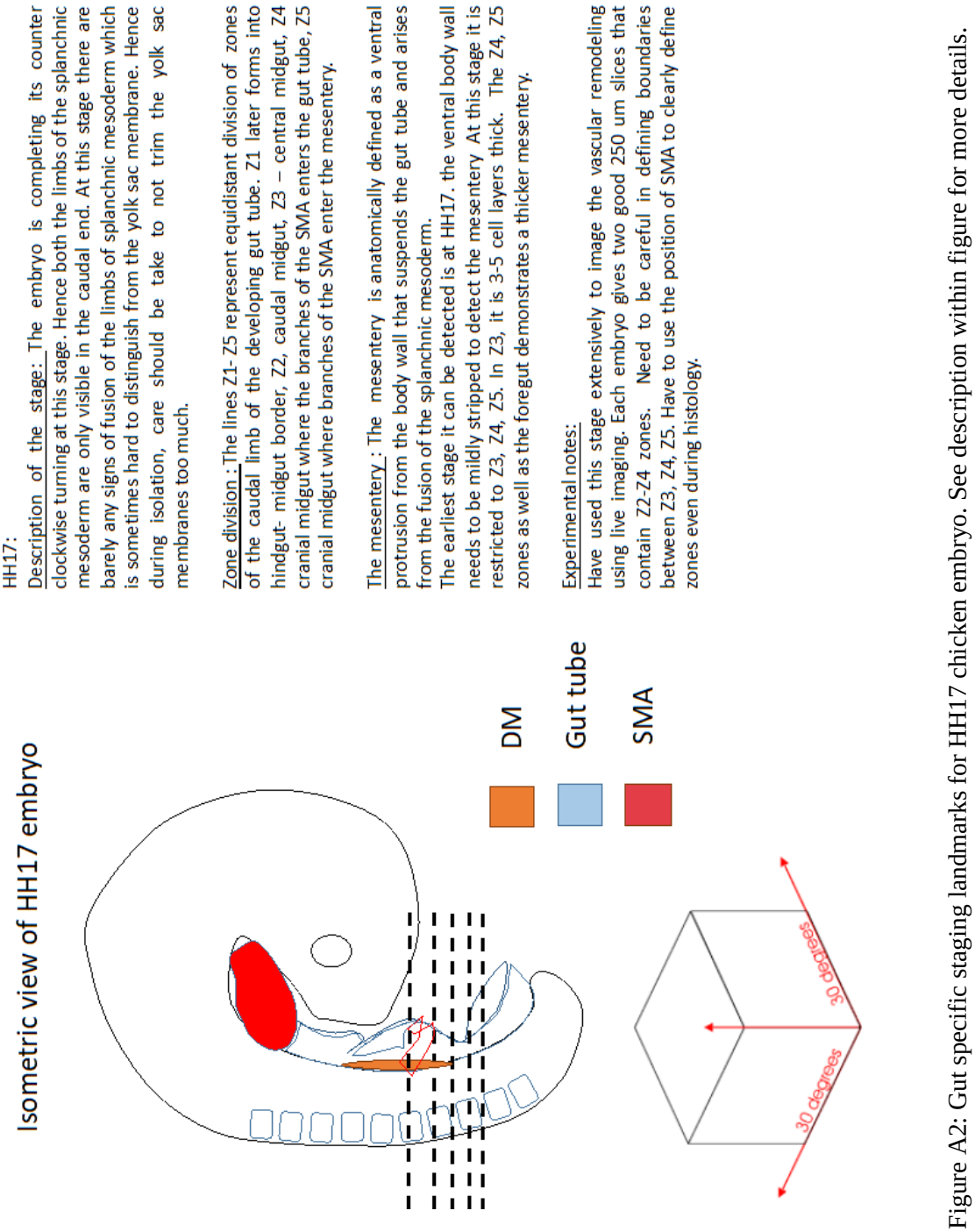

Figure A2: Gut specific staging landmarks for HH17 chicken embryo. See description within figure for more details.

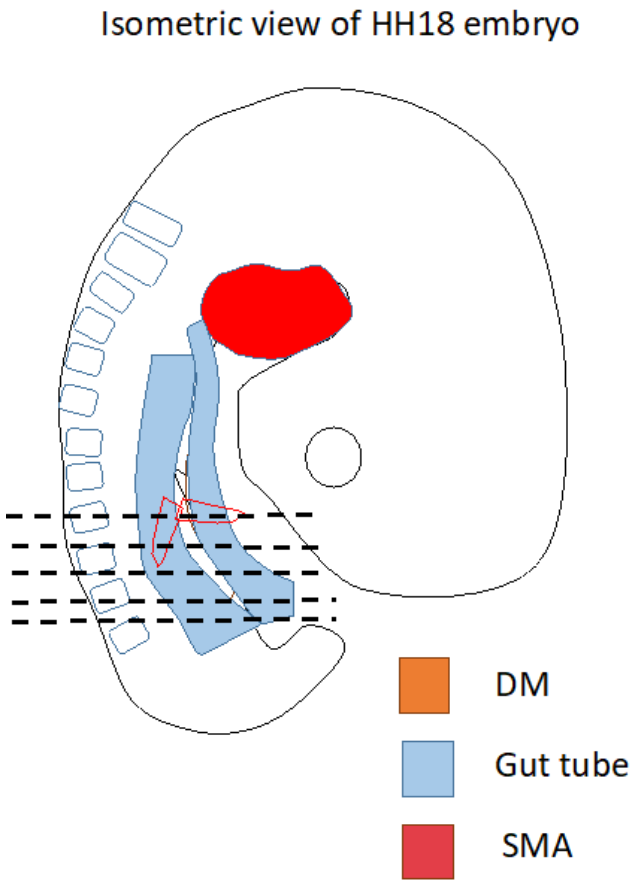

HH18:

Description of the stage: the embryo takes 4 hours to reach this stage from HH17. At this stage, the embryo has completed its counter clockwise turning at this stage. Hence both the limbs of the splanchnic mesoderm are visible when seen from the isometric view. At this stage the limbs of splanchnic mesoderm begin to fuse at the cranial and caudal ends and proceed towards the center. It is a bit easier to distinguish the splanchnic mesoderm from the yolk sac during isolations and care should be taken while isolations to prevent damage to the splanchnic mesoderm. I would still recommend not trimming the yolk sac until your eyes are trained to distinguish them

Zone division : The lines Z1- Z5 represent equidistant division of zones of the caudal limb of the developing gut tube. At the level of Z1 the limbs of the splanchnic mesoderm ventrally fuse first even before the endodermal fusion protrudes below the body wall. Z2, Z3, Z4, Z5 remain unfused.

The mesentery : The mesentery can be detected in Z2, Z3, Z4,Z5. the central midgut mesentery Z3 and Z4 are `10-15 cell layers thick and demonstrate asymmetry at this stage.

Experimental notes:

This stage is morphologically easy to distinguish from HH17 as the turning is completed. However, this stage is most dynamic with respect to the cellular architecture. So to get embryos perfectly at HH18, once the embryos reach Hh17, I will check them hourly once and isolate them as soon as they are detectably HH18 (usually 3-4 hours from HH17) . Always expect a range when collecting this stage – late HH17- early HH19 in terms of the histology and vascular phenotypes.

Figure A3: Gut specific staging landmarks for HH18 chicken embryo. See description within figure for more details.

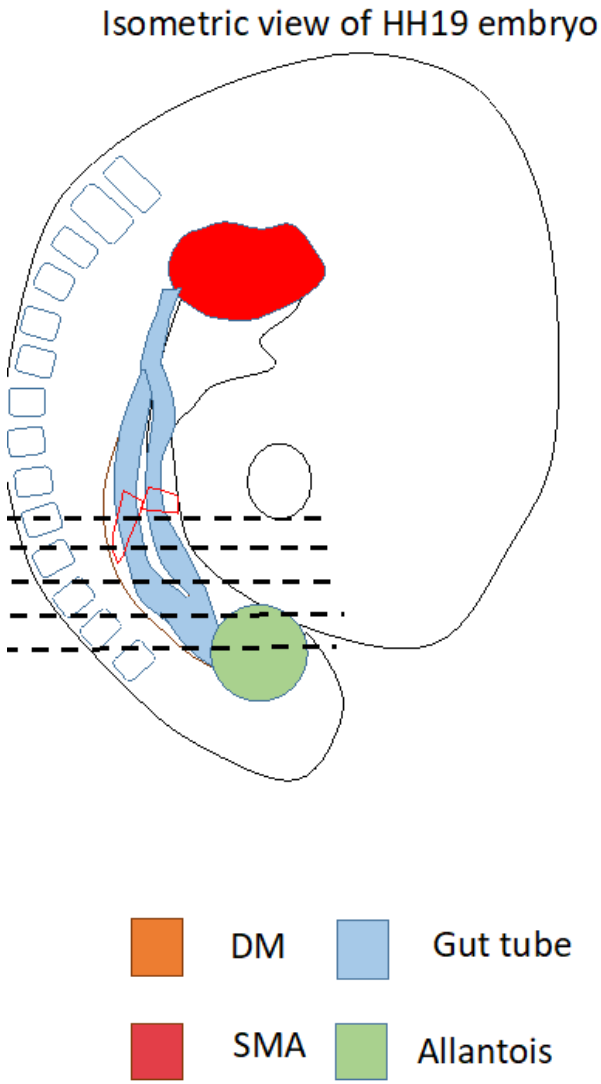

HH19:

Description of the stage:. At this stage, the body wall extends ventrally to cover the mesentery. Hence to look at the DM, the body wall must be stripped. At this stage the splanchnic mesoderm has fused in cranial and caudal ends . splanchnic mesoderm acquire gut tube like characteristics at the ventral end and can easily be distinguished from the yolk sac membranes during isolations. The gut tube also begins to distally elongate in the midgut region

Zone division :. At the level of Z1 and Z2 , the limbs of the splanchnic mesoderm are fused to form a tube. Z3, Z4, Z5 remain unfused.

The mesentery : The mesentery can be detected in all zones. Asymmetry can be seen in all zones except Z1.

Experimental notes:

This stage is morphologically easy to distinguish from HH18. However, this stage is long and it lasts for easily 8 hours. There are differences between early stage 19 and late stage 19 but it has been hard to quantify due to variations. A spectrum of phenotypes can be expected when collecting at this stage and the development of the limb bud and the gut tube should be taken into consideration for appropriate staging.

Figure A4: Gut specific staging landmarks for HH19 chicken embryo. See description within figure for more details.

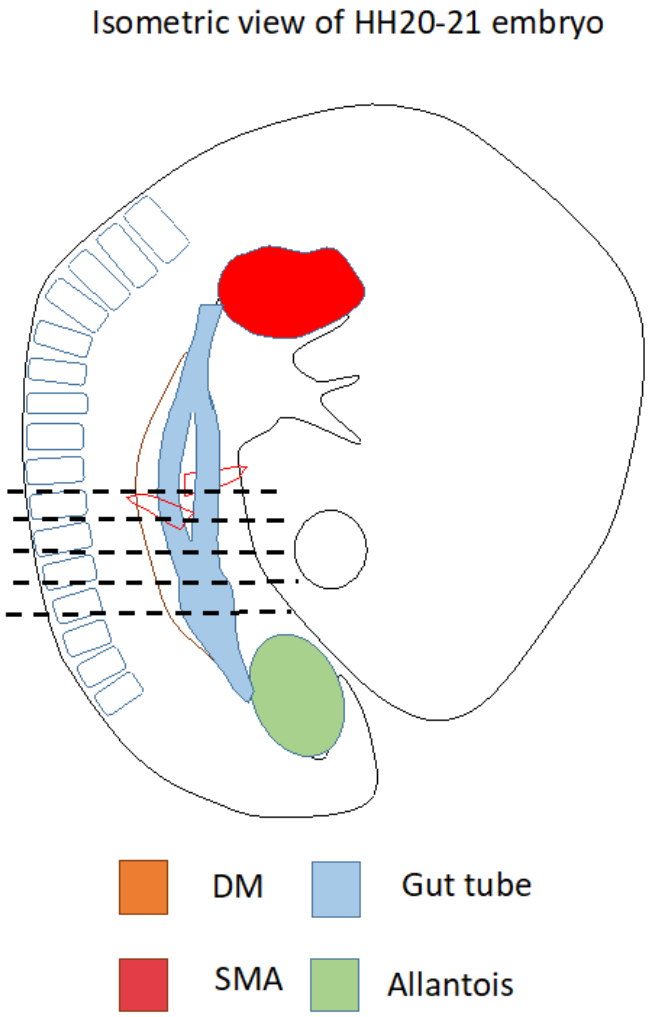

HH20-21:

Description of the stage:. To look at the DM at these stages, the body wall must be stripped. At this stage the fusion of splanchnic mesoderm has progressed in cranial and caudal ends and the gut tube in the caudal region begins to develop characteristic features like the primitive swelling of the cecum. The gut tube also has elongated further along the ventral direction in the midgut region. A pronounced leftward tilt of the gut tube between the midgut and cecum can be detected that can be considered to be the hallmark of this stage.

The mesentery : The mesentery can be detected in all zones. Asymmetry can be seen in all zones except Z1. At the level of Z4 we see that the fusion of SMA is complete and the right sided branch of SMA is slightly caudally placed compared to the left as a consequence of the leftward tilt

Experimental notes:

These stages are morphologically easy to distinguish from HH19 . It is very hard to distinguish these changes between HH20 and HH21 due to variations in gut development observed between the embryo and for most practical purposes these stages can be considered equivalent. These can only be distinguished when H & E is performed and by characterizing the extent to which the right epithelia's cell shape changes and the separation from the dorsal body wall is defined.

In terms of vasculature, once again variation is observed. It needs to be characterized based on the number of DV cords per stage as defined by Mahadevan et al, 2014.

Figure A5: Gut specific staging landmarks for HH20-21 chicken embryo. See description within figure for more details.

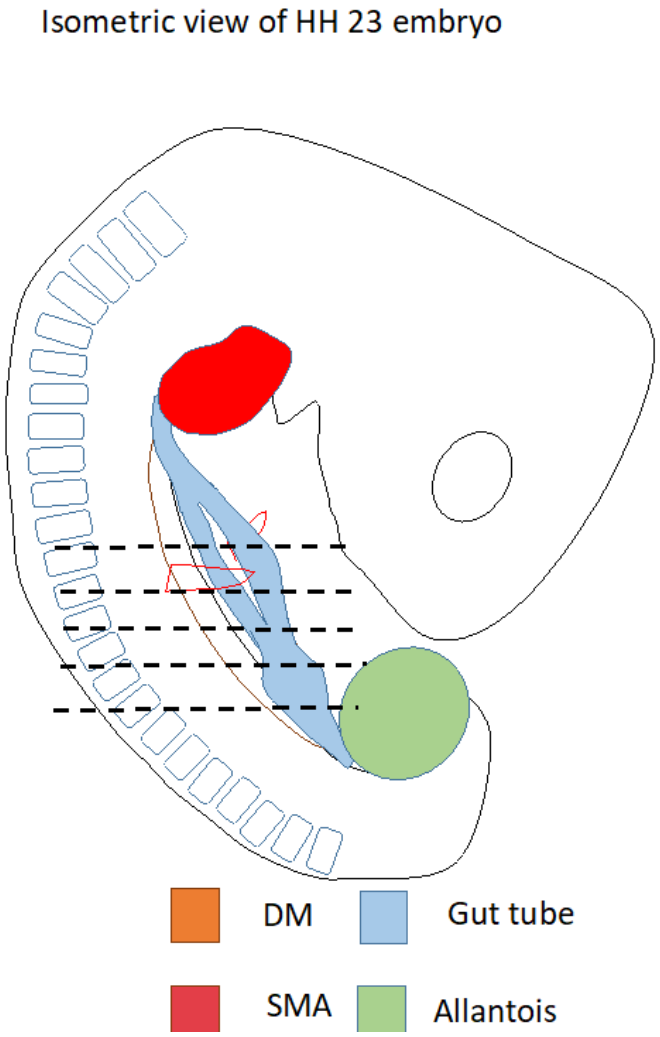

HH23:

Description of the stage:. The ventral body wall has significantly extended to cover the gut tube. Thus even the gut tube is not going to be properly visualized till the body wall is stripped. At this stage the fusion of splanchnic mesoderm is completed at the cranial and caudal ends, leaving a smaller potion unfused. The swelling of the cecum is much more pronounced . The midgut from the duodenum to cecum is more ventrally extended compared to other regions. A well pronounced leftward tilt of the gut tube between the midgut and cecum can be seen.

The mesentery : Z1, Z2, Z3 have closed gut tubes. Only Z4 and Z5 have open gut tubes. the fusion of SMA is complete and the positioning of its branches along the cranial caudal direction is significantly different showing the progression of the leftward tilt.

Experimental notes:

H & E characterization reveal that the asymmetry begin to disappear in Z4 and Z3. Z2 and Z1 now show pronounced asymmetries.

In terms of vasculature, there is some variation observed. 1. the primary LA is fully formed in 100 % of the embryos. However, some of them also have the initiation of formation of secondary LA. Hence a range of phenotypes can be expected and needs to be characterized based on the number of DV cords per stage as defined by Mahadevan et al, 2014 and Sivakumar et al , 2017.

Figure A6: Gut specific staging landmarks for HH23 chicken embryo. See description within figure for more details.

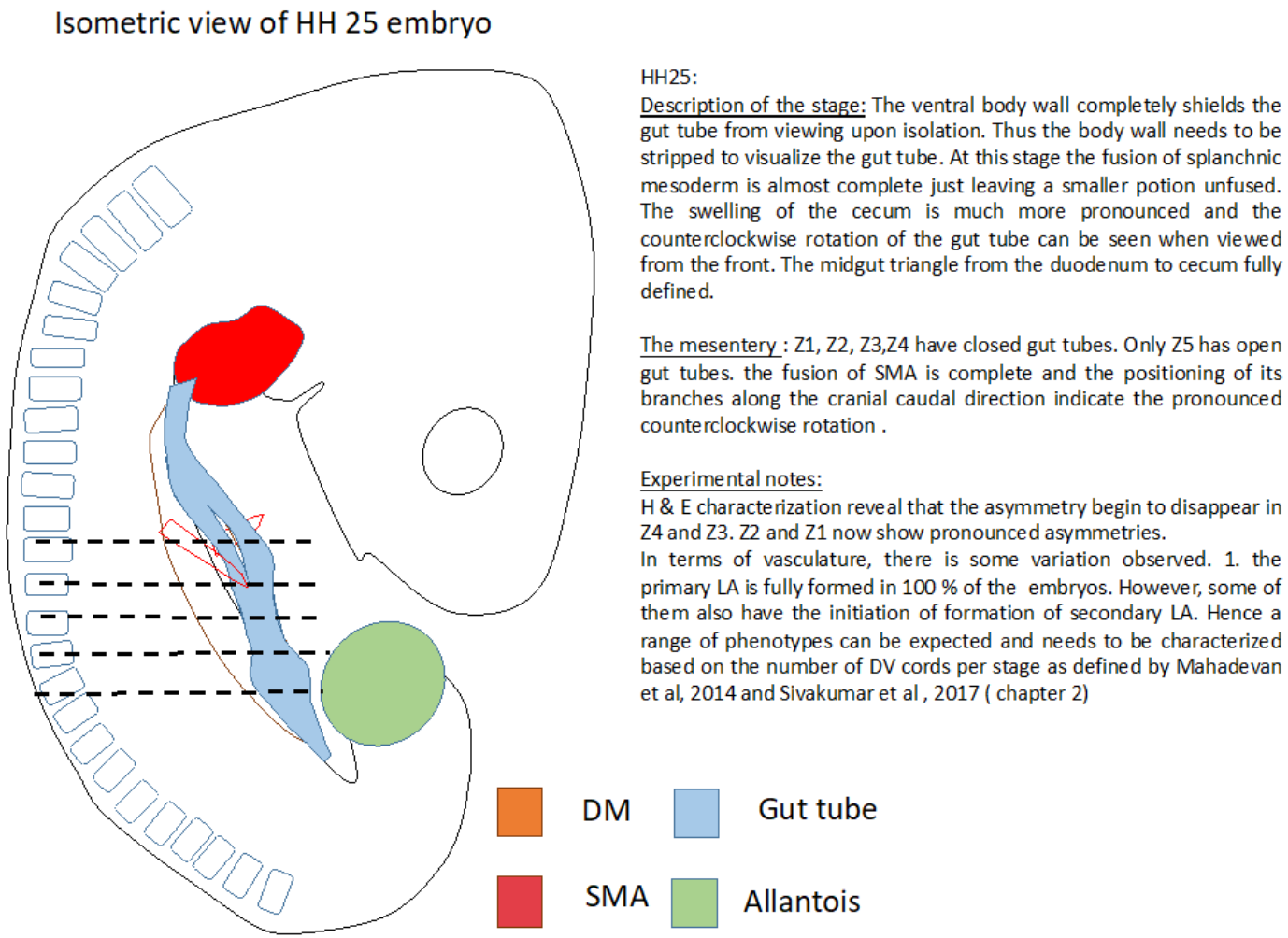

Figure A7: Gut specific staging landmarks for HH25 chicken embryo. See description within figure for more details.

AA2 Embryology: Characterization of looping topology in chicken and mice embryos

Since 2009, the Kurpios lab and others have heavily focused on understanding mechanisms responsible for the early leftward tilt which initiates the counterclockwise rotation. However, the mechanisms that are responsible for the formation of the subsequent loops have been largely uninvestigated. While work by (Savin et al ,2011) on growth and form of gut reveal that the differences in growth rate between the gut tube and the dorsal mesentery gives rise to isotropic tensile forces that results in bending of the gut tube to establish the loops, the authors have for the most part ignored the differences in the loops formed across the different regions of the gut tube. Moreover, empirical observations that I have carried out in the Kurpios lab reveal that the curvature and the timing of formation of these loops are significantly different for the different regions, but yet for the most part stereotypical and largely conserved, suggesting that a lot remain unknown about the mechanisms of formation and positioning of these loops during gut development. Furthermore, a seminal paper by (Soffers et al, 2015) performed an in-depth quantitative morphometric study on the growth and development of the human mesentery and intestine and by characterizing the looping topology across stages, they had come to similar conclusions. However, since the looping topology widely varies between species, a similar detailed characterization has not been carried out for other species such as the mouse and the chick. While some efforts have been made to study the formation of duodenum outside the initial counterclockwise rotation in mice by Sawa et al, 2013, 2015, A lot more is needed to understand the mechanisms that regulate the formation of the loops that form subsequent to the primary rotation. In the following section, I outline the key features of looping in chick and mice and the methodology I have adopted for characterizing the loops.

Establishment of loops in mice embryos:

The establishment of loops of the gut tube in mice occurs across three generations similar to the human. The first generation involves establishment of the primary loop, where the cranial limb of the of the midgut acquires a position to the right of and at the same transverse level as the caudal limb. As this rotation occurs, the gut tube extends into the umbilical cord. In mice, the gut tube, comprising the foregut, midgut, and hindgut, is formed between E9.0 and E9.5. Simultaneously, the midgut elongates, rotate and extends into the umbilical cord as a primary gut loop starting at around E10.5. the cranial limb and the caudal limb reach the same transverse level at E12.5 indicating the complete establishment of the primary loops. The second generation of loops involves establishment of four secondary loops similar to as observed in humans. The first secondary loop, also referred to as the duodenal flexure, forms between the duct of the ventral pancreas and the passage of the midgut through the umbilical orifice. It expands caudally and rightward on the right side of superior mesenteric artery and eventually extends leftward to establish the duodenal rotation. In mice, the establishment of the duodenal flexure occurs between E10.75- E13.5 as described in (Onouchi et al ,2013; Onouchi et al ,2015). While the first secondary loop develops intra-abdominally, the other loops develop extra abdominally. The 2nd and 3rd loop (coded yellow and green, respectively) develops from the remaining part of the cranial limb of the midgut and expands caudally and then leftward on the right side of the axis formed by the SMA, right vitelline vein, and the mesenteric rod. The 2nd loop is formed in the proximal part of the cranial limb of the midgut that extends into the umbilicus, while the 3rd loop is formed in the distal part of the cranial limb. The 4th loop develops from the caudal limb of the midgut between the apex and the cecum and expands cranially on the left side of the axis. While the formation of the 2nd loop initiates in mice by E12.5, the 3rd and the 4th loop develop from apex of the midgut which

undergoes a leftward cranial tilt. This positions the cecum pointing ventrally, perpendicular to the caudal cranial axis. Analysis of multiple WT embryos at E12.5, when the cranial tilt is most pronounced show that this orientation of cecum is highly conserved. and by E13.5, all of the secondary loops are fully established. Thus the establishment of the secondary loops in mice mirrors the establishment of secondary loops in human. Subsequent to the establishment of secondary loops, with drastic lengthening of the GI tract, tertiary loops form within the secondary loops. At E14, the tertiary loops in the 3rd and the 4th secondary loops initiate first. The positioning of the tertiary loops indeed demonstrates some variability. Subsequently, the resolution of the umbilical hernia occurs, which results in the formation of quaternary loops and in mice, this is complete by E16.5.

Establishment of loops in chicken embryos

In the chick, similar to mice, the establishment of loops occurs across three generations. The first generation involves the establishment of the primary loop resulting in the cranial and the caudal limbs of the gut tube occurring in the same transverse plane. This primary loop initiates via the leftward tilt of the caudal midgut observed at HH21 and is fully defined by HH25. Subsequently, four secondary loops are established similar to humans and mice however with minor differences with orientation with respect to mice and humans. The first secondary loop, the duodenal flexure, forms between the duct of the ventral pancreas and the cranial limb of the midgut. However, unlike in mice and humans where It expands caudally, in chick, it expands cranially and rightward on the right side of SMA. The formation of flexure initiates at HH24 (E4) and is complete by HH32 (E7.5). Similar to mice and humans, the 2nd loop is formed in the proximal part of the cranial limb of the midgut, while the 3rd loop is formed in the distal part of the cranial limb and the 4th loop is formed in the distal part of the caudal limb between the SMA and cecum. the 3rd and the 4th loop

develop from apex of the midgut which undergoes a leftward cranial tilt. Compared to the mouse, where the formation of the 3rd and the 4th loop is almost simultaneous, the curvature and the timing of complete establishment of the 3rd and 4th loop drastically differs in chickens possibly because the positioning of the cecum is different in chickens, and a larger region of the gut tube in the ileocecal part of the gut tube have to be established. The formation of the 3rd loop initiates by HH30 (E6.5) with the cranial limb flexing more cranially and the cranial limb flexing more caudally at the apex of the midgut and is fully established by HH35 (E9) (E9). The formation of the 2nd loop is intimately tied with the formation of the 3rd loop, where the proximal part of the cranial limb moves caudally as the distal part moves cranially. The formation of the 4th loop which appear to initiate by HH32 is formed by the cranial movement of the ileocecal part of the gut tube and is only complete by HH36 (E10). Thus by HH36 E10.5, all the secondary loops are fully established (as shown in Figure A8). The formation of the tertiary and the quaternary loops is completely different in chickens due to the lack of the umbilical orifice and have been characterized in some detail in (Southwell, 2006).

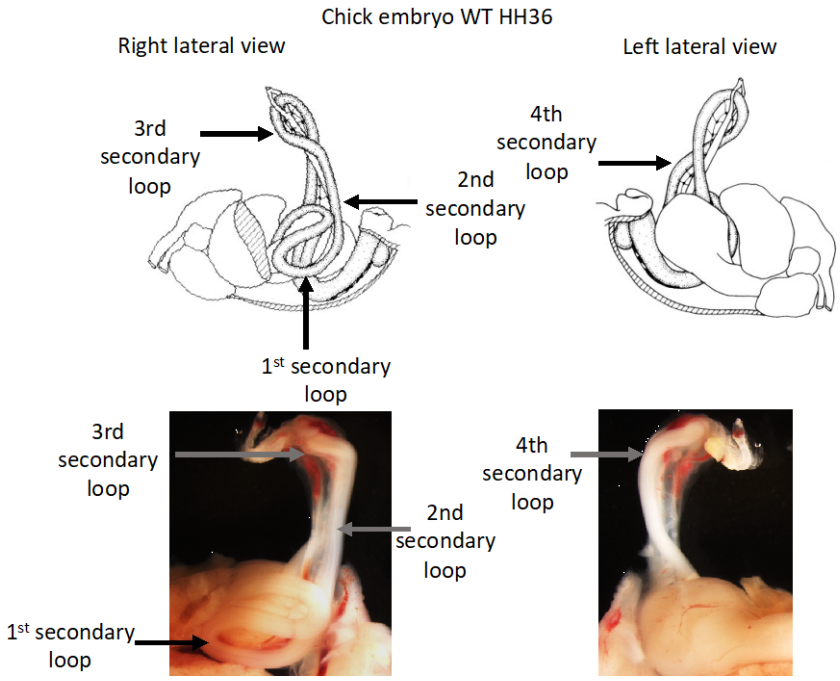

Figure A8: Example of looping in HH36 WT chicken embryo. At this stage the 4 secondary loops across the different regions of the intestine are fully established. Illustrations adapted from Southwell, 2006.

Methodology of characterizing the looping topology at the later stages:

To characterize the 3-D looping topology at the later stages,

1. After isolation of the embryo, the intestines along with the stomach need to be completely separated from the body cavity.
2. The intestines are fixed in 4% PFA overnight in large 20 ml vials to preserve the looping topology.
3. The intestines are subsequently imaged in at least 4 different orientations, and the loops are traced out.

Examples for tracing the loops for mouse E12.5, E13.5 and E18.5 are provided in Figure A9.:

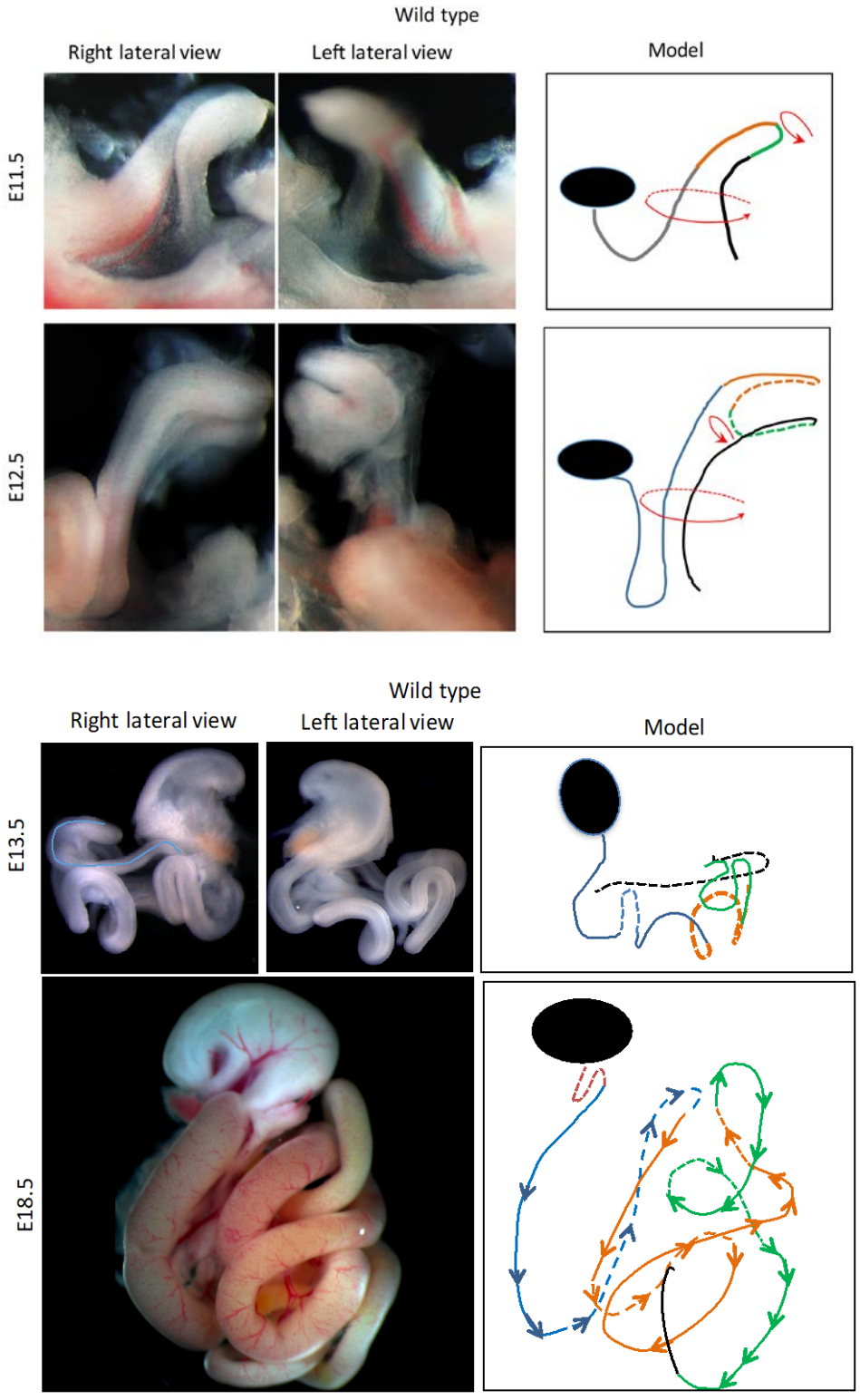

Figure A9: Tracing of loops in mice embryos of different stages. Duodenal flexure (blue line), duodenum/proximal jejunum (grey line), distal jejunum (orange line), ileum (green line) and colon (black line) have been traced.

AA3 Embryology: Processing of embryos for paraffin and cryo-sectioning

To generate tissue sections of embryos, two methods are currently being followed: A. Embedding them in paraffin B. Embedding them in OCT compound (TissueTek). The following protocol outlines the procedures for paraffin and OCT embedding of embryos.

While cryosections generally give better results for most insitu and immunostaining protocols, histology and RNAScope protocols require paraffin embedding as thinner sections can be generated while retaining the best tissie morphology. These procedures are adapted from the standard Kurpios lab protocol.

Procedure for paraffin embedding of embryos:

1. Sample preparation:
    a. For insitus and immunos : Dissect mice or chicken embryos of the required stage in PBS and immediately fix in 4% PFA (mice embryos) or 2% PFA (chicken embryos) overnight at 4°C .Subsequently, wash embryos 3 X 10 minutes in 1 X PBS at room temperature.
    b. For histology: Dissect mice or chicken embryos of the required stage in cold PBS. Remove PBS as much as possible and immediately fix the embryos in Bouin's fixative for 2 hours at room temperature and give it 10 hourly washes of 70% ethanol at room temperature till the yellow color from the Bouin's fixative is almost washed away. Subsequently, give two 100% Ethanol washes. The embryos can then can be stored for months at -20C. After that follow steps 4-8
2. If embedding in paraffin, bring the PFA fixed embryos though series of ethanol gradients (25% in PBS, 50% in PBS, 75% in water and 100%). Ensure embryos are immersed and allowed to equilibrate for at least 10 minutes in each gradient. Proper dehydration is critical. Follow steps 4 – 8.
3. Wash embryos in 1:1 ratio of 100% ethanol: xylene for 10 mins.
4. Wash embryos 2 X 15 mins in 100% xylene.
5. Wash embryos in 1:1 ratio of xylene:paraffin for 15 mins at 65°C.
6. Wash embryos in paraffin 3 X 45 mins at 65°C.
7. In an embedding mold, align embryos as required in paraffin and let it solidify. These blocks of embryos can be stored at room temperature till they are ready to be sectioned.

Procedure for cryo embedding of embryos:

1. Sample preparation: Dissect mice or chicken embryos of the required stage in PBS and immediately fix in 4% PFA (mice embryos) or 2% PFA (chicken embryos) overnight at 4°C. Subsequently wash embryos 3 X 10 minutes in 1 X PBS at room temperature.

2. After the 1X PBS wash, bring them through series of sucrose gradients (25% of 30% sucrose, 50% of 30% sucrose, 75% of 30% sucrose and 30% sucrose). The sucrose gradients should be prepared in PBS. Embryos should be washed in each gradient till they sink to the bottom of the vial, implying they have been equilibrated. Leave embryos shaking in 30% sucrose overnight. The 30% sucrose has the same density as OCT.
3. Wash embryos in 1:1 ratio of 30% sucrose:OCT for 30 mins.
4. Embed embryos after aligning them as required in the 30% sucrose/OCT mix, and place the molds containing the embryos in 2-methylbutane, cooled with liquid nitrogen. Ensure that methylbutane does not enter the cavity containing the embryos which might cause creation of bubbles. Once the 30% sucrose/OCT mix has solidified, immediately wrap the mold with the embryos in aluminum foil and store at –80°C till they are ready to be sectioned. Store slides in -80C after sectioning.

AB1 Histology: Hematoxylin and Eosin staining

The following protocol outlines the procedure for the Hemotoxylin and Eosin staining. Hemotoxylin is a basic dye which reacts with anionic components of the cells like nucleic acids and gives a purplish blue stain. Eosin is an acidic dye that reacts with the cationic components of the cells such as proteins and other components of the cytoplasm and gives it a red or pink stain depending on the acidity. Thus, the nucleus, and parts of the cytoplasm that contain RNA will stain in purple, and the rest of the cytoplasm stains up in pink. This protocol includes differentiation of colors using acid ethanol and ammonium hydroxide for color differentiation. Two protocols are included for staining paraffin embedded embryos and cryosections. Best results are obtained when embryos are fixed with Bouin's fixative.

Solutions:

1. Harris hematoxylin
2. Eosin Y (1% stock):
   Preparation notes: Add 2.0 g of water-soluble eosin Y to 40 mL of double-distilled H_2O, and mix until dissolved. Then add 160 mL of 95% ethanol, and mix. Store at room temperature.
3. Eosin Y (0.25% working stock)
   Preparation notes: Take 47 ml of water. Add 251 ml of 95% Ethanol. Add 100 ml of Eosin Y and 2 ml of Glacial acetic acid to make 400 ml of working solution.
4. Acid Ethanol:
   Preparation notes: Add 2 ml of conc. HCl in 70% Ethanol
5. Ammonium Hydroxide water
   Preparation notes: Add 6 drops of Ammonium hydroxide in 350 ml of water
6. 400 ml Xylenes – distributed in 2 containers
7. 200 ml of the following dilutions of ethanol in water : 50%, 60%, 70% , 80% ,95% poured into separate containers kept in Kurpios right
8. 2 containers containing RO H_2O

Procedure for staining paraffin sections:

(For cryo sections: Bring sections to room temperature, rehydrate sections by giving 3 washes using 1X PBS and directly go to step 4)

1. Bake slides at 60 C for at least 20 minutes. Cool slides down to room temperature for 15 minutes.
2. Place slides in slides holder and give two washes in Xylenes for 10 minutes each.
3. Remove slide holder from Xylene container, dab the slide holder in paper towels to remove excess xylenes and place the container in the following solutions:
    a. 100% Ethanol for two minutes,
    b. 95% Ethanol for two minutes
4. Remove slide holder from the 95% ethanol , dab the slide holder to remove excess Ethanol and follow it up with a 2 minute wash with RO H20 for 2 minutes.
5. Remove slide holder, dab the slide holder in paper towels to remove excess water, and place it in the hematoxylin solution for 3 minutes.
6. Remove slide holder and dab the slide holder in paper towels to remove excess hematoxylin and wash it in RO H2O for two minutes.
7. To differentiate the color, follow this water wash with a dip in acid ethanol solution for 3 seconds. **(Note: Extremely time sensitive step !!)**
8. wash it in RO H_2O for two minutes.
9. Transfer the slide holder to ammonium hydroxide water solution for 15-30 seconds. For younger embryos, stick to 15 seconds (< HH25) For older embryos (>HH25) having a 30 second expose differentiates color beautifully.
10. Quickly remove slide holder, dab the slide holder in paper towel to remove excess ammonium hydroxide and follow it up with the following time sensitive alcohol washes
    a. 50 % Ethanol for 1 minute
    b. 60% Ethanol for 1 minute
    c. 70% Ethanol for 1 minute
11. Remove slide holder and dab the slide holder in paper towels to remove excess Ethanol and dip slide holder in 0.25% Eosin for 1.5 minutes.
12. Quickly remove slide holder, dab the slide holder in paper towel to remove excess Eosin and follow it up with the following time sensitive alcohol washes.
    a. 80% Ethanol for 30 seconds
    b. 95% Ethanol for 30 seconds
    c. 100% Ethanol for 45 seconds.
13. Remove slide holder and dab the slide holder in paper towels to remove excess Ethanol and give two washes in Xylenes for 10 minutes each.
14. Mount slides using permount.

AB2 Histology: Alcian blue staining

Alcian blue stains acid mucosubstances and acetic mucins. Excessive amounts of non-sulfated acidic mucosubstances are seen in mesotheliomas, certain amounts occur normally in blood vessel walls but increase in early lesions of atherosclerosis. Alcian blue is a large planar pthalocyanine molecule with a copper atom in the center. The molecule also contains four basic isothiouronium groups which carry a positive charge. The positive charge imparted by these groups results in the attraction of the alcian blue dye molecules to the anionic sites in mucin molecules. Like mucicarmine, alcian blue does not stain neutral mucins.

Varying the pH of the alcian blue solution is a useful means for further characterization of the subtypes of acid mucins present in a tissue specimen. All acidic mucins whether carboxylalid or sulfated will ionize at --a pH of 2.5 to produce anionic groups (COO, SO3). Thus the standard alcian blue – pH 2.5 stains all acidic mucins (Figure 3). In contrast, mucins that contain predominately carboxylated carbohydrates will stain strongly with alcian blue – pH 2.5 but not with alcian blue at a pH of 1.0. The carboxyl groups do not ionize at this lower pH and as a result the mucins will display neutral characteristics. The more acidic sulphonic groups are capable of ionization at a pH of 1 and therefore stain at this pH.

Fixation: PFA fixed, Bouin's solution fixed, paraffin embedded sections. (Works best in Bouin's fixed embryos) **Positive Controls:** Small intestine, appendix, or colon.

Solutions and Reagents:

1. 3% Acetic Acid Solution
   Preparation notes: 3mL of glacial acetic acid in 97mL of distilled water
2. Alcian Blue Solution (pH 2.5)
   Preparation notes: 1g of alcian blue, 8GX in 100mL of 3% acetic acid solution. Mix well and adjust pH to 2.5 with acetic acid.
3. Alcian Blue Solution (pH 1.0)

Preparation notes: 1g of alcian blue, 8GX in 100mL of 0.1N hydrochloric acid solution. To prepare HCl 0.1 N, 8.2mL hydrochloric acid concentrate should be added to 991.8mL distilled water.

4. 0.1% Nuclear fast red solution
   Preparation notes: 0.1g Nuclear fast red, 5g of ammonium sulfate in 100mL distilled water. Dissolve ammonium sulfate in water. Add nuclear fast red and slowly heat to boil and cool. Filter and add a grain of thymol as a preservative.

Procedure for Alcian blue staining at pH 2.5 (Originally from Natasza):

1. Deparaffinize slides and hydrate to distilled water.
2. Stain in alcian blue solution pH 2.5 for 30 minutes.
3. Wash in running tap water for 2 minutes.
4. Rinse in distilled water.
5. Counterstain in nuclear fast red solution for 5 minutes.
6. Wash in running tap water for 1 minute.
7. Dehydrate and through 95% alcohol, 2 changes of absolute alcohol, 3 minutes each.
8. Clear in xylene or xylene substitute.
9. Mount with resinous mounting medium.

NOTE: There is a short version of this protocol developed by Jose from the Tabin Lab, where the samples are washed in 3% acetic acid for 3 mins in distilled water, and then stained in 0.15mg/mL (in 5% acetic acid solution) for 30 mins-several hours. It is advisable to try both to see which works better for your specific tissue sample.

Procedure for Alcian blue staining at pH 1.0:

1. Deparaffinize slides and hydrate to distilled water.
2. Briefly rinse in 0.1 N HCl to protect the subsequent Alcian Blue Solution from pH changes due to the introduction of water.
3. Stain in alcian blue solution for pH 1.0 for 2 hours.
4. Briefly rinse in 0.1 N HCl.
5. Blot sections dry with fine filter paper after this step. Do not wash with water as this will cause a change in pH and potentially cause nonspecific staining in the tissue section.
6. Counterstain in nuclear fast red solution for 5 minutes.
7. Rinse well in distilled water, dehydrate and through 95% alcohol, 2 changes of absolute alcohol, 3 minutes each.
8. Clear in xylene or xylene substitute.
9. Mount with resinous mounting medium.

Anticipated results:

1. Strongly acidic sulfated mucosubstances stain blue
2. Nuclei stain pink to red and cytoplasm stains pale pink

AB3 Histology: Trichrome staining

This stain that can be used to differentiate between collagen and smooth muscle in addition to staining the different components of the tissues listed below.

Tissue Type	Color with trichrome stain
Collagen, Bone	Green-blue
Muscle, Fibrin, Cytoplasm,	Red
Red blood cells	Yellow or red
Nuclei	Dark red-black

The procedure uses Bouin's solution as a mordant to intensify the stain. Hemotoxylin stains nuclei while cytoplasm and muscle are stained red with Biebrich scarlet-acid fuchsin. Following this, the samples are treated with polyacids phosphotungstic acid (PTA) and phosphomolybdic acid (PMA), which causes the Biebrich saelet -acid Fuschin to diffuse out of collagen fibers decolorizing them. This is followed by stained with trichrome blue, containing aniline blue which stain collagens blue. Finally, an acetic acid solution is used to rinse the sections after staining which produces a more delicate shade of tissue coloration.

Samples: Works best with Boiun;s fixed paraffinized embryos. PFA fixed tissues that are paraffin embedded can also be used.

Procedure (Adapted from Sigma protocol and Rosen Lab protocols):

1. Bake slides at 60 for 20 minutes and let the slides cool for 15 minutes.
2. Transfer slides to a slide holder.
3. Deparaffinize by using the following washes
    a. Two washes Xylenes 10 minutes each.
    b. 100% Ethanol 5 minutes
    c. 75% Ethanol / water 5 minutes
    d. 50% Ethanol/water 5 minutes
    e. 25% Ethanol/water water 5 minutes
    f. Rinse in deionized H2O
4. Place slides horizontally in a flat slidebox and cover the slides with Boiun's for overnight at room temperature. (Mordant step)
5. Transfer slides to slide holder and wash sections with running water for 5 minutes to remove the Bouin's solution.

6. Make ***Weigert Hematoxylin Solution fresh*** by adding equal volumes ***of Solution A (1% Hematoxylin in 95% EtOH)*** and ***Solution B (1.2% Ferric Chloride and 1% Acetic Acid in distilled water)***. Dip the slide holder in the fresh made up solution of Weigert solution for 5 minutes at room temperature.
7. Wash in running tap water for 5 minutes.
8. Wash in dH2O for 5 minutes
9. Transfer the slide holder to the container containing the ***Biebrich Scarlet-Acid Fuchsin***. This wash has to be given for 5 minutes.
10. Wash in dH2O for 5 minutes.
11. ***Freshly*** prepare ***Phosphotungstic/Phosphomolybdic Acid Solution by mixing 1 volume of Phosphotungstic Acid Solution and 1 volume of Phosphomolybdic Acid Solution with 2 volumes of distilled wate***r. To be discarded after one use. Precipitates should be filtered out using whatman filter paper. Transfer the slides holder to this solution and keep it immersed for 10 minutes.
12. Stain section in ***aniline blue*** for 5 minutes
13. Wash slides using dH2O for 2 minutes
14. Place slides in freshly prepred 1% acetic acid solution for 5 minutes.
15. Wash slides using dH20 for 2 minutes.
16. Give the following ethanol washes
    a. 25% Ethanol/water 5 minutes
    b. 50% Ethanol/water 5 minutes
    c. 75% Ethanol / water 5 minutes
    d. 100% Ethanol 5 minutes
    e. Two washes Xylenes 10 minutes each.
17. Mount using Permount.

AC1 Gene expression and manipulation: RNAScope

RNA SCOPE is a proprietary insitu hybridization method by ACD Cell Bio, which substantially improves the signal to noise ratio of RNA insitu hybridization. The technique uses two independent Z branched probes that are designed to bind to the target in tandem (next to each other). Each of the Z probes contain an 18-25 base pair long lower region of the Z probe that is complementary to the target RNA, a spacer sequence that connect the lower and upper regions, and an upper region that consists of 14 base pair that is complementary to the pre- amplifier probe. The two tails from the double Z probe forms a 28 base binding pair. Since the probability that two independent probes will hybridize to a non-specific target right next to each other is very low, this design concept ensures selective amplification of target-specific signals. For each target RNA species, ~20 double Z target probe pairs are designed to specifically hybridize to the target molecule, but not to non-targeted molecules. The procedure initiates with hybridization of the Z probes to the RNA target, followed by hybridization of the preamplifiers to the upper tails of the double Z probe. Amplifiers are then added which bind to the multiple sites in the pre amplifier and finally, labeled probes, containing a fluorescent molecule or chromogenic enzyme, bind to the numerous binding sites on each amplifier to give rise to the signal.

While a variety of procedures are available for RNAScope technique, the procedure below is for RNAScope manual 2.5 HD red assay. this was developed when myself and Adam O Neal, another graduate student visited Dr.Suneel Apte lab at Cleveland Clinic to learn the technique from Dr. Sumeda Nandadasa**.**

Procedure:

Sectioning and preparation: For RNA Scope analysis to work you will need to section within 24hrs of running the protocol although the fresh sections can come from blocks which are years old. When sectioning first lay out the slides onto the warming plate and then place a drop of DI water onto the slide allowing it to warm for about 5 minutes before placing the section on top of the water droplet. Cut one section at a time and do not over crowd the slide. 2-3 sections per slide is sufficient. Will outline samples with hydrophobic pen so need sufficient distance between sample sections on the slide. Best not to exceed 12 slides due to carrying capacity of slide rack used for wash steps.

Use sterile DI water in the bottle throughout every step in this protocol. Also always use fresh histoclear (same as Xylenes) and ethanol in clean containers.

(I advise starting as early as possible)

1. Bake slides for 30-40min @ 60°C
   while slides are baking conduct the following:
   1a. Set oven to 40°C. Wet humidifying paper with sterile DI water and warm for 30min.
   1b. Prepare **Pretreat #2** (50ml of 10X + 450ml sterile DI water) store @ RT
   **bring to boil in microwave right before use, no longer than 30min out. Do not boil longer than 30min as is sensitive to heat and time*
   1c. Set incubator to 40°C

2. Histoclear 2x 5min. (must be fresh, use afterwards to replace old histoclear in the H&E station)
3. 100% ethanol 2x 1min.
4. Air dry slides 5min.
5. Circle sections on slide with PAP pen (vector lab. Cat No. H-4000, Immedge pen)
6. Add **Pretreat #1** – Cover section for 10min. **move quick, add pretreat #1 after outlining w/PAP**
7. Wash with sterile DI water 2x (this is done in slide holder)
8. Submerge in **Pretreat #2** for 15min boiling
9. Submerge in sterile DI water 2x (do not slides cool between boiling and submerging in water)
10. 100% ethanol 1min 3-5x up and down
11. Air dry slides for 5min. @ RT
12. Re-circle sections with PAP-pen – 2min. dry time before next step
13. Add **Pretreat #3** (5 drops per section)
14. Place slides in 40°C oven for 30min.
    while slides are incubating conduct the following:
    14a. Warm probe @ 40°C for 10min in incubator then cool to RT
15. Add Probe for 2hrs. @ 40°C.
    while probe is hybridizing conduct the following:
    15a. 15-20min before incubation is complete warm wash buffer for 20min. @ 40°C
    15b. Bring **AMPs 1-6** to RT
16. 1X wash buffer 2min.

17. **AMP#1** for **30min.** @ 40°C
18. 1X wash buffer 2x 2min. (4min.)
19. **AMP#2** for **15min** @ 40°C
20. 1X wash buffer 1x 2min (2min.)
21. **AMP#3** for **30min** @ 40°C
22. 1X wash buffer 1x 2min (2min.)
23. **AMP#4** for **15min** @ 40°C
24. 1X wash buffer 1x 2min (2min.)
25. **AMP#5** for **30min** @ **RT**
26. 1X wash buffer 1x 2min (2min.)
27. **AMP#6** for **15min** @ **RT**
28. 1X wash buffer 2x 2min (4min.) **start making **Red Working Solution** while waiting**
29. Add **Red Working Solution** (~120ul/slide) for 10min @ RT (1:60 ratio RedB:RedA) (17ul:980ul ≈ 1ml) *RedA is alcohol sensitive and the entire rxn is light sensitive*
30. Wash with sterile DI water 2X
31. 50% Hematoxylin staining (~2min. @ RT: Optional)
32. Wash with sterile DI water until cleared
33. Add 0.025% ammonia water for ~10sec. (until blue)
34. Wash with sterile DI water 3-5X
35. Dry slides 15min. @ 60°C (shake well before)
36. Dry additional 5min. @ RT
37. Dip in xylene for -2min (make sure pen marks removed to avoid air bubbles)
38. Mount in Cytoseal 60
39. Image the following day once dried

AC2 Gene expression and manipulation: Design and preparation of Morpholinos for electroporations

Morpholino oligos are short chains of about Morpholino subunits about 25 subunits in length with each subunit comprising of a nucleic acid base, a morpholine ring and a non-ionic phosphorodiamidate intersubunit linkage. Morpholinos do not degrade their RNA targets, but instead act via a steric blocking mechanism independent of RNase H. They have higher binding affinity than DNA-based antisense oligos and are also designed to have a higher degree of complementarity with their target RNA's to minimize off targeting effects. These factors enable them to reproducibly target RNA and yield predictable results. The Morpholino oligos can be used to perform two kinds of RNA targeting. A. blocking of translation initiation B. modify pre- mRNA splicing. For designing what strategy would be the most effective way against the target of interest, the following questions need to be considered.

a. What is the extent to which the target sequences are known (are they predicted mRNA sequences/ confirmed and verified mRNA sequences etc., is enough known about the sequences upstream of the start codon to design translation blocking oligos etc.)
b. What is known about the structure of target mRNA?
c. Does the target sequence share homology with undesirable gene targets?
d. How to assay for successful gene knockdown.
e. What is the method of delivery?

The key features of an ideal Morpholino sequence is as follows

a. The base sequence of the oligo should have very little self-complementarity.
b. The oligo will be about 25 bases long and has a GC content of 40-60%. (25 bases is considered from the view point of efficacy of blocking)

c. Oligos should not have four or more contiguous G's for sake of solubility.

Ideally, my recommendation is to design both translation blocking and splice blocking morpholinos to target a gene of interest.

Things to keep in mind for designing translation blocking Morpholinos:

While the GeneTools representative in general designs the best possible Morpholino for you, it is imperative that we should be familiar with the criteria of the ideal translational Morpholino. Gene tools defines an ideal translational blocking oligo as "An optimal translation blocking Morpholino is an oligo that lies within the region from the 5' cap through the first 25 bases of coding sequence, has 40-60% GC content and has little or no secondary structure."

Usually it should be possible to find at least two non-overlapping oligo targets within the 5 'cap to start region that can meet the criterion. In such cases, it would be better to order the different oligos and do preliminary testing to determine which oligo produces the best results. It is also common practice to use two non-overlapping oligos targeting the same RNA as a specificity control set. If the oligos (used in separate experiments) phenocopy one another, that indicates that the phenotype is most likely due to interaction with the target RNA and not an unexpected interaction with a different RNA. If co-administration of the two oligos shows dose synergy when compared to the individual-administration experiments, that also supports the hypothesis that they are interacting with the same target RNA.

It is always important to BLAST Morpholino designs that the gene tools representative gives to see if they bind unexpected sequences.

Things to keep in mind for designing splice blocking Morpholinos:

Designing oligos to interfere with pre- mRNA splicing can create specific desired effects such as exon deletion or intron insertion which can be quantitated by RT-PCR which is ideal for genes for which antibodies do not exist. To design oligos that can interefere with pre-mRNA splicing, the following guidance have been given by GeneTools in their website.

1. "Targeting exon-intron boundaries or intron-exon boundaries of internal exons generally results in complete or partial deletion of the abutting exon along with its flanking introns." – when this happens, it should be taken care that the deletion of the exon causes a frame shift and either brings premature termination codon in-frame or trigger nonsense-mediated decay of the transcript.
2. However, in cases where there is a great deal of divergence in splice sites from consensus, it is also possible to generate intron insertions." – Not my favorite. But in some situations this might be needed.
3. "Targeting a splice junction of the first or last exon in a pre-mRNA generally triggers a complete or partial intron inclusion".

When designing splice Morpholinos, irrespective of the strategy, it is important to have a high RNA binding affinity.

Nature of oligos to be ordered:

GeneTools offers different types of Morpholinos. The kind of Morpholinos that are generally recommended for chick electroporations are standard oligo controls with a 3' fluorescein cap. While GeneTools offer red, blue and green fluorescent tags (the GeneTools blue, carboxyfluorescein and lissamine (rhodamine b) respectively), the red would be my last choice because it tends to decrease the solubility of Morpholinos when conjugated to the

oligo. GeneTools blue is fairly close to DAPI in its fluorescence and a DAPI filter set works, but to optimize the fluorescence signal you need a custom filter set. That leaves carboxyfluorescein, which is a bright fluor but like all fluoresceins it will photobleach in intense light. I prefer carboxyfluorescein, minimizing bright light exposure until it is time for a measurement. Regarding the amount of Morpholinos to order, In general, I recommend starting with 300nmol vial of the custom oligo of your interest as that will last at least 10 rounds of electroporations.

Making stock solution of morpholino oligos and storage:

The Morpholinos arrive in brown vials that contain lyophilized powder. It is best to reconstitute in the same vial. Morpholinos should be stored at room temperature as they are much more stable than DNA, and at the same time freezing will affect its solubility. While Gene Tools recommends to make the stock solutions of Morpholinos at 1 mM concentration. For chick electroporation, Dr. Marcos Simoes Costa advised me to make the stock solutions at 2 mM concentration. So care should be taken while reconstituting so that the stock solution is at 2 mM concentration.

Electroporation mix using Morpholinos:

Dr. Marcos Simoes Costra recommends to electroporate Morpholinos with a carrier DNA (a promoterless vector- In my case, I have used pSlax) and he says that this helps with better delivery of DNA.

In addition, he recommends, adding Tris pH 8 for extra stability of morpholinos.

For a 20 ul electroporation mix:

Morpholinos of interest (2mM) = 10 ul
Carrier DNA: dilute to 1ug/ul
Tris ph8 (100uM): diluted to a final concentration of 10uM
Luna mix: 6.6 ul.
H20: to make it up to 20ul.

This should last for electroporating 100 embryos.

This would dilute the concentration to 1mM which is then ultimately diluted to a 100 uM concentration that we are injecting into the HH14 embryo, that takes about about 10 ul in wet volume. Thus the Theoretical concentration that is being delivered to cells is between 1-10 uM

AC3 Gene expression and manipulation: Preparation of MU-Xyloside soaked beads

4-Methylumbelliferyl-β-D-Xyalopyranoside (MU- Xyl) is a flurogenic substitute of B-D-Xyloside and is a substrate for B- xylosidase. When incubated wit hcells such as chondrocytes, Mu-Xyl acts as the primers for the exo-polymerases that add glucuronic acid to the xyloside primer to make up the glycosaminoglycan (GAG) chains. In fact, adding Mu-Xyl in excess, results in secretion of fluorgenic GAG into the medium that have 4- methylumbelliferone in the reducing termini. This results in depletion of endogenous levels of sugars and that drastically affect the synthesis of GAGs that require glucuronic acid such as Hyaluronan and Chondroitin Sulfate. Since it functions as B-Xyloside primer, it is less toxic than 4 MU itself which has other side effects that causes the toxicity.

Reagents:

1. Pen-Strep (SV20010-Fisher)
2. Resin beads (143-1255-BioRad)
3. 4-Methylumbelliferyl-β-D-Xyalopyranoside-Sigma #M7008 .
4. Luna Mix.

Storage: 0C or -20C.

Several references exist that have used Mu-Xyl in invtro culture at 1 mM. For in vivo beading, I have performed empherical trials with the following concentrations: 1,5, 10 , 20, 40, 80, 120nM. Typically, I see the strongest phenotype between 5 mM and 120 mM.

To get the maximal survival rate, I have standardized the concentration to 40mM

Procedure:

1. Weigh 0.2-0.3g of the beads into a 1.5mL centrifuge tube.
2. Wash beads 3X with 1mL of 1XPBS by centrifuging at 5000G for 1 min each time.
3. In a separate tube, weigh out 12 mg of Mu- Xyl and dissolve it in 1 ml of DMSO by repeated pippeting.[for 40mM]
4. Add MU-Xyl to the tube containing beads and allow the beads to soak in MU-Xyl overnight at RT, with gentle rotation of the tube.
5. Add 5ul of Luna mix to 200ul of the inhibitor/beads mix and let the tube rotate for another 2 hours at RT, till the beads are no longer colorless.
6. Use beading technique as described in Aparna Mahadevan's thesis (Aparna Mahdevan, 2016 – Section A7)

AD1 Immunostaining: HABP staining on tissue sections

Hyaluronan (HA) is non-immunogenic (i.e. antibodies cannot be raised against it). However, it can be detected in tissues and cells by use of a "hyaluronan – binding – protein" (HABP). Typically, HABP is isolated from bovine nasal cartilage and is comprised of a combination of G1 and the cartilage "Link" protein (both of which have conserved linkmodule HA binding domains. Biotinylated HABP permits the addition of a variety of fluorophore or enzymatic (i.e. horseradish peroxidase or alkaline phosphatase) streptavidin constructs for fluorescent or light microscopy. The following protocol has been Adapted and modified from Programs of excellence in Glycosciences, Cleveland Clinic's HABP protocol (NHLBI P01HL1071247) and amsbio protocol for HABP http://www.amsbio.com/protocols/HABP-Protocols-for-IHC-and-ELISA.pdf

Reagents:

1. Blocker (3% HIGS in PBST): Add 1. 5 ml of Heat inactivated goat serum (Invitrogen, cat number: 16210072) to 50 ml PBS.
2. Biotinylated Hyaluronan Binding Protein (EMD/Millipore/Calbiochem #385911, 50 ug)
Reconstitution: Add 100 microliters of water to 50 mg HABP. Vortex, and let sit at room temperature for 20 minutes. Vortex again, centrifuge and make 10 aliquots of 10 µl each. Store at –80 C indefinitely. Use at 1:40.
3. Fluorescent streptavidin secondary antibody: Streptavidin, Alexa Fluor 488 conjugate (green) (S32356 Invitrogen).
4.Fluorescent Mounting medium: Prolong Anti fade (Vector Laboratories, H-1200)

Protocol:

Note: the following protocol is for cryosections (15-20 microns thick). For paraffin sections (recommended thickness 6-10 microns), after overnight drying at 37 C, bake slides for 20 minutes @ 60 C followed by a 10 min cool down. Transfer slides to a slide holder and do the following washes: 2 X wash with Xylenes 10 min each, ethanol gradients washes (100%, 75%, 50%, 25% dilutions of ethanol made in dH20) 10 min each, 2X washes in dH20, followed by antigen retrieval [1ml of antigen unmasking solutions (H3300 vector labs) in 100 ml of water, microwaved up to boiling point, cool down at 4C for 20 min] before following the protocol below.

1. Rehydrate slides by washing slides with PBS - 10 min, 3X at RT.

2. Rinse slides in PBST (PBS + 0.03% Tween) [Note, addition of tween helps in proper spreading of blocker solution]

3. Place slides in humidified chamber; apply sufficient amount (500 ul- 1 ml) of blocker per slide to cover the sections. Let the slides sit in RT for 45 mins.

4. Dilute HABP 1:40 (mixed with another primary antibody in the same tube if you have one) in blocker. Decant blocker from slide onto a paper towel, by tapping the slide to the paper towel, and add the HABP (with second primary if you have one) to the section in a sufficient quantity to cover it. Let it sit at room temperature for 45 min.

5. Decant the antibody solution onto a paper towel and wash the slides with PBST 3X, 5 min, RT

6. Dilute the streptavidin 1:500 and DAPI (1: 2000) in blocker. Apply sufficient amount of streptavidin –DAPI mix to cover sections. Incubate at room temperature for 45 min in dark.

7. Give 3 washes in PBST, 2 washes in PBS, 1X H20 and apply few drops of Prolong antifade. Place cover slip, wipe excess antifade, and apply nail polish on edges of cover slip.

Recommended controls:

1. Positive control: Any sections that contain neural tube and notochord of embryos (preferably at stages HH17 and above.) You should see signal surrounding the neural tube, and the signal surrounding the notochord {note: notochord by itself does not have any HA signal)

2. Negative controls:

a) Hyaluronidase treatment: Use adjacent sections of the tissue that you are investigating for this treatment. This treatment has to be done after rehydration with PBS and before rinsing with PBST. (between steps 1 and 2)

Reagent: Streptomyces hyalurolyticus; EMD/Millipore Product #389561)

Reconstituting hyaluronidase to conc of 0.2 TRU/ ul or 200 TRU/ml.: Add 500 µl 100 mM ammonium acetate to one ampule of Streptomyces hyaluronidase containing 100 TRU of enzyme. Incubate at RT 20 min. Rotate the ampule to make sure that the liquid comes into contact with the entire surface of the bottom quarter of the ampule. Make 25 µl aliquots in PCR tubes. Store at –80 C indefinitely. Final concentration: 0.2 TRU/µl

Hyaluronidase treatment prescribed by amsbio protocol:

After rehydration with PBS, Treat slides with reaction buffer of Hyaluronidase (100mM Sodium acetate buffer, pH6.0) for 15min at 37°C. No wash .
Treat with Hyaluronidase (200TRU/mL; 100mM Sodium acetate buffer, pH6.0) for 2hrs at 60°C.
Wash with PBS 3X 5 min, RT.
Resume with Blocking. (Steps 2,3)

b) No primary control – (To detect background staining by secondary and to look at autoflourescence of tissues) – Sometimes, basement lamina, red blood cells are likely to autofluresce.

AE1 Live imaging: Ex vivo live imaging of embryonic explants

This is a technique that I had developed to study the cellular and vascular dynamics of embryonic gut explants to understand the asymmetric processes that are happening in the DM. I have used electroporated chick explants to investigate the cellular processes in left and right DM. I have used transgenic quails (Tie1-H2b-YFP) to characterize the vascular dynamics and I have used Prox-1 GFP mice to characterize lymphatic development in the gut. This technique is best used for studying left right asymmetries and is not optimal for analyzing processes that happen in three dimensions such as vascular remodeling.

Before start of experiment:

Have clean chilled PBS (1 L) along with 4 falcon tubes ready.

Have petri dishes for doing the dissections ready.

Have cleaned forceps, spatula ready.

Have a falcon tube containing 50 ml of F12 media+10mM HEPES+ 1X P/S ready in an ice bucket. (Another tube as backup)

Have another falcon tube containing 10 ml F12 media + 1% agarose ready at room temperature. (Another tube as backup)

Have imaging slots booked at least 3 days before the experiment.

Keep a falcon tube containing 50 ml of 1X PBS, in a plastic beaker in the 37 C incubator at the core facility at least 3 hours before starting the experiment.

Sample preparation:

1. Electroporated Chick embryo explants:
    a. Plan in such a way that the eggs will be HH14 for elextroporations and have reached HH17 in time for the live imaging slot.
    b. Embryo dissection. Carefully and quickly dissect out the embryos at HH17. Have clean chilled PBS ready. Transfer into chilled PBS once dissected. Remove head and limb buds.
2. Transgenic Quail explants:
    a. Plan in such a way that the eggs will be HH17 four hours before the imaging starts. The timing of the quail embryos is slightly different from the chick and the experiments should be planned accordingly.

b. Embryo dissection: Carefully and quickly dissect out the embryos at HH17. Have clean chilled PBS ready. Transfer into chilled PBS once dissected. Remove head and limb buds.

3. Mice explants:
    a. Mice dissection. Carefully and quickly dissect out the embryos at E 11.0. Have clean chilled PBS ready. Transfer into chilled PBS once dissected. Remove head and limb buds.

Procedure:

1. Preparation of embryonic slices:

    Take the dissected embryo, one at a time, place it in tissue chopper with clean mica plate, remove excess water with Kim wipes, but hold the embryo using the forceps while doing this to prevent loss of embryo. (Excess water can result in tissue sliding in-between chopping- can result in loss of slices)

    a. Set chopper to chop at 200 um thickness. Once the embryo is chopped, remove the mica plate, and squirt down clean PBS using a Pasteur pipette to transfer the slices into a glass dish.
    b. Once the slices are in the dish, sort out the best slices that contain intact mesentery using fine forceps, and carefully chop of the body wall remains. The slices tend to be sticky. Take the selected slices carefully and transfer them to a vial that has F12 media + 10mM HEPES+ P/S and keep the vial in ice. If there are more than 10 slices, prepare back up vial(s) each containing 10 slices. (Transfer can be done using Pasteur pipettes)
    c. Do this for other embryos.
    d. Carefully pack the vial containing the slices with para-film along with forceps+ media falcon tubes+ the live imaging dishes + 1 glass dish+ a plastic beaker (to hold the agarose – media falcon tube while microwaving in a tray and head to imaging core facility at Weill Hall.

2. Embedding of the slice explants:

    a. Transfer slices from the vial to a glass dish under the stereoscope in Zipfel lab (the glass dish contain PBS/Media (@ 37C).

    b. Open the live imaging dish, open its cover and keep it ready under the stereoscope.

    c. Take the falcon tube containing F12 + agarose to Becky's (Warren Zipfel) lab microwave. Do 5 second bursts (4 times- 20 seconds total heating) and remove the falcon tube from the microwave when the media is bubbling. Heating in 5 seconds intervals gives greater control and prevents spillage of media in the microwave oven. Immediately proceed to embed the slices in the agarose/F12 mix before the agarose solidifies. ***NOTE: If there is a mistake in embedding, the agarose/F12 cannot be re-melted. This damages the tissue irreversibly.***

d. Take a Pasteur pipette and place a decent size agarose media bubble in the **center**. Quickly add slices+ very little media. Using good forceps, manipulate the slices such that a) the slices are as flat as possible with no damage b) the slices are in the center of the dish. (Best embedding is achieved with not more than 5 slices per plate since proper embedding needs to be completed before agar solidifies.
e. Wait for agar to solidify. Add surrounding layer to root the agar bubble firmly on the dish. Make the subsequent layer thin but strong enough to cover the whole agar. Wait for this layer to solidify before adding the F12 media+ HEPES+ P/S . Add enough to submerge the whole bubble layer. Keep it in 37C incubator and proceed to turn on the microscope.

3. Basic microscope settings (This only describes the minimal settings to keep in mind. Proper training on the microscope is strongly advised, with either Dr. Rebecca Williams or Dr. Warren Zipfel. Also mention the intention of your experiment when getting trained to receive the most optimal training)

a. Have incubator along with the CO2 chambers set up.
b. Use the following parameters for image acquisition:
    Image acquisition: 1024*1024 pixels
    Bit size: 16 bits
    Acquisition speed: 7 or 8.
    Zoom: 0.6- 0.7 to capture both dorsal/ ventral and to allow for XY drift.)
    Laser settings: not more than 6-7 %
    Pinhole: 1 AU (essential for Z acquisition)
c. Set appropriate Z intervals to minimize time of acquisition.
d. Trial images have to be conducted to set the frequency of imaging in time lapse.
e. After finalizing parameters, set acquisition for overnight and acquire.